

Analysis and Control of Partly-Developed Leading-Edge Vortices

Andreas Norbert Hövelmann

Vollständiger Abdruck der von der Fakultät für Maschinenwesen der Technischen Universität München zur Erlangung des akademischen Grades eines
Doktor-Ingenieurs
genehmigten Dissertation.

Vorsitzender: Prof. Dr.-Ing. Mirko Hornung
Prüfer der Dissertation: 1. apl. Prof. Dr.-Ing. habil. Christian Breitsamter
2. Prof. Arthur Rizzi, Ph.D.

Die Dissertation wurde am 03.03.2016 bei der Technischen Universität München eingereicht und durch die Fakultät für Maschinenwesen am 22.06.2016 angenommen.

© Andreas Hövelmann, 2016

All rights reserved. No part of this publication may be reproduced, modified, re-written, or distributed in any form or by any means, without the prior written permission of the author.

Typesetting: **L^AT_EX**

"You can't connect the dots looking forward; you can only connect them looking backwards. So you have to trust that the dots will somehow connect in your future. You have to trust in something - your gut, destiny, life, karma, whatever. This approach has never let me down, and it has made all the difference in my life."

Steve Jobs

Vorwort

Die vorliegende Arbeit entstand während meiner Tätigkeit als wissenschaftlicher Mitarbeiter am Lehrstuhl für Aerodynamik und Strömungsmechanik der Technischen Universität München. An dieser Stelle möchte ich all denen, die mich in dieser Zeit begleitet haben, herzlich danken. Besonders hervorheben möchte ich jene Personen, die einen ganz besonderen Anteil am Gelingen dieser Arbeit hatten. Ohne deren Unterstützung wäre ich nicht an dieses Ziel gelangt.

Für die ausgezeichnete Betreuung und Unterstützung während der gesamten Zeit gilt zuallererst mein besonderer Dank meinem Doktorvater Herrn apl. Prof. Dr.-Ing. habil. Christian Breit-samter. In allen Phasen der Arbeit war er für mich jederzeit ansprechbar und hatte immer ein offenes Ohr, um in fachlicher Hinsicht über die Probleme und Herausforderungen, aber auch die Lichtblicke und Erfolge der täglichen Arbeit zu diskutieren. Zudem möchte ich ihm auch Danke sagen dafür, dass ich die Gelegenheit wahrnehmen durfte, zusätzlich zu meinem Forschungsprojekt SAGITTA von Airbus Defence & Space in internationalen NATO-STO-Forschungsgruppen mitzuarbeiten. Die damit verbundenen Erfahrungen haben maßgeblich zum Erfolg der Arbeit beigetragen und mich fachlich wie auch persönlich enorm vorangebracht.

Ebenfalls bedanke ich mich bei Herrn Prof. Arthur Rizzi, Ph.D., der die Aufgabe des Zweitprüfers übernommen hat. Seit meiner Studienzeit an der KTH Stockholm im Rahmen eines Doppeldiplomprogramms im Jahr 2008/2009 sind wir uns wiederholt in der Aerodynamikwelt begegnet. So war ich sehr froh, als er in diesem Frühjahr zustimmte, die Aufgabe des Zweitprüfers wahrzunehmen. Für die Übernahme des Prüfungsvorsitzes danke ich zudem Herrn Prof. Dr.-Ing. Mirko Hornung sehr herzlich.

Die internationalen Kontakte, die ich während meiner Arbeit knüpfen konnte, waren immer wieder wertvolle und motivierende Gesprächspartner für mich. Mein Dank gilt hier besonders den Herren Okko J. Boelens, Jim Luckring, Ph.D., Dr.-Ing. Stephan M. Hitzel, Dr.-Ing. Andreas Schütte, Prof. a.D. Dr.-Ing. Dietrich Hummel, Neal Frink, Ph.D., und Frau Kerstin Huber.

Weiterhin möchte ich allen Kollegen/-innen am Lehrstuhl Danke sagen für die gemeinsame Zeit. Besonders erwähnen möchte ich in diesem Zusammenhang die Herren Florian Knoth, Moritz Gra-wunder, Andrei Buzica, David Schwalb, Patrick Pözlbauer und Stefan Pfnür, die mich als Studenten und Kollegen in meinen Projekten unterstützt und so wertvolle Beiträge geleistet haben.

Den wohl wichtigsten Anteil am Gelingen dieser Arbeit hatte aber zweifelsohne meine Familie. Vor allem die bedingungslose Unterstützung meiner Eltern Annick und Heinz-Clemens, meines Bruders Thomas, und meiner Freundin Johanna hat mir immer geholfen, das große Ziel nicht aus den Augen zu verlieren und gezielt auf den erfolgreichen Abschluss hinzuarbeiten. Dir, Johanna, vielen lieben Dank für all den Rückhalt, den du mir jeden Tag gibst, und die Freude, die unser gemeinsames Leben auszeichnet.

München, im August 2016

Andreas Hövelmann

Abstract

Comprehensive aerodynamic investigations of leading-edge vortex flow phenomena are presented in this thesis on moderately-swept, low-aspect-ratio wing configurations with rounded leading edges and spanwise-varying leading-edge contours. As a result of relevant design criteria of unmanned (combat) aerial vehicles (U(C)AV), these types of wing configurations have become subject of aerodynamic research for the past decade. The respective flow physics is commonly associated with the existence of partly-developed leading-edge vortices, as both attached flow and separated vortex flow regions are observed with increasing angle of attack along the wing span. Considering the rounded leading edge, the flow separation onset occurs from a smooth surface separation. Amongst others, the location depends on the angle of attack, the wing sweep angle, the leading-edge radius, and the boundary-layer characteristics determined by the Reynolds number. In this context, the present thesis focuses on the analysis and control of partly-developed leading-edge vortices on two diamond wing configurations, namely the AVT-183 and the SAGITTA configuration. The corresponding investigations are undertaken by a combined experimental and numerical approach at low-speed wind tunnel (W/T) conditions.

The analysis of the AVT-183 configuration with entirely rounded leading edge provides a consistent flow-physical description of the leading-edge vortex formation from a smooth surface separation on boundary-layer level in the incipient separation region. More downstream, the vortical structure then appears as a large-scale leading-edge vortex on the diamond wing surface. The leading-edge vortex is characterized by wake-type vortex core flow and instantaneously shows vortex bursting tendencies. Local turbulent maxima are identified as well in this region and decrease towards the trailing edge. The observed flow field phenomena are characteristic of moderately-swept and vortex-dominated wing configurations with rounded leading edges.

The effects of leading-edge contour modifications are discussed on the SAGITTA configuration, which features a spanwise-varying leading-edge contour. In total six different configurations are considered in the analysis, thus defining various concepts of passive flow control. The existence of a non-uniform leading-edge geometry is motivated by mission requirements of related U(C)AV applications with respect to aerodynamic performance, stability concerns, and low-signature design criteria. In consequence of the increased airfoil thickness of the SAGITTA configuration compared to the AVT-183 configuration, the formation of leading-edge vortices based on smooth surface separations is considerably delayed to higher angles of attack. Sharp leading-edge segments are mostly required to promote leading-edge vortex flow at low to moderate angles of attack. Depending on the applied leading-edge contour modifications, leading-edge vortices due to rounded leading edges finally emerge with increasing angle of attack. The integral aerodynamic characteristics are therefore influenced, especially the drag and the pitching-moment coefficients. Consequently, the longitudinal stability behavior is thereby controlled. The lift coefficients are rather insensitive to the leading-edge shape, and thus determined by the wing planform.

Zusammenfassung

Die vorliegende Arbeit befasst sich mit der aerodynamischen Untersuchung von Vorderkantenwirbelphänomenen an moderat gepfeilten Flügelkonfigurationen mit kleinem Seitenverhältnis, welche runde oder spannwitig variierende Vorderkanten aufweisen. Resultierend aus Designkriterien von unbemannten Luftfahrzeugen sind diese innerhalb des letzten Jahrzehnts zum Gegenstand aerodynamischer Forschung geworden. Die damit verbundene Strömungsphysik ist mit der Existenz von teilentwickelten Vorderkantenwirbeln verknüpft, die mit steigendem Anstellwinkel sowohl Bereiche anliegender als auch wirbeldominierter abgelöster Strömung ausbilden. Im Fall der runden Vorderkante ist die Strömungsablösung örtlich nicht fixiert. Der zugehörige Ort ist dabei unter anderem vom Anstellwinkel, dem Pfeilungswinkel, dem Vorderkantenradius und dem durch die Reynolds-Zahl bedingten Grenzschichtzustand abhängig. Die vorliegende Arbeit konzentriert sich in diesem Zusammenhang auf die Analyse und Kontrolle von teilentwickelten Vorderkantenwirbeln an zwei Diamantflügelkonfigurationen, der AVT-183- und der SAGITTA-Konfiguration. Die Untersuchungen liegen einem kombinierten experimentellen und numerischen Ansatz zugrunde und werden bei Niedergeschwindigkeits-Windkanalbedingungen durchgeführt.

Die Analyse der AVT-183-Konfiguration mit komplett runder Vorderkante liefert eine konsistente strömungsphysikalische Beschreibung der Vorderkantenwirbelbildung durch die Strömungsablösung nahe der Flügelvorderkante und innerhalb der Grenzschicht. Erst weiter stromab bildet sich die Wirbelstruktur dann als großskaliger Vorderkantenwirbel aus. Dieser ist durch Untergeschwindigkeiten im Wirbelkern gekennzeichnet und zeigt umgehend Anzeichen von Wirbelaufplätzen. Lokale Turbulenzmaxima sind folglich in diesem Bereich ausgeprägt und nehmen in Richtung der Flügelhinterkante ab. Die auftretenden Strömungsphänomene sind charakteristisch für eine moderat gepfeilte, wirbeldominierte Flügelkonfiguration mit runder Vorderkantengeometrie.

Die Effekte von Vorderkantengeometriemodifikationen in spannwitiger Richtung werden an der SAGITTA-Konfiguration diskutiert. Die Analyse beruht auf sechs verschiedenen Konfigurationen, welche für sich jeweils Konzepte passiver Strömungskontrolle beschreiben. Die Modifikationen leiten sich aus Missionsanforderungen im Hinblick auf die aerodynamische Leistung, Stabilitätsanforderungen und Designkriterien bzgl. radararmer Signatur ab. Durch das aufgedickte Flügelprofil der SAGITTA-Konfiguration gegenüber der AVT-183-Konfiguration entstehen die Vorderkantenwirbel infolge runder Vorderkanten erst bei höheren Anstellwinkeln. Um Vorderkantenwirbel auch bei niedrigeren Anstellwinkeln zu erzeugen, ist eine scharfe Vorderkante erforderlich. Abhängig von den untersuchten Konfigurationen findet mit steigendem Anstellwinkel dann teilweise auch eine Vorderkantenwirbelbildung infolge der Strömungsablösung an der runden Vorderkante statt. Die integralen aerodynamischen Charakteristika werden dadurch beeinflusst, besonders die Widerstands- und Nickmomentenkoeffizienten. Das Stabilitätsverhalten der Längsbewegung wird folglich ebenfalls kontrolliert. Die Auftriebsbeiwerte sind durch die Vorderkantengeometriemodifikationen nur schwach veränderlich und sind daher durch die Flügelgrundrissform bestimmt.

Table of Contents

List of Figures	v
List of Tables	xiii
Nomenclature	xv
1 Introduction	1
1.1 Background and Motivation	1
1.2 State of the Art	3
1.3 Research Objectives	8
1.4 Analyzed Diamond Wing Configurations	10
1.5 Thesis Outline	12
2 Fundamentals	15
2.1 Similarity and Dimensionless Parameters	15
2.2 Flow Physics of Three-Dimensional Separated Flows	16
2.3 Leading-Edge Bluntness Effects on Vortex Separation	20
3 Experimental Approach	29
3.1 Wind Tunnel Test Facility	29
3.2 Wind Tunnel Models and Test Set-Up	30
3.2.1 AVT-183 Diamond Wing Configuration	30
3.2.2 SAGITTA Diamond Wing Configuration	32
3.3 Wall Roughness Effects	35
3.3.1 General Remarks	35
3.3.2 Basic Principles	36
3.3.3 Application Guidelines	38
3.3.4 Trip Strips at the AVT-183 Diamond Wing Configuration	39
3.3.5 Trip Strips at the SAGITTA Diamond Wing Configuration	42
3.4 Measurement Techniques	43
3.4.1 Force Measurements	43
3.4.2 Surface Pressure Measurements	45
3.4.3 Stereo Particle Image Velocimetry	46
3.4.4 Hot-Wire Anemometry	49

Table of Contents

4	Numerical Approach	53
4.1	Geometry Models	53
4.2	Computational Grids	54
4.2.1	Grid Generation Process	54
4.2.2	Resulting Grids	57
4.3	Flow Solver	58
4.3.1	Governing Equations	58
4.3.2	The DLR TAU-Code	64
4.3.3	Applied Numerical Set-Up	69
5	Analysis of Partly-Developed Leading-Edge Vortices	71
5.1	Experimental Investigations	72
5.1.1	Leading-Edge Roughness Effects	72
5.1.2	Flow Physics Analysis	80
5.1.3	Longitudinal Aerodynamic Coefficients	89
5.1.4	Synthesis	92
5.2	Numerical Investigations	93
5.2.1	Validation of the Numerical Method	93
5.2.2	Flow Physics Analysis	99
5.2.3	Flow Separation Onset Characteristics	104
5.2.4	Flow Topology Interpretation	114
5.2.5	Synthesis	119
6	Passive Flow Control by Leading-Edge Contour Modifications	123
6.1	Reference Configuration	123
6.1.1	Validation of the Numerical Method	123
6.1.2	Flow Physics Analysis	130
6.1.3	Synthesis	138
6.2	Sharp and Rounded Leading-Edge Contour	139
6.2.1	Flow Physics Analysis	140
6.2.2	Longitudinal Aerodynamic Coefficients	144
6.2.3	Synthesis	151
6.3	Leading-Edge Shape Modifications	153
6.3.1	Flow Physics Analysis	153
6.3.2	Longitudinal Aerodynamic Coefficients	160
6.3.3	Synthesis	164
6.4	Leading-Edge Twist Modification	165
6.4.1	Flow Physics Analysis	165
6.4.2	Longitudinal Aerodynamic Coefficients	170
6.4.3	Synthesis	174

7 Conclusion and Outlook	177
References	183
A Experimental Approach	195
B Analysis of Partly-Developed Leading-Edge Vortices	197
C Passive Flow Control by Leading-Edge Contour Modifications	199

List of Figures

Fig. 1.1	Examples of current U(C)AV concepts.	2
Fig. 1.2	Effect of the leading-edge shape on the pressure distribution at the VFE-1 configuration for $Ma = 0.4$, $Re_{mac} = 9 \cdot 10^6$ and $\alpha = 10^\circ$ [36].	4
Fig. 1.3	Flow field characteristics and flow topology of the VFE-2 configuration with rounded leading edges.	5
Fig. 1.4	SACCON UCAV low-speed wind tunnel model [23].	6
Fig. 1.5	SACCON vortex flow phenomena, $\alpha = 16.83^\circ$ [39, 86].	6
Fig. 1.6	Overview of selected research programs associated with non-slender, low-aspect-ratio wing configurations.	7
Fig. 1.7	Scenario of the flow separation onset at a non-slender wing with rounded leading edge [63].	9
Fig. 1.8	SAGITTA demonstrator configuration.	9
Fig. 1.9	Planform comparison of the analyzed diamond wing configurations, top view xy plane.	10
Fig. 1.10	Spanwise-varying leading-edge contours of the SAGITTA configuration (right wing).	11
Fig. 1.11	Leading-edge twist modification (nose coordinate) for configuration SG Geo 4.	12
Fig. 2.1	Simple concepts of flow separation [27].	17
Fig. 2.2	Nature of three-dimensional flow separation [18].	17
Fig. 2.3	Singular points in a cross-section of a flow field [16, 127].	18
Fig. 2.4	Leading-edge bluntness effect on vortex formation and progression [89].	20
Fig. 2.5	Reynolds number effect on blunt leading-edge vortex separation [89].	21
Fig. 2.6	Reynolds number effect on vortex formation along rounded leading edges [57].	22
Fig. 2.7	Mach number effect on blunt leading-edge vortex separation [89].	23
Fig. 2.8	Bluntness effect on leading-edge vortex separation [88].	24
Fig. 2.9	Bluntness and Mach number effect on leading-edge vortex separation [87].	24
Fig. 2.10	Bluntness and Reynolds number effect on leading-edge vortex separation [88].	25
Fig. 2.11	Wing planform and angle-of-attack effect on leading-edge vortex separation [19].	26
Fig. 2.12	Wing planform and relative thickness effect on leading-edge vortex separation [9].	27

List of Figures

Fig. 3.1	W/T facility A of TUM-AER.	29
Fig. 3.2	AVT-183 W/T model, top view xy plane.	30
Fig. 3.3	AVT-183 W/T model components.	31
Fig. 3.4	AVT-183 W/T model without the pressure side shell.	32
Fig. 3.5	AVT-183 W/T model within the W/T facility A of TUM-AER.	32
Fig. 3.6	SAGITTA W/T model, top view xy plane.	33
Fig. 3.7	SAGITTA W/T model components.	34
Fig. 3.8	SAGITTA W/T model without the pressure side shell.	35
Fig. 3.9	SAGITTA W/T model within the W/T facility A of TUM-AER.	35
Fig. 3.10	Skin-friction coefficient versus Reynolds number on a flat plate at zero incidence and zero pressure gradient, see Truckenbrodt [131].	37
Fig. 3.11	Summary of the applied trip strips at the AVT-183 W/T model.	40
Fig. 3.12	Geometric properties of the applied trip strips at the AVT-183 W/T model.	41
Fig. 3.13	Trip strips at the SAGITTA W/T model.	42
Fig. 3.14	Determination of the aerodynamic coefficients at the AVT-183 W/T model.	43
Fig. 3.15	Determination of the aerodynamic coefficients at the SAGITTA W/T model.	44
Fig. 3.16	Overview of the applied Stereo PIV set-ups within the W/T facility A of TUM-AER.	47
Fig. 3.17	Position of the laser sheet optic and the sCMOS cameras in relation to the diamond wing configurations.	48
Fig. 3.18	Overview of the applied hot-wire set-up within the W/T facility A of TUM-AER.	49
Fig. 4.1	Numerical geometry model of the SAGITTA configuration.	54
Fig. 4.2	Hybrid grid of the AVT-183 configuration.	55
Fig. 4.3	Hybrid grid of the SAGITTA configuration.	56
Fig. 4.4	Dual grid approach – Secondary grid data based on the cell-vertex grid metric [44].	65
Fig. 4.5	Multigrid method – Agglomeration of control volumes to form a coarser mesh [44].	68
Fig. 5.1	Leading-edge roughness effects at the AVT-183 configuration — Lift coefficient C_L and pitching-moment coefficient C_{my} versus angle of attack α	72
Fig. 5.2	Leading-edge roughness effects at the AVT-183 configuration — Lilienthal polar C_L versus C_D	73
Fig. 5.3	Leading-edge roughness effects at the AVT-183 configuration — Zero-lift drag coefficient $C_{D,0}$ and skin-friction coefficient C_f versus total roughness height $h_{ad} + k_s$	73
Fig. 5.4	Leading-edge roughness effects at the AVT-183 configuration – Surface pressure coefficient $\overline{c_p}$ versus semi-span $y/s(x)$ at $\alpha = 12^\circ$	75

Fig. 5.5	Leading-edge roughness effects at the AVT-183 configuration – Minimum surface pressure coefficient $\bar{c}_{p,min}$ and corresponding spanwise locations versus angle of attack α	77
Fig. 5.6	Short-term repeatability issues of case W/T Forced Transition 110mu — Pitching-moment coefficient C_{my} versus angle of attack α and surface pressure coefficient \bar{c}_p versus semi-span $y/s(x)$ at $\alpha = 14^\circ$ and $x/c_r = 0.405$	78
Fig. 5.7	Short-term repeatability issues of case W/T Forced Transition 150mu Dots — Pitching-moment coefficient C_{my} versus angle of attack α and surface pressure coefficient \bar{c}_p versus semi-span $y/s(x)$ at $\alpha = 14^\circ$ and $x/c_r = 0.405$	79
Fig. 5.8	Long-term repeatability issues of case W/T Forced Transition 150mu Dots — Pitching-moment coefficient C_{my} versus angle of attack α and surface pressure coefficient \bar{c}_p versus semi-span $y/s(x)$ at $\alpha = 14^\circ$ and $x/c_r = 0.405$	80
Fig. 5.9	Flow physics analysis of the AVT-183 configuration – Axial vorticity contours $\bar{\omega}_x \cdot l_\mu/U_\infty$ and absolute velocity contours \bar{V}/U_∞ at $\alpha = 12^\circ$	81
Fig. 5.10	Flow physics analysis of the AVT-183 configuration – Surface pressure coefficient \bar{c}_p versus semi-span $y/s(x)$ at $\alpha = 12^\circ$	82
Fig. 5.11	Flow physics analysis of the AVT-183 configuration – Axial vorticity contours $\bar{\omega}_x \cdot l_\mu/U_\infty$ and absolute velocity contours \bar{V}/U_∞ at $\alpha = 12^\circ$	83
Fig. 5.12	Flow physics analysis of the AVT-183 configuration – Lateral velocity component contours \bar{v}/U_∞ and normal velocity component contours \bar{w}/U_∞ at $\alpha = 12^\circ$	84
Fig. 5.13	Flow physics analysis of the AVT-183 configuration – Power spectral densities of unsteady surface pressure fluctuations at $\alpha = 12^\circ$	85
Fig. 5.14	Flow physics analysis of the AVT-183 configuration – Turbulent kinetic energy contours k at $\alpha = 12^\circ$	87
Fig. 5.15	Flow physics analysis of the AVT-183 configuration – Power spectral densities of velocity fluctuations at $\alpha = 12^\circ$ close to local turbulence maxima. The locations can be observed from Figure 5.14e and Figure 5.14f.	88
Fig. 5.16	Flow physics analysis of the AVT-183 configuration – Power spectral densities of velocity fluctuations at $\alpha = 12^\circ$ outside of the leading-edge vortex. The locations can be observed from Figure 5.14e and Figure 5.14f.	89
Fig. 5.17	Longitudinal aerodynamic characteristics of the AVT-183 configuration — Lift coefficient C_L and derivative $C_{L,\alpha}$ versus angle of attack α	90
Fig. 5.18	Longitudinal aerodynamic characteristics of the AVT-183 configuration — Drag coefficient C_D versus angle of attack α and Lilienthal polar C_L versus C_D	91
Fig. 5.19	Longitudinal aerodynamic characteristics of the AVT-183 configuration — Pitching-moment coefficient C_{my} and derivative $C_{my,\alpha}$ versus angle of attack α	91

List of Figures

Fig. 5.20	CFD validation of the AVT-183 configuration – Computed y^+ levels.	94
Fig. 5.21	CFD validation of the AVT-183 configuration – Longitudinal aerodynamic coefficients for different grid resolutions at $\alpha = 12^\circ$	95
Fig. 5.22	CFD validation of the AVT-183 configuration – Longitudinal aerodynamic coefficients versus angle of attack α	96
Fig. 5.23	CFD validation of the AVT-183 configuration – Axial vorticity contours $\overline{\omega_x} \cdot l_\mu/U_\infty$	97
Fig. 5.24	CFD validation of the AVT-183 configuration – Absolute velocity contours \overline{V}/U_∞	98
Fig. 5.25	CFD validation of the AVT-183 configuration – Surface pressure coefficient $\overline{c_p}$ versus semi-span $y/s(x)$	99
Fig. 5.26	Flow physics analysis of the AVT-183 configuration – Surface pressure coefficient c_p including skin-friction lines.	100
Fig. 5.27	Flow physics analysis of the AVT-183 configuration – Surface pressure coefficient c_p versus semi-span $y/s(x)$	101
Fig. 5.28	Flow physics analysis of the AVT-183 configuration – Absolute velocity contours V/U_∞	102
Fig. 5.29	Flow physics analysis of the AVT-183 configuration – Axial vorticity contours $\omega_x \cdot l_\mu/U_\infty$ and absolute velocity contours V/U_∞ at $\alpha = 12^\circ$	103
Fig. 5.30	Flow separation onset characteristics of the AVT-183 configuration – Axial vorticity contours $\omega_x \cdot l_\mu/U_\infty$ including skin-friction lines at $\alpha = 12^\circ$	104
Fig. 5.31	Flow separation onset characteristics of the AVT-183 configuration at $\alpha = 12^\circ$ (I).	106
Fig. 5.32	Flow separation onset characteristics of the AVT-183 configuration at $\alpha = 12^\circ$ (II).	108
Fig. 5.33	Flow separation onset characteristics of the AVT-183 configuration at $\alpha = 12^\circ$ – Near-wall velocity profiles in streamwise and crossflow direction along the leading-edge vortex core.	109
Fig. 5.34	Flow separation onset characteristics of the AVT-183 configuration at $\alpha = 12^\circ$ (III).	110
Fig. 5.35	Flow separation onset characteristics of the AVT-183 configuration at $\alpha = 12^\circ$ – Near-wall velocity profiles in streamwise and crossflow direction along one particular skin-friction line.	111
Fig. 5.36	Flow separation onset characteristics of the AVT-183 configuration – Location of characteristic points versus angle of attack α	112
Fig. 5.37	Flow separation onset characteristics of the AVT-183 configuration – Skin-friction lines including field streamlines colored by absolute velocity V/U_∞	113
Fig. 5.38	Flow topology interpretation of the AVT-183 configuration at $\alpha = 12^\circ$ – Three-dimensional views.	115

Fig. 5.39	Flow topology interpretation of the AVT-183 configuration at $\alpha = 12^\circ$ – Sectional cuts (I).	117
Fig. 5.40	Flow topology interpretation of the AVT-183 configuration at $\alpha = 12^\circ$ – Sectional cuts (II).	118
Fig. 6.1	CFD validation of configuration SG Geo 1 – Computed y^+ levels.	124
Fig. 6.2	CFD validation of configuration SG Geo 1 – Longitudinal aerodynamic coefficients for different grid resolutions at $\alpha = 12^\circ$	125
Fig. 6.3	CFD validation of configuration SG Geo 1 – Longitudinal aerodynamic coefficients versus angle of attack α	126
Fig. 6.4	CFD validation of configuration SG Geo 1 – Lift coefficient versus angle of attack α	127
Fig. 6.5	CFD validation of configuration SG Geo 1 – Axial vorticity contours $\overline{\omega_x} \cdot l_\mu / U_\infty$	128
Fig. 6.6	CFD validation of configuration SG Geo 1 – Absolute velocity contours \overline{V} / U_∞	129
Fig. 6.7	CFD validation of configuration SG Geo 1 – Surface pressure coefficient $\overline{c_p}$ versus semi-span $y/s(x)$	130
Fig. 6.8	Flow physics analysis of configuration SG Geo 1 – Surface pressure coefficient $\overline{c_p}$ including field streamlines, and axial vorticity contours $\overline{\omega_x} \cdot l_\mu / U_\infty$	132
Fig. 6.9	Flow physics analysis of configuration SG Geo 1 – Surface pressure coefficient $\overline{c_p}$ including skin-friction lines.	133
Fig. 6.10	Flow physics analysis of configuration SG Geo 1 – Axial vorticity contours $\overline{\omega_x} \cdot l_\mu / U_\infty$ and absolute velocity contours \overline{V} / U_∞ at $\alpha = 24^\circ$	134
Fig. 6.11	Flow physics analysis of configuration SG Geo 1 – Surface pressure coefficient $\overline{c_p}$ including field streamlines, and axial vorticity contours $\overline{\omega_x} \cdot l_\mu / U_\infty$ at $\beta = -10^\circ$	136
Fig. 6.12	Flow physics analysis of configuration SG Geo 1 – Surface pressure coefficient $\overline{c_p}$ versus semi-span $y/s(x)$ at $\beta = -10^\circ$	137
Fig. 6.13	Flow physics analysis of configuration SG Geo 1 – Absolute velocity contours \overline{V} / U_∞ at $\beta = -10^\circ$	137
Fig. 6.14	Flow physics analysis of configuration SG Geo 5 – Surface pressure coefficient $\overline{c_p}$ including field streamlines, and axial vorticity contours $\overline{\omega_x} \cdot l_\mu / U_\infty$	141
Fig. 6.15	Flow physics analysis of configuration SG Geo 5 – Absolute velocity contours \overline{V} / U_∞	142
Fig. 6.16	Flow physics analysis of configuration SG Geo 6 – Surface pressure coefficient $\overline{c_p}$ including field streamlines, and axial vorticity contours $\overline{\omega_x} \cdot l_\mu / U_\infty$	143
Fig. 6.17	Flow physics analysis of configuration SG Geo 6 – Surface pressure coefficient $\overline{c_p}$ including skin-friction lines.	144
Fig. 6.18	Longitudinal aerodynamic coefficients of configurations SG Geo 5 and SG Geo 6 – Lift coefficient C_L and derivative $C_{L,\alpha}$ versus angle of attack α	145

List of Figures

Fig. 6.19	Longitudinal aerodynamic coefficients of configurations SG Geo 5 and SG Geo 6 – Drag coefficient C_D versus angle of attack α and Lilienthal polar C_L versus C_D	147
Fig. 6.20	Longitudinal aerodynamic coefficients of configurations SG Geo 5 and SG Geo 6 – Pitching-moment coefficient C_{my} and derivative $C_{my,\alpha}$ versus angle of attack α	148
Fig. 6.21	Longitudinal stability investigation of configurations SG Geo 5 and SG Geo 6 – Local center of pressure x_d/c_r and stability value $ (x_{mrp} - x_n)/l_\mu $ vs. angle of attack α	148
Fig. 6.22	Longitudinal stability investigation of configurations SG Geo 5 and SG Geo 6 – Surface pressure coefficient \bar{c}_p	150
Fig. 6.23	Flow physics analysis of configuration SG Geo 2 – Surface pressure coefficient \bar{c}_p versus semi-span $y/s(x)$	153
Fig. 6.24	Flow physics analysis of configuration SG Geo 2 – Surface pressure coefficient \bar{c}_p including field streamlines, and axial vorticity contours $\bar{\omega}_x \cdot l_\mu/U_\infty$	154
Fig. 6.25	Flow physics analysis of configuration SG Geo 2 – Surface pressure coefficient \bar{c}_p including skin-friction lines.	155
Fig. 6.26	Flow physics analysis of configuration SG Geo 3 – Surface pressure coefficient \bar{c}_p including field streamlines, and axial vorticity contours $\bar{\omega}_x \cdot l_\mu/U_\infty$	156
Fig. 6.27	Flow physics analysis of configuration SG Geo 3 – Surface pressure coefficient \bar{c}_p including skin-friction lines at $\alpha = 12^\circ$	157
Fig. 6.28	Flow physics analysis of configuration SG Geo 3 – Surface pressure coefficient \bar{c}_p including skin-friction lines.	158
Fig. 6.29	Flow physics analysis of configuration SG Geo 3 – Axial vorticity contours $\bar{\omega}_x \cdot l_\mu/U_\infty$ and absolute velocity contours \bar{V}/U_∞ at $\alpha = 24^\circ$	159
Fig. 6.30	Longitudinal aerodynamic coefficients of configurations SG Geo 2 and SG Geo 3 – Lift coefficient C_L and derivative $C_{L,\alpha}$ versus angle of attack α	160
Fig. 6.31	Longitudinal aerodynamic coefficients of configurations SG Geo 2 and SG Geo 3 – Drag coefficient C_D versus angle of attack α and Lilienthal polar C_L versus C_D	161
Fig. 6.32	Longitudinal aerodynamic coefficients of configurations SG Geo 2 and SG Geo 3 – Pitching-moment coefficient C_{my} and derivative $C_{my,\alpha}$ versus angle of attack α	162
Fig. 6.33	Longitudinal stability investigation of configurations SG Geo 2 and SG Geo 3 – Local center of pressure x_d/c_r and stability value $ (x_{mrp} - x_n)/l_\mu $ vs. angle of attack α	163
Fig. 6.34	Longitudinal stability investigation of configuration SG Geo 3 – Surface pressure coefficient \bar{c}_p	163

Fig. 6.35	Flow physics analysis of configuration SG Geo 4 – Surface pressure coefficient \bar{c}_p including field streamlines, and axial vorticity contours $\bar{\omega}_x \cdot l_\mu / U_\infty$	166
Fig. 6.36	Flow physics analysis of configuration SG Geo 4 – Surface pressure coefficient \bar{c}_p including skin-friction lines.	168
Fig. 6.37	Flow physics analysis of configuration SG Geo 4 – Axial vorticity contours $\bar{\omega}_x \cdot l_\mu / U_\infty$ and absolute velocity contours \bar{V} / U_∞ at $\alpha = 24^\circ$	169
Fig. 6.38	Longitudinal aerodynamic coefficients of configuration SG Geo 4 – Lift coefficient C_L and derivative $C_{L,\alpha}$ versus angle of attack α	171
Fig. 6.39	Longitudinal aerodynamic coefficients of configuration SG Geo 4 – Drag coefficient C_D versus angle of attack α and Lilienthal polar C_L versus C_D	171
Fig. 6.40	Longitudinal aerodynamic coefficients of configuration SG Geo 4 – Pitching-moment coefficient C_{my} and derivative $C_{my,\alpha}$ versus angle of attack α	172
Fig. 6.41	Longitudinal stability investigation of configuration SG Geo 4 – Local center of pressure x_d / c_r and stability value $ (x_{mrp} - x_n) / l_\mu $ vs. angle of attack α	172
Fig. 6.42	Longitudinal stability investigation of configuration SG Geo 4 – Surface pressure coefficient \bar{c}_p	173
Fig. B.1	Sketch of mirrored W/T test section for the applied W/T correction [35].	197
Fig. C.1	CFD validation – Lateral aerodynamic coefficients versus angle of attack α at $\beta = -10^\circ$, configuration SG Geo 1.	200
Fig. C.2	CFD validation – Surface pressure coefficient \bar{c}_p versus semi-span $y/s(x)$ at $\beta = -10^\circ$, configuration SG Geo 1.	201
Fig. C.3	Flow physics analysis of configuration SG Geo 1 – Surface pressure coefficient \bar{c}_p including streamlines, and axial vorticity contours $\omega_x \cdot l_\mu / U_\infty$ at $\beta = 10^\circ$	202

List of Tables

Tab. 2.1	Geometric details of wing configurations featuring rounded leading edges.	25
Tab. 3.1	Wing planform parameters of the AVT-183 W/T model.	30
Tab. 3.2	Chordwise sections for surface pressure measurements at the AVT-183 W/T model.	31
Tab. 3.3	Wing planform parameters of the SAGITTA W/T model.	33
Tab. 3.4	Chordwise sections for surface pressure measurements at the SAGITTA W/T model.	34
Tab. 3.5	Geometric properties of the applied trip strips at the AVT-183 W/T model.	41
Tab. 3.6	Post-processing parameters of the Stereo PIV measurements.	48
Tab. 3.7	Velocity field information of the Stereo PIV measurements, AVT-183 W/T model.	49
Tab. 3.8	Velocity field information of the Stereo PIV measurements, SAGITTA W/T model.	49
Tab. 4.1	Grid parameters of the computational grids, AVT-183 configuration.	57
Tab. 4.2	Grid parameters of the computational grids, SAGITTA configuration.	58
Tab. 4.3	Grid sizes of the computational grids, SAGITTA configuration.	58
Tab. 4.4	High-level control parameters of the DLR TAU-Code in the applied numerical set-ups.	69
Tab. 5.1	CFD validation of the AVT-183 configuration – Longitudinal aerodynamic coefficients for different grid resolutions at $\alpha = 12^\circ$	94
Tab. 6.1	CFD validation of configuration SG Geo 1 – Longitudinal aerodynamic coefficients for different grid resolutions at $\alpha = 12^\circ$	125
Tab. A.1	Characteristic data of the W/T facility A of TUM-AER.	195
Tab. A.2	Flow quality of the W/T facility A of TUM-AER.	195

Nomenclature

Arabic Characters

b	wing span, m
C_D	drag coefficient
$C_{D,0}$	zero-lift drag coefficient
C_L	lift coefficient
$C_{L,\alpha}$	lift slope
C_Y	side force coefficient
C_f	skin-friction coefficient
C_l	rolling-moment coefficient
C_{my}	pitching-moment coefficient
$C_{my,\alpha}$	pitching-moment derivative
C_n	yawing-moment coefficient
c_r	wing root chord, m
c_t	wing tip chord, m
c_p	pressure coefficient
\bar{c}_p	mean (time-averaged) pressure coefficient
c'_p	pressure coefficient fluctuations
c_p	heat capacity at constant pressure, J/K
c_v	heat capacity at constant volume, J/K
D	drag, N
d	distance, m
d_{par}	particle diameter, m
d_{pt}	diameter of the pressure tap orifices, m
d_{td}	trip-dot diameter, m
E	power, J
E	specific total energy, J
\vec{e}_i	unit vectors in coordinate directions
F	focal length, m
F_x	axial force, N
F_y	side force, N
F_z	normal force, N
$\bar{\mathbf{F}}$	flux tensor
$\vec{F}, \vec{G}, \vec{H}$	flux vector in coordinate directions

Nomenclature

f	frequency, Hz
f_{lpf}	low-pass filter frequency, Hz
H	specific total enthalpy, J
h_{ad}	height of trip-strip adhesive layer, m
h_{gap}	height of seal between wind tunnel model and peniche, m
h_{pen}	peniche height, m
k	non-dimensional turbulent kinetic energy
k	roughness height, m
k_{crit}	critical surface roughness height, m
k_{per}	permissible surface roughness height, m
k_{red}	reduced frequency
k_s	sand roughness, m
k_s	trip-strip roughness height, m
L	lift, N
l	length scale, m
$l_{arc,cg}$	chordwise extension of carborundum grit type, m
$l_{arc,td}$	chordwise position of trip-dot centers, m
$l_{spa,td}$	spacing of trip-dot centers, m
l_μ	mean aerodynamic chord / longitudinal reference length, m
Ma	Mach number
M_x	rolling moment, Nm
M_y	pitching moment, Nm
M_z	yawing moment, Nm
N, N'	node, half-node
\vec{n}	outer normal vector
Pr	Prandtl number
p	static pressure, N/m ²
p^*	effective turbulent pressure, N/m ²
q	dynamic pressure, N/m ²
\vec{q}_i	thermal flux vector, W/m ²
R	specific gas constant, J/(kg K)
Re	Reynolds number
r_{le}	leading-edge radius, m
S	boundary surface, m ²
S, S'	saddle, half-saddle
\tilde{S}	scalar velocity gradient for the Spalart-Allmaras turbulence model, 1/s
Str	Strouhal number
S_{ref}	wing reference area, m ²
$S_{c'_p}$	one-sided power spectrum of the pressure coefficient fluctuations, 1/Hz

$S_{u'_i}$	one-sided power spectrum of the velocity fluctuations, $(\text{m/s})^2/\text{Hz}$
s	semi-wing span / lateral reference length, m
T	temperature, K
Tu_i	turbulence intensity
t	time, s
U	velocity, m/s
u, v, w	velocity components, m/s
$\bar{u}, \bar{v}, \bar{w}$	mean (time-averaged) velocity components, m/s
u', v', w'	velocity fluctuation components, m/s
$u_{rms}, v_{rms}, w_{rms}$	root mean square (RMS) velocity components of u', v', w' , m/s
V	volume, m^3
V	absolute velocity, m/s
\bar{V}	mean (time-averaged) absolute velocity, m/s
\vec{W}	vector of the conservative variables
$X_{c'_p}$	Fourier-transformed quantity of the pressure coefficient fluctuations, 1/Hz
$X_{u'_i}$	Fourier-transformed quantity of the velocity fluctuations, $(\text{m/s})/\text{Hz}$
x, y, z	cartesian coordinates, m
x_{cg}	x-coordinate of the center of gravity, m
x_d	x-coordinate of the local center of pressure, m
x_{mrp}	x-coordinate of the moment reference point, m
x_n	x-coordinate of the neutral point, m
y^+	dimensionless wall distance

Greek Characters

α	angle of attack, deg
β	angle of sideslip, deg
β	Prandtl-Glauert factor
δ_0, δ_1	wind tunnel correction factors
δ_{99}	boundary-layer height, m
δ_{ij}	Kronecker delta
ϵ	glide angle, deg
Θ_x	frictional heat, $(\text{kg K})/\text{m}^2 \text{ s}$
κ	heat capacity ratio
Λ	wing aspect ratio
λ	wing taper ratio
λ	thermal conductivity, $\text{W}/(\text{m K})$
μ	dynamic viscosity, $\text{kg}/(\text{m s})$
ν	kinematic viscosity, m^2/s
$\tilde{\nu}$	kinematic viscosity for the Spalart-Allmaras turbulence model, m^2/s

Nomenclature

ρ	density, kg/m ³
$\bar{\tau}$	shear stress tensor, N/m ²
τ	shear stress, N/m ²
φ	wing sweep angle, deg
χ	damping factor for the Spalart-Allmaras turbulence model
ψ	wave length, m
ω	angular frequency, 1/s
ω_x	axial vorticity component, 1/s
$\bar{\omega}_x$	mean (time-averaged) axial vorticity component, 1/s

Subscripts

A	wind-fixed coordinate system
A	attachment
burst	first occurrence of vortex bursting at the trailing edge
i	inviscid
le	leading edge
l	laminar
M	model-fixed coordinate system
mac	mean aerodynamic chord
max	maximum
meas	measurement
min	minimum
ref	reference value
S	separation
sfl	skin-friction-line coordinate system
sim	simulation time
t	turbulent
t	trip point
te	trailing edge
ts	test section
v	viscous
w	wall
w,n	normal direction to the wing surface
∞	free stream value

Acronyms

AGARD	Advisory Group for Aerospace Research and Development
AVL	Athena Vortex Lattice
AVT	Applied Vehicle Technology

BL	boundary layer
BLV	boundary-layer vortex
CFD	Computational Fluid Dynamics
CFL	Courant-Friedrichs-Lewy
CRM	Common Research Model
CTA	constant-temperature anemometer
DLR	Deutsches Zentrum für Luft- und Raumfahrt (German Aerospace Center)
GCS	Gauss Centre for Supercomputing
HWA	Hot-Wire Anemometry
IB	inboard
IV	inner vortex
LE	leading edge
LEV	leading-edge vortex
LRZ	Leibnitz Supercomputing Centre
LUSGS	Lower-Upper Symmetric Gauss-Seidel
MB	midboard
MP	monitor point
MRP	moment reference point
NACA	National Advisory Committee for Aeronautics
NASA	National Aeronautics and Space Administration
NATO	North Atlantic Treaty Organization
OB	outboard
PAL	primary attachment line
PIV	Particle Image Velocimetry
PSL	primary separation line
RCS	radar cross-section
RMS	root mean square
RTO	Research and Technology Organization
SACCON	Stability and Control Configuration
SA-Neg	Spalart-Allmaras turbulence model, modified version
SAO	Spalart-Allmaras turbulence model, original version
SAL	secondary attachment line
SARC	Spalart-Allmaras turbulence model, with rotation correction
SCMOS	scientific complementary metal-oxide semiconductor
SG	SAGITTA
SSL	secondary separation line
STO	Science and Technology Organization
TTCP	Technical Cooperation Program
TUM-AER	Institute of Aerodynamics and Fluid Mechanics, Technische Universität München

Nomenclature

U(C)AV	unmanned (combat) aerial vehicle
(U)RANS	(Unsteady) Reynolds-Averaged Navier-Stokes
VFE	Vortex Flow Experiment
W/T	wind tunnel

Chapter 1

Introduction

1.1 Background and Motivation

The analysis of leading-edge vortices at highly- and moderately-swept, low-aspect-ratio wing configurations has been subject of aerodynamic research for a long time. During the past approximately 60 years, the flow phenomena associated with leading-edge vortices were investigated in great detail. The main influence parameters promoting vortex flow have been identified, which are, in particular, the wing planform including the wing sweep, the leading-edge contour, and the angle of attack. Additionally, the Mach number, the Reynolds number including the boundary-layer characteristics, the airfoil shape with varying thickness and camber, and the angle of sideslip have been found to influence the existence and the character of leading-edge vortices under certain circumstances. Overall, the influence parameters mainly determine the location of the flow separation onset, the leading-edge vortex progression, its effective strength, and unsteady flow phenomena such as vortex bursting.

Over the last decades, numerous analyses were conducted for slender delta wing planforms ($\varphi_{le} \geq 60^\circ$) with sharp leading edges, for which the flow separation onset is geometrically fixed. For this type of wing configuration, the occurring flow phenomena are to a large extent understood, and are well documented in the literature, see Section 1.2. In recent years, the focus of vortex flow research has increasingly been placed on wing configurations with changed planform parameters and airfoil shapes. Reduced wing sweeps, swept trailing edges (as found at lambda- and diamond-shaped wing configurations), and rounded leading edges are particularly investigated. Spanwise-varying leading-edge contours are also looked at in this context. Section 1.2 gives a brief outline of relevant work in this field of research. The investigation of modified wing configurations has especially become relevant due to the design and development of today's low-signature fighter aircraft (e.g. B-2, F-117, F-22, Suchoi T-50), and similarly by low-signature, low-aspect-ratio unmanned (combat) aerial vehicle concepts (U(C)AV, e.g. Neuron, X47-A, X-47B, Taranis). To design and develop future aircraft configurations, these U(C)AV concepts are currently built and tested for demonstration purposes and specific capabilities. Figure 1.1 shows a selection of them. For suchlike wing configurations, competing mission requirements are present in the relevant application scenarios. In the context of aerodynamic design, these requirements range from an optimized flight performance in high subsonic maneuver flight conditions and a

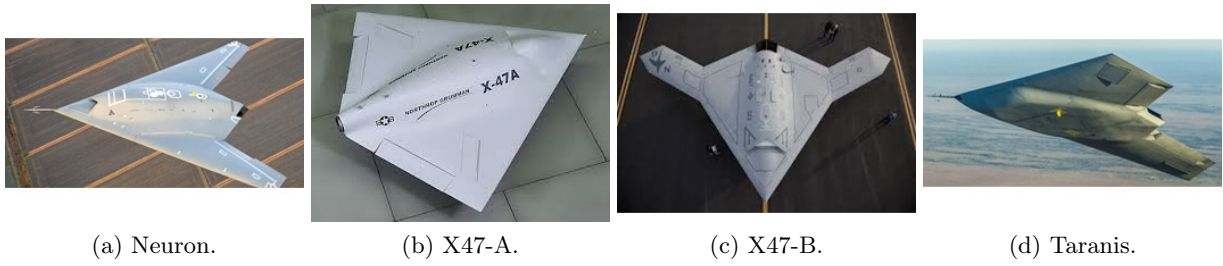


Figure 1.1: Examples of current U(C)AV concepts.

desired stability behavior to relevant engine intake and radar cross-section (RCS) issues of the vehicle [53, 99]. Consequently, the characteristics of current low-aspect-ratio wing configurations are mainly determined by these requirements. As a result, present-day U(C)AV wing designs often feature moderate leading-edge sweep angles of $50^\circ < \varphi_{le} < 60^\circ$ (defined as non-slender, $\varphi_{le} < 60^\circ$), including rounded leading edges or spanwise-varying leading-edge contours.

For this type of non-slender wing configuration, partly-developed leading-edge vortices are commonly observed. In case of an exclusively rounded leading-edge contour, the flow separation onset is no longer geometrically fixed. In the outboard wing sections, separated vortex flow is often noticed with increasing angle of attack while attached flow is still present in the more inboard wing regions. Fully-developed leading-edge vortices along the entire wing span, as known from slender wing configurations with sharp leading edges, do no longer exist. Furthermore, vortex bursting phenomena occur at lower angles of attack, and usually before the flow separation onset has moved up to the apex of the wing. In addition, both the flow separation onset and the leading-edge vortex progression are now particularly influenced by the leading-edge radius, the Mach and Reynolds number, and by the corresponding boundary-layer characteristics. Section 2.3 provides a summary of these aspects. Three-dimensional effects significantly determine the boundary-layer separation, which is decisive for the vortex formation and progression. The occurring flow phenomena thereby become more complex compared to the case with sharp leading edges. To date, these have not yet entirely been understood and are subject of current research, see Section 1.2. More specifically, a complete flow-physical scenario of the flow separation onset at rounded leading edges based on boundary-layer flow phenomena has not been formulated so far. In this context, related theoretical approaches on the topological interpretation of three-dimensional separated flows are introduced in Section 2.2. In the course of this thesis, they are reviewed and discussed with current results.

If spanwise-varying leading-edge contours are present on low-aspect-ratio wing configurations, partly-developed leading-edge vortices are usually observed as a result of the chosen airfoil shape along the wing span. Specific regions of attached flow and separated vortex flow are thus promoted a priori. The need for varying airfoil shapes originates, on the one hand, from the above mentioned design requirements of current low-signature wing configurations. On the other hand, the leading-edge contour modifications represent a concept of passive flow control, which is used to influence

the performance and the stability behavior of wing configurations. Operating at low to moderate angles of attack, the aerodynamic characteristics are generally more efficient employing rounded leading-edge contours. With respect to low-signature issues and the agility of the aircraft at higher angles of attack, however, sharp leading edges are preferred in most cases. As a result, spanwise-varying leading-edge contours lead in many cases to complex flow phenomena and to vortex-vortex interactions between the occurring vortical structures at higher angles of attack. This provides design space for optimization purposes as the combination of different leading-edge vortices can be best utilized. An appropriate combination of sharp and rounded airfoil shapes along the wing span of respective wing configurations thus allows for a marked improvement in the overall aerodynamic characteristics. RCS concerns and other configurational design drivers are still respected or remain unaffected at the same time. For this reason, such passive flow control concepts are currently being reviewed in the present field of research. Specifically for the design of future U(C)AV wing configurations, they can contribute to a low-signature wing design with optimized aerodynamic characteristics.

1.2 State of the Art

The following section provides a survey on the state of the art of vortex flow research. First of all, the most fundamental investigations of slender delta wing configurations with sharp leading edges are summarized briefly. Next, the focus is upon recent studies of low-aspect-ratio wing configurations with rounded leading edges and spanwise-varying leading-edge contours. Non-slender wing configurations with moderately-swept leading edges are regarded as well. In this context, Luckring gives a broad and detailed overview of the topic [86]. This part of the review is further subdivided into two sections, which are structured as follows: At the beginning, recent research conducted within the framework of the NATO Science and Technology Organisation (STO) (formerly known as RTO, Research and Technology Organization, and AGARD, Advisory Group for Aerospace Research and Development), Applied Vehicle Technology (AVT) panel, are presented. Afterwards, other selected research activities are introduced, which are related to non-slender low-aspect-ratio wing configurations and are also relevant for this research.

Basis for Vortex Flow Research – Slender Delta Wings with Sharp Leading Edges

Initiated by early W/T experiments of Hummel [59] and Lambourne [82], the flow physics of leading-edge vortices at slender delta wings with sharp leading edges was extensively studied around the 1960s. With this fundamental research, they greatly contributed to the foundations of present-day fighter-type aircraft aerodynamics (e.g. F-15, F-16, F/A-18, EF2000), but also to current research regarding U(C)AV-related, low-aspect-ratio wing configurations. Unsteady flow phenomena occurring at high angles of attack, such as vortex bursting, were further discovered and looked at for the first time [60, 83]. The influence of the boundary-layer characteristics on the leading-edge vortex formation was also investigated later on [61]. In effect, the cumulative

research in this field led to key improvements of fighter-type aircraft aerodynamics until the 1990s. With regard to practical applications, the focus of further research was placed specifically upon the associated unsteady flow phenomena, which were identified to influence the performance, the stability, and the structural loads of the aircraft [17, 49]. As a result, the flow phenomena occurring for this type of wing configuration are well understood since these days. Comprehensive review articles summarizing the relevant experimental and numerical investigations were published by Peake [100], Hummel [56, 58], Gursul [50], and Breitsamter [16].

Vortex Flow Investigations - NATO Research Task Groups

The effects of rounded leading edges on the vortex formation and progression were first studied in the International Vortex Flow Experiment 1 (VFE-1) [31]. In the early 1980s, it was initiated as a joint program of national research institutes, industry partners, and universities to validate computational fluid dynamics (CFD) methods at that time. Numerous investigations were conducted on a slender delta wing configuration with varying Mach number, Reynolds number, and different leading-edge shapes (one sharp, three rounded). Summaries of the results are given by Elsenaar [36] and Luckring [89]. Related comprehensive data sets, as provided for instance by the National Aeronautics and Space Administration (NASA), can be found in Reference [21]. Depending on the applied leading-edge shape, different flow field characteristics were observed, see Figure 1.2. It

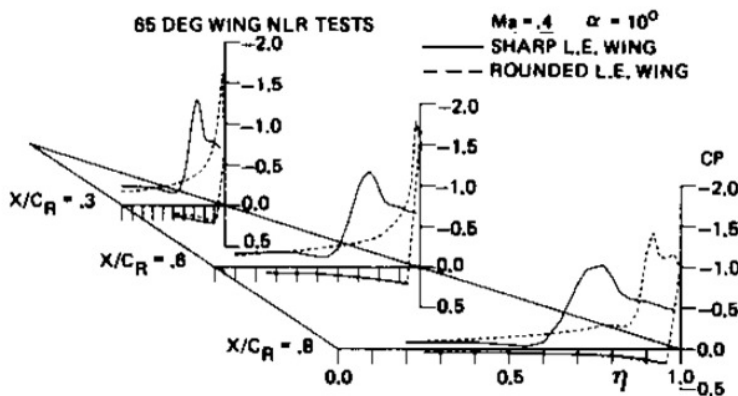


Figure 1.2: Effect of the leading-edge shape on the pressure distribution at the VFE-1 configuration for $Ma = 0.4$, $Re_{mac} = 9 \cdot 10^6$ and $\alpha = 10^\circ$ [36].

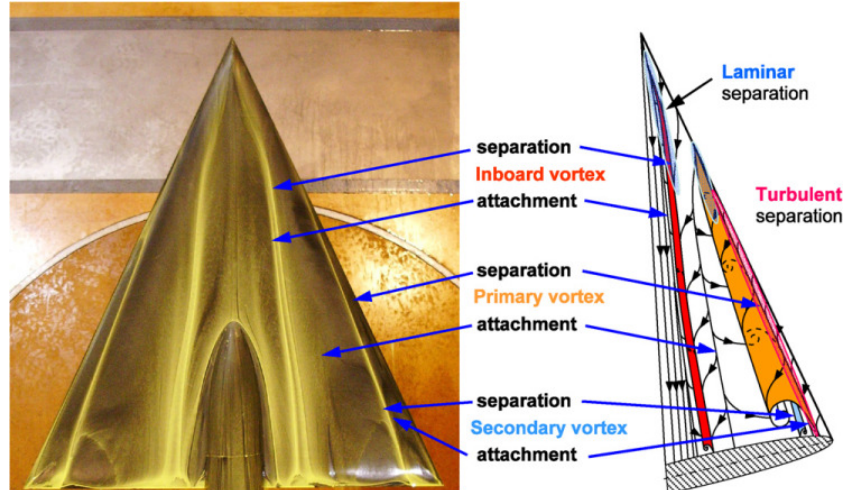
turned out that the primary flow separation is significantly dependent on the leading-edge radius and the Reynolds number [88, 90]. Compressibility effects were also observed [87]. In particular, regions of attached flow upstream of the vortex formation were identified, which is related to the flow phenomenon of part-span vortex separation or partly-developed leading-edge vortices. This work also contributed to an AGARD symposium [36] and to the NATO RTO research task group AVT-080, in which specifically the ability of CFD methods to predict vortical flow structures on delta wings was considered [107].

Caused by the great enhancements of Navier-Stokes CFD methods in the 1990s, and by the need for further experimental data for CFD code validation, the VFE-1 research found a continuation within the International Vortex Flow Experiment 2 (VFE-2), see Hummel [62]. As a follow-up to AVT-080, extensive experimental and numerical work was conducted in the research task group AVT-113. The focus was put on the fundamental investigation of the vortex formation at the 65°

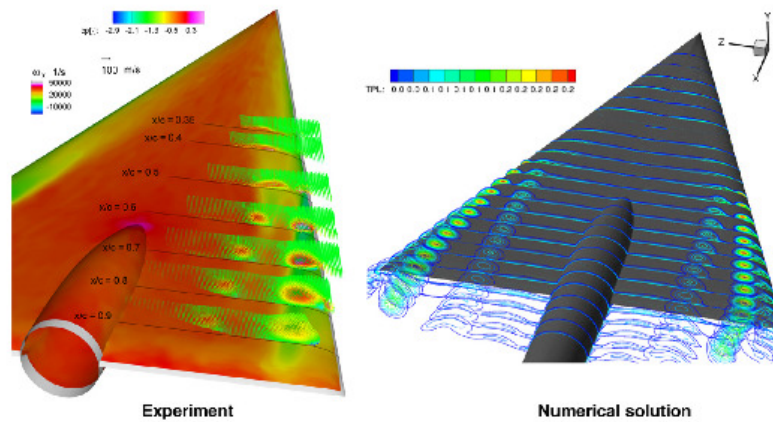
leading-edge sweep VFE-2 delta wing configuration with the medium-radius rounded leading edge of the VFE-1 wing. The influence of the boundary-layer characteristics on the flow separation onset was studied in detail. Relevant foundations for this analysis were summarized by Hummel [57]. In addition, more aircraft-oriented work on the F16-XL-1 was also considered by the research task group [11, 12, 41, 47, 98, 103]. Overall, outstanding advancements were made due to the results of AVT-113. With respect

to the VFE-2 configuration, the understanding of partly-developed leading-edge vortices and the vortex formation at rounded leading edges was improved extensively. The influence of the boundary-layer characteristics on the vortex separation was demonstrated. Moreover, new flow phenomena such as a weak "inner vortex", which is induced by a laminar flow separation on the inboard wing, were observed under certain Reynolds number conditions [24, 40, 43, 79, 91, 113]. Figure 1.3 introduces the corresponding flow field characteristics of the VFE-2 configuration at $\alpha = 13^\circ$ and a flow topology interpretation. The final results of the research task group are published in Reference [106], and the lessons learned are summarized by Luckring and Hummel [93].

The increasing demands for research on low-aspect-ratio wing configurations, which are more representative for current U(C)AV-related wing designs, subsequently led to the next NATO RTO research task group, namely AVT-161 [108]. In a combined experimental and numerical approach, it focused among other aspects on the stability and control characteristics of a non-slender UCAV wing design, the Stability and Control Configuration (SACCON) [23]. This lambda-shaped



(a) $Ma = 0.14$, $Re_{mac} = 2 \cdot 10^6$ and $\alpha = 13^\circ$ [43].



(b) $Ma = 0.4$, $Re_{mac} = 3 \cdot 10^6$ and $\alpha = 13^\circ$ [93].

Figure 1.3: Flow field characteristics and flow topology of the VFE-2 configuration with rounded leading edges.

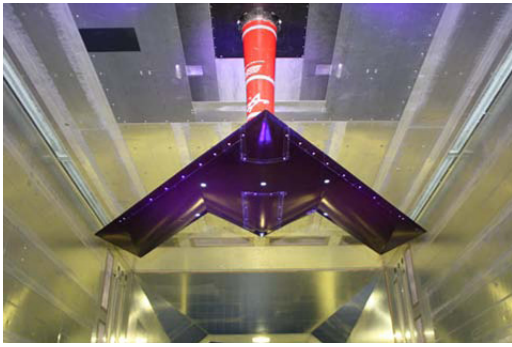


Figure 1.4: SACCON UCAV low-speed wind tunnel model [23].

wing configuration is characterized by a leading-edge sweep angle of $\varphi_{le} = 53^\circ$, see Figure 1.4. In addition, it features spanwise-varying leading-edge contours with sharp and rounded leading-edge segments. Compared to the VFE-2 delta wing configuration, considerably larger leading-edge radii are present, in particular in the mid-span region. As emphasized by Schütte et al., the geometry thus respects the main design requirements of relevant U(C)AV applications [112]. Usually this leads, as mentioned above, to complex aerodynamic characteristics associated with leading-edge vortices. Suchlike flow phenomena, including vortex-vortex interactions and corresponding pitching-moment instabilities, were consequently observed for the SACCON configuration as well [23, 39, 104, 105, 112, 129, 133]. They originate from the spanwise-varying leading-edge contours as the outboard blunt leading-edge vortex rapidly moves forward at higher angles of attack. Figure 1.5 exemplarily depicts the present vortex flow phenomena. With increasing angle of attack, the SACCON flow pattern consists of regions with attached flow and leading-edge vortices occurring from the sharp and the rounded leading-edge segments.

Due to analyses conducted within AVT-161, the occurring flow field characteristics were largely understood for the specific SACCON configuration. For a fundamental understanding of the flow

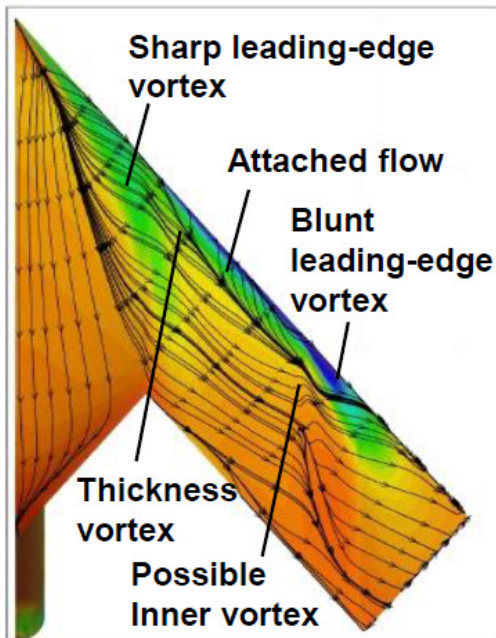


Figure 1.5: SACCON vortex flow phenomena, $\alpha = 16.83^\circ$ [39, 86].

separation onset at rounded leading-edge contours, however, new research questions were brought up. The exploitation of different leading-edge vortices for passive flow control concepts was not addressed in the research task group, but the observed interactions between the vortex structures pointed at the importance of further research in this area. More aircraft-oriented work on another complex full-aircraft geometry, namely the X-31 configuration, was also conducted within AVT-161 [8, 78, 96, 111, 115]. For the analyses, the vortex flow associated with the present rounded leading edges was investigated by CFD methods and in W/T test campaigns. It turned out that gaps on the leading-edge flaps significantly affect the vortex separation at rounded leading edges. Hence, they need to be modeled in CFD investigations as well. With respect to practical applications, this is a major concern for further research, when leading-edge controls are considered additionally.

Vortex Flow Investigations - Other Research Activities

Parallel to the mentioned activities coordinated by NATO, vortex flow research was conducted also in the context of other collaborative research programs on representative low-aspect-ratio wing configurations during the last decade. By way of example, two of them are introduced here. In the research program AER-TP5, organized and executed by the Technical Cooperation Program (TTCP), the 1303 configuration was considered [4], see Figure 1.6a. A Swedish research program analyzed the Swing configuration [123], see Figure 1.6b. Both configurations consist of a lambda-shaped wing with a thickened fuselage section. The leading-edge sweep angles are $\varphi_{le} = 47^\circ$ for the 1303 configuration and $\varphi_{le} = 56^\circ$ for the Swing lambda wing. Both configurations feature rounded leading-edge contours with medium to large nose radii. Except for the spanwise-varying leading-edge contours, they are therefore comparable to SACCON.

The research program AER-TP5 focused in detail on the onset and progression of the leading-edge vortex separation at rounded leading edges. CFD validation purposes were addressed as well. Moreover, different leading-edge shapes with varying bluntness were investigated and compared to each other. Figure 1.6c shows a sample result with attached flow in the midboard wing section and a vortex separation in the more outboard wing sections. In accordance with the results obtained for the SACCON configuration, adverse pitch-up characteristics were found in certain angle-of-attack regimes that occur from the lambda-shaped wing and resulting partly-developed leading-edge vortices. With regard to practical applications, this is a major challenge for stability and control, which makes the lambda-shaped wing planform rather disadvantageously. Since the 1303 configuration, however, was not intended to be a full aircraft design, detailed analyses were undertaken on these moment non-linearities to enhance the understanding of the observed flow phenomena. Similarly to the SACCON configuration, the moment characteristics could thus be linked to the flow field characteristics occurring for the 1303 wing configuration.

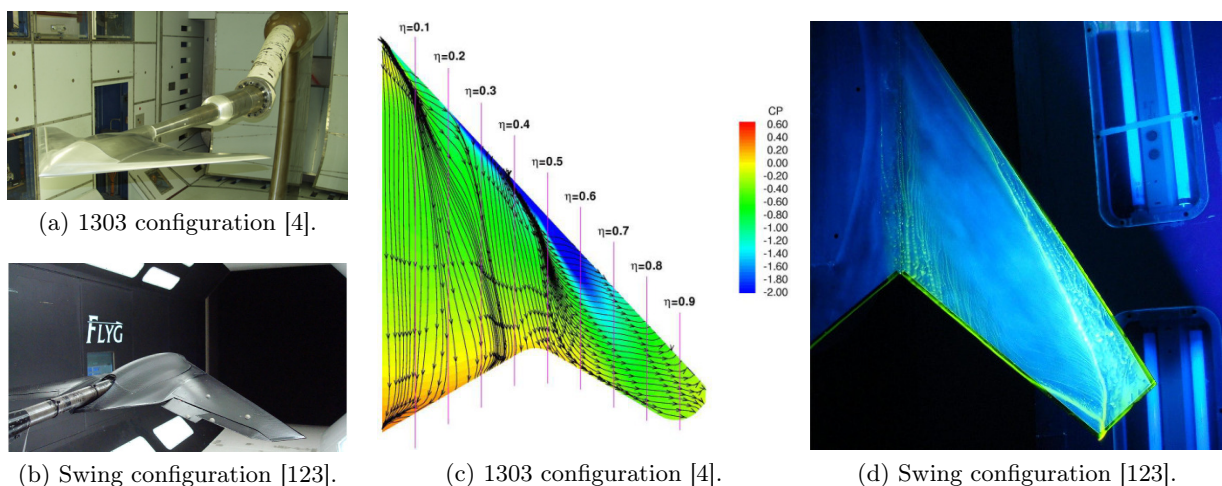


Figure 1.6: Overview of selected research programs associated with non-slender, low-aspect-ratio wing configurations.

The research conducted on the Swing configuration focused in particular on stability and control of the tailless wing with different trailing-edge controls, but valuable information on the flow field characteristics was collected as well. Figure 1.6d depicts an oil flow pattern of the Swing configuration, showing the partly-developed leading-edge vortex in the more outboard wing sections. Compared to the SACCON and the 1303 configuration, the occurring flow phenomena were of similar type, and pitch-break instabilities were found as well with increasing angle of attack [123].

Synthesis

The introduced research programs greatly contributed to improvements in the research field of partly-developed leading-edge vortices at wing configurations with rounded or spanwise-varying leading-edge contours. Important foundations were laid during the last 25 years, upon which subsequent research could be based. With respect to a better understanding of both the flow physics on the fundamental side and present-day U(C)AV concepts on the application side, however, it turned out that other wing planforms than the challenging lambda-shaped wing configuration should be considered additionally. For this reason, diamond-shaped wing configurations came more and more into the focus of relevant research in this field.

1.3 Research Objectives

The main results and findings of the collaborative research groups AVT-113, AVT-161 and AER-TP5 in particular led to the formation of another follow-up research task group within the NATO STO framework, namely AVT-183, in 2010. It was tasked to focus in greater detail on the "Reliable Prediction of Separated Flow Onset and Progression for Air and Sea Vehicles" [92], and was active until the end of 2014. In order to overcome the pitch instabilities found for lambda-shaped wings such as the SACCON and the 1303 configuration, this time a diamond wing configuration was considered. On a newly designed and more simple wing configuration with completely rounded leading edges, the vortex formation caused by a smooth surface separation was to be studied as an isolated phenomenon [10]. According to Luckring and Boelens, the resulting flow problem was thus reduced to a so-called "combined-unit flow problem" [92]. Thereby, the flow separation onset at the rounded leading-edge contour and the vortex progression could be examined in detail. In a combined approach, both experimental and numerical investigations were undertaken at low-speed wind tunnel (W/T) conditions. CFD code validation was addressed as well by the task group, since advancements in the numerical prediction of respective aerodynamic characteristics are still required for today's state-of-the-art turbulence models.

Key parts of the research conducted for this thesis were meant to drive the overall progress of AVT-183 and helped shaping its final outcome [68, 69, 71, 72, 124]. Accordingly, one main objective of the present thesis was derived from the scope of this task group. In particular, the question regarding the location of the flow separation onset was of great importance for the work

within AVT-183. In this context, a basic sketch by Hummel [63] is introduced, see Figure 1.7. It defines the first main objective of this thesis, namely the analysis of the partly-developed leading-edge vortex on the AVT-183 diamond wing configuration. Both experimental and numerical investigations are used to analyze the flow separation onset and progression. A consistent flow-physical description of the flow

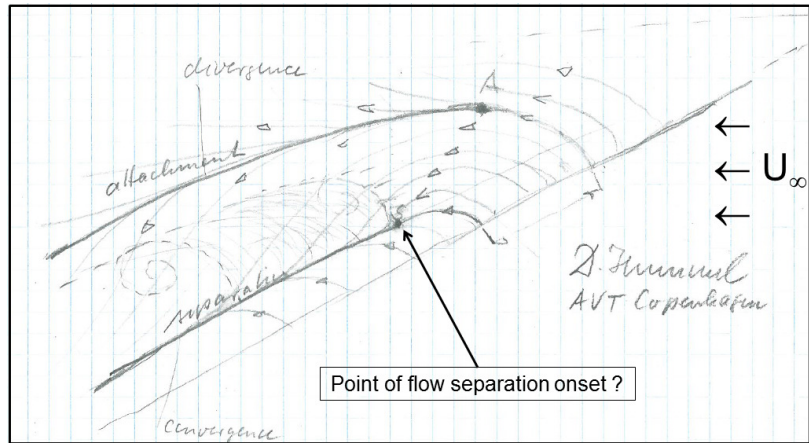


Figure 1.7: Scenario of the flow separation onset at a non-slender wing with rounded leading edge [63].

separation onset on boundary-layer level is especially sought for. On the experimental side, a study of leading-edge roughness effects is additionally conducted, which provides fixed transition conditions in the W/T experiments. Altogether, the overall understanding of smooth surface separations at wing configurations with rounded leading edges shall thereby be enhanced. The following Section 1.4 gives an overall description of the AVT-183 diamond wing configuration. The work approach within this thesis is then outlined in Section 1.5.

The second main objective of the present research pertains to the control of partly-developed leading-edge vortices. In this regard, leading-edge contour modifications including spanwise-varying leading-edge contours are examined. Concepts of passive flow control are thereby investigated. Low-speed W/T conditions are considered exclusively, and Mach number and Reynolds number effects are out of the scope. For the analysis, another diamond wing configuration is looked at, namely SAGITTA (Latin for "arrow"). Its geometric details are stated in Section 1.4. This low-signature, low-aspect-ratio U(C)AV configuration is associated with a research program launched by Airbus Defence and Space in 2011, which follows a so-called "Open Innovation" approach [117]. Several partners from German universities and research institutions each work on specific aspects of the project. Additionally, a flying demonstrator is constructed jointly, see Figure 1.8. The first flight of the vehicle is scheduled for fall 2016.



Figure 1.8: SAGITTA demonstrator configuration.

Within this part of the thesis, several leading-edge contour modifications in spanwise direction are investigated, for which varying flow field characteristics are expected. By means of these modifications, different partly-developed leading-edge vortices are created and controlled. As a result, the flow field characteristics include regions of attached flow and separated vortex flow. With increasing angle of attack, vortex-vortex interactions are also looked at. Overall, the analyses are mainly conducted by numerical investigations. For the reference configuration, comprehensive W/T tests are performed also, and therefore the numerical method is validated. Hence, this study aims at improving the stability, controllability and agility of the SAGITTA diamond wing configuration. The obtained differences are assessed and rated with respect to the flight performance and resulting RCS issues. This work thereby contributes to a generally improved understanding of partly-developed leading-edge vortices at wing configurations that are relevant for practical U(C)AV applications.

1.4 Analyzed Diamond Wing Configurations

This section introduces the two diamond wing configurations considered in the present research. First, the AVT-183 configuration is regarded, which originates from the related STO task group AVT-183. Figure 1.9a shows the wing planform that was designed as a semi-span wing configuration. Consequently, the analyses only deal with the longitudinal motion. Boelens et al. summarized the development process of the diamond wing configuration in detail [10]. The wing was designed in a way that the desired flow phenomenon of blunt-leading-edge vortical separation occurs for given low-speed W/T conditions at moderate angles of attack. The resulting diamond wing features a 53° leading-edge sweep, -26.5° trailing-edge sweep angle and is equipped along the entire span with a rounded leading-edge contour of NACA 64A006 type. Along the wing span, the leading-edge radius to chord ratio is constant with $r_{le}/c = 0.23\%$.

Second, the full-span SAGITTA diamond wing configuration is introduced, see Figure 1.9b. Compared to the AVT-183 configuration, the SAGITTA configuration features very similar leading-edge and trailing-edge sweep angles, respectively ($\varphi_{le} = 55^\circ$ and $\varphi_{te} = -25^\circ$). The

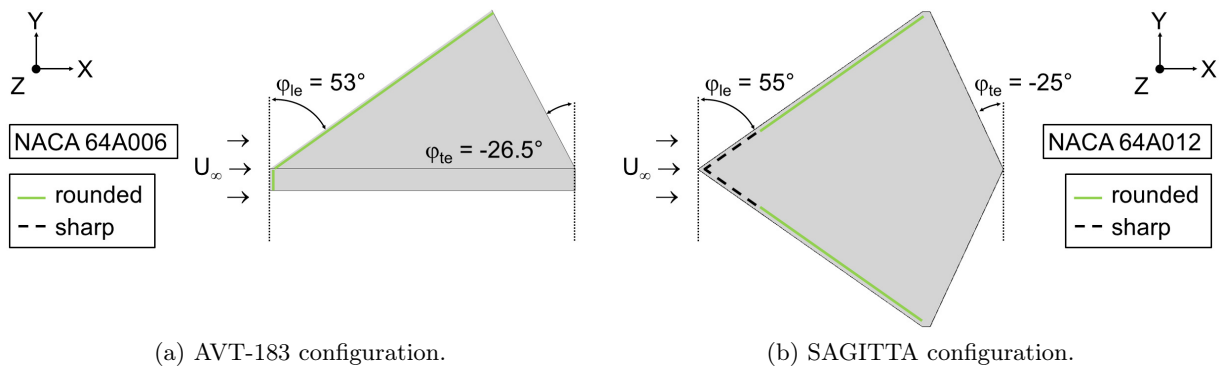


Figure 1.9: Planform comparison of the analyzed diamond wing configurations, top view xy plane.

1.4 Analyzed Diamond Wing Configurations

chosen airfoil originates from the same NACA airfoil family (64A0XX), but the relative thickness is however twice as thick with 12% relative thickness. This is a result from relevant constraints within the SAGITTA research program. Since no explicit fuselage is present, the available installation space must be spread over the whole diamond wing volume. Thereby, the SAGITTA configuration features a relatively thick airfoil with significantly large nose radii of the rounded leading edge ($r_{le}/c = 0.99\%$). Based on present RCS requirements as introduced above, the inner 20% of each semi-span wing were furthermore replaced by a sharp leading-edge contour, see Figure 1.9b. In consequence, the SAGITTA configuration exhibits spanwise-varying leading-edge contours. The thick airfoil and the leading-edge geometry influence the vortex flow characteristics considerably. Early studies on this 12% relative thickness U(C)AV configuration showed that wing segments with rounded leading-edge contours are still at moderate angles of attack dominated by attached flow (apart from the wing tip area). Up to $\alpha = 18^\circ$, vortex formation only takes place by the inboard sharp leading-edge contour [65–67, 70].

The concepts of passive flow control are reviewed on five leading-edge contour modifications. By the choice of the actual leading-edge geometry, spanwise sections of attached flow and separated flow (vortex flow) shall be provoked. To control the occurring partly-developed leading-edge vortices most efficiently, additional segments with sharp leading edges are introduced at the leading edge of the SAGITTA configuration in spanwise direction. Based on a parametric geometry model [66], the reference geometry and five configurations with modified spanwise-varying leading-edge contour were defined, see Figure 1.10. The reference configuration shown in Figure 1.10a is designated as SG Geo 1. It features a sharp leading edge in the inboard section named LE segment I. The leading-edge contour of the remaining wing sections is of basic NACA 64A012 type. The second configuration, namely SG Geo 2, was derived from the reference configuration

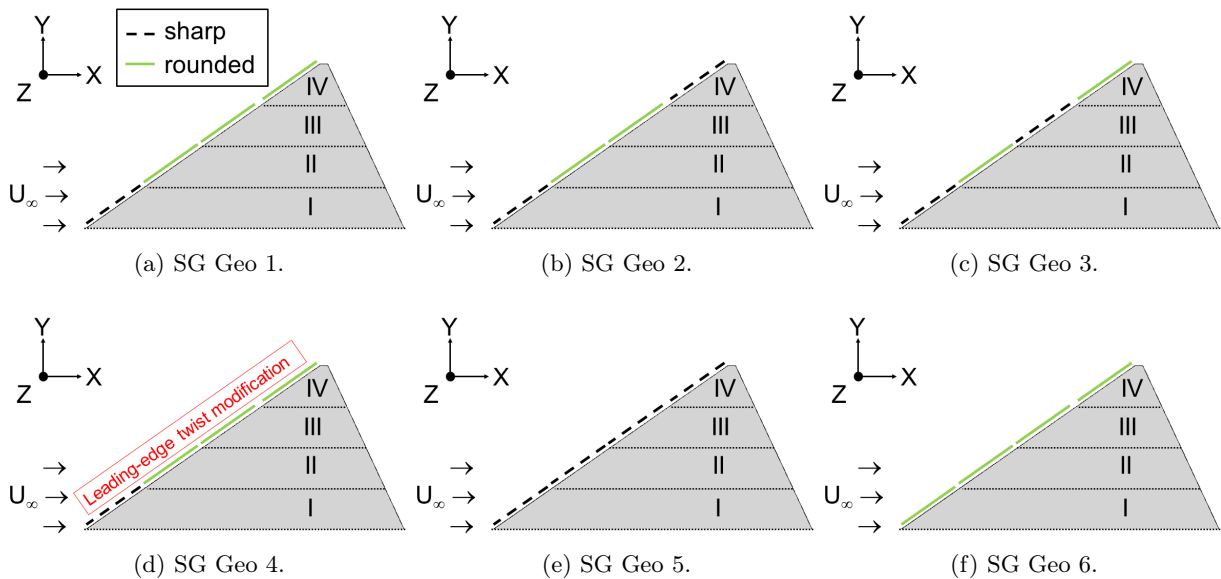


Figure 1.10: Spanwise-varying leading-edge contours of the SAGITTA configuration (right wing).

SG Geo 1 by adding a sharp leading-edge contour to the outboard wing section LE segment IV, see Figure 1.10b. Configuration SG Geo 3 exhibits a sharp leading-edge contour in LE segment I and LE segment III while the remaining segments are of basic NACA 64A012 type with rounded leading-edge contour, see Figure 1.10c.

Configuration SG Geo 4 is characterized by a leading-edge twist modification. It was derived from a related U(C)AV concept of Airbus Defence & Space that was designed to operate up to high subsonic Mach numbers. The leading-edge shape is equal to that of reference configuration SG Geo 1, see Figure 1.10d. The leading-edge coordinate, however, is twisted along the wing span in z-direction. Figure 1.11 depicts the resulting z-offset along the leading edge in spanwise direction. For most of the wing sections along the span, it can be seen that the leading-edge nose is shifted up so that the effective local angle of attack is increased. Therefore,

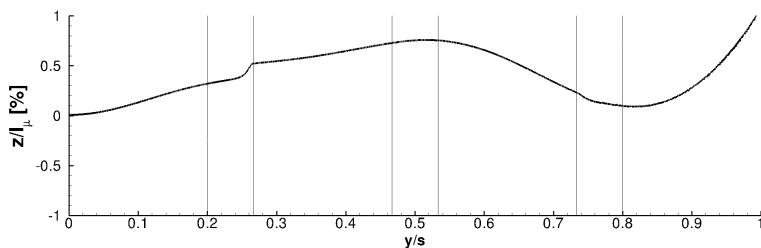


Figure 1.11: Leading-edge twist modification (nose coordinate) for configuration SG Geo 4.

leading-edge vortex formation due to rounded leading edges is promoted. The last two configurations, namely SG Geo 5 and SG Geo 6, are considered for comparison purposes. They feature exclusively sharp and rounded leading-edge contours, see Figure 1.10e and 1.10f. Except for the different

airfoil thickness and the slightly varying leading- and trailing-edge sweep angles, configuration SG Geo 6 is thus equal to the AVT-183 configuration. Consequently, the fundamental effects of airfoil thickness and leading-edge radius on the vortex formation can directly be compared and discussed.

1.5 Thesis Outline

A brief outline on the following chapters of the present thesis is provided. Chapter 2 introduces important fundamentals that are relevant for this work. In addition to basic relations for similarity and dimensionless parameters, an overview of the flow physics is given with regard to three-dimensional separated flows. In particular, theoretical considerations on the topological interpretation are reviewed. Afterwards, leading-edge bluntness effects on vortex separations are considered. The main influence parameters and the effects with respect to the occurrence of partly-developed leading-edge vortices are thereby summarized.

In Chapter 3, the experimental approach is presented. At first, the W/T test facility that was used for the experimental analyses is introduced. Section 3.2 then explains the W/T models and the corresponding measurement test set-ups. Afterwards, wall roughness effects in experimental investigations are treated. In combination with the explanation of theoretical aspects, relevant trip-strip methods and cases to fix the laminar-turbulent transition on the W/T models are

examined. This aspect is of great importance for the present work, especially for the analyses associated with the AVT-183 configuration. Chapter 3 finally concludes with the description of the applied measurement techniques.

The numerical approach in Chapter 4 is divided into three parts. First of all, the geometry models relevant for the numerical investigations are introduced. Subsequently, the grid generation process and the resulting grids are presented for both the AVT-183 configuration and the SAGITTA configuration. Finally, the applied flow solver is regarded. The governing equations are stated and the main features of the flow solver are introduced in this context. The relevant numerical set-ups are also summarized.

The analysis and discussion of the results are spread over two comprehensive chapters. At first, the analysis of partly-developed leading-edge vortices is considered in Chapter 5. This work has been conducted for the AVT-183 configuration. The sub-structure is organized by different sections for the experimental and numerical investigations. The experimental part, see Section 5.1, first of all deals with leading-edge roughness effects on the flow separation onset and progression of the emanating leading-edge vortex. Subsequently, the overall flow field characteristics are regarded and the integral aerodynamic coefficients are discussed. The main results and major findings of the AVT-183 W/T experiments are thus presented in detail. The numerical part, see Section 5.2, starts with the validation of the numerical method. Thereafter, the flow physics analysis of the partly-developed leading-edge vortex is extended by the CFD computations, and comprehensive analyses on the flow separation onset characteristics close to the diamond wing surface are presented. Finally, the flow topology is reviewed, which characterizes the flow-physical mechanisms of the smooth surface separation and the leading-edge vortex formation.

The results obtained for the SAGITTA configuration are regarded in Chapter 6, which focuses on the investigation of passive flow control concepts by leading-edge contour modifications. The reference configuration SG Geo 1 is considered in Section 6.1. First, the numerical method is validated by experimental results. Then, the flow physics of the reference configuration is analyzed, as both the longitudinal and the lateral motion are discussed. The subsequent sections depict the results of the other configurations with modified leading-edge contours, see Section 6.2 to Section 6.4. They are based on numerical investigations only and concentrate on the longitudinal motion. The sections are each sub-structured by a flow physics analysis and investigations of the longitudinal aerodynamic coefficients. The corresponding derivatives and respective stability investigations are also covered for the considered cases. Thereby, the different leading-edge modifications are assessed with respect to stability and control as well as flight performance issues. Finally, the results are each compared to those of the reference configuration SG Geo 1.

The thesis finishes with a conclusion of the presented results. The regarded research fields are summarized, and the major findings of the AVT-183 and the SAGITTA analyses are highlighted. The outcome of the respective investigations is linked together, as the key results are set in context to each other. Thereby, a final assessment of the research topic is provided, which emphasizes the lessons learned on the analysis and control of partly-developed leading-edge vortices.

Chapter 2

Fundamentals

2.1 Similarity and Dimensionless Parameters

Dimensionless parameters play a key role in aerodynamics with respect to the similarity of flow fields. In particular, they have to be considered in experimental analyses, in which scaled models are commonly regarded. Compared to full-scale conditions or related numerical investigations, the flow field characteristics only fit together if the dimensionless parameters are kept constant. According to Truckenbrodt, the similarity of two flow fields is in general obtained only if geometric and relevant physical quantities correspond to a fixed ratio for any correspondent position within the two flow fields [130]. In practical applications, one often considers only the most relevant quantities. They have to be determined in preparation of the experiments and numerical simulations, respectively. Finally, this then leads to the resulting dimensionless parameters.

In the context of the present research, the focus was laid on the Mach number, the Reynolds number, and the Strouhal number. The Mach number gives a measure of the ratio of inertial to elastic forces, and the Reynolds number depicts the ratio of inertial to viscous forces. If unsteady flow phenomena are present, one additionally considers the Strouhal number. In the following, it is expressed by the reduced frequency. Thereby, significant frequencies of unsteady flow phenomena are directly accessible. Hence, the relevant dimensionless parameters are defined as follows:

$$\text{Mach number:} \quad Ma = \frac{U_\infty}{\sqrt{\kappa RT}} , \quad (2.1)$$

$$\text{Reynolds number:} \quad Re = \frac{U_\infty \cdot l_\mu}{\nu} , \quad (2.2)$$

$$\text{Strouhal number:} \quad St = \frac{f \cdot l_\mu}{U_\infty} = k_{red} . \quad (2.3)$$

Since the considered diamond wing configurations do not refer to explicit full-scale flight vehicles, the experimental results represent the source data for subsequent analyses. To ensure flow field similarity in the combined experimental/numerical approach, which was applied in the course of

this thesis, the dimensionless parameters of the numerical investigations were accordingly derived from the W/T experiments. A correct installation of the W/T models in the test facility and a sufficient accurate flow field quality within the experimental analyses compared to the CFD investigations were naturally required in this context.

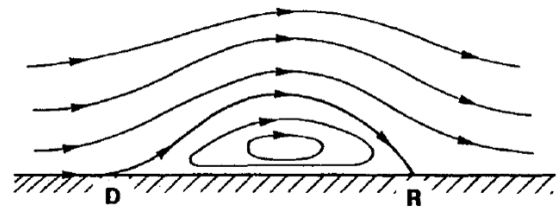
The geometric similarity of the wing configurations, including comparable reference lengths for the dimensionless parameters, was a priori given between the experiments and the numerics, since the W/T model sizes were directly used for the entire numerical investigations, see Section 4.1. Due to variations of ambient pressure and temperature in the W/T facility during the experimental investigations, the Mach and Reynolds number similarity required more attention. Since the flow separation onset and progression of partly-developed leading-edge vortices are, in case of low-speed W/T conditions, much more sensitive to the Reynolds number than to the Mach number, the Reynolds number was kept constant in the experiments in the first instance. The variations in the free stream Mach number were negligible in this context. Section 3.2 presents the corresponding data for the respective measurement test set-ups of both regarded wing configurations. Hence, the Mach and Reynolds number similarity between the W/T experiments and the CFD computations was guaranteed in all cases. The last aspect to be addressed pertains to the similarity of the wall roughness. The CFD computations were run fully turbulent, see Section 4.3.3. Since the boundary-layer characteristics in the W/T experiments, however, could be expected as partly laminar for the applied model sizes and Reynolds numbers, special attention was thus laid on flow tripping. Section 3.3 focuses on this issue in detail, including overall information on wall roughness effects in low-speed W/T investigations. Thereby, the similarity of the boundary-layer flow between the experimental and the numerical investigations was ensured. Especially with respect to the analysis of vortex-dominated wing configurations, this aspect is of great importance.

2.2 Flow Physics of Three-Dimensional Separated Flows

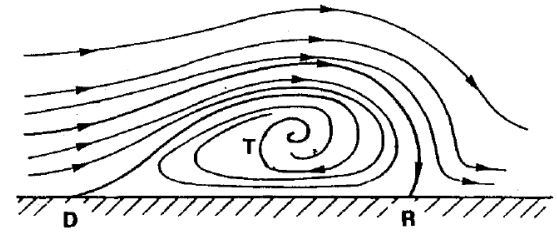
General Remarks

The flow field of low-aspect-ratio wing configurations, as considered in this thesis, is in general characterized with increasing angle of attack by vortical flow, which arises from a three-dimensional flow separation. In this case, a viscous flow sheet, which was previously confined in the boundary-layer region attached to the wall, rolls up and suddenly springs into the outer non-dissipative flow [27]. The flow separation entails the formation of vortical structures and, depending on several influence parameters, partly-developed leading-edge vortices may occur, see Section 2.3. From a flow-physical point of view, the phenomena associated with three-dimensional separated flows are still not understood to the fullest, although they have been studied for a long time. In particular, a clear flow-physical understanding of the flow separation onset, especially for smooth surface separations, is of major interest. In a brief summary, fundamental remarks are given next on this aspect with respect to the present thesis.

The description of three-dimensional separated flows is challenging in many aspects, since it is more complex compared to two-dimensional considerations. The classical definition of flow separation in two dimensions with $\tau_w = 0$ at the separation point is not sufficient any longer for three-dimensional flows. Generally, there are no privileged directions along which the sign of the skin friction - which is now a vector - has a well-defined physical meaning, see Délerly [27]. The separated flow can always escape in the transverse dimension, see the vortical structure (T) in Figure 2.1b. Hence, a three-dimensional flow separation is rather induced by a separation line, where the boundary layer, actually two converging boundary layers, separates from the body surface [51]. By way of example, this is schematically shown in Figure 2.2. According to



(a) Two-dimensaional flow.



(b) Three-dimensaional flow.

Figure 2.1: Simple concepts of flow separation [27].

Hirschel [51], three-dimensional flow separation in general can thus be defined as follows: "Separation is present in three-dimensional flows, if vorticity is transported away from the body surface by convection, and subsequently vortex sheets and vortices are formed". This understanding also corresponds to definitions given by Hummel, which were proposed in this regard [63].

On the basis of detailed experimental analyses and the respective state-of-the-art numerical models, the investigation of three-dimensional separated flows was intensively studied from a fundamental point of view over the last decades. In this context, theoretical approaches were also worked out. The flow physics of the overall flow phenomenon could thereby be identified and

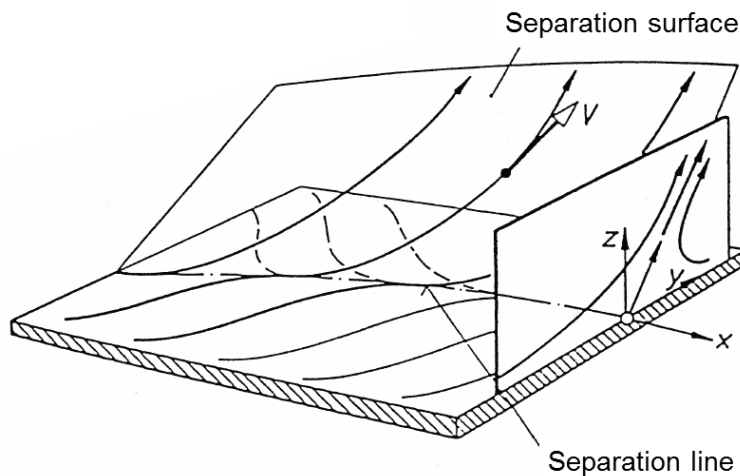


Figure 2.2: Nature of three-dimensional flow separation [18].

understood to a greater extent. In particular, the interpretation of the resulting flow topology always raised the research interest, since the physical mechanisms associated with three-dimensional separated flows can therefore be detected. Moreover, they can be linked together for both the surface quantities and the flow field offside the surface.

Topological-Physical Interpretation

To overcome the lack of adequate theoretical concepts for the description of three-dimensional separated flows in the early days of the analysis, specific research was conducted already from the 1950s on. Based on initial studies by Legendre [84], important notions such as skin-friction lines, critical points, as well as separation (or attachment) lines and surfaces were introduced and discussed [28]. For the first time, this allowed a consistent theoretical description of the flow field, in which three-dimensional separation effects occur. Major contributions were given in this context, for instance, by Davey [25], Lighthill [85], Hunt [64], and Tobak and Peake [127]. Overall, it turned out that three-dimensional separated flows can be classified by topological rules, which are closely coupled with the critical-point theory. According to Délery [27], the application of this theory allows to correctly interpret the surface flow patterns that constitute the imprints of the outer flow. A rational and coherent description of the vortical system generated by three-dimensional separation is thereby provided. Consequently, the topological considerations are a powerful tool for specific flow field diagnostics of three-dimensional separated flows.

For the infinity number of trajectories, which are identified with the skin-friction lines along a body surface, in general only one trajectory passes through a point on the surface. This holds for the entire continuous vector field of skin-friction lines except for explicit singular points, where the two wall shear stress components, namely τ_{wx} and τ_{wz} , vanish simultaneously and

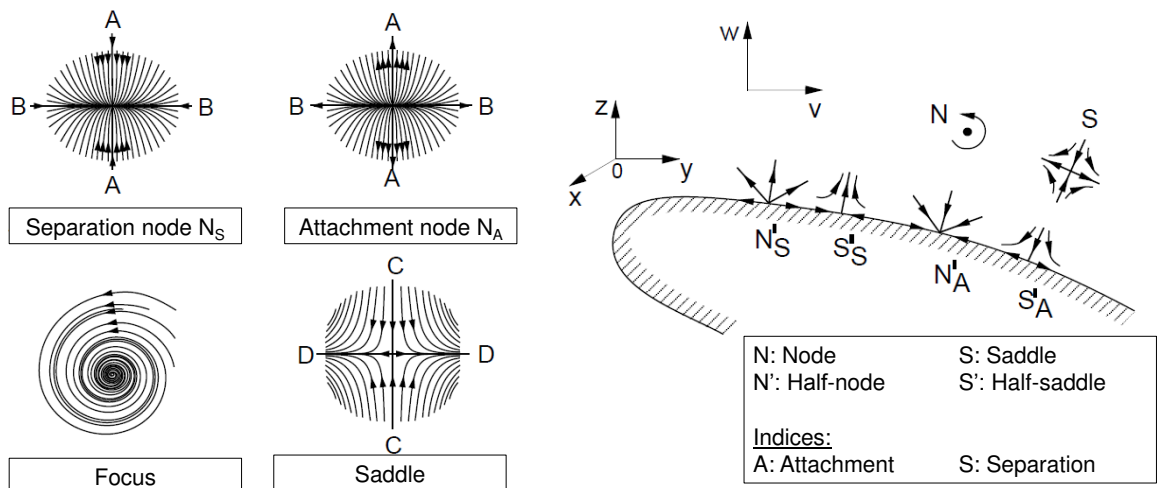


Figure 2.3: Singular points in a cross-section of a flow field [16, 127].

are identically zero. Accordingly, these points define locations of separation and attachment, respectively. Depending on the actual flow field characteristics, the singular points are of different type and can be classified into nodes, foci, and saddles, see Figure 2.3. As summarized by Tobak and Peake [127], they can be characterized as follows, see Figure 2.3a. At a nodal point, all of the skin-friction lines except one (A-A) are tangential to a single line B-B. The direction of the skin-friction lines further defines if a nodal point of separation (N_S , directed inward) or a nodal point of attachment (N_A , directed outward) is present. A focus is characterized by the absence of a common tangent line. Based on the spiral around the singular point, a focus of separation (spiral points into it) or a focus of attachment (spiral points away from it) can be observed. Finally, a saddle point features two particular lines, C-C and D-D, which pass through the singular point. One is pointed inward, and the other one is pointed outward. All of the other skin-friction lines do not reach the singular point and take directions along the two particular lines. Thereby, a corner-flow-type pattern is present in four segregated sectors. If the singular points are adjacent to a body surface, the nodes and saddles are furthermore transferred to half-nodes and half-saddles, see Figure 2.3b.

As a result of the critical-point theory, different topological rules can be formulated and applied to any flow field with three-dimensional separated flows. They connect the topography of skin-friction lines and field streamlines based on the occurring singular points. In every relevant flow pattern, the topological rules must be obeyed. Tobak and Peake [127] presented five different rules, two of which are introduced in this research. The first rule concerns the skin-friction or velocity field on a three-dimensional body and was first formulated by Davey [25] and Lighthill [85], respectively. For the following relation, one should further mention that foci are counted as nodes as well:

$$\sum N - \sum S = 2 . \quad (2.4)$$

If a two-dimensional plane cut of a three-dimensional body is considered, the topological rule proposed by Hunt et al. [64] must further be valid:

$$\left(\sum N + \frac{1}{2} \sum N' \right) - \left(\sum S + \frac{1}{2} \sum S' \right) = -1 . \quad (2.5)$$

In the present research, the topological rules are applied to resulting near-wall flow field characteristics. This allows for the analysis and the review of the occurring leading-edge vortex separations. In particular, the AVT-183 configuration is regarded in this context, for which the flow separation onset associated with rounded leading-edge contours is studied. The topological interpretation of the resulting flow fields shall help to identify the physical mechanisms of the smooth surface separation in more detail. Due to the rounded leading edges, the three-dimensional flow separation is in general less understood than the case including sharp leading edges. Relevant parameters that influence the overall appearance of vortical structures due to rounded leading-edge contours are therefore discussed in the following section.

2.3 Leading-Edge Bluntness Effects on Vortex Separation

Compared to the sharp-edged case, Mach and Reynolds number effects including varying boundary-layer characteristics are much more pronounced with rounded leading edges. In addition, the leading-edge radius, the leading-edge sweep angle and the airfoil thickness play a designated role on the flow separation onset and progression. Due to the comprehensive experimental data set including Mach and Reynolds number variations, which is available for the VFE-1 delta wing configuration [21, 87–90], the corresponding results are considered below. Characteristic leading-edge bluntness effects on vortex separation are thereby introduced.

Reynolds Number Influence

The Reynolds number effect on blunt leading-edge vortex separation was summarized by Luckring, see Figure 2.5. It is closely coupled with the occurring boundary-layer characteristics that may differ with increasing Reynolds number, the local position on the wing, and the angle of attack. Thereby, different flow separation onset characteristics are obtained for various Reynolds numbers. For the lower Reynolds number of $Re = 6 \cdot 10^6$ and the angle of attack of $\alpha = 13^\circ$ on the left-hand side, the sectional surface pressure distributions show attached flow up to $x/c_r \approx 0.3$. Then, the leading-edge vortex formation is observed, which is due to laminar flow separation. The results for the higher Reynolds number of $Re = 60 \cdot 10^6$ on the right-hand side indicate attached flow up to the region of $x/c_r \approx 0.6$, before vortex separation occurs based on turbulent boundary-layer flow. Accordingly, the flow separation onset is considerably delayed with increasing Reynolds number. In this context, Hummel introduced a schematic representation of the vortex formation along rounded leading edges [57], which is shown in Figure 2.6. Depending on laminar, transitional or

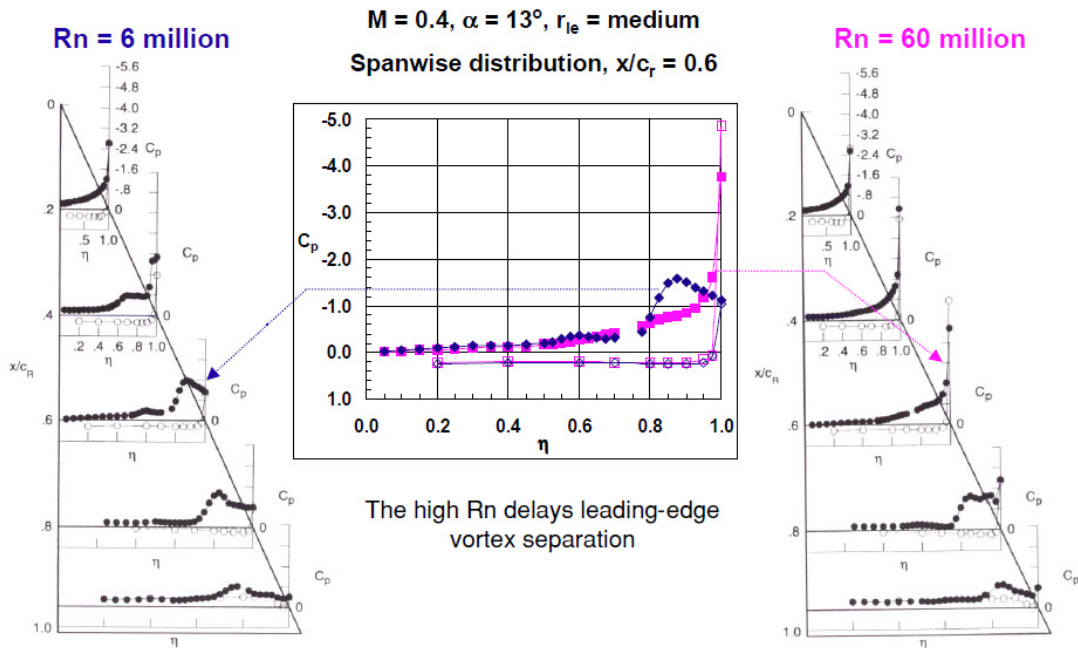


Figure 2.5: Reynolds number effect on blunt leading-edge vortex separation [89].

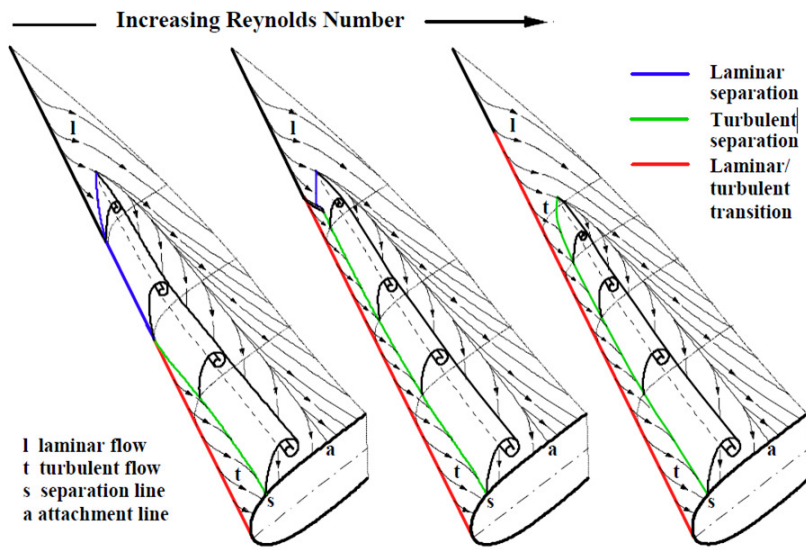


Figure 2.6: Reynolds number effect on vortex formation along rounded leading edges [57].

edge moves upstream, and diminishes the region of laminar flow separation (mid sketch). The primary separation line is now completely offside the leading edge. Finally, turbulent flow separation takes place along the entire primary separation line, which is exclusively located on the upper wing surface, right plot of Figure 2.6. If the transition laminar/turbulent reaches the wing apex region, the flow separation onset resulting from turbulent flow separation is delayed as compared with the laminar case, since the turbulent boundary layer is better suited to withstand the adverse pressure gradients. Therefore, the region of attached flow in the apex region is larger for the turbulent case at high Reynolds numbers than for the laminar case at low Reynolds numbers as shown in Figure 2.5 [57]. The right plot of Figure 2.6 furthermore depicts the situation of a smooth surface separation with consecutive vortex formation as introduced in Figure 1.7. In particular, it shows the flow topology, which analysis is of central concern within this thesis. The onset location of the separation line on the upper wing surface is not known so far. For this reason, the present research focuses amongst others on this aspect, see Section 1.3. Although low-speed W/T conditions including low Reynolds numbers are regarded only, the case of turbulent flow separation is relevant for the present analysis. This is due to an appropriate flow tripping in the W/T experiments and fully-turbulent CFD computations, see Section 2.1.

Mach Number Influence

Figure 2.7 presents the compressibility effect on blunt leading-edge vortex separation based on experimental results of the VFE-1 delta wing configuration. In general, an increase in Mach number can significantly influence the flow separation onset and progression. For the angle of attack of $\alpha = 13^\circ$ and $x/c_r = 0.4$, well-developed vortex flow is observed at $Ma = 0.6$, whereas the flow separation onset just begins at $Ma = 0.4$. The results thereby show an upstream movement

turbulent boundary-layer characteristics, the behavior of the flow around the leading edge differs from each other. Moving downstream, one can notice two different regions, which are set by the transition point laminar-turbulent, left-hand side of Figure 2.6. In this case, the primary separation line is either located on the upper wing surface or, in certain regions, at the leading edge. With increasing Reynolds number, the point of transition at the leading

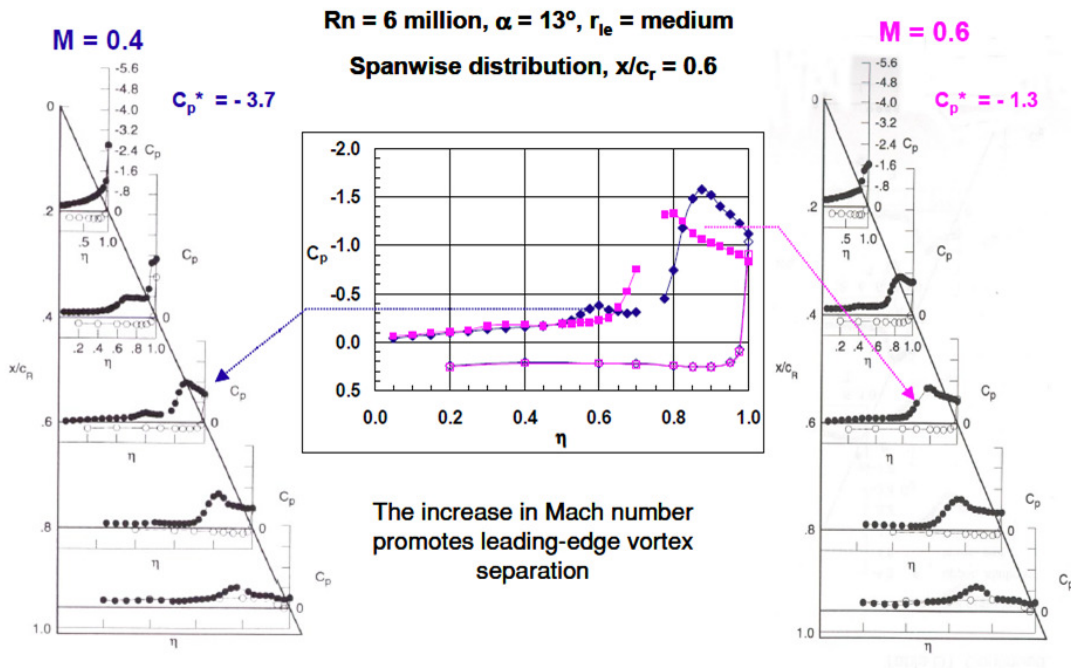


Figure 2.7: Mach number effect on blunt leading-edge vortex separation [89].

of the incipience of blunt leading-edge vortex separation with increasing Mach number. Moreover, this holds for the entire angle-of-attack range. Thus, compressibility promotes blunt leading-edge vortex separation, and the flow separation onset is shifted upstream [89]. The result is contrary to the above discussed Reynolds number influence. If the flow separation onset characteristics with regard to either Reynolds or Mach number variations are to be studied separately, both effects must consequently be isolated. With respect to the results of the present thesis, this was a priori given, since compressibility effects are not relevant to this work.

Bluntness Influence

The influence of varying leading-edge bluntness is reviewed next. In particular, the leading-edge radius is decisive in this context. Figure 2.8 depicts Luckring's results of the VFE-1 delta wing configuration including three rounded leading-edge shapes [88]. The corresponding nose radii r_{le}/c are stated in Table 2.1. For comparison, the nose radii of the wing configurations considered in this thesis are also provided. The plots in Figure 2.8 show the leading-edge suction levels versus the angle of attack. Increasing suction levels at low to moderate angles of attack generally indicate attached flow. The flow separation onset is characterized by a following pressure drop, since the pressure minimum moves inwards to the position of the primary vortex axis. As it can be noticed for the various chordwise sections, the flow separation onset is delayed with increasing leading-edge bluntness to higher angles of attack and to the more downstream wing sections. The peak pressures show a continuous trend, which is consistent to basic airfoil aerodynamics. The larger the leading-edge radius is, the later flow separation occurs. With respect to the low-speed

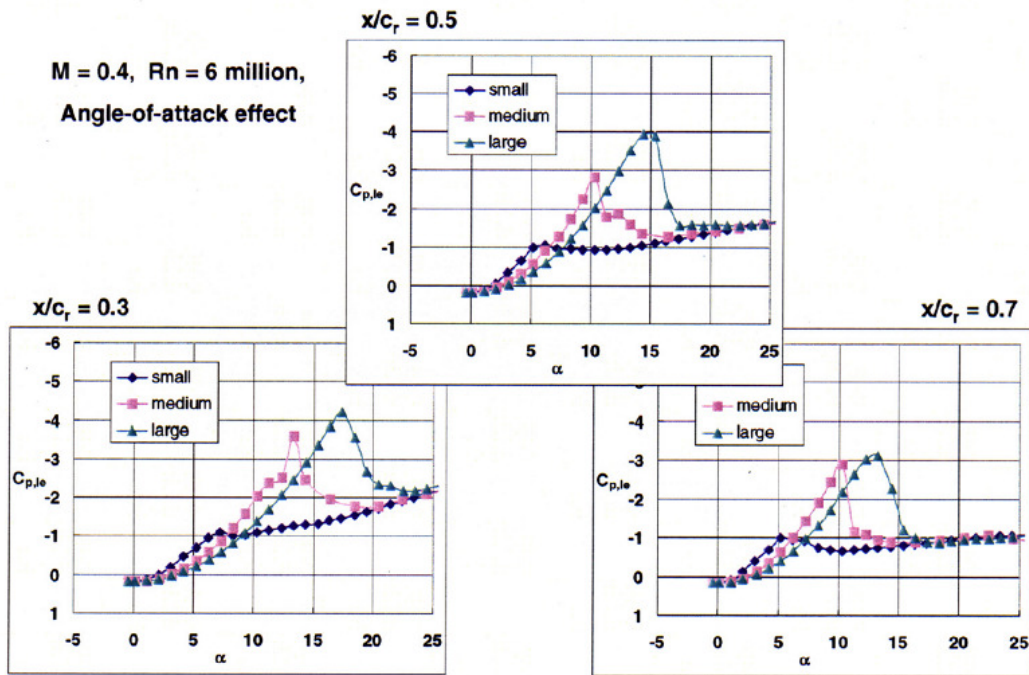


Figure 2.8: Bluntness effect on leading-edge vortex separation [88].

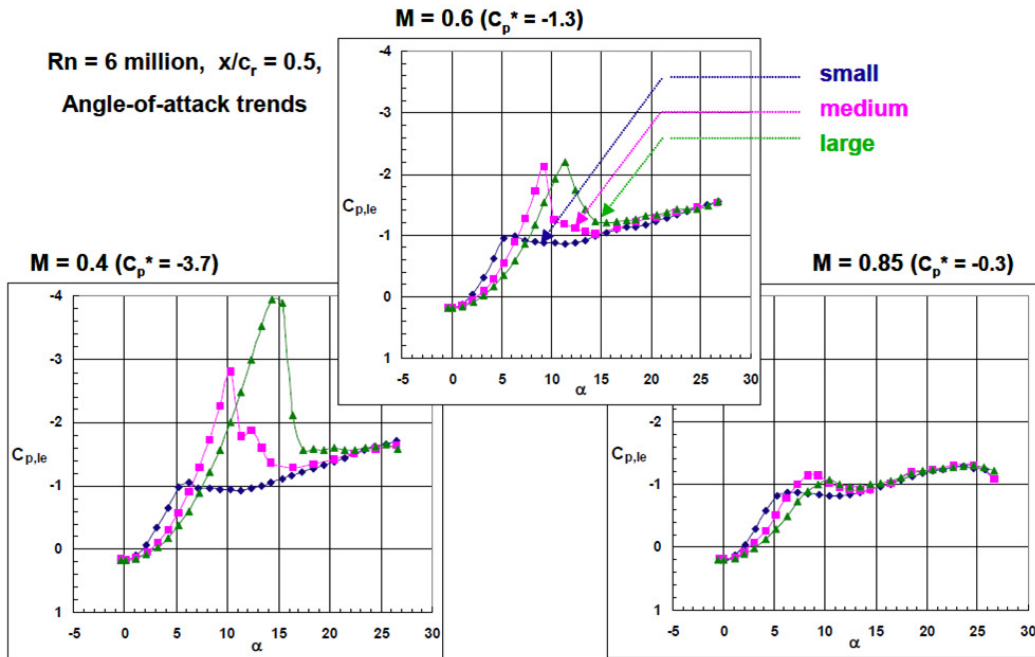


Figure 2.9: Bluntness and Mach number effect on leading-edge vortex separation [87].

W/T conditions and the low Reynolds numbers regarded in the present research, this clearly shows the pronounced influence of varying leading-edge bluntness on the flow separation onset and progression. For the two considered wing configurations of this thesis, remarkable differences are thus expected in the leading-edge vortex formation.

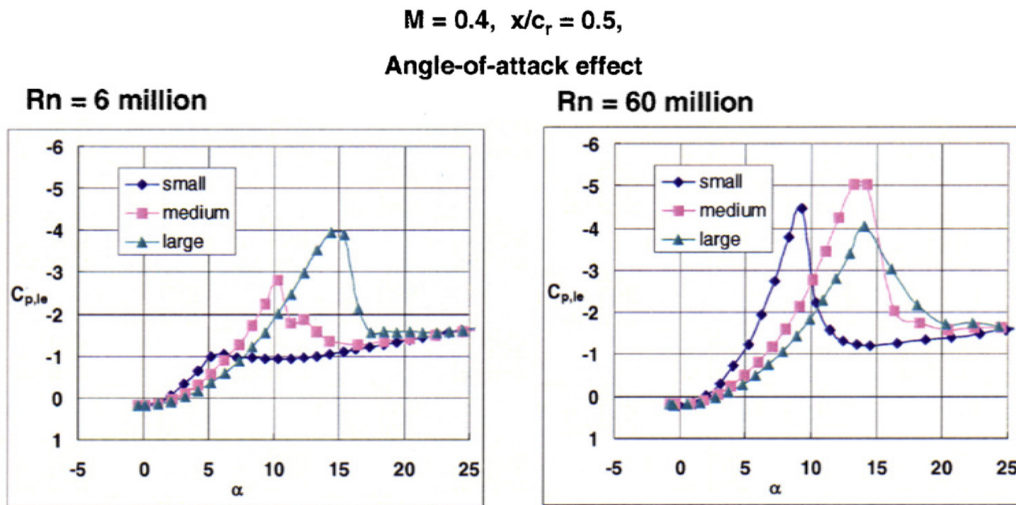


Figure 2.10: Bluntness and Reynolds number effect on leading-edge vortex separation [88].

Configuration	VFE-1	VFE-1	VFE-1/2	VFE-1	AVT-183	SAGITTA
LE shape	sharp	round	round	round	round	round
$r_{le}/c, \%$	0	small 0.05	medium 0.15	large 0.30	0.23	(/sharp) 0.99 (/0)
φ_{le}, deg	65	65	65	65	53	55

Table 2.1: Geometric details of wing configurations featuring rounded leading edges.

The bluntness influence on vortex separation is further dependent on varying Mach and Reynolds number. Figure 2.9 and Figure 2.10 document this aspect. The results demonstrate that the flow separation onset sensitivity is reduced for different leading-edge bluntness with both increasing Mach and Reynolds numbers. In compressible flow approaching transonic conditions, the differences occurring from varying leading-edge bluntness become considerably less. With increasing Reynolds numbers, the continuous trend as observed before is not present any longer.

Wing Planform Influence

The wing planform and especially the leading-edge sweep angle have a considerable influence on the vortex separation and progression. If rounded leading edges are present, in particular the existence of the different flow stages occurring for leading-edge vortices are affected. Depending on angle of attack and leading-edge sweep, Breitsamter has classified this schematically for thin wings [19], see Figure 2.11. Compared to the sharp-edged case, fully-attached flow is present for small angles of attack. With decreasing leading-edge sweep, these characteristics remain at the wing up to higher angles of attack (0). Vortex formation then occurs with increasing angle of attack, and partly-developed leading-edge vortices occur (1). Regions of vortex-separated flow in the outboard

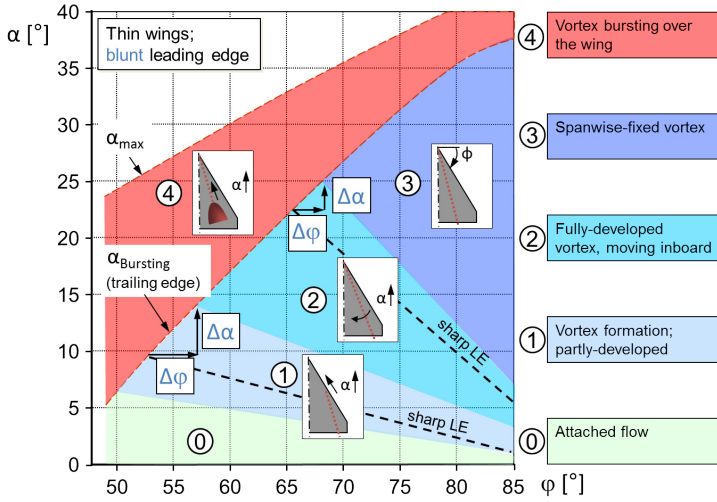


Figure 2.11: Wing planform and angle-of-attack effect on leading-edge vortex separation [19].

and attached flow in the inboard wing sections are observed as introduced above. For non-slender wing planforms with leading-edge sweep angles of $\varphi_{le} \leq 57^\circ$, vortex bursting effects immediately become relevant subsequently (4). The intermediate flow stages of the fully-developed and spanwise-fixed leading-edge vortex, in contrast, are only reached with higher leading-edge sweep angles (2,3). Therefore, vortex bursting at the trailing edge occurs with decreasing leading-edge sweep angle at much lower angles of attack.

With respect to the existence region of the fully-attached flow stage (0), Elsenaar et al. report different observations due to the additional wing thickness influence [36]. During the Vortex Flow Experiment 1, the flow separation onset characteristics were also discussed for leading-edge sweep changes from $\varphi_{le} = 65^\circ$ to $\varphi_{le} = 55^\circ$ (rounded leading-edge contour). As an outcome of different trends as introduced below, it turned out that the beginning vortex separation for reduced wing sweeps occurs at lower angles of attack and moves upstream more rapidly along the leading edge. Recent results by Boelens [9] or Hitzel et al. [55] support this observation. By way of example, Figure 2.12 presents initial results of Boelens' early CFD work to design the AVT-183 configuration. With decreasing leading-edge sweep angle and at constant angle of attack, one can clearly notice the upstream movement of the flow separation onset. According to Elsenaar et al., this is caused by three trends. On the one hand, a smaller sweep angle reduces the normal angle of attack α_n , which delays the vortex separation. On the other hand, the normal Mach number Ma_n is increased, which leads to a hastened vortex separation. These trends are also stated by Staudacher [122]. Moreover, the airfoil sections in a direction normal to the leading edge are effectively thinner with decreasing leading-edge sweep, when the same streamwise basic airfoil shape is present. This also favors early separation. In total, the latter two effects are dominant, and the flow separation onset is thus promoted with reduced wing sweep. Nevertheless, vortex bursting phenomena occur, as stated by Breitsamter, with decreased leading-edge wing sweep shortly after at considerably lower angles of attack.

Depending on varying leading-edge wing sweep, the resulting vortex structure furthermore differs in its occurrence. The overall strength of the leading-edge vortex and the corresponding axial velocity distribution along the vortex core axis in downstream direction are particularly influenced in this context. Slender wing planforms that feature a fully-developed leading-edge vortex commonly show jet-type vortex core flow, before vortex bursting phenomena including

2.3 Leading-Edge Bluntness Effects on Vortex Separation

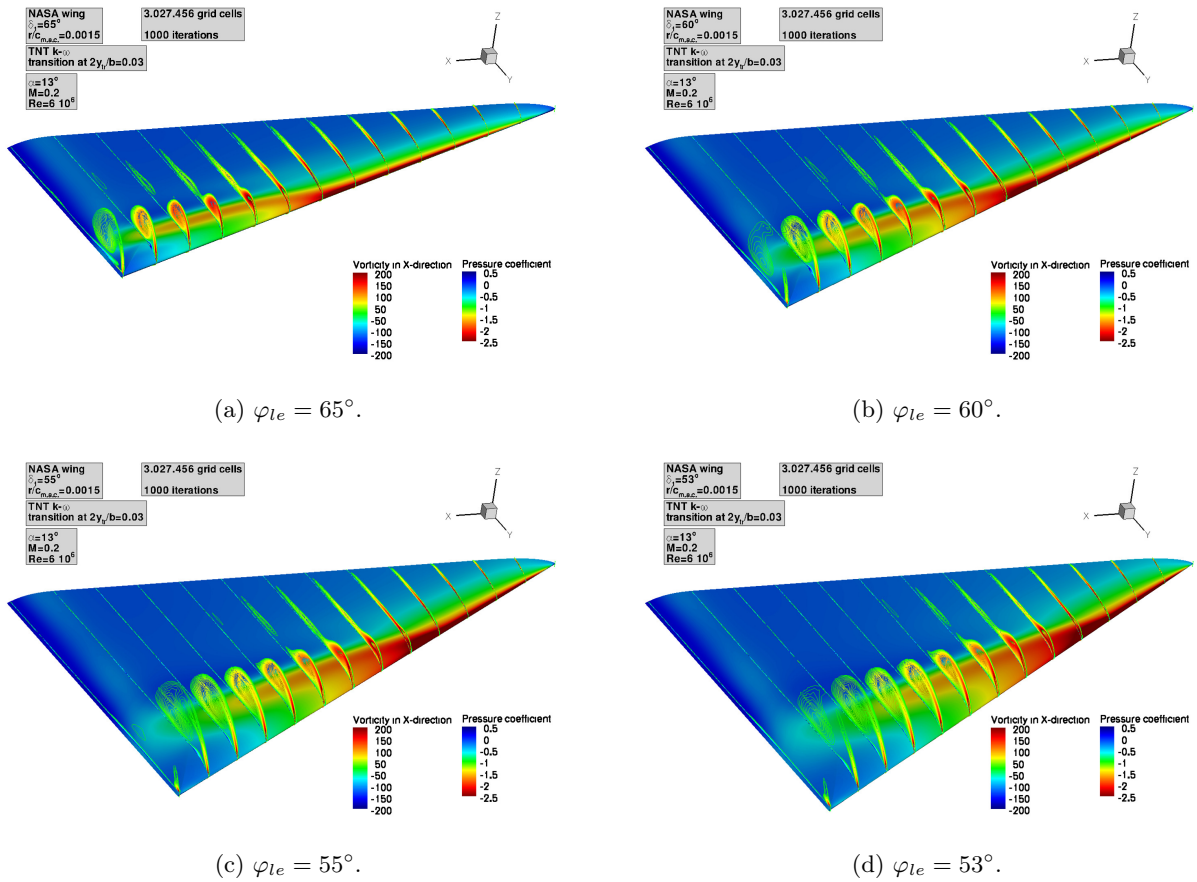


Figure 2.12: Wing planform and relative thickness effect on leading-edge vortex separation [9].

reduced or negative axial velocities occur rapidly at high angles of attack. Non-slender wing planforms, in contrast, often exhibit wake-type vortex core flow only, see Hitzel et al. [52, 54, 55]. The vortex strength is reduced and the flow structures occur closer to the wing surface. With decreasing leading-edge sweep, this phenomenon is intensified, and the beginning vortex bursting effects are not as obvious at first sight. However, they are present closely downstream of the flow separation onset. With increasing angle of attack, the partly-developed and burst leading-edge vortices still move further upstream, until the region of attached flow is diminished and the maximum lift is reached. With decreasing leading-edge sweep, the angle of maximum lift consequently decreases. Since the two diamond wing configurations considered in this research feature leading-edge sweep angles of $\varphi_{le} = 53^\circ$ and $\varphi_{le} = 55^\circ$, see Table 2.1, this type of flow field characteristics is thus expected in the present analysis.

Wing Thickness Influence

The last aspect to be addressed in this section pertains to the effect of airfoil thickness on vortex-dominated wing configurations. In general, it also influences the overall strength of the leading-edge vortex. With increasing airfoil thickness, the vortex intensity is reduced and vice

versa. Moreover, the wing thickness is often coupled to the leading-edge radius. For basic airfoil types such as NACA profiles, both parameters are directly linked to each other. Consequently, an increase in airfoil thickness leads to a delayed flow separation onset and progression. In sum, vortex separation thus occurs for thicker wings at higher angles of attack and more downstream while it is promoted by thinner airfoils. This is valid for all vortex flow stages as shown in Figure 2.11, except for the vortex bursting phenomena, which existence region remains unchanged. As a result, the minimum leading-edge sweep angle required for vortex separation increases with increasing wing thickness. For non-slender wing configurations with thick airfoils, different flow phenomena can be present, which are not of vortex type. For instance, this class of wing configurations often results in irregular separated flow in the outboard wing sections, which is not a matter of vortical flow, but belongs to a conventional leading-edge separation at the tapered wing tip due to high local lift coefficients. These characteristics also apply to the SAGITTA configuration, as early analyses document the mentioned separation behavior at moderate to higher angles of attack up to $\alpha = 18^\circ$ [65–67, 70].

Chapter 3

Experimental Approach

3.1 Wind Tunnel Test Facility

The experimental analyses undertaken for this research were all conducted in the Göttingen-type low-speed W/T facility A of the Institute of Aerodynamics and Fluid Mechanics of the Technische Universität München (TUM-AER), see Figure 3.1. The atmospheric tunnel can be operated in either a closed (solid wall) or an open (floor only) configuration. For the present investigations, however, the open test section was relevant exclusively. The dimensions of the open test section read 1.8 m x 2.4 m x 4.8 m (height x width x length). The corresponding maximum velocity is $U_\infty = 65 \text{ m/s}$ while the free stream turbulence intensity results in values less than 0.4%. The uncertainty in the temporal and the spatial mean velocity distribution is less than 0.7%. The uncertainty in free stream direction is below 0.2° and static pressure variations are below 0.4%. Further information on the W/T facility is additionally stated in Appendix A. Overall, the facility has, amongst others, a well-recognized capability for force and moment testing, surface pressure measurements, and detailed flow field analyses by different approaches. With respect to the present research, all of them were applied in the corresponding W/T investigations. The relevant measurement techniques are therefore introduced in Section 3.4.

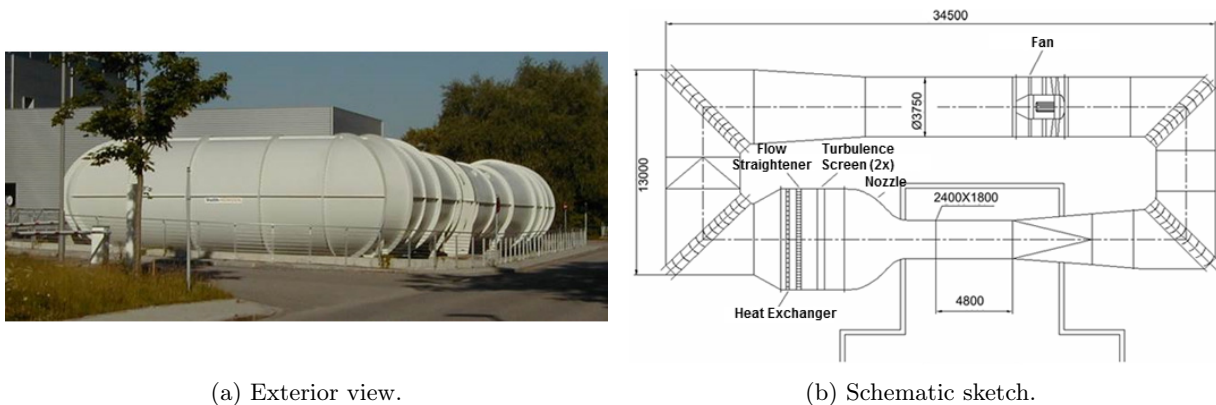


Figure 3.1: W/T facility A of TUM-AER.

3.2 Wind Tunnel Models and Test Set-Up

3.2.1 AVT-183 Diamond Wing Configuration

The AVT-183 diamond wing W/T model was constructed as a semi-span model, since the "combined-unit flow problem" addressed in the NATO research task group required only symmetric flow conditions without sideslip angles [92]. It was manufactured from the aluminum alloy Certal[®], which allows for W/T operation at cryogenic conditions as well. For the dimensioning of the W/T model, the test section size of the low-speed W/T facility A at TUM-AER was deciding, since the entire experimental analyses within AVT-183 were undertaken at this site [69, 72]. The resulting wing planform parameters are summarized in Table 3.1 and Figure 3.2. Overall, the W/T model features a root chord length of $c_r = 1.2\text{ m}$, and the semi-span results in $s = 0.657\text{ m}$. In order to mitigate influences of the W/T floor boundary layer on the semi-span model, it is further mounted on a peniche. The corresponding height was chosen to $h_{pen} = 0.09\text{ m}$ ($h_{pen}/s = 13.7\%$), since benchmark data of the W/T floor boundary layer indicated an approximate boundary layer thickness of $\delta_{99} \approx 0.05\text{ m}$ at the wing-root trailing-edge coordinate of the W/T model. Therefore, minimal influence of the W/T floor should be observed on the flow around the W/T model.

The main components of the AVT-183 diamond wing W/T model are shown in Figure 3.3. They consist of a main suction and pressure side shell, six leading-edge inserts, the peniche including seal and a balance mounting adapter. The leading-edge inserts were designed for an improved pressure instrumentation process, since most of the pressure taps are located closely

c_r	c_t	λ	φ_{le}	φ_{te}	s	S_{ref}	Λ	l_μ	x_{mrp}	h_{pen}
1.2 m	0 m	0	53°	-26.5°	0.657 m	0.394 m	2.191 m ²	0.8 m	0.491 m	0.09 m

Table 3.1: Wing planform parameters of the AVT-183 W/T model.

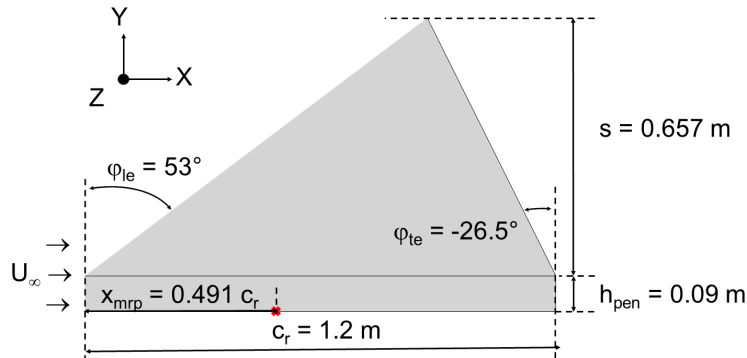


Figure 3.2: AVT-183 W/T model, top view xy plane.

to the leading edge in the area of the inserts. Based on preliminary CFD analyses [10], eight chordwise sections were defined for surface pressure measurements along the semi-span of the W/T model. The corresponding geometry information can be obtained from Table 3.2. At $x/c_r \approx 0.3$ and $x/c_r \approx 0.4$, respectively, two measurement sections were defined close to each other, since the flow separation onset was expected in this region for the selected low-speed W/T conditions. In total, 145 pressure taps are located on the suction side shell, of which eight are instrumented with unsteady Kulite sensors. For the number of pressure taps, only time-averaged steady surface pressure measurements can be undertaken, whereas the Kulite sensors record time-accurate data as well. The corresponding pressure taps are located in four different chordwise sections ($x/c_r = [0.295, 0.405, 0.500, 0.600]$), and at two spanwise locations each ($y/s(x) = [0.650, 0.750]$). On the pressure side shell, 17 pressure taps are located. The peniche contains nine additional pressure taps. All pressure taps are aligned in normal direction to the wing surface, and the diameter of the orifices yields $d_{pt} = 0.3 \text{ mm}$. Figure 3.4 depicts the instrumented W/T model without the pressure side shell and the pressure side peniche. The pressure tubes are collected within the pressure side shell and the pressure side peniche. The pressure tubes are collected within the model and are led bundled out of the model through the W/T floor.

The W/T model itself is mounted on the W/T balance with a balance adapter, see Figure 3.3 and Figure 3.4. Hence, the aerodynamic forces and moments acting on the W/T model can be measured with the external balance placed below the W/T test section. Between W/T model and W/T floor, the peniche is located. As already explained above, it is incorporated in the test set-up, since the boundary layer of the W/T floor should not affect the flow at the diamond wing configuration itself. Between peniche and W/T model, a labyrinth seal employing a small gap of $h_{gap} \approx 1 \text{ mm}$ is placed. Any connection of both components is thereby avoided. Aerodynamic forces and moments acting on the peniche itself are thus not accounted for in the

x/c_r	0.100	0.200	0.295	0.305	0.395	0.405	0.500	0.600
$x, \text{ m}$	0.120	0.240	0.354	0.366	0.474	0.486	0.600	0.720
$s(x), \text{ m}$	0.090	0.181	0.267	0.276	0.357	0.366	0.452	0.543

Table 3.2: Chordwise sections for surface pressure measurements at the AVT-183 W/T model.

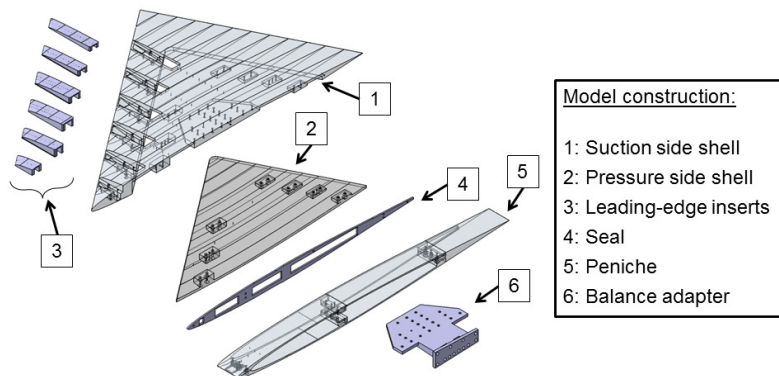


Figure 3.3: AVT-183 W/T model components.

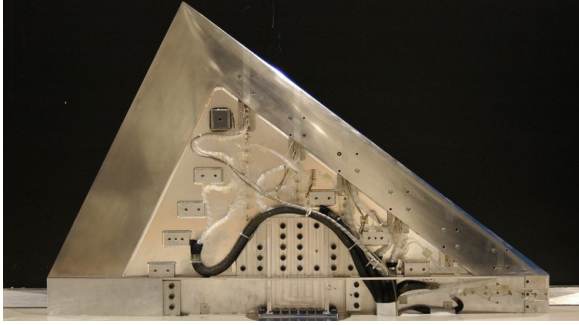


Figure 3.4: AVT-183 W/T model without the pressure side shell.

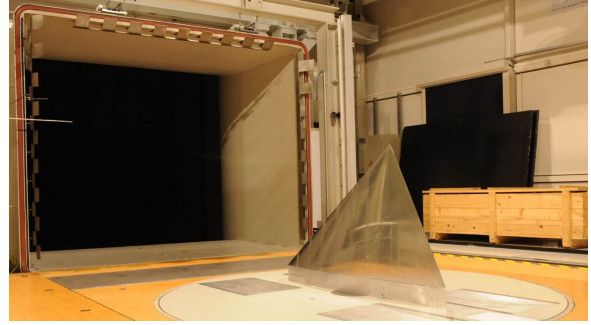


Figure 3.5: AVT-183 W/T model within the W/T facility A of TUM-AER.

force measurements. Load checks during the W/T measurements confirmed the absence of load transfer due to the pressure tubes. Both the leading-edge inserts and the pressure side shell are screwed into the main suction side shell from the pressure side. Hence, the more important suction side of the W/T model is free from any surface disturbances. The resulting test set-up of the AVT-183 diamond wing W/T model within the open test section of the W/T facility is shown in Figure 3.5. The flow direction is from left to right. The W/T model is placed centrally on a turn table that allows for the angle-of-attack adjustment.

The experimental investigations of the AVT-183 diamond wing configuration were undertaken at a Reynolds number of $Re_\infty = 2.7 \cdot 10^6$ based on the mean aerodynamic chord of $l_\mu = 0.8 \text{ m}$ and a Mach number of $Ma_\infty = 0.15$. Due to the atmospheric conditions within the W/T facility A of TUM-AER and the slightly varying W/T blockage at different angles of attack, however, matching of both characteristic numbers Re and Ma at once was not exactly met over time. In the first instance, the W/T velocity was adjusted to meet the Reynolds number requirement while the resulting differences to the target Mach number were less than 5%. Depending on temperature and ambient pressure variations within the W/T test section, the free stream velocity of the experiments varied between $51 \text{ m/s} \leq U_\infty \leq 55 \text{ m/s}$. This corresponds to a free stream Mach number variation of $0.143 \leq M_\infty \leq 0.157$, which is noted as insignificant. For the force and the surface pressure measurements, angles of attack between $-2^\circ \leq \alpha \leq 20^\circ$ were considered with an angle-of-attack increment of $\Delta\alpha = 1^\circ$. For angles of attack of $8^\circ \leq \alpha \leq 16^\circ$, the increment was reduced to $\Delta\alpha = 0.5^\circ$. Subsequent to initial W/T experiments with free transition, target flow conditions with a fixed transition location close to the leading edge were set based on a trip-strip analysis, see Section 3.3.4 and Section 5.1.1. One specific trip strip was finally selected, which was used for the subsequent flow field W/T investigations at $\alpha = 10^\circ$ and $\alpha = 12^\circ$, see Section 5.1.2.

3.2.2 SAGITTA Diamond Wing Configuration

The W/T model of the SAGITTA diamond wing configuration is represented by a 1:10-scaled version of an abstract full-scale reference geometry, which was defined by Airbus Defence and

Space for the SAGITTA research analyses [117]. It was built as an aluminum full-span model from Certal[®] and features a root chord length of $c_r = 1.2\text{ m}$. Thus, it exhibits the same root chord length compared to the AVT-183 W/T model. The full wing span reads $b = 1.235\text{ m}$. Table 3.3 and Figure 3.6 depict the resulting wing planform parameters. Furthermore, the W/T model allows for the study of different leading-edge contours, as the model features exchangeable leading-edge segments. This can be noticed from Figure 3.7, in which the main components of the SAGITTA diamond wing W/T model are introduced. Thereby, leading-edge geometry modifications can be treated within the experimental investigations. So far, however, the leading-edge contour of the reference configuration SG Geo 1 is available exclusively.

In addition to the leading-edge segments, the SAGITTA W/T model is composed of a main suction and pressure side shell, two wing tips and a sting-hull shell, and five leading-edge inserts for instrumentation purposes. All components are screwed together from the pressure side shell, so that surface disturbances are avoided on the suction side of the W/T model. The force and moment acquisition is accomplished by an internal six-component balance, which connects the W/T model to a centric rear sting. A three-axis model support is used to mount the W/T model with the rear sting in the test section, see Figure 3.8 and Figure 3.9. The angle of attack, the sideslip angle and the roll angle of the W/T model can thus be adjusted computer-controlled. For the surface pressure measurements, 192 pressure taps are available on the SAGITTA diamond wing W/T model. All of them are prepared for time-averaged measurements. Every orifice is aligned in normal direction to the wing surface and features a diameter of $d_{pt} = 0.3\text{ mm}$. 160 pressure taps are located on the suction side of the right wing half in seven different chordwise

c_r	c_t	λ	φ_{le}	φ_{te}	b	S_{ref}	Λ	l_μ	x_{mrp}
1.2 m	0.03 m	0.025	55°	-25°	1.235 m	0.759 m ²	2.001	0.801 m	0.501 m

Table 3.3: Wing planform parameters of the SAGITTA W/T model.

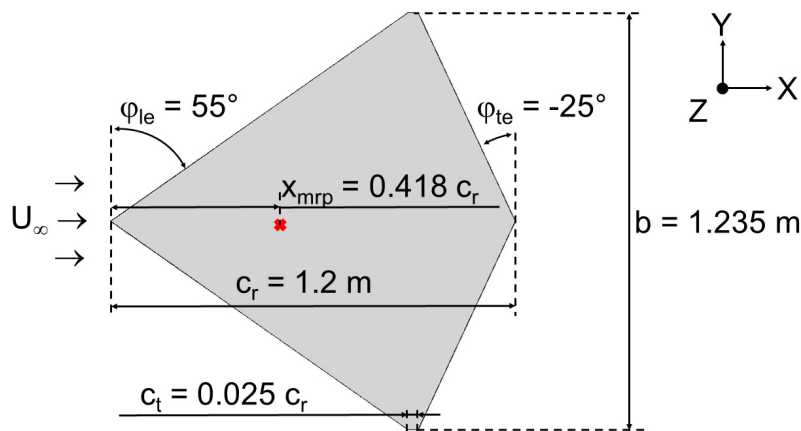


Figure 3.6: SAGITTA W/T model, top view xy plane.

Experimental Approach

sections ($x/c_r = 0.1$ to $x/c_r = 0.7$ with $\Delta x/c_r = 0.1$), see Table 3.4. Approaching the leading edge of each section along the semi-span wing, the spacing of the pressure taps becomes closer to get additional pressure information in the regions of interest. To study symmetry concerns with respect to the x-y and the x-z plane, 32 additional pressure taps are further located on the pressure side of the right wing half and the suction side of the left wing half.

The W/T tests of the SAGITTA diamond wing configuration were conducted at atmospheric low-speed conditions with a Reynolds number of $Re_\infty = 2.3 \cdot 10^6$ based on the mean aerodynamic chord of $l_\mu = 0.801 \text{ m}$ and a Mach number of $Ma_\infty = 0.13$. With respect to the ambient W/T conditions, the corresponding free stream velocity resulted in $44 \text{ m/s} \leq U_\infty \leq 46 \text{ m/s}$, which corresponds to a free stream Mach number variation of $0.127 \leq Ma_\infty \leq 0.133$. The determination of the aerodynamic forces and moments as well as the steady surface pressure measurements were undertaken for angles of attack of $-4^\circ \leq \alpha \leq 20^\circ$ with an angle-of-attack increment of $\Delta\alpha = 1^\circ$. The flow field measurements close to the wing surface were performed for three different angles of attack, namely $\alpha = 12^\circ$, $\alpha = 16^\circ$, and $\alpha = 24^\circ$. Overall, the W/T measurements were executed both with free and fixed transition. Based on the outcome of the trip-strip analysis conducted for the AVT-183 configuration, an equivalent trip strip was chosen for the SAGITTA diamond wing W/T model, see Section 3.3.5.

x/c_r	0.100	0.200	0.300	0.400	0.500	0.600	0.700
$x, \text{ m}$	0.120	0.240	0.360	0.480	0.600	0.720	0.840
$s(x), \text{ m}$	0.084	0.168	0.252	0.336	0.420	0.504	0.588

Table 3.4: Chordwise sections for surface pressure measurements at the SAGITTA W/T model.

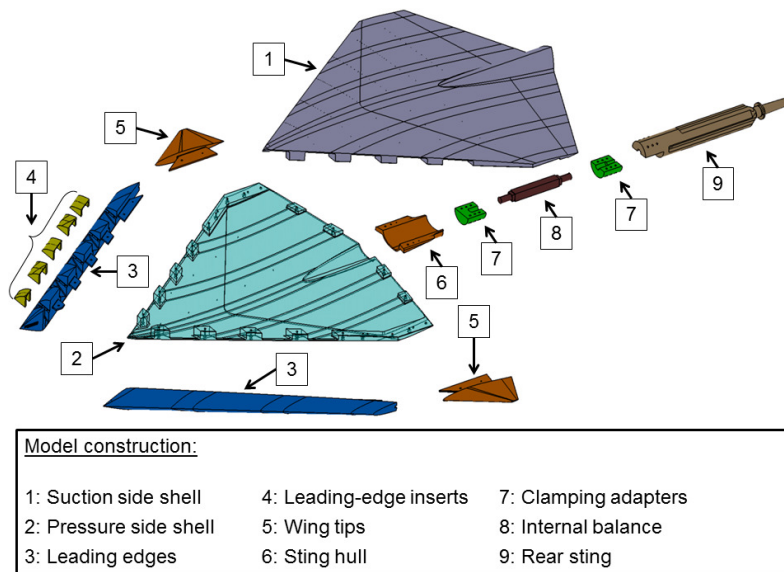


Figure 3.7: SAGITTA W/T model components.



Figure 3.8: SAGITTA W/T model without the pressure side shell.

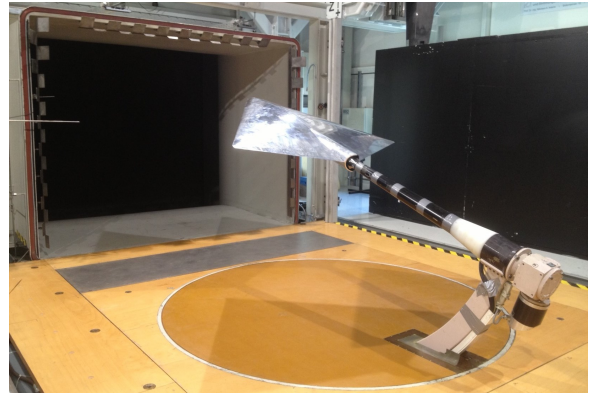


Figure 3.9: SAGITTA W/T model within the W/T facility A of TUM-AER.

3.3 Wall Roughness Effects

3.3.1 General Remarks

The application of trip strips plays a major role in W/T investigations, when the fixation of the transition from laminar to turbulent boundary-layer flow is favored. This happens, for instance, if the Reynolds number attainable in the experiments is too small to provide realistic boundary-layer characteristics compared to full-scale conditions of a vehicle [51]. Especially for W/T models that are tested in the low-speed environment, a fixed trip location is thus commonly desired. A further requirement for tripped flow at W/T models occurs, when numerical results shall be compared to experimental data. In nowadays CFD computations, the approach employing fully-turbulent boundary-layer characteristics is well established, especially for the Reynolds-Averaged Navier-Stokes (RANS) equations. To survey the results obtained from both data sources with comparable boundary-layer characteristics and according to the similarity rules, see Section 2.1, the need for reasonably-tripped flow at low-speed W/T models further becomes obvious.

In the present research, the application of suitable trip strips was investigated in detail on the AVT-183 configuration, since two of the main aims of the AVT-183 task group were the validation of present CFD codes and the improvement of state-of-the-art turbulence models [92]. For this reason, the initial W/T experiments thoroughly focused on flow tripping, and comprehensive analyses were undertaken. Based on flow-physical relevance and repeatability issues, a specific trip strip was finally selected for the definition of target flow conditions. They are characterized by fully-turbulent boundary-layer characteristics on the entire W/T model surface. The chosen trip strip was then used for the subsequent W/T flow field investigations. For the experimental analyses relevant for the SAGITTA configuration, the outcome of the results on the AVT-183 W/T model was used as well.

Overall, trip strips including artificial roughness are known in various types. The most common ones used in practical applications can be found in literature, see Barlow et al. [6], Elsenaar and Russo (Section 2.3.1-2 of [1]), or Reference [26]. The location of the boundary-layer tripping

device on the W/T model and the roughness height are decisive in this regard. The effectiveness of the device, and the avoidance of "over-tripping", which would falsify the properties, are also major issues of a reasonable application of trip strips, see Hirschel et al. [51]. In the experimental analyses of the present research, two different types of trip strips were considered. On the one hand, a so-called grit was applied, which consists of an adhesive layer and carborundum particles. Thereby, a continuous rectangular, three-dimensional trip strip is obtained. On the other hand, circular trip dots were used, which are placed on the W/T model surface in a row with equal spacing. The pros and cons of each method, such as the application, the coating and repeatability issues, are summarized for instance by Barlow et al. [6]. In recent years, both types of trip strips were widely used in respective experimental investigations, which aimed at the generation of high-quality data sets for comparison with numerical data. Within the scope of international research collaborations, a carborundum grit was used for instance as flow tripping device in low-speed W/T tests of a low-aspect-ratio wing configuration (SACCON, NATO RTO AVT-161) [133]. Trip dots were extensively used in the transonic W/T investigations of the drag prediction workshop series, in which a transport aircraft configuration (NASA Common Research Model (CRM)) was considered [102].

3.3.2 Basic Principles

Along with the study of overall boundary-layer phenomena, the problem of wall roughness effects in experimental investigations and laminar-turbulent transition has comprehensively been treated for almost 100 years. Detailed overviews are given by Schlichting [109], Lachmann (ed.) [81] and Tani [125]. Initiated by early experiments of Nikuradse [97] and Prandtl [128], numerous analyses were conducted around the 1950s. More specifically, W/T investigations of the flow along flat plates were undertaken in that time, focusing on the laminar-turbulent transition and the accurate flow tripping. Overall, correlations of the free stream Reynolds number and the roughness height, shape, and position of the flow tripping devices were in particular sought for. The most important contributions are summarized and reviewed by Braslow [13] and Dryden [32]. To date, the boundary-layer tripping methods used for experimental W/T investigations of aeronautical applications still rely on the basic principles obtained for rather simple geometries such as flat plates, since the theoretical treatment of realistic geometries is rather inaccessible. For this reason, fundamental relations are reviewed for the flat plate at zero incidence and zero pressure gradient, see Schlichting and Truckenbrodt [110, 131]. The height and position of suitable trip strips, which were used in the present research, are thereby motivated and defined.

Figure 3.10 displays the skin-friction coefficient versus the Reynolds number for the flow along a flat plate. The diagram shows different areas that are relevant for laminar boundary-layer flow, and areas characterized by turbulent boundary-layer flow at hydraulically smooth and rough walls. In addition, the case of laminar-turbulent transition is also included. The limits are derived from experimental investigations, which led to empirical relations as stated in Equations 3.1 to 3.4. The transition region between smooth and rough walls in fully-developed turbulent

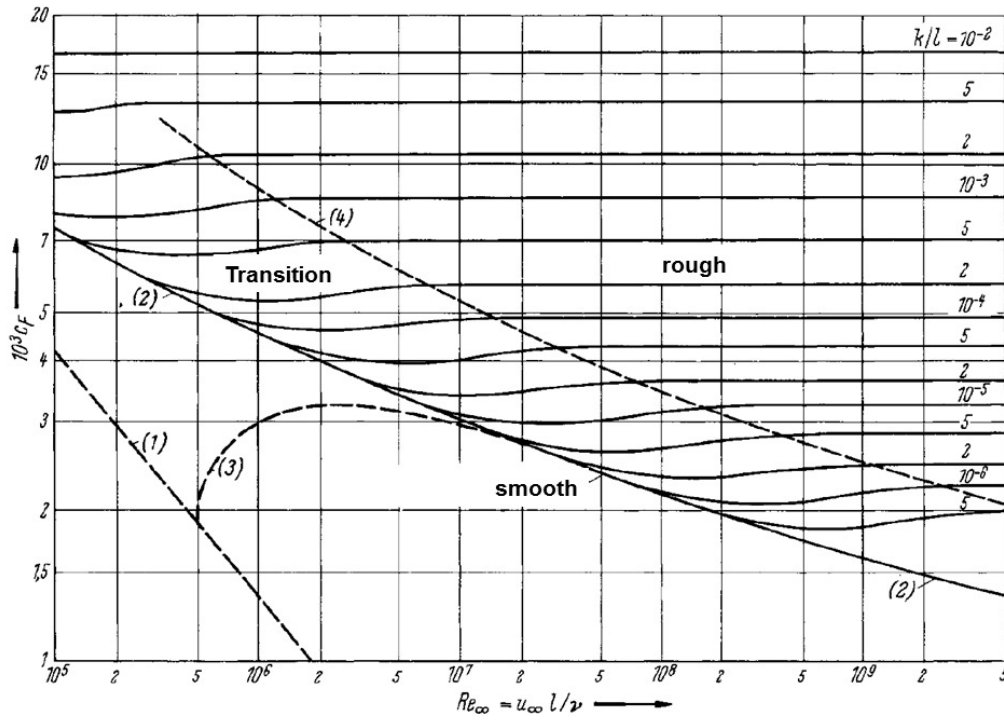


Figure 3.10: Skin-friction coefficient versus Reynolds number on a flat plate at zero incidence and zero pressure gradient, see Truckenbrodt [131].

Fig. 3.10, Curve (1): $C_f = \frac{1.328}{\sqrt{Re_\infty}}$ (laminar) (3.1)

Fig. 3.10, Curve (2): $C_f = \frac{0.455}{(\lg \cdot Re_\infty)^{2.58}}$ (turbulent, hydraulically smooth) (3.2)

Fig. 3.10, Curve (3): $C_f = \frac{0.455}{(\lg \cdot Re_\infty)^{2.58}} - \frac{1700}{Re_\infty}$ (laminar-turbulent) (3.3)

Fig. 3.10, Curves k/l : $C_f = 0.024 \cdot \left(\frac{k}{l}\right)^{\frac{1}{6}}$ (turbulent, hydraulically rough) (3.4)

Fig. 3.10, Curve (4): Limit for completely hydraulically rough wall.

boundary-layer flow is linked to the definition of the terms hydraulically smooth and rough, respectively. In general, a wall is characterized as hydraulically smooth, if the surface roughness k_s is lower than the viscous sub-layer of the boundary layer. Hence, the permissible surface roughness for hydraulically smooth walls is defined by

$$k_{per} < \frac{100 \cdot \nu}{U_\infty}. \quad (3.5)$$

It turns out that this value is independent on the run length and the thickness of the boundary layer. The corresponding skin-friction coefficient is a function of the Reynolds number only, see Equation 3.2. If the surface roughness exceeds the height of the viscous sub-layer, a transition process is initiated and finally, the wall is referred to as hydraulically rough. In this case, the skin-

friction coefficient is only dependent on the relative wall roughness k/l , see Equation 3.4. Beyond the limit of curve (4) in Figure 3.10, completely hydraulically rough walls are thus present.

The minimum surface roughness, which triggers the transition from laminar to turbulent boundary-layer flow, is defined as the critical roughness height. For smaller roughness heights, no effects are observed on the skin-friction coefficient, since the laminar boundary layer is in general rather insensitive to roughness effects. In this case, Equation 3.1 is relevant for the determination of the skin-friction coefficient. For larger roughness heights, the transition to turbulent boundary-layer flow is initiated. The skin-friction coefficient then increases significantly, see curve (3) of Figure 3.10. The determination of the critical roughness height was studied experimentally in numerous analyses for a long time [14, 118, 126, 134]. The measurements were comprehensively reviewed and are documented as introduced above [13, 32, 110, 131]. Based on the final relation proposed by Tani [126], the critical roughness height can also be formulated in dependence on the free stream velocity and the kinematic viscosity. Thereby, a consistent description, compared to the permissible roughness height, is obtained. According to Breitsamter [18], the critical roughness height results in

$$k_{crit} = 26 \cdot x^{\frac{1}{4}} \cdot \left(\frac{\nu}{U_{\infty}} \right)^{\frac{3}{4}} . \quad (3.6)$$

In contrast to the permissible roughness height, the critical roughness height is dependent on the run length of the boundary layer as well. This observation is of great importance for the practical application of flow tripping devices, since the height and the position of the trip strips to be applied correlate with each other.

When the relations of the permissible roughness height for smooth walls in turbulent boundary-layer flow and the critical roughness height in laminar boundary-layer flow to force laminar-turbulent transition are compared, the following ratio can be derived [18]:

$$\frac{k_{crit}}{k_{per}} = 0.26 \cdot Re_x^{\frac{1}{4}} = \begin{cases} 4.6 & \text{at } Re_x = 10^5 \\ 8.2 & \text{at } Re_x = 10^6 \\ 1.0 & \text{at } Re_x \approx 2.19 \cdot 10^3 \end{cases} . \quad (3.7)$$

For local Reynolds numbers of $Re_x > 2.19 \cdot 10^3$, the critical roughness height is larger than the permissible roughness height of hydraulically smooth walls. In this relation, however, effects of flow acceleration and pressure gradients are not considered, which are of major importance in practical applications. In the following section, specific guidelines are therefore given.

3.3.3 Application Guidelines

The outcome of the theoretical analysis considered in the previous section is summarized. The findings determine the application rules to be followed in experimental investigations, when laminar boundary-layer characteristics shall be precluded on the W/T model surfaces by a fixed location of the laminar-turbulent transition. One should however mention that the above rela-

tions were derived for a flow problem without surface curvature, pressure gradient and complex boundary-layer profile. These effects are commonly present at wing configurations and can significantly influence the boundary-layer transition. To estimate and size the flow tripping devices prior to the W/T investigations in the first instance, the derived relations though give a rough indication that can be reviewed subsequently in respective experiments:

- To force transition from laminar to turbulent boundary-layer flow, local trip strips with, at least, the height of the critical roughness height are required, see Equation 3.6. In this context, the position of the flow-tripping devices is linked to the critical roughness height.
- Ideally, the transition excited by the critical roughness height still leads to the condition of hydraulically smooth walls, see Equation 3.5. This requirement, however, is not met in most cases due to high local Reynolds numbers and large critical roughness heights.
- If a hydraulically rough disturbance is already present due to the flow tripping devices, too large roughness heights should be prevented, since the additional roughness height directly results in more skin friction. The risk of "over-tripping" is present, which can lead to unwanted premature separation of the flow and different aerodynamic characteristics.

With respect to the low-speed W/T investigations of this research, both the critical and the permissible roughness height were consequently estimated based on the above defined relations. Since the flow tripping, however, was applied closely to the wing leading edge, where the associated area is affected by flow acceleration and thus a negative pressure gradient, a modified velocity in the denominator of Equation 3.5 and Equation 3.6 was considered for the estimates. Under consideration of Bernoulli, the assumption of loss-free flow around the leading edge, and surface pressure coefficient results of early CFD computations, which were run to design the W/T experiments [10], the applied velocity for the estimates was thus assumed to be between $U_\infty \leq U_\infty^* \leq U_\infty \cdot \sqrt{1 - c_{p,le}}$. For the present free stream conditions of $U_\infty \approx 53 \text{ m/s}$ and $\nu \approx 1.5 \cdot 10^{-5} \text{ m}^2/\text{s}$, a laminar boundary-layer run length of $x \approx 0.01 \text{ m}$, and surface pressure coefficients up to $c_{p,le} \approx -5$ in attached flow around the leading edge (from CFD), this finally led to a critical roughness height estimate of $50 \mu\text{m} \leq k_{crit} \leq 100 \mu\text{m}$ and a permissible roughness height estimate for hydraulically smooth walls in turbulent boundary-layer flow of $10 \mu\text{m} \leq k_{per} \leq 30 \mu\text{m}$. For the final application on the W/T model, the decision was therefore taken to start with the upper bound of the critical roughness height estimate as a localized surface roughness to evoke laminar-turbulent transition, see Section 3.3.4.

3.3.4 Trip Strips at the AVT-183 Diamond Wing Configuration

Figure 3.11 shows a summary of the resulting trip-strip cases applied on the AVT-183 W/T model. Overall, one should bear in mind that the initial estimations as introduced above only gave first indications, but could not directly be transferred to the application on the diamond wing configuration with rounded leading-edge contour. For the carborundum grit type, different

Experimental Approach

adhesive layers and roughness heights were studied, see Figure 3.11c to Figure 3.11f. Due to the thickness of the adhesive layer, it turned out that even the upper bound of the estimated critical roughness height was hardly achievable. In one case, the adhesive layer was thereby used without additional carborundum particles, see Figure 3.11a. Consequently, the natural roughness of the double-sided adhesive layer was left only, and this case defines the lowest roughness height that was possible in the present experimental investigations. The second type of trip strip, namely the trip dots, was only applied with one roughness height, see Figure 3.11b. This test case was not studied in the same W/T entry as the carborundum grit test cases. Therefore, the outcome of the initial W/T investigations applying the carborundum grit was already known.

The geometric properties of each test case are documented in Table 3.5 and Figure 3.12. On the left-hand side, an overview of the trip-strip application at the leading edge is given. Overall, the trip strips were applied on both the upper and the lower wing surface. The carborundum grit was attached around the leading edge up to $l_{arc, cg}/l_\mu = 1.5\%$ along the arc length on both sides of the wing. Figure 3.12a further highlights the composition of the adhesive layer and the carborundum grit. For the trip-dot test case, the leading edge was not coated, but the trip dots were located slightly downstream of the leading edge ($l_{arc, td}/l_\mu = 0.875\%$), see Figure 3.12c. The position was the result of several pre-tests, in which the chosen trip-strip height was tested at several trip-dot locations aft of the leading edge. In each case, the trip-dot diameter was $d_{td} = 1.27 \text{ mm}$, and the spacing along the leading edge in spanwise direction was constant with $l_{spa, td}/d_{td} = 50\%$. Since the adhesive layer and the roughness height are realized in one piece when using the trip

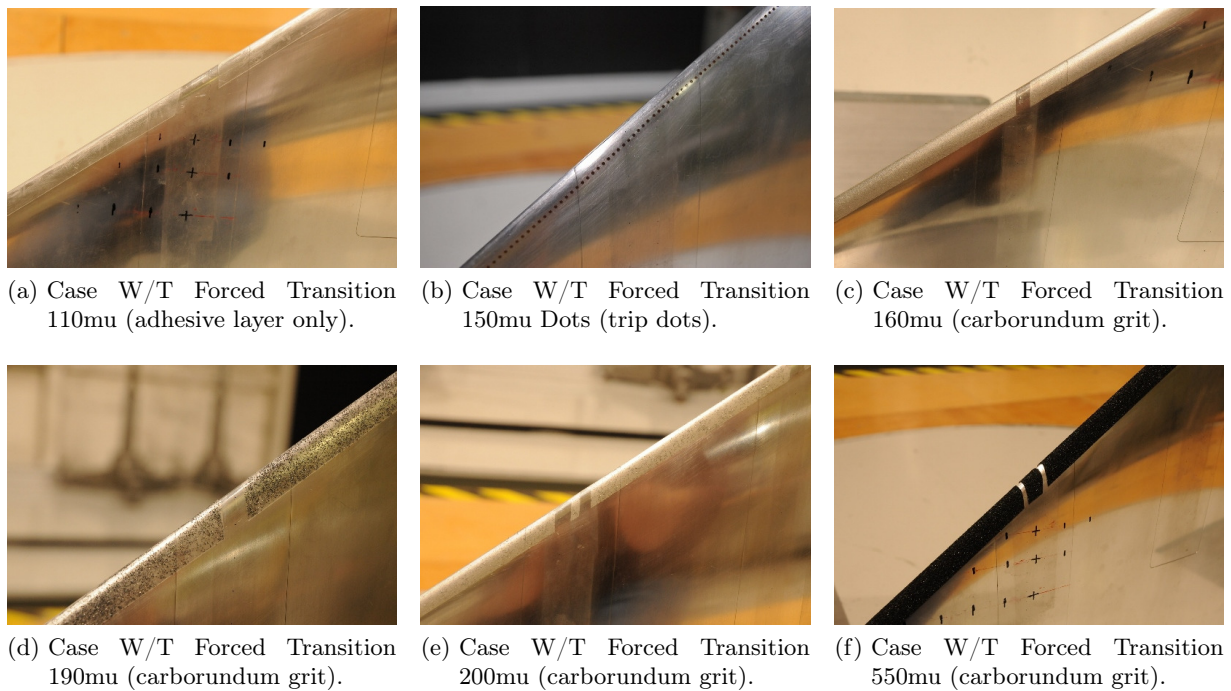


Figure 3.11: Summary of the applied trip strips at the AVT-183 W/T model.

3.3 Wall Roughness Effects

dots, only one component was present. Due to a special tape with integrated surface roughness, this was however also valid for the carborundum grit case with the highest roughness height of $k_s = 550 \mu\text{m}$, see Table 3.5. In all other carborundum grit cases, the double-sided adhesive layer was used and the carborundum particles were manually distributed on the tape, see Figure 3.12a.

Test case	Height of adhesive h_{ad} , m	Roughness height k_s , m	Total height $h_{ad} + k_s$, m
W/T Forced Transition 110mu	$0.11 \cdot 10^{-3}$	/	$0.11 \cdot 10^{-3}$
W/T Forced Transition 150mu Dots	/	$0.15 \cdot 10^{-3}$	$0.15 \cdot 10^{-3}$
W/T Forced Transition 160mu	$0.12 \cdot 10^{-3}$	$0.04 \cdot 10^{-3}$	$0.16 \cdot 10^{-3}$
W/T Forced Transition 190mu	$0.11 \cdot 10^{-3}$	$0.08 \cdot 10^{-3}$	$0.19 \cdot 10^{-3}$
W/T Forced Transition 200mu	$0.12 \cdot 10^{-3}$	$0.08 \cdot 10^{-3}$	$0.20 \cdot 10^{-3}$
W/T Forced Transition 550mu	/	$0.55 \cdot 10^{-3}$	$0.55 \cdot 10^{-3}$

Table 3.5: Geometric properties of the applied trip strips at the AVT-183 W/T model.

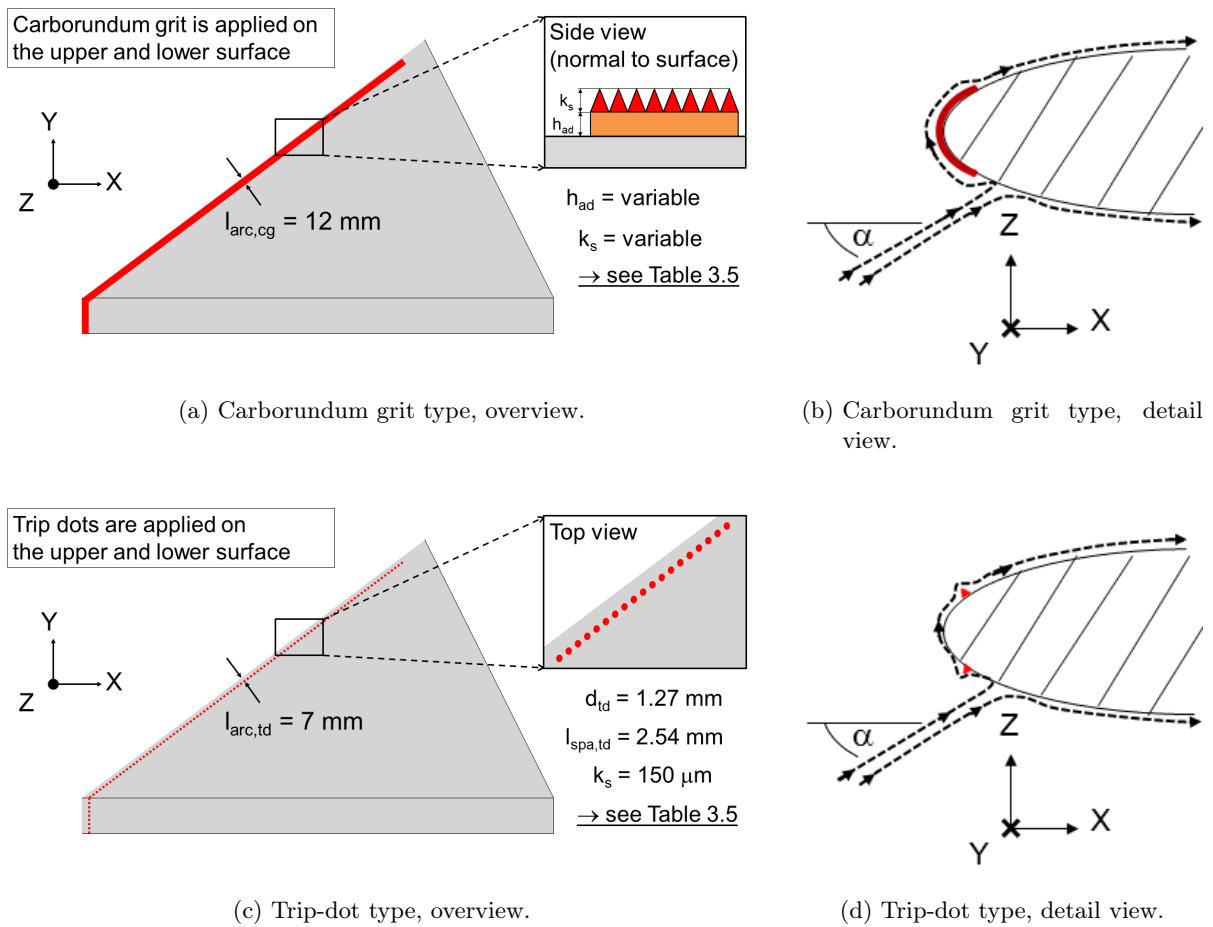


Figure 3.12: Geometric properties of the applied trip strips at the AVT-183 W/T model.

On the right-hand side of Figure 3.12, schematic streamlines are shown around the leading edge with present angle of attack for both types of trip strips. With regard to the flow separation onset to be studied on the AVT-183 W/T model, turbulent boundary-layer characteristics were already desired for the flow around the leading edge. For this reason, the flow was initially tripped at the lower wing surface. The dividing streamline on the pressure side of the airfoil, where the flow splits into the suction and the pressure side flow, moves in general further downstream with increasing angle of attack. Assuming this streamline is located downstream of the end of the trip strip, the flow around the leading edge is already exposed to the roughness height, applied on the lower surface. Then, the laminar-turbulent transition is initiated right before the air flows around the leading edge. The inspection of skin-friction lines in preliminary CFD analyses supported this assumption [10]. In the case of the carborundum grit, this results in a forward and a backward facing step, and the leading-edge radius is slightly changed, see Figure 3.12b. With increasing roughness heights, the leading-edge radius increases, and undesired premature flow separation characteristics are maybe present. For the trip-dot case, the original leading-edge shape is maintained in contrast, which is considered favorable. The ratio of the trip-dot height and location, however, is decisive in this regard. With respect to the only available trip-dot height in this analysis, a too aft trip-dot location could not trip the flow and no differences to the case W/T Free Transition were found. In case of a trip-dot location very close to the leading edge, undesired premature flow separation characteristics were obtained. Due to clarity reasons, only the final layout as introduced in Figure 3.12c is therefore considered in this thesis. Moreover, the initial pre-tests further gave evidence that the flow separation characteristics are mainly influenced by the trip dots on the lower side. Compared to the final test set-up, the application of the trip dots on the lower side alone already indicated a dominant role with respect to the vortical flow separation on the upper wing surface. Thereby, the assumptions made in Figure 3.12d are further proven.

3.3.5 Trip Strips at the SAGITTA Diamond Wing Configuration

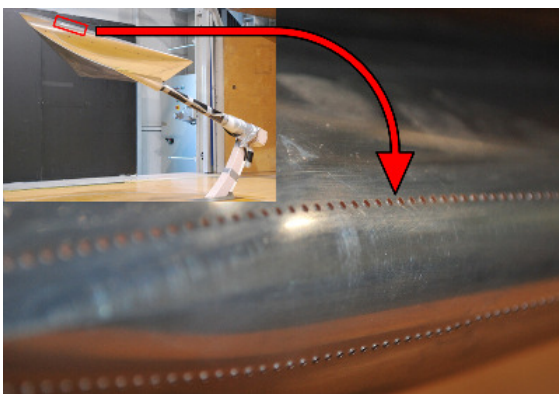


Figure 3.13: Trip strips at the SAGITTA W/T model.

The trip strips applied in the W/T investigations of the SAGITTA configuration were selected based on the trip-strip analysis, which was conducted for the AVT-183 W/T model, see Section 3.3.4 and Section 5.1.1. Based on these results, trip dots were used exclusively for the flow tripping, see Figure 3.13. Compared to the application on the AVT-183 W/T model, the same roughness height with $k_s = 150 \mu m$ was chosen. The position aft of the leading edge and the spanwise spacing were furthermore equal. Therefore, the sketch as shown in Figure 3.12c with its geometry parameters is

also valid for the SAGITTA configuration. The trip dots were applied on both the upper and the lower wing surface, and on the right and the left side of the diamond wing configuration. For the measurements with fixed transition location, turbulent boundary-layer characteristics were thus assured on the entire SAGITTA W/T model.

3.4 Measurement Techniques

3.4.1 Force Measurements

AVT-183 Diamond Wing Configuration

To obtain the aerodynamic coefficients of the AVT-183 diamond wing configuration, the forces and moments were measured with an external six-component balance of piezo-electric stain-gauge type, which is located below the W/T test section. The balance is designed to sustain maximum loads of 1500 N, 3000 N, and 3000 N for axial, lateral and normal forces, respectively (general W/T coordinate system). The maximum sustainable moments read 700 Nm, 500 Nm, and 700 Nm for rolling, pitching, and yawing moments, respectively. As already described in Section 3.2.1, the forces acting on the peniche were not considered by the W/T balance in the present test set-up. Thus, the measured values are directly linked to the loads acting on the diamond wing surface. For every measured data point, the forces and moments were time-averaged over a measurement time of $t_{meas} = 20$ s. Based on the occurring loads in the present experimental analyses, the accuracy of the external W/T balance in the aerodynamic coefficients of the longitudinal motion reads $\Delta C_D = \pm 0.0003$, $\Delta C_L = \pm 0.0011$ and $\Delta C_{my} = \pm 0.0002$.

Since the pitching-moment reference point of the W/T balance does not coincide with the desired pitching-moment reference point of the AVT-183 W/T model located at the geometric neutral point of the diamond wing ($x_{mrp}^{Model} = 0.491$ m), the measured pitching moment must further be altered. Together with the reference quantities displayed in Table 3.1, the pitching-moment reference point of the W/T balance ($x_{mrp}^{Balance} = 0.6$ m) and Figure 3.14, the aerodynamic force and moment coefficients related to the longitudinal motion can be derived from

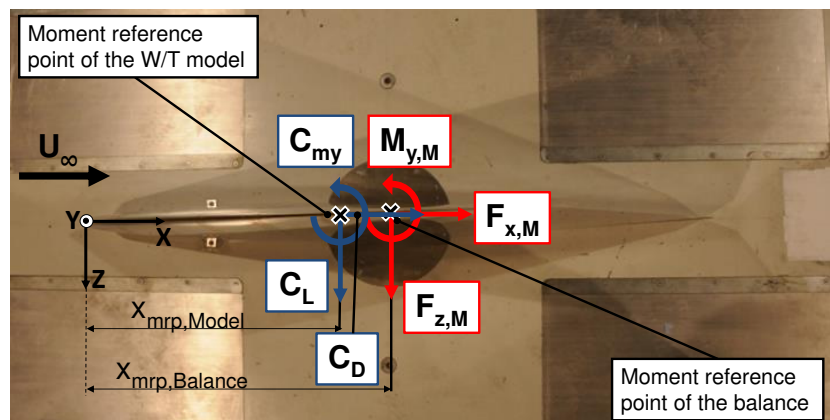


Figure 3.14: Determination of the aerodynamic coefficients at the AVT-183 W/T model.

$$C_D = \frac{F_{x,M} \cdot \cos \alpha + F_{z,M} \cdot \sin \alpha}{\frac{1}{2} \cdot \rho \cdot U_\infty^2 \cdot S_{ref}}, \quad (3.8)$$

$$C_L = \frac{-F_{x,M} \cdot \sin \alpha + F_{z,M} \cdot \cos \alpha}{\frac{1}{2} \cdot \rho \cdot U_\infty^2 \cdot S_{ref}}, \quad (3.9)$$

$$C_{my} = \frac{M_{y,M} - F_{z,M} \cdot (x_{mrp}^{Balance} - x_{mrp}^{Model})}{\frac{1}{2} \cdot \rho \cdot U_\infty^2 \cdot S_{ref} \cdot l_\mu}. \quad (3.10)$$

SAGITTA Diamond Wing Configuration

The application of an internal six-component balance in the SAGITTA W/T model to determine the aerodynamic coefficients has already been introduced in Section 3.2.2. The maximum allowable loads are 900 N, 450 N, and 2500 N for axial, lateral and normal forces, respectively (model-fixed coordinate system). The maximum sustainable moments read 120 Nm, 160 Nm, and 120 Nm for rolling, pitching, and yawing moments [15]. For the data acquisition, a measurement time of

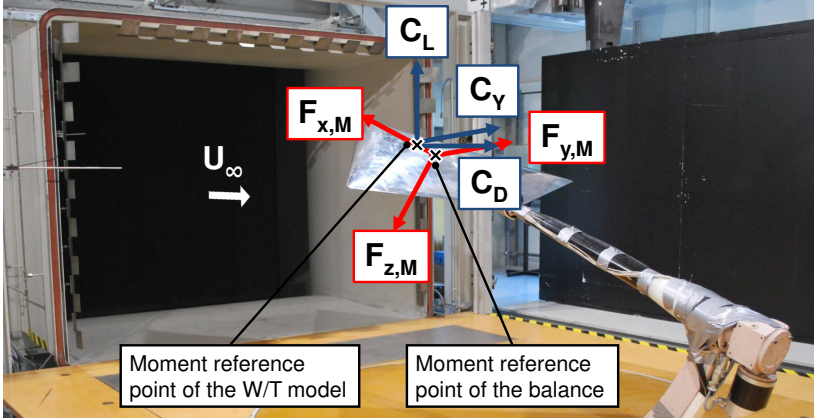


Figure 3.15: Determination of the aerodynamic coefficients at the SAGITTA W/T model.

$t_{meas} = 20 \text{ s}$ was chosen with a sampling rate of $f_{meas} = 1200 \text{ Hz}$. The results of the aerodynamic coefficients presented in this research are however time-averaged values only. The accuracy of the internal W/T balance in the aerodynamic coefficients of the longitudinal motion reads for the present test set-up $\Delta C_D = \pm 0.0011$, $\Delta C_L = \pm 0.0028$ and $\Delta C_{my} = \pm 0.0003$.

The internal balance measures the forces and moments in a right-hand-oriented model-fixed coordinate system (index M) as displayed in Figure 3.15. For the determination of the aerodynamic coefficients, the transformation matrix

$$\mathbf{T}_{AM} = \begin{pmatrix} \cos \alpha \cdot \cos \beta & -\sin \beta & \sin \alpha \cdot \cos \beta \\ \cos \alpha \cdot \sin \beta & \cos \beta & \sin \alpha \cdot \sin \beta \\ -\sin \alpha & 0 & \cos \alpha \end{pmatrix} \quad (3.11)$$

was used. With the common definition of the drag coefficient pointing downstream and the lift coefficient pointing upwards, the aerodynamic force coefficients read, in consideration of Table 3.3, in the wind-fixed coordinate system (no index or index A, respectively)

$$\begin{pmatrix} C_D \\ C_Y \\ C_L \end{pmatrix} = \frac{1}{\frac{1}{2} \cdot \rho \cdot U_\infty^2 \cdot S_{ref}} \cdot \mathbf{T}_{AM} \cdot \begin{pmatrix} -F_{x,M} \\ F_{y,M} \\ -F_{z,M} \end{pmatrix}. \quad (3.12)$$

The aerodynamic moment coefficients are calculated according to the model-fixed coordinate system (index M). Additional force terms have to be considered, since there is a difference in the moment reference points of the W/T balance ($x_{mrp}^{Balance} = 0.687 \text{ m}$) and the W/T model ($x_{mrp}^{Model} = 0.501 \text{ m}$, see Table 3.3):

$$\begin{pmatrix} C_{mx,M} \\ C_{my,M} \\ C_{mz,M} \end{pmatrix} = \frac{1}{\frac{1}{2} \cdot \rho \cdot U_\infty^2 \cdot S_{ref}} \cdot \begin{pmatrix} \frac{1}{s} & 0 & 0 \\ 0 & \frac{1}{l_\mu} & 0 \\ 0 & 0 & \frac{1}{s} \end{pmatrix} \cdot \left[\begin{pmatrix} M_{x,M} \\ M_{y,M} \\ M_{z,M} \end{pmatrix} + \begin{pmatrix} F_{x,M} \\ F_{y,M} \\ F_{z,M} \end{pmatrix} \times \begin{pmatrix} x_{mrp}^{Balance} - x_{mrp}^{Model} \\ 0 \\ 0 \end{pmatrix} \right]. \quad (3.13)$$

For zero sideslip angle, the pitching moment can also be expressed in the wind-fixed coordinate system (no index or index A, respectively) as

$$C_{my} = C_{my,M}, \forall \beta = 0. \quad (3.14)$$

3.4.2 Surface Pressure Measurements

The time-averaged surface pressure measurements were conducted with three electronic pressure scanning modules (Scanivalve ZOC33), which were located below the W/T test section for the AVT-183 W/T model and within the W/T model for the SAGITTA configuration. The sampling rate applied to each W/T measurement run and pressure tap was set to $f_{meas} = 200 \text{ Hz}$ with an averaging time of $t_{meas} = 10 \text{ s}$. The corresponding measurement accuracy of the system reads with respect to the resulting flow field for the AVT-183 configuration $\Delta \bar{c}_p = \pm 0.007$ and for the SAGITTA configuration $\Delta \bar{c}_p = \pm 0.013$, respectively. These values represent the averaged deviation over all pressure taps and considered angles of attack for selected repeatability measurements. Based on the definition of the surface pressure coefficient

$$c_p(t) = \frac{p(t) - p_\infty}{\frac{1}{2} \cdot \rho \cdot U_\infty^2}, \quad (3.15)$$

the corresponding time-averaged pressure coefficient \bar{c}_p is defined as follows:

$$\bar{c}_p = \frac{1}{t_{meas}} \cdot \int_0^{t_{meas}} c_p(t) dt. \quad (3.16)$$

Experimental Approach

The time-dependent surface pressure measurements were carried out with Kulite pressure transducers (XCS-093 series). For the AVT-183 configuration, eight pressure taps are equipped with unsteady pressure sensors, see Section 3.2.1. The SAGITTA W/T model does not feature any time-accurate pressure sensors. The time-dependent measurements were performed with a sampling rate of $f_{meas} = 4000 \text{ Hz}$ and a measurement time of $t_{meas} = 20 \text{ s}$. The frequency of the applied analog low-pass filter was set to $f_{lpf} = 1000 \text{ Hz}$. The fluctuating pressure coefficient in general reads

$$c'_p(t) = c_p(t) - \overline{c_p} . \quad (3.17)$$

Accordingly, the mean square value of the fluctuating pressure coefficient can be written as

$$\overline{c_p'^2} = \frac{1}{t_{meas}} \cdot \int_0^{t_{meas}} [c_p(t) - \overline{c_p}]^2 dt . \quad (3.18)$$

The root mean square value thus results in

$$c_{p,rms} = \sqrt{\overline{c_p'^2}} . \quad (3.19)$$

To study the characteristics of the pressure coefficient fluctuation intensity, spectral analyses are applied. The fluctuation part $c'_p(t)$ is Fourier transformed based on the relation

$$X_{c'_p}(\omega) = \lim_{t_{meas} \rightarrow \infty} \int_0^{t_{meas}} c'_p(t) \cdot e^{-i\omega t} dt . \quad (3.20)$$

The multiplication of the Fourier-transformed quantity $X_{c'_p}(\omega)$ with its conjugated complex quantity $X_{c'_p}^*(\omega)$ leads to the one-sided power spectral density function

$$S_{c'_p}(\omega) = \lim_{t_{meas} \rightarrow \infty} \frac{2}{t_{meas}} \cdot X_{c'_p}^*(\omega) \cdot X_{c'_p}^T(\omega) . \quad (3.21)$$

3.4.3 Stereo Particle Image Velocimetry

The Stereo Particle Image Velocimetry (Stereo PIV) was applied to obtain the near-wall flow field characteristics of the regarded configurations in different chordwise sections. Due to the diverse layouts of the AVT-183 and the SAGITTA W/T models (semi-span versus full-span model), different measurement set-ups had to be chosen for the flow field analyses close to the wing surfaces. To improve and optimize the applied Stereo PIV set-ups, valuable information gathered from former studies dealing with Stereo PIV measurements of swept wing configurations was used [42, 43, 80, 105]. Figure 3.16 introduces an overview of the final Stereo PIV set-ups for each W/T model. The experiments with the SAGITTA W/T model used a standard approach with the PIV measurement components located next to the open W/T test section, see Figure 3.16b. A three-axis traversing system allows for the exact positioning of the laser sheet and the corresponding

measurement field of view. For the semi-span AVT-183 W/T model, a revised arrangement of the PIV measurement components was realized within the W/T facility A of TUM-AER, see Figure 3.16a. All relevant components were located above the open W/T test section, but they could nevertheless move on a three-axis traversing system that is mounted close to the ceiling of the W/T facility.

For the laser light sheet generation, a double-pulsed Nd:Yag laser with a maximum power of $E = 325 \text{ mJ}$ per pulse was used. The associated wave length reads $\psi = 532 \text{ nm}$, appearing in visible green light. The measurement field of view was defined by a laser sheet optic (cylindrical lens), which converts the laser beam to a sheet and aligns the resulting laser sheet normally to the chord line of the diamond wing surfaces. Up- and downstream of the laser sheet optics, two high-speed sCMOS cameras with a resolution of 2560×2160 pixels were placed. In the present measurement set-ups, NIKON objective lenses with a focal length of $F = 135 \text{ mm}$ were used. The application of two cameras allows for the simultaneous measurement of all three velocity components in the measurement field of view (Stereo PIV, 2D-3C). Furthermore, Scheimpflug adapters were mounted between the sCMOS sensor plane and the lens to account for tilting the sCMOS sensor plane with respect to the off-axis camera [101]. In order to minimize reflections of the laser sheet on the W/T models seen by the cameras, the relative position of the up- and downstream cameras and the laser sheet optics was aligned with the angle of attack of the diamond wing configurations, see Figure 3.17a and Figure 3.17b. Thus, the optical axes of the cameras were almost tangential to the wing surfaces, respectively. Moreover, the W/T models did not need coating in the applied Stereo PIV measurement set-ups for minimizing reflections. In case of the AVT-183 W/T model, the floor of the open W/T test section was covered with an orange laminate, since it considerably minimized the reflections of the W/T floor. Thus, the flow field measurements were still feasible in the vicinity of the W/T model surfaces.

When it comes to the actual measurements, seeding particles with an approximate size of $d_{par} \approx 1 \mu\text{m}$ are intermixed with the air in the W/T test section. At two instants ($\Delta t = 10 \text{ ns}$

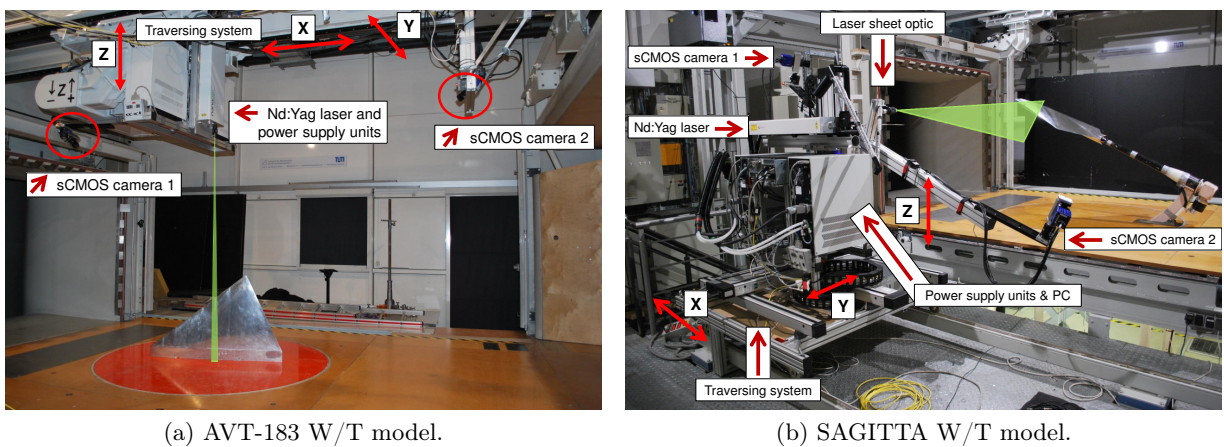


Figure 3.16: Overview of the applied Stereo PIV set-ups within the W/T facility A of TUM-AER.

Experimental Approach

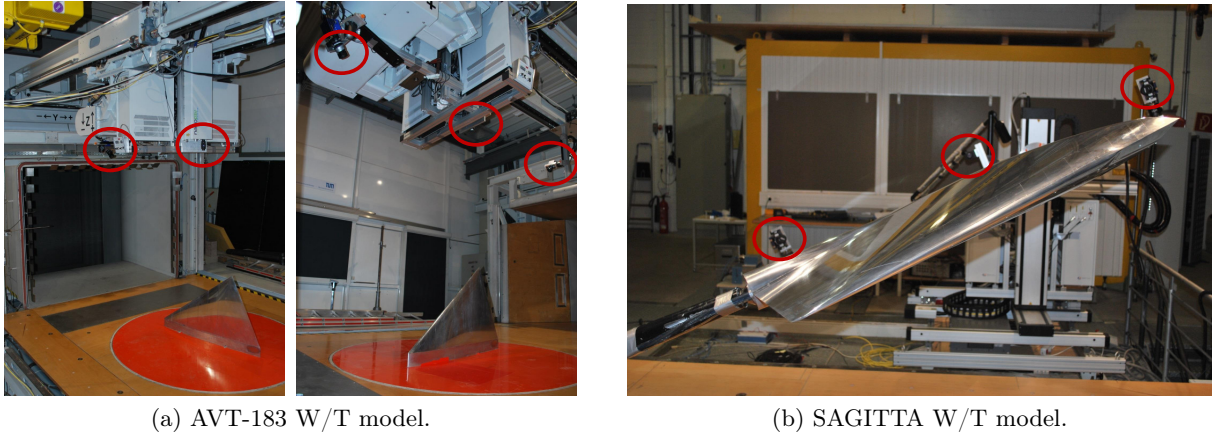


Figure 3.17: Position of the laser sheet optic and the sCMOS cameras in relation to the diamond wing configurations.

Main algorithm	Stereo cross-correlation with image deformation
Iteration options	Multi-pass, decreasing size, 4 passes
Size of final interrogation window	32 x 32 pixel
Overlapping	0%

Table 3.6: Post-processing parameters of the Stereo PIV measurements.

for the AVT-183 investigations and $\Delta t = 12 \text{ ns}$ for the SAGITTA investigations, respectively), the double-pulsed laser illuminates the shaded W/T facility and the sCMOS cameras each record two raw images. Based on the relative movement of the particles between the two instants, the velocity components are calculated by mathematical and statistical methods [101]. The main evaluation parameters used within the post-processing of the current raw data are stated in Table 3.6. For one W/T run and per measurement slice, 400 sequences were each recorded with a sampling frequency of $f_{meas} = 15 \text{ Hz}$. Based on the post-processing, the velocity components were thus derived. The corresponding equations for the further analysis are stated in Section 3.4.4. Within the Stereo PIV measurements, the calibration of the entire optical set-up was crucial for the overall quality of the results. According to Stanislas et al., typical precisions of the determined displacements for a proper calibration read around 0.1 to 0.3 pixels for each camera image [121]. This was nearly achieved with the present Stereo PIV measurement set-ups. Subsequently, the resulting velocity uncertainty was estimated at 2% with respect to the free stream velocity for the three components, respectively. Overall, the Stereo PIV measurements were conducted on the AVT-183 W/T model in 13 chordwise sections. Beginning at $x/c_r = 0.1$, the measurement slices extended with an interval of $\Delta x/c_r = 0.05$ to the chordwise section of $x/c_r = 0.6$. At $x/c_r \approx 0.3$ and $x/c_r \approx 0.4$, the sections were chosen in line with the available pressure tap sections. On the SAGITTA W/T model, selected chordwise sections were measured from $x/c_r = 0.2$ to $x/c_r = 0.7$ with an interval of $\Delta x/c_r = 0.05$. Information on the resulting vector fields can be obtained from Table 3.7 and Table 3.8.

Final field of view	220 mm to 280 mm x 200 mm
Number of vectors per slice	≈ 4500 to 6500
Spatial resolution	3 mm x 3 mm

Table 3.7: Velocity field information of the Stereo PIV measurements, AVT-183 W/T model.

Final field of view	600 mm x 155 mm
Number of vectors per slice	≈ 6500
Spatial resolution	3.7 mm x 3.7 mm

Table 3.8: Velocity field information of the Stereo PIV measurements, SAGITTA W/T model.

3.4.4 Hot-Wire Anemometry

For a better quantification of the near-wall fluctuating quantities with respect to the temporal resolution, hot-wire (HWA) measurements were additionally undertaken for the AVT-183 W/T model, see Figure 3.18. The measurements were guided by numerous previous W/T investigations with hot-wire probes at TUM-AER [17, 20, 42, 43]. For the near-wall flow field in the vicinity of the AVT-183 diamond wing W/T model, cross-wire probes consisting of $5 \mu\text{m}$ diameter

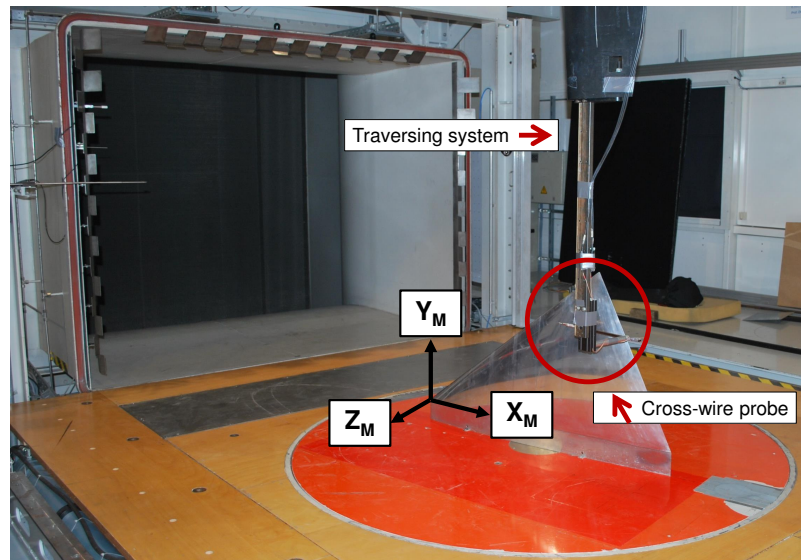


Figure 3.18: Overview of the applied hot-wire set-up within the W/T facility A of TUM-AER.

platinum-plated tungsten wires were used with a three-axis traversing system. Based on the assumption that the best angular resolution is obtained with pairs of perpendicular wires, the corresponding sensor angle was limited to 45° . As summarized by Furman and Breitsamter [43], the use of cross-wire probes generally assumes some knowledge of the flow field, such as a known flow direction to which the probe must be aligned. To determine the three velocity components, the probe had to be rotated around its axis by 90° to adjust the wire plane once horizontally and once vertically against the main flow direction. Hence, two triggered W/T runs were necessary to obtain the entire velocity information.

The probes were operated by a multi-channel constant-temperature anemometer (CTA) system. By means of its signal conditioner modules, the bridge output voltages were low-pass filtered (3^{rd} order, butterworth type) at $f_{lpf} = 1000 \text{ Hz}$ before digitization for optimal signal level. The

Experimental Approach

measurement time applied reads $t_{meas} = 6.4 \text{ s}$ and the sampling rate was set to $f_{meas} = 3000 \text{ Hz}$, resulting in 19200 values for each measured time series. Based on look-up tables derived from a calibration of the cross-wire probe over a defined velocity and flow angle range, the hot-wire voltages were processed to evaluate the time-dependent velocity components. Prior to processing, the voltage signals were additionally corrected for varying temperature conditions within the W/T test facility. The hot-wire measurements relevant for this research were conducted in three chordwise sections of the AVT-183 W/T model, namely at $x/c_r = [0.405, 0.500, 0.600]$. The spatial resolution was chosen to be $\Delta y = \Delta z = 5 \text{ mm}$, which led to vector fields up to 315 measurement points. With respect to statistical accuracy of the calculated quantities, random error calculations resulted in accuracies of 0.5%, 2%, and 3.5% for the mean deviation, the standard deviation and spectral density estimation, respectively.

The velocity components and the derived quantities of the Stereo PIV and HWA measurements are discussed in the course of this research in a right-hand-oriented model-fixed coordinate system. It has been introduced in Figure 3.2 and Figure 3.6 for the wing planforms of the regarded W/T models. The x-coordinate points downstream from the leading to the trailing edge, the y-coordinate points from the root chord to the tip chord section, and the z-coordinate points in normal direction to the wing surface. Figure 3.18 recalls the three axes again, since their orientations are deciding for the determination of the velocity components. For the Stereo PIV measurements, the desired coordinate system was instantly met by the orientation of the laser light sheet, which was aligned normally to the wing surface. In case of the HWA measurements, however, the corresponding raw data must first be transformed, since the hot-wire probe measured the velocity in the wind-fixed W/T coordinate system.

Accounting for these issues, the mean velocity components \bar{u}_i are then derived from the time-dependent velocity components of each Stereo PIV and HWA W/T run, respectively. They are converted into a non-dimensional value by

$$\frac{\bar{u}_i}{U_\infty} = \frac{1}{t_{meas}} \cdot \int_0^{t_{meas}} \frac{u_i(t)}{U_\infty} dt . \quad (3.22)$$

The corresponding mean axial vorticity component $\bar{\omega}_x$ results in non-dimensional form in

$$\frac{\bar{\omega}_x \cdot l_\mu}{U_\infty} = \left(\frac{d\bar{w}}{dy} - \frac{d\bar{v}}{dz} \right) \cdot \frac{l_\mu}{U_\infty} , \quad (3.23)$$

and the non-dimensional absolute velocity reads

$$\frac{\bar{V}}{U_\infty} = \sqrt{\frac{\bar{u}^2 + \bar{v}^2 + \bar{w}^2}{U_\infty^2}} . \quad (3.24)$$

For the derivation of the turbulent flow field characteristics, the fluctuation part of the velocity components is each described by

$$u'_i(t) = u_i(t) - \bar{u}_i . \quad (3.25)$$

Accordingly, the mean square value of the velocity fluctuations therefore is

$$\overline{u'^2_i} = \frac{1}{t_{meas}} \cdot \int_0^{t_{meas}} [u_i(t) - \bar{u}_i]^2 dt . \quad (3.26)$$

The root mean square value, defined again as a non-dimensional value, results in

$$\frac{u_{i,rms}}{U_\infty} = \frac{\sqrt{\overline{u'^2_i}}}{U_\infty} . \quad (3.27)$$

Finally, the equation for the turbulent kinetic energy k is given in non-dimensional form by

$$k = \frac{u_{rms}^2 + v_{rms}^2 + w_{rms}^2}{2 \cdot U_\infty^2} . \quad (3.28)$$

For spectral analyses, the fluctuation part of the velocity components $u'_i(t)$ is Fourier transformed based on the relation

$$X_{u'_i}(\omega) = \lim_{t_{meas} \rightarrow \infty} \int_0^{t_{meas}} u'_i(t) \cdot e^{-i\omega t} dt . \quad (3.29)$$

The multiplication of the Fourier-transformed quantity $X_{u'_i}(\omega)$ with its conjugated complex quantity $X_{u'_i}^*(\omega)$ then leads to the one-sided power spectral density function

$$S_{u'_i}(\omega) = \lim_{t_{meas} \rightarrow \infty} \frac{2}{t_{meas}} \cdot X_{u'_i}^*(\omega) \cdot X_{u'_i}^T(\omega) . \quad (3.30)$$

Chapter 4

Numerical Approach

4.1 Geometry Models

The numerical analyses were all conducted for the W/T model sizes of the AVT-183 configuration and the SAGITTA configuration as introduced in Section 3.2. The outer shells that were relevant for the manufacturing of the W/T models thus served as source data for the grid generation process, see Section 4.2.1. Prior, however, the numerical geometry models were slightly adapted to account for specific requirements of the numerical investigations. In general, the pressure tap holes were not included in the CFD analyses.

The numerical geometry model of the AVT-183 configuration differs from the W/T model only in the wing tip section and the transition from the peniche to the semi-span wing. For an improved grid generation process at the wing tip, the taper ratio was altered to $\lambda = 0.02$. Therefore, the semi-span was reduced by 2%. Since the flow was expected to separate at the wing tip with $\lambda = 0$ at very low angles of attack, this modification is justifiable. Furthermore, the gap between the peniche and the semi-span wing was not considered. The computed forces and moments, however, were evaluated for the semi-span wing surface only. In all other respects, the numerical geometry model equals the W/T model as presented in Figure 3.2 and Table 3.1.

For the SAGITTA configuration, a semi-span wing was regarded as well to define the numerical geometry model. Table 3.3 and Figure 3.6 depict the corresponding reference data of the full-span W/T model. The rear sting mount of the W/T model as shown in Figure 3.9 was additionally considered for the CFD analyses, see Figure 4.1. Previous investigations of vortex-dominated wing configurations showed that the consideration of the sting is significant, when numerical results are compared to experimental data [39, 114, 115]. In particular, the pitching moment and the aerodynamic coefficients of the lateral motion can be influenced. The sting was modeled up to one root chord length downstream of the root chord trailing-edge coordinate, which is supposed to be appropriate for the numerical analyses. The further sting support of the SAGITTA W/T model was not considered in the numerical geometry model, but the sting was rounded with a hemisphere. To avoid discontinuities, the sting-hull radius of the W/T model was used for the modeled sting. Similar to the strategy followed for the peniche on the AVT-183 configuration, the gap between the sting hull at the wing surface and the sting itself was closed. The force and moment contribution of the sting is however not respected in the aerodynamic coefficients of

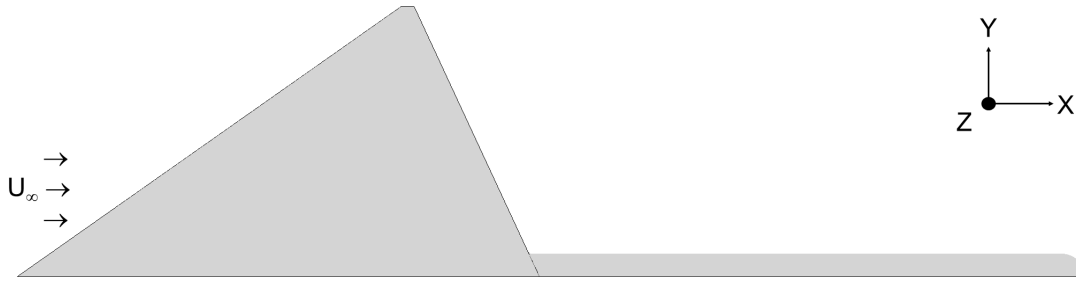


Figure 4.1: Numerical geometry model of the SAGITTA configuration.

the present results. According to the leading-edge contour modifications as introduced in Figure 1.10, the leading-edge shape was finally adjusted for the different configurations to be studied. Altogether, this led to the basis for the grid generation process of the SAGITTA configuration.

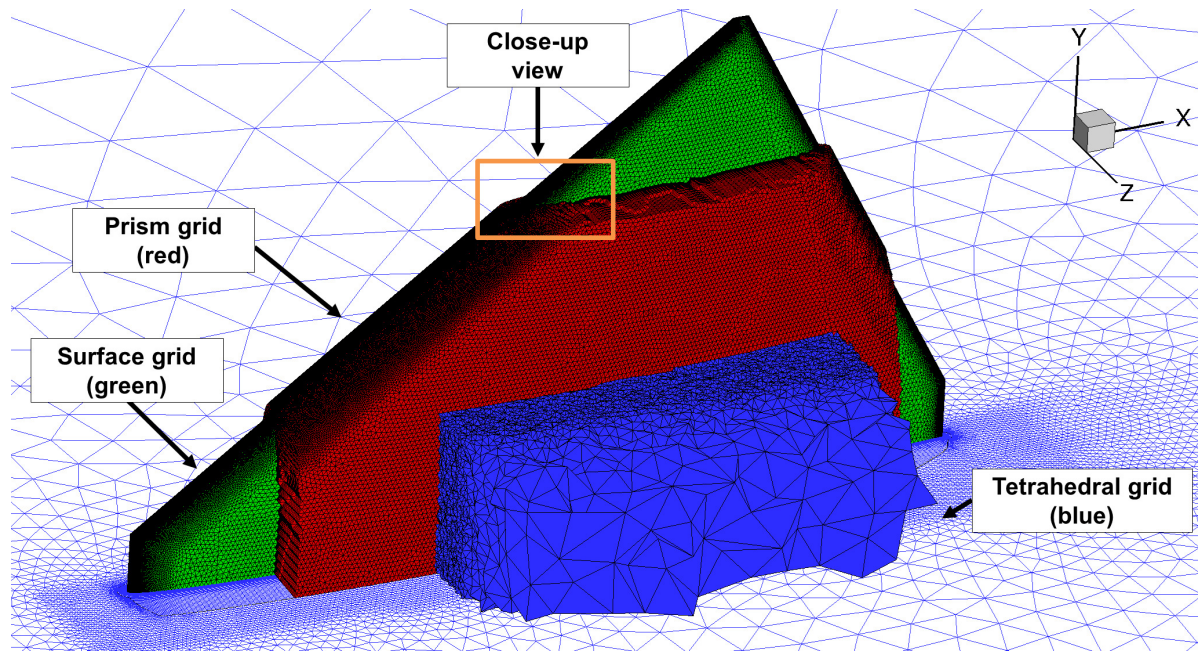
4.2 Computational Grids

4.2.1 Grid Generation Process

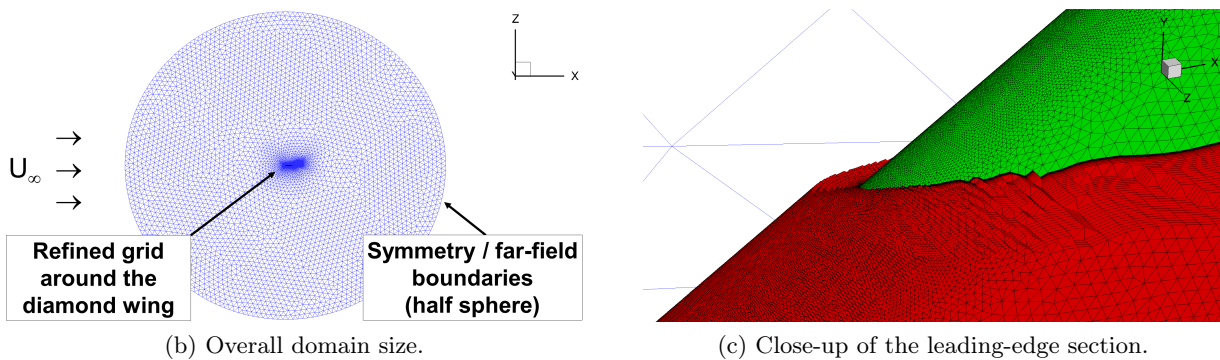
The numerical investigations of this study rely on hybrid grids, which were generated with the commercial grid generation software CENTAUR by CentaurSoft¹. For a variety of engineering problems, it produces high-quality grids in a robust and automatic way for even the most complex geometries. CENTAUR offers multiple types of computational elements and grid generation techniques to obtain hybrid grids with minimum user interaction. In this context, Melber-Wilkending et al. provide a detailed introduction to the software package [95]. For aeronautical applications, the meshing philosophy is as follows: Based on an unstructured surface grid consisting of triangles and quadrilaterals, semi-structured elements of prismatic and hexahedral type are used close to the surfaces in the boundary-layer region of the geometry. Elsewhere in the computational domain up to the far-field boundaries, tetrahedral elements are used. For the transition from prisms to tetrahedrons, pyramidal elements are further introduced to the hybrid grid.

This meshing philosophy was also followed for the grid generation process of both diamond wing configurations regarded in this thesis. By way of example, Figure 4.2a depicts a break-up for one resulting grid of the AVT-183 configuration. Thereby, the grid generation approach is further introduced. To better resolve the occurring vortex structures close to the diamond wing surfaces, the prism grids were further extended on the upper wing side in normal direction, see Figure 4.2c. The transition from hexahedral to tetrahedral elements is thereby shifted out of the vortex flow phenomena, which are thus resolved completely within the semi-structured domain of the overall grid. The tetrahedral elements were additionally refined above and behind the wing configurations, see Figure 4.2a and Figure 4.2b. The overall tetrahedral grid then extends to the far-field boundaries located at 30 aerodynamic reference lengths l_μ away from the geometry, see Figure 4.2b. The limiting far-field boundaries are characterized by a half sphere. Overall, the

¹<https://www.centaursoft.com>, retrieved February 2016



(a) Overall break-up of the different grid types.



(b) Overall domain size.

(c) Close-up of the leading-edge section.

Figure 4.2: Hybrid grid of the AVT-183 configuration.

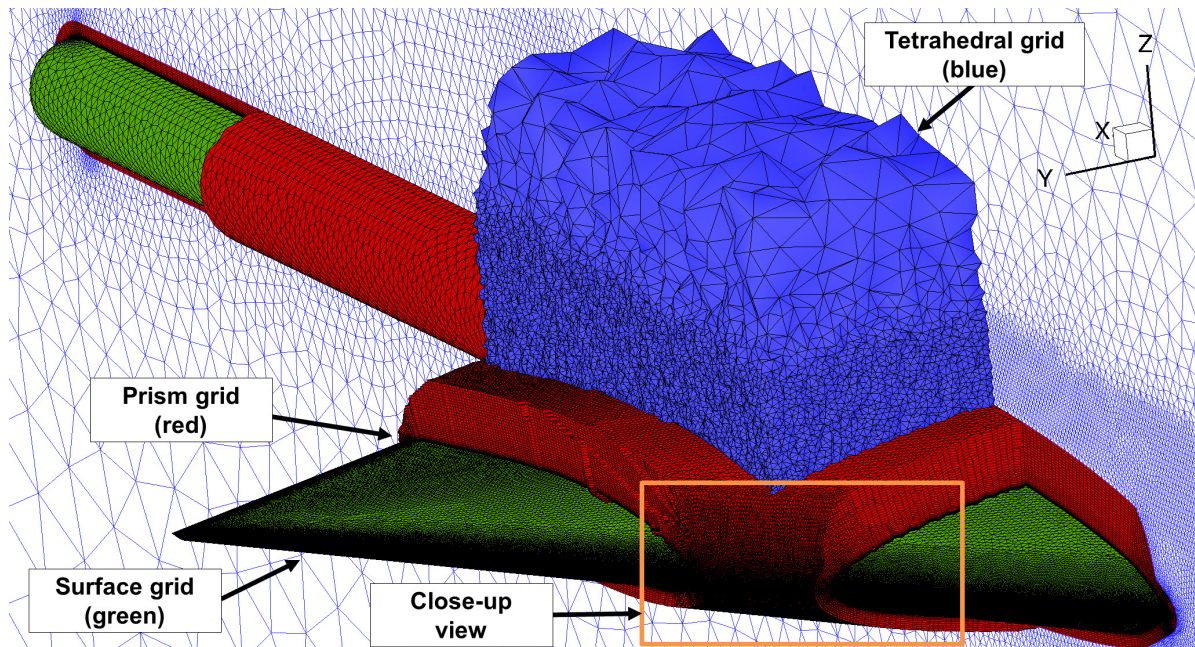
resulting grids are thus suited for polar computations with varying angle of attack, for which the occurring vortex structures are captured and resolved.

With respect to grid sensitivity, different resolutions of the hybrid grids were realized for both diamond wing configurations. Details are given in Section 4.2.2. In the following, key parameters that were altered for the different grid resolutions are briefly discussed. Comparable studies of similar vortex-dominated, low-aspect-ratio wing configurations showed that the surface grid should considerably be refined in the leading-edge region [12, 112, 113]. Especially for the accurate prediction of the flow separation onset associated with rounded leading-edge contours, the grid resolution chosen at the leading edge is crucial. Figure 4.2c exemplarily presents the applied leading-edge refinement for one resulting grid of the AVT-183 configuration. Moreover, a target y^+ value of $y^+_{max} = 1$ was requested to resolve the viscous sublayer. It characterizes the non-dimensional wall distance and is defined by

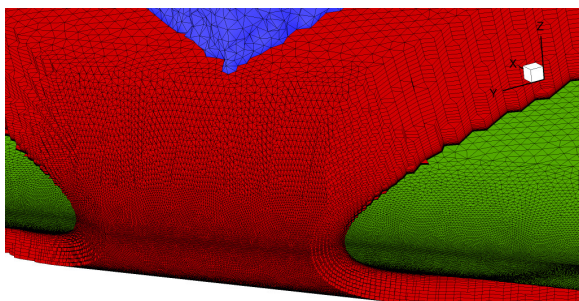
$$y^+ = \frac{\sqrt{\rho_w \tau_w}}{\mu_w} \cdot y . \quad (4.1)$$

The initial prism layer thickness, the cell stretching factor applied in normal direction to the wing, and the overall height of the prism grid were accordingly of great importance for the grid generation process. The boundary layer close to the wing surfaces and the near-wall vortex flow phenomena are thus accurately resolved. Finally, the size of the tetrahedral elements adjacent to the prism grid was of high relevance. Depending on the tetrahedral grid refinement, vortex flow phenomena occurring outside the semi-structured prism layers and the wake vortices behind the wing are thereby captured with varying accuracy.

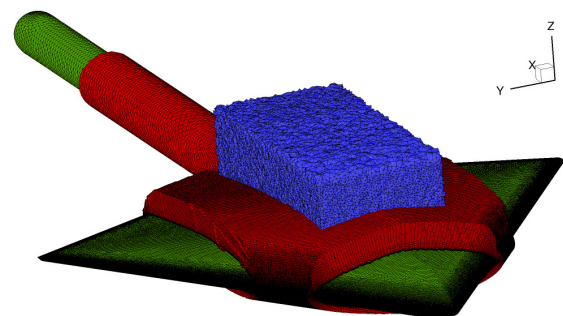
Figure 4.3 shows one of the resulting grids associated with the SAGITTA configuration. As introduced in Section 4.1, the grid generation process first was based on the semi-span wing configuration only. In case of numerical analyses related to the longitudinal motion, this approach



(a) Overall break-up of the different grid types.



(b) Close-up of the leading-edge section.



(c) Full-span wing configuration.

Figure 4.3: Hybrid grid of the SAGITTA configuration.

is sufficient and the computational domain is limited by the plane of symmetry, see Figure 4.3a. For numerical investigations with present sideslip angle, the generated grid was mirrored to obtain a full-span wing configuration, see Figure 4.3c. The far-field domain boundaries are then given by a sphere. Following this approach, a fully-symmetric grid is ensured on both semi-span wing surfaces. This is of great importance for numerical computations with unstructured grids. Former investigations with non-symmetric unstructured grids showed, even for computations in the longitudinal motion, asymmetric flow phenomena such as varying flow separation onset and progression or different vortex bursting locations, which obviously were induced by the grids [9].

4.2.2 Resulting Grids

Table 4.1 and Table 4.2 present the overall grid sizes and the key parameters of the grids that were generated for the AVT-183 configuration and the SAGITTA configuration (reference configuration SG Geo 1). With respect to the applied parameters, a consistent approach was ensured. Due to minor concerns, the boundary-layer resolving cells are slightly different for both diamond wing configurations. The total prism grid height on the upper wing surface, however, is equal in both cases.

To show the convergence in the resulting aerodynamic coefficients and to validate the numerical method, three different grid resolutions were each provided. The results of the corresponding grid resolution studies are presented in Section 5.2.1 and Section 6.1.1. In case of the SAGITTA configuration, further grids were relevant due to the investigated leading-edge contour modifications. Table 4.3 specifies the corresponding grids for all considered configurations. The medium grid of the reference configuration SG Geo 1 was chosen as basis for the subsequent configurations with modified leading-edge contours. Due to the small geometry changes in the leading-edge sections, the overall grid sizes do not vary remarkably, and comparable grids were therefore obtained.

	Coarse Grid	Medium Grid	Fine Grid
Total number of grid points, 10^6	5.4	15.4	27.1
Total number of grid elements, 10^6	14.5	47.0	98.2
Leading-edge surface spacing, mm	0.5	0.25	0.25
Wing surface spacing, mm	6	3	2
Tetrahedral spacing in the wing region, mm	6	3	2
Initial wall-normal spacing, mm	0.003	0.003	0.003
BL resolving layers	32	32	32
BL stretching ratio	1.25	1.25	1.25
LE vortex resolving layers	52	52	52
Max. height of prism layer, mm	67	67	67

Table 4.1: Grid parameters of the computational grids, AVT-183 configuration.

Numerical Approach

	Coarse Grid	Medium Grid	Fine Grid
Total number of grid points, 10^6	4.8	13.8	25.0
Total number of grid elements, 10^6	13.1	43.8	96.1
Leading-edge surface spacing, mm	0.5	0.25	0.25
Wing surface spacing, mm	6	3	2
Tetrahedral spacing in the wing region, mm	6	3	2
Initial wall-normal spacing, mm	0.003	0.003	0.003
BL resolving layers	34	34	34
BL stretching ratio	1.25	1.25	1.25
LE vortex resolving layers	52	52	52
Max. height of prism layer, mm	67	67	67

Table 4.2: Grid parameters of the computational grids, SAGITTA configuration.

	SG Geo 1	SG Geo 2	SG Geo 3	SG Geo 4	SG Geo 5	SG Geo 6
Grid points, 10^6	13.8	13.8	13.8	13.8	13.8	13.8
Grid elements, 10^6	43.8	43.8	43.9	43.6	44.0	43.6

Table 4.3: Grid sizes of the computational grids, SAGITTA configuration.

4.3 Flow Solver

This section gives an overview of the flow solver used for the CFD analyses. First of all, fundamental relations are given to define the governing equations that are relevant for the present numerical investigations. The applied flow solver is introduced subsequently, namely the DLR TAU-Code. In particular, the main characteristics and features of the code are briefly summarized. Finally, the numerical set-up applied to the CFD analyses of both regarded diamond wing configurations is presented. A summary of the considered simulation cases is provided as well in this context.

4.3.1 Governing Equations

Navier-Stokes Equations

A viscous compressible flow is described in general by the Navier-Stokes equations. This set of equations originates from the conservation laws of mass, momentum and energy, see Truckenbrodt [130] or Schlichting [109]. The equations consist of coupled non-linear partial differential equations and read in conservative form, without volume forces and in index notation (Einstein summation convention)

$$\frac{\partial \rho}{\partial t} + \frac{\partial (\rho u_i)}{\partial x_i} = 0, \quad (4.2)$$

$$\frac{\partial (\rho u_i)}{\partial t} + \frac{\partial (\rho u_i u_j)}{\partial x_j} = -\frac{\partial p}{\partial x_i} + \frac{\partial \tau_{ij}}{\partial x_j}, \quad (4.3)$$

$$\frac{\partial \rho E}{\partial t} + \frac{\partial (\rho E u_i)}{\partial x_i} = -\frac{\partial (p u_i)}{\partial x_i} + \frac{\partial (u_i \tau_{ij})}{\partial x_j} - \frac{\partial q_i}{\partial x_i}. \quad (4.4)$$

In the course of this analysis, the Newtonian fluid air is considered exclusively. Therefore, the Stokes hypothesis is used to express the viscous shear stress tensor τ_{ij} by

$$\tau_{ij} = \mu_l \cdot \left(\frac{\partial u_i}{\partial x_j} + \frac{\partial u_j}{\partial x_i} - \frac{2}{3} \delta_{ij} \frac{\partial u_k}{\partial x_k} \right). \quad (4.5)$$

The dependency of the laminar dynamic viscosity μ_l on the fluid temperature results, according to Sutherland's law, in

$$\mu_l = \mu_{l,ref} \left(\frac{T}{T_{ref}} \right)^{\frac{3}{2}} \frac{T_{ref} + 110.4 \text{ K}}{T + 110.4 \text{ K}}, \quad (4.6)$$

with

$$\mu_{l,ref} = 1.716 \cdot 10^{-5} \frac{\text{m}^2}{\text{s}}, \quad \text{and} \quad T_{ref} = 273.15 \text{ K}. \quad (4.7)$$

To close the Navier-Stokes equations, further relations have to be stated. In the following, the fluid is considered as an ideal gas. Regarding the energy equation, the specific total energy E and the thermal flux q_i are then described by

$$E = \left(c_v \cdot T + \frac{u_i u_i}{2} \right), \quad \text{and} \quad q_i = -\lambda_l \cdot \frac{\partial T}{\partial x_i}. \quad (4.8)$$

Under consideration of the laminar Prandtl number, the thermal conductivity λ_l is written as

$$\lambda_l = \frac{\mu_l}{Pr_l} \cdot \frac{\kappa}{\kappa - 1}, \quad \text{with} \quad Pr_l = 0.72. \quad (4.9)$$

The ideal gas law as thermal equation of state and the caloric equations are finally used to close the set of equations:

$$p = \rho R T, \quad \text{with} \quad R = c_p - c_v, \quad \text{and} \quad \kappa = \frac{c_p}{c_v}. \quad (4.10)$$

The corresponding heat capacity ratio of air and the gas constant read

$$\kappa = 1.4, \quad \text{and} \quad R = 287.058 \frac{\text{J}}{\text{kg K}}. \quad (4.11)$$

Reynolds-Averaged Navier-Stokes Equations

Since the direct numerical simulation of Equations 4.2 to 4.4 is often not feasible for aeronautical applications, other approaches have been found in computational fluid dynamics for solving the Navier-Stokes equations. To reduce complexity, Reynolds suggested a time-averaging method, which led to the Reynolds-Averaged Navier-Stokes (RANS) equations, see Truckenbrodt [130] or Ferziger [37]. In this case, the flow is split into a mean flow and a turbulent fluctuation part. The time dependency of the turbulence is eliminated while the other time-dependent flow phenomena remain untouched. Thereby, the mean flow is resolved, but the turbulent fluctuations have to be modeled. For compressible flows, it is however more advisable to apply a mass-weighted decomposition as introduced by Favre, see Blazek [7]. Altogether, it turned out that employing Reynolds-averaging for density and pressure, and Favre-averaging for other variables such as velocity, internal energy, enthalpy and temperature, is the most convenient way in CFD applications. As a result of the mentioned averaging methods, the linear terms of the fluctuation part vanish in the Navier-Stokes equations, but non-linear fluctuation terms remain within the mass-weighted RANS equations. In order to describe them, turbulence models are introduced to close the system of equations.

For the numerical finite volume approach presented in the following, the Navier-Stokes equations are reformulated by the Reynolds transport theorem in conservative integral form [30]. Under consideration of the averaging methods according to Reynolds and Favre, the three-dimensional mass-weighted RANS equations for turbulent flows can be written for an arbitrary volume V with the boundary S and the outer normal \vec{n} as

$$\frac{\partial}{\partial t} \iiint_V \vec{W} dV = - \iint_S \bar{\mathbf{F}} \cdot \vec{n} dS . \quad (4.12)$$

The vector \vec{W} represents the averaged conserved quantities

$$\vec{W} = \begin{pmatrix} \bar{\rho} \\ \bar{\rho}\bar{u} \\ \bar{\rho}\bar{v} \\ \bar{\rho}\bar{w} \\ \bar{\rho}\bar{E} \end{pmatrix} , \quad (4.13)$$

in which $\bar{\rho}$ describes the density, \bar{u} , \bar{v} and \bar{w} the velocity components and \bar{E} the specific total energy. The time- and mass-weighted quantities are indicated by an overline bar. The flux tensor $\bar{\mathbf{F}}$ is composed of the flux vectors \vec{F} , \vec{G} and \vec{H} in the three different spatial directions

$$\bar{\mathbf{F}} = \vec{F} \otimes \vec{e}_x + \vec{G} \otimes \vec{e}_y + \vec{H} \otimes \vec{e}_z . \quad (4.14)$$

The flux vectors can be divided into inviscid (index i) and viscous (index v) terms in the form

$$\vec{F} = \left(\vec{F}_i + \vec{F}_v \right) , \quad \vec{G} = \left(\vec{G}_i + \vec{G}_v \right) , \quad \vec{H} = \left(\vec{H}_i + \vec{H}_v \right) . \quad (4.15)$$

The respective components of the flux vectors read in detail

$$\vec{F}_i = \begin{pmatrix} \bar{\rho}\bar{u} \\ \bar{\rho}\bar{u}\bar{u} + \bar{p} \\ \bar{\rho}\bar{u}\bar{v} \\ \bar{\rho}\bar{u}\bar{w} \\ \bar{\rho}\bar{u}\bar{H} \end{pmatrix}, \quad \vec{F}_v = - \begin{pmatrix} 0 \\ \bar{\tau}_{xx} - \overline{\rho u' u'} \\ \bar{\tau}_{xy} - \overline{\rho u' v'} \\ \bar{\tau}_{xz} - \overline{\rho u' w'} \\ \bar{u}\bar{\tau}_{xx} + \bar{v}\bar{\tau}_{xy} + \bar{w}\bar{\tau}_{xz} + (\lambda_l + \lambda_t) \frac{\partial \bar{T}}{\partial x} - \frac{\partial \overline{\rho H' u'}}{\partial x} \end{pmatrix}, \quad (4.16)$$

$$\vec{G}_i = \begin{pmatrix} \bar{\rho}\bar{v} \\ \bar{\rho}\bar{v}\bar{u} \\ \bar{\rho}\bar{v}\bar{v} + \bar{p} \\ \bar{\rho}\bar{v}\bar{w} \\ \bar{\rho}\bar{v}\bar{H} \end{pmatrix}, \quad \vec{G}_v = - \begin{pmatrix} 0 \\ \bar{\tau}_{yx} - \overline{\rho v' u'} \\ \bar{\tau}_{yy} - \overline{\rho v' v'} \\ \bar{\tau}_{yz} - \overline{\rho v' w'} \\ \bar{u}\bar{\tau}_{yx} + \bar{v}\bar{\tau}_{yy} + \bar{w}\bar{\tau}_{yz} + (\lambda_l + \lambda_t) \frac{\partial \bar{T}}{\partial y} - \frac{\partial \overline{\rho H' v'}}{\partial y} \end{pmatrix}, \quad (4.17)$$

$$\vec{H}_i = \begin{pmatrix} \bar{\rho}\bar{w} \\ \bar{\rho}\bar{w}\bar{u} \\ \bar{\rho}\bar{w}\bar{v} \\ \bar{\rho}\bar{w}\bar{w} + \bar{p} \\ \bar{\rho}\bar{w}\bar{H} \end{pmatrix}, \quad \vec{H}_v = - \begin{pmatrix} 0 \\ \bar{\tau}_{zx} - \overline{\rho w' u'} \\ \bar{\tau}_{zy} - \overline{\rho w' v'} \\ \bar{\tau}_{zz} - \overline{\rho w' w'} \\ \bar{u}\bar{\tau}_{zx} + \bar{v}\bar{\tau}_{zy} + \bar{w}\bar{\tau}_{zz} + (\lambda_l + \lambda_t) \frac{\partial \bar{T}}{\partial z} - \frac{\partial \overline{\rho H' w'}}{\partial z} \end{pmatrix}. \quad (4.18)$$

Considering the momentum equations, the viscous flux vectors consist on the one hand of the viscous shear stress tensor $\boldsymbol{\tau}$, which has already been defined in Equation 4.5. This time, the mass-weighted notation is applied. On the other hand, the non-linear fluctuation terms that remain due to the Reynolds- and Favre-averaging occur additionally, see the right-hand side of Equation 4.16 to Equation 4.18. According to the Boussinesq hypothesis, a tensor called Reynolds stress tensor is introduced, which is assumed to scale with the shear of the flow similar to the regular viscous shear stress tensor. Hence, the non-linear fluctuation terms are expressed as

$$-\overline{\rho u'_i u'_j} = \bar{\tau}_{ij} = (\mu_l + \mu_t) \cdot \left(\frac{\partial \bar{u}_i}{\partial x_j} + \frac{\partial \bar{u}_j}{\partial x_i} - \frac{2}{3} \delta_{ij} \frac{\partial \bar{u}_k}{\partial x_k} \right) - \frac{2}{3} \delta_{ij} \bar{\rho} k, \quad (4.19)$$

in which k defines the turbulent kinetic energy. It reads

$$k = \frac{\bar{u}'_i \bar{u}'_i}{2}. \quad (4.20)$$

With regard to the energy equation, the turbulent fluxes $-\frac{\partial \overline{\rho H' u'_i}}{\partial x_i}$ have to be treated additionally. The terms are built by the heat fluxes $-\frac{\partial \overline{\rho \Gamma' u'_i}}{\partial x_i}$ and an additional term Θ_x , which describes the frictional heat:

$$-\frac{\partial \overline{\rho H' u'_i}}{\partial x_i} = -\frac{\partial \overline{\rho \Gamma' u'_i}}{\partial x_i} - \Theta_x. \quad (4.21)$$

The heat fluxes are modeled by

$$-\frac{\overline{\partial \rho \Gamma' u_i'}}{\partial x_i} = \lambda_t \frac{\partial \bar{T}}{\partial x_i}, \quad (4.22)$$

and the frictional heat term is composed of

$$\Theta_x = \left(\mu_l + \frac{\mu_t}{Pr_k} \right) \frac{\partial k}{\partial x_i}. \quad (4.23)$$

Under consideration of the turbulent Prandtl number, the corresponding thermal conductivity can be calculated by

$$\lambda_t = \frac{\mu_t}{Pr_t} \cdot \frac{\kappa}{\kappa - 1}, \quad \text{with} \quad Pr_t = 0.90. \quad (4.24)$$

The last term to be discussed is the inviscid flux term of the energy equation, $\bar{\rho} \bar{u}_i \bar{H}$, which contains the specific total enthalpy. It reads for the mass-weighted RANS equations

$$\bar{H} = \bar{E} + \frac{p^*}{\bar{\rho}}, \quad (4.25)$$

with the effective turbulent pressure

$$p^* = \bar{p} + \frac{2}{3} \bar{\rho} k, \quad (4.26)$$

and the specific total energy

$$\bar{E} = c_v \cdot T + \frac{\bar{u}_i \bar{u}_i}{2} + k. \quad (4.27)$$

In contrast to the definition of the specific total energy in the general Navier-Stokes equations according to Equation 4.8, this time the turbulent kinetic energy k is to be considered as well. With the introduced equations, the mass-weighted RANS formulation can now be closed by appropriate turbulence models, in which the turbulent eddy viscosity μ_t and the kinetic energy k are finally set. The corresponding definitions depend on the turbulence model and can significantly vary in complexity. Specific information with relevance for the present research follow below.

Spalart-Allmaras One-Equation Turbulence Model

In the numerical analyses of this research, the one-equation turbulence model by Spalart and Allmaras (SA model) was applied. It was originally presented in 1992 [119] and in 1994 in a slightly revised form [120]. In 2012, Allmaras et al. published modifications to the SA turbulence model [2], of which some are introduced below. The main motivation for the application of the Spalart-Allmaras turbulence model was derived from former numerical results of vortex-dominated wing configurations [112, 113, 115]. Especially for pitching-moment characteristics at higher angles of attack, this turbulence model was found to result in better characteristics

compared to experimental data than other two-equation turbulence models applied. In addition, the convergence stability of the SA model and the passable numerical effort with respect to the conducted polar computations led to this decision. A rotational correction (SARC model) was not applied, since test computations showed a disproportionately upstream promotion of the leading-edge vortex separation onset. The results gained with the SA model, in contrast, showed good correlations with the experimental data, see Section 5.2.1 and Section 6.1.1.

In general, the Spalart-Allmaras turbulence model formulates one additional transport equation for the turbulent viscosity μ_t . The contribution of the turbulent kinetic energy k is neglected. To define a formulation for the turbulent viscosity μ_t , a working variable is introduced, namely the SA viscosity $\tilde{\nu}$. It is linked to the turbulent viscosity μ_t by

$$\mu_t = \bar{\rho}\nu_t, \quad \text{and} \quad \nu_t = \tilde{\nu}f_{v1}(\chi). \quad (4.28)$$

$f_{v1}(\chi)$ represents a damping function. In the standard formulation of the turbulence model, smooth walls are regarded, for which the parameter χ is described by the viscosity ratio

$$\chi = \frac{\tilde{\nu}}{\nu_l}. \quad (4.29)$$

In case of rough walls, the definition of χ is altered according to Aupoix and Spalart [5]. With the sand roughness k_s and the wall distance d , the new formulation results in

$$\chi = \frac{\tilde{\nu}}{\nu_l} + 0.5 \cdot \frac{k_s}{d}. \quad (4.30)$$

The transport equation that is formulated for the SA viscosity $\tilde{\nu}$ reads in general notation

$$\begin{aligned} \frac{D\tilde{\nu}}{Dt} = & t_{prod}(\tilde{S}, \tilde{\nu}, k_s, d) - t_{dest}(\tilde{\nu}, k_s, d) - t_{diff}(\tilde{\nu}) \\ & + t_{comp}(\tilde{\nu}) + t_{trip}(d, d_t, \omega_t). \end{aligned} \quad (4.31)$$

$t_{prod}(\tilde{S}, \tilde{\nu}, k_s, d)$ represents the production term, $t_{dest}(\tilde{\nu}, k_s, d)$ is the destruction term, and $t_{diff}(\tilde{\nu})$ characterizes the diffusion term. The other terms are modifications for compressibility ($t_{comp}(\tilde{\nu})$) and turbulence onset ($t_{trip}(d, d_t, \omega_t)$), which are, depending on the different model versions, active or not. \tilde{S} describes the modified vorticity, k_s the sand roughness, d the wall distance, d_t the distance from the trip point, and ω_t the vorticity at the trip point.

Two different model versions of the SA one-equation turbulence model are considered in more detail. On the one hand, this is the original SA model (SAO) presented by Spalart and Allmaras in 1992 [119]. For this implementation, neither the compressibility term, nor the trip term of Equation 4.31 are considered. The exact definition of the other three terms and the proposed model constants can be obtained from the main references [119, 120]. On the other hand, the negative SA model (SA-Neg) is introduced, which was devised by Allmaras et al. [2]. For the

present numerical investigations, this model version was applied exclusively. In general, the SA viscosity $\tilde{\nu}$ must always be positive, but the solution algorithm implemented in the original SA model may result in negative values, too. The new SA-Neg model copes with negative values of the SA viscosity $\tilde{\nu}$ as well, without degrading the numerics and the aerodynamic solution either. The production term, the destruction term, and the diffusion term of Equation 4.31 are modified for this purpose, as they are reformulated in regions of the flow field with negative $\tilde{\nu}$ values. Implementation details are found in Reference [2]. If the SA viscosity $\tilde{\nu}$ is positive, the standard SA model is followed, which was devised by Allmaras et al. in 2012 as well. The only difference of the standard SA model to the original SA model is the different definition of the scalar velocity gradient parameter \tilde{S} , which deviates from the original implementation for values of $\tilde{S} < 0.3 \cdot S$. Thereby, positive values of \tilde{S} are guaranteed for every non-zero vorticity S without any need for limiting. Furthermore, the SA-Neg model includes the compressibility term of Equation 4.31 as well. The trip term, however, is not included.

Finally, the boundary values of $\tilde{\nu}$ required for the SA transport equation are discussed. At the far-field boundaries, Allmaras et. al. recommend $(\tilde{\nu}/\nu)_\infty$ values of $(\tilde{\nu}/\nu)_\infty = 3 \dots 5$. For the conducted CFD computations, a value of

$$(\tilde{\nu}/\nu)_\infty = 3.8 \quad (4.32)$$

was used with the SA-Neg model. Due to historical reasons of the applied flow solver, $(\tilde{\nu}/\nu)_\infty$ is defined differently for the SAO model [30]. At smooth walls, the zero turbulence condition yields

$$\tilde{\nu}|_w = 0 . \quad (4.33)$$

Special attention is required for rough walls, for which the log-law almost extends down to the wall [5]. The wall value of $\tilde{\nu}$ is non-zero and corresponds to the log-law value at some offset d_0 from the wall. With u_τ being the friction velocity, it results according to Aupoix and Spalart in

$$\tilde{\nu}|_w = \bar{\rho} u_\tau \kappa d_0 , \quad \text{with} \quad d_0 = \exp(-8.5\kappa) h_s \approx 0.03 h_s . \quad (4.34)$$

4.3.2 The DLR TAU-Code

The numerical investigations performed for this research were computed with the TAU-Code, a CFD solver developed at the DLR (German Aerospace Center) Institute of Aerodynamics and Flow Technology [46, 116]. Using a finite volume approach, it solves the three-dimensional compressible steady or unsteady Reynolds-Averaged Navier-Stokes equations on hybrid grids. Moreover, it is developed for optimized parallel efficiency on high-performance computing systems. In this section, the main characteristics of the DLR TAU-Code are introduced, such as the dual grid approach, the discretization schemes, multigrid concerns, and the boundary treatment. Overall, the DLR TAU-Code consists of several modules, of which the preprocessor and the solver modules are the most important ones. Depending on the number of domains for parallel compu-

tations, the preprocessing module computes both the secondary grid data according to the dual grid approach and the coarse grids required for multigrid calculations. The solver module then performs the flow computations based on the applied numerical schemes. In addition, the DLR TAU-Code provides a grid adaptation module to improve the accuracy of a computed solution [3]. Based on pre-defined indicators of solution variables, local grid refinement is applied to the hybrid grid in regions of interest to efficiently resolve detailed flow features. In other regions of the flow field, the amount of grid points may be reduced, which leads to optimized grid sizes required for efficient numerical simulations.

Dual Grid Approach

In order to solve the RANS system of equations numerically, see Equation 4.12, the flow variables are computed at discrete points. According to the integral formulation, appropriate control volumes have to be defined. Based on the computational grid provided by the grid generation process, which is defined in TAU as initial (primary) grid, a secondary grid is constructed within the preprocessing module according to the cell-vertex grid metric. This modus operandi is known as dual grid approach [37, 44]. The secondary grid is constructed from the primary mesh data, as the grid points of the primary mesh are chosen to be the discrete points, for which the flow variables are computed. The primary and the secondary grid thus share the same points in physical space. The secondary grid, however, consists of control volumes surrounding each grid point. As it can be noticed from Figure 4.4, each face of the secondary grid control volumes is thereby associated with an edge of the corresponding primary grid point. On the boundary of the computational domain, the control volumes of the secondary grid are closed with respect to the boundary surfaces of the primary grid.

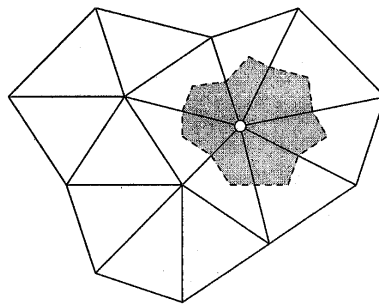


Figure 4.4: Dual grid approach – Secondary grid data based on the cell-vertex grid metric [44].

Finite Volume Discretization

The governing equations of the RANS formulation consist of integral expressions with partial differential equations, which contain a number of different partial derivative terms. In order to solve them efficiently with the DLR TAU-Code based on the secondary grid data, a finite volume approach is used. The integral expressions are transferred to sum equations and are discretized

in space. The control volumes of the secondary grid cells, as indicated in Figure 4.4, do not have to be stored any longer, since the fluxes to be analyzed are summed up over the control volume surfaces, which are already available in the secondary grid data. Since the flow variables are computed at the grid points themselves, the partial derivative terms of the RANS equations are further replaced by finite difference quotients. This results in a linear set of finite difference equations, which is an algebraic linearization of the partial differential equations [30]. Due to the finite difference formulation, the fluxes can be expressed at each face of the defined control volumes. In addition, the fluxes are assumed to be constant at each control volume face.

The computation of the finite differences is accomplished in the DLR TAU-Code by several available upwind and central schemes. They differ in complexity, computational cost and the resulting accuracy. For the present investigations, a second-order central scheme introduced by Jameson was applied for the spatial discretization [76]. The convective fluxes are computed at the faces of the control volumes from the arithmetic average of the conservative variables on both sides of the faces. Due to numerical stability reasons, artificial dissipation is further added to the flux equation, for which either the scalar or matrix dissipation scheme is applied. The scalar dissipation approach follows the strategy described by Mavriplis et al. [94]. Compared to the original scheme devised by Jameson et al. [76], an adequate scaling of the dissipation is reached for highly-stretched cells, which are typically present in hybrid grids. In case of the matrix dissipation approach, the required artificial viscosity is added by a matrix valued coefficient. In contrast to the scalar scheme, which can add too much viscosity to the slower waves, the matrix viscosity gives an appropriate viscosity for each wave component. Thereby, the central difference scheme becomes closer to upwind biased methods [132]. Consequently, the matrix dissipation scheme was applied to the numerical investigations of this thesis.

Discretization in Time

For the time discretization, both explicit Runge-Kutta and implicit Backward-Euler schemes are available in the DLR TAU-Code. In general, explicit schemes can easily be solved numerically and exhibit low memory requirements, but they have severe restrictions on the time step described by the Courant-Friedrichs-Lewy number (CFL number) [22]. Implicit schemes allow for considerably larger time steps, which leads to an accelerated convergence, but the computational cost is much higher. For each time step, the Jacobian matrix has to be computed. It contains information on the gradients at all grid points [34]. Several algorithms have been introduced to cope with the implicit Backward-Euler scheme, and the Lower-Upper Symmetric Gauss-Seidel algorithm (LUSGS) is one of the most famous ones [77]. It is aimed to improve the convergence while the low memory requirement and robustness of an explicit Runge-Kutta scheme shall be maintained [33]. For this reason, the implicit LUSGS scheme was used for the CFD analyses of the present research.

Depending on steady-state or time-accurate computations, different time stepping methods are used in the DLR TAU-Code. For steady-state problems, the time-independent solution of the

RANS equations is computed based on a pseudo time t^* , for which the steady-state solution is sought. The local time stepping method is applied, which allows in each control volume variable time steps that depend on the local CFL number only [76]. In consequence, the local time stepping method operates at its stability limit everywhere in the flow field [30]. The convergence of the solution to steady-state is thus accelerated. Moreover, the multigrid technique can be used for steady-state problems to further accelerate the convergence [74]. Details are given in the following paragraph.

In case of time-accurate computations, global or dual time stepping methods are applied. The global time stepping method requires a minimum time step, which is given globally over all grid points of the secondary grid [75]. For this reason, the dual time stepping method was used in the conducted CFD computations. It follows a combined strategy, as pseudo time steps are introduced to the discretized equations in addition to the physical time steps [73]. For every physical time step, the partial differential equations are then solved based on the pseudo time t^* to find out a converged solution. Numerical techniques to accelerate the convergence such as implicit schemes, local time stepping and multigrid can still be applied without restrictions. Hence, the time-dependent problem is solved by a sequence of non-linear steady-state problems. The physical time step size itself is chosen in line with time-dependent flow features of the present flow problem that shall be resolved.

Multigrid

Since the 1980s, the multigrid method has been found to be a powerful instrument to accelerate the convergence of numerical solutions apart from time discretization techniques [74]. For this reason, it is implemented in the DLR TAU-Code as well. When the multigrid method is applied, the RANS system of equations is solved for every iteration on several grids with different refinement levels. Overall, the multigrid algorithm speeds up the convergence, since the coarser grids allow for larger time steps and are more dissipative. Undesired oscillations in the solution are thus damped more effectively. In addition, the solutions on the coarser grids represent a rough start solution for the iteration on the finer grids.

In general, several approaches exist for the generation of the different multigrid levels [44]. In the DLR TAU-Code, the used multigrid algorithm corresponds to an upward/downward cycle. Based on the secondary grid, which defines the finest mesh of the multigrid levels, the control volumes are fused together in the upward cycle to form the coarser grids. This part of the multigrid method is referred to as topological fusing part. Figure 4.5 displays the agglomeration process in a basic sketch. In a subsequent downward cycle named physical fusing part, the entire information about the coordinates of the coarse grid and the relationship between the volumes of the coarse and the fine grid is determined based on the fine grid information. The coarse grid is checked whether the total size and the integrals of the surfaces of each control volumes are correct [30]. In addition, the physical fusing part also contains the computation of the coarse grid's inner and boundary faces.

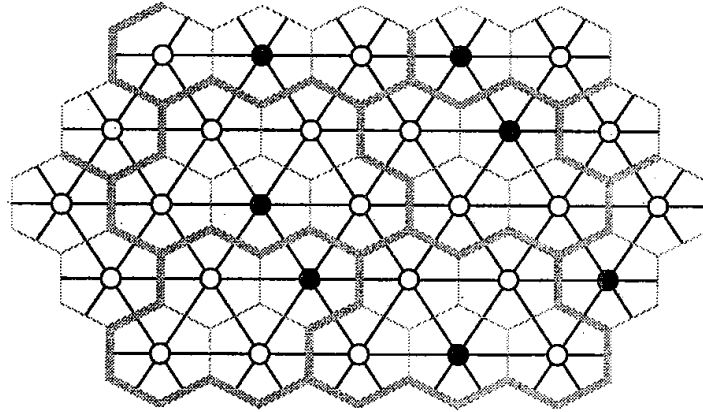


Figure 4.5: Multigrid method – Agglomeration of control volumes to form a coarser mesh [44].

The coarser grids are composed of a data structure similar to the data structure of the secondary grid, since the connectivities of the coarser grids are formed explicitly during the fusion process. Hence, the coarser grids contain all relevant information for the flow solver. Moreover, the control volumes of the coarser grids can be evaluated in the same way as the control volumes of the secondary grid itself [30]. The number of multigrid levels and the cycle to be performed are given by the user. Depending on the chosen cycle, the computational cost and the numerical accuracy may slightly differ. In the course of this research, 3w-type multigrid cycles were applied to the performed CFD computations. In the preprocessing module of the DLR TAU-Code, two coarser multigrids were thus generated based on the secondary grid. In general, the flow solver then computes the solution on all three different grids, starting with the finest grid.

Boundary Treatment

The DLR TAU-Code is able to cope with a series of different boundary types [29]. During the preprocessing, they are assigned to each surface of the geometry and the bounding surfaces of the computational domain. The flow solver treats the different parts of the grid according to their boundary type. In the present research, fully-turbulent CFD computations were considered exclusively. For this reason, the entire wing surfaces were regarded as turbulent viscous walls, where the corresponding flow condition reads $\vec{V} = 0$. By default, smooth walls are supposed. If roughness effects are considered as well, the differentiation is respected by the varying formulations of the turbulence model at the viscous walls, see Section 4.3.1.

The limiting far-field surfaces of the computational domain are regarded with a combined inflow/outflow boundary type. At this boundary surface, all gradients are assumed to be zero, and therefore no viscous effects are taken into account. Typically, the boundary surface is far away from the investigated geometry, see Section 4.2.1. Then, no influence of the bounding surfaces on the wing configuration should be obtained. Moreover, the free stream turbulence is initialized at the far-field boundary surfaces, see Section 4.3.1. Start values for the flow solver are thereby provided.

Depending on computations in the longitudinal and the lateral motion, respectively, the wing geometries are regarded as a semi-span or as a full-span wing configuration, see Section 4.2.1. In case of semi-span wing configurations, the computational domain is closed by a boundary surface in the plane of symmetry. The corresponding boundary type of the DLR TAU-Code projects the momentum flow variables onto the symmetry plane.

4.3.3 Applied Numerical Set-Up

Table 4.4 presents the high-level control parameters of the DLR TAU-Code that were applied in the CFD computations of the present research. All of them have been introduced in the previous paragraphs and are characteristic of the DLR TAU-Code. The numerical investigations were run in parallel mode with up to 840 cores on the supercomputer SuperMUC at the Leibniz Supercomputing Centre (LRZ), which is part of the Gauss Centre for Supercomputing (GCS) [135]. For the present research, computation time was granted by LRZ to efficiently conduct the required CFD computations (project pr86fi)². The funding of this project by providing computing time on the GCS Supercomputer SuperMUC at LRZ is gratefully acknowledged.

The numerical investigations were conducted for the W/T model sizes of the regarded diamond wing configurations, see Section 4.1. Consequently, the free stream conditions of the CFD computations were chosen in line to the experimental analyses. Specific details with respect to each configuration are stated in the following two paragraphs. Moreover, the reference quantities of each W/T model as defined in Section 3.2 were used as well. For the determination of the aerodynamic coefficients and the resulting flow field quantities, the equations introduced for the experimental analyses in Section 3.4 were, if necessary and applicable, also applied to the CFD computations. Consistent data sets were therefore obtained for the CFD and the W/T data, respectively.

²http://www.gauss-centre.eu/gauss-centre/EN/Projects/ScientificEngineering/2015/breitsamter_AER.html?nn=1236240, retrieved February 2016

Governing equations	(U)RANS
Turbulence model	SA-Neg
Dual grid approach	Cell-vertex grid metric
Finite volume discretization	Central scheme with matrix dissipation
Discretization in time	Implicit Backward-Euler scheme with LUSGS algorithm Local time stepping scheme (steady-state computations) Dual time stepping scheme (time-accurate computations)
Multigrid	3w-type
Boundary treatment	Turbulent viscous walls (wing geometry) Far field / symmetry (computational domain)

Table 4.4: High-level control parameters of the DLR TAU-Code in the applied numerical set-ups.

AVT-183 Diamond Wing Configuration

The CFD analyses conducted for the AVT-183 configuration were all based on steady-state computations with the local time stepping scheme. The low-speed W/T conditions with a Reynolds number of $Re_\infty = 2.7 \cdot 10^6$ based on the mean aerodynamic chord of $l_\mu = 0.8 \text{ m}$ and a Mach number of $Ma_\infty = 0.15$ were further considered. The corresponding moment reference point for pitching-moment calculation was set, according to the W/T model, to $x_{mrp} = 0.491 \text{ m}$ aft of the diamond wing nose. Although the focus of the resulting analysis is mostly put on the angle of attack of $\alpha = 12^\circ$ and specific target flow conditions as derived in Section 5.1.1, the numerical investigations were performed for a complete angle-of-attack polar of $0^\circ \leq \alpha \leq 24^\circ$. This nearly corresponds to the polars measured within the W/T experiments. Aerodynamic coefficients and surface pressures that are available from the experimental data can thus be compared to the CFD results over the full range of angles of attack.

SAGITTA Diamond Wing Configuration

The numerical investigations on the SAGITTA configuration comprise both steady-state and time-accurate CFD computations. In accordance with the atmospheric low-speed conditions of the W/T experiments, a Reynolds number of $Re_\infty = 2.3 \cdot 10^6$ based on the mean aerodynamic chord of $l_\mu = 0.801 \text{ m}$ and a Mach number of $Ma_\infty = 0.13$ were applied. The moment reference point for pitching- and yawing-moment calculation was set with respect to the W/T model to $x_{mrp} = 0.501 \text{ m}$ aft of the diamond wing nose. In the longitudinal motion, all of the different SAGITTA configurations were considered, and the angle of attack was varied between $0^\circ \leq \alpha \leq 24^\circ$. For the reference configuration SG Geo 1, additional CFD analyses were undertaken in the lateral motion. Using the full-span wing configuration, two sideslip angles with $\beta \pm 10^\circ$ were investigated for the entire angle-of-attack range.

At first, steady-state computations were conducted with the local time stepping scheme, respectively. For angles of attack of $\alpha \geq 10^\circ$, time-accurate simulations were run subsequently. Based on restart solutions of the steady-state computations, the time-accurate CFD simulations were performed with the dual time stepping scheme. For these computations, the time step was set to $\Delta t = 0.0004 \text{ s}$ and the overall simulation time reads $t_{sim} = 0.4 \text{ s}$, including 150 inner iterations per time step. If it is not explicitly indicated, the graphs and figures presented in the following refer to the mean values of the time-accurate CFD computations. For the results of the lower angles of attack with $\alpha < 10^\circ$, in contrast, the converged solution of the steady-state computations is used within the plots.

Chapter 5

Analysis of Partly-Developed Leading-Edge Vortices

The following chapter deals with the analysis of leading-edge vortex flow phenomena that are associated with the AVT-183 configuration. It consists of two main sections, which separately focus on experimental and numerical investigations. The large-scale formation and progression of the partly-developed leading-edge vortex structure is discussed in Section 5.1 by the experimental results. The content refers to pre-publications of the author, which were composed to document the key results and major findings of the experimental analyses within the AVT-183 task group [69, 72, 124]. Special emphasis is laid on the effects of different leading-edge roughness, which was applied in the W/T experiments at the wing leading edge to fix turbulent boundary-layer characteristics, see Section 3.3.4. Differences in the flow separation onset occur, and their effects on the emerging leading-edge vortex are assessed in detail. In this context, measurement repeatability issues are reviewed as well. As an outcome, one specific leading-edge roughness is selected for flow tripping, thus providing the baseline for the subsequent flow physics analysis at the angle of attack of $\alpha = 12^\circ$. Details of the partly-developed leading-edge vortex are thereby analyzed and discussed. Finally, the longitudinal aerodynamic coefficients are considered. The effects of the leading-edge vortex on the overall aerodynamic characteristics are thus demonstrated.

Section 5.2 concentrates on the numerical analyses of the partly-developed leading-edge vortex at the AVT-183 configuration. Based on a grid sensitivity study and the available experimental data, the numerical method is validated first. Then, the flow physics analysis is extended to other angles of attack, and additional data beyond the experimental results is reviewed. The main characteristics of the large-scale formation and progression of the leading-edge vortex are therefore highlighted. Next, the focus is set on the flow separation onset characteristics in the incipient separation region. Selected near-wall velocity profiles are discussed on boundary-layer level along selected skin-friction lines, which show the flow separation onset most efficiently. Thereby, a flow-physical description of the leading-edge vortex formation is given, and the onset location of the flow separation is derived on the AVT-183 diamond wing surface. Finally, the discussion is supported by topological-physical interpretations of the near-wall flow field phenomena. The numerical analyses are thus used to demonstrate the nature of the occurring three-dimensional flow separation according to topology rules as introduced in Section 2.2.

5.1 Experimental Investigations

5.1.1 Leading-Edge Roughness Effects

Longitudinal Aerodynamic Coefficients

The effects of different trip strips on the longitudinal aerodynamic coefficients are presented in Figure 5.1 and Figure 5.2. The data refers to the trip-strip cases that have been introduced in Figure 3.11 and Table 3.5. For the lift coefficient C_L , almost no effect can be observed, see Figure 5.1a. All applied trip-strip cases result in a comparable lift polar and do not show significant differences to the free transition case without any flow tripping. The pitching-moment coefficient C_{my} , in contrast, deviates for the different trip strips with increasing angle of attack, see Figure 5.1b. Compared to the case W/T Free Transition, the deviations due to different roughness heights are noted as significant. For angles of attack higher than $\alpha > 8^\circ$, the curves additionally become non-linear. The deviations are mainly attributed to different flow separation onsets and the subsequent vortex formation close to the diamond wing leading edge, which is discussed later on in this section. In consequence, the pressure distribution changes on the wing surface and therefore influences the pitching-moment coefficient.

The drag coefficient C_D is affected as well by the different trip strips, see the Lilienthal polar in Figure 5.2a. Deviations are observed between the considered cases for the entire angle-of-attack polar. To examine the differences occurring at low angles of attack more precisely, Figure 5.2b depicts a detailed view. The effects of different roughness heights on the drag coefficient characteristics therefore become visible. In particular, the zero-lift drag coefficient $C_{D,0}$ varies with increasing leading-edge roughness, and, compared to the case W/T Free Transition, the values are considerably larger for the cases with forced transition. Consequently, this emphasizes the trip-strip influence in general for the present low-speed conditions, and it indicates the existence of, at least, partly laminar flow regions on the AVT-183 wing surface without flow tripping. A

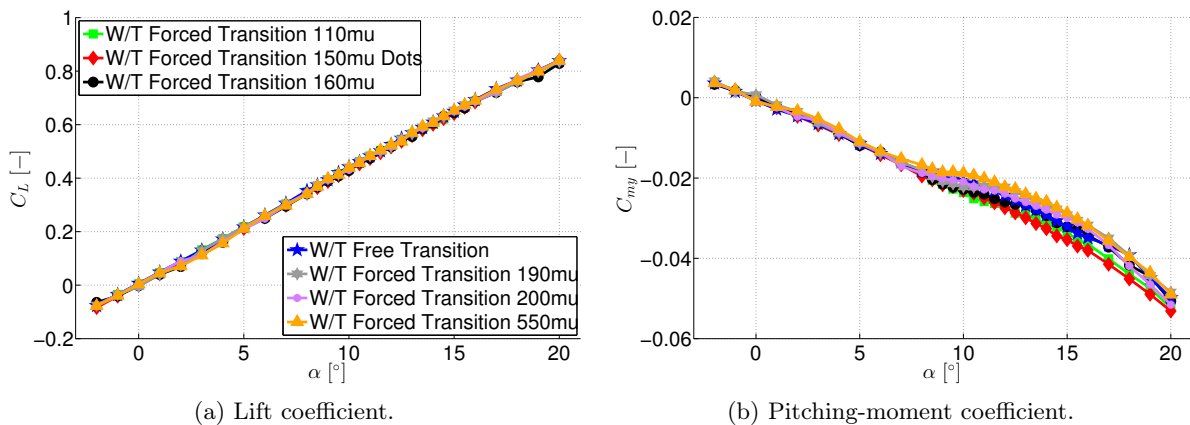


Figure 5.1: Leading-edge roughness effects at the AVT-183 configuration — Lift coefficient C_L and pitching-moment coefficient C_{my} versus angle of attack α .

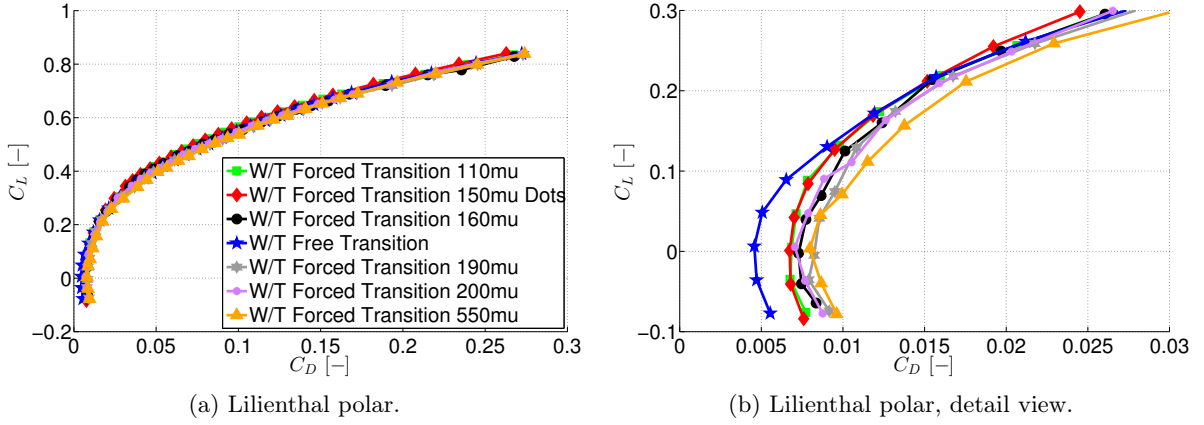


Figure 5.2: Leading-edge roughness effects at the AVT-183 configuration — Lilienthal polar C_L versus C_D .

comparison with the skin-friction coefficient for completely laminar boundary-layer flow according to Equation 3.1, however, confirms that these regions can not be very extensive, since the estimated skin-friction is much smaller in this case ($C_f \approx 0.001$).

To highlight the drag coefficient dependence on the surface roughness in more detail, Figure 5.3 introduces the $C_{D,0}$ values of the different trip-strip cases versus the total roughness height that was applied to the leading edge. In addition to the discrete data points, a polynomial curve fit was added so that the general trend with increasing roughness height is emphasized. Moreover, the empirical relations of turbulent boundary-layer flow according to Equation 3.2 and Equation 3.4 are evaluated as well, as both cases with hydraulically smooth and rough surfaces are regarded. The subsequent discussion relies on a comparison of the complete zero-lift drag coefficient $C_{D,0}$ that was measured within the W/T experiments, and the skin-friction drag coefficient C_f according to the empirical relations for the flat plate. In consequence, the form drag contribution $C_{D,p}$ of the AVT-183 configuration is not considered.

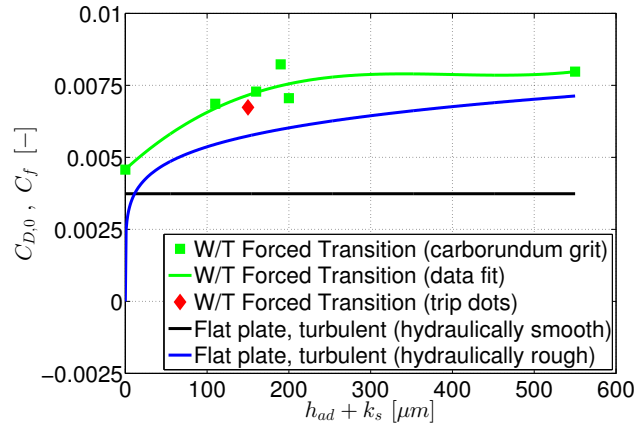


Figure 5.3: Leading-edge roughness effects at the AVT-183 configuration — Zero-lift drag coefficient $C_{D,0}$ and skin-friction coefficient C_f versus total roughness height $h_{ad} + k_s$.

Overall, the experimental results confirm an increase of the zero-lift drag coefficient with increasing roughness height. This holds particularly for the carborundum grit cases W/T Forced Transition 110 μ m, 160 μ m and 550 μ m. The comparison of the experimental curve fit and the empirical relation for hydraulically rough surfaces further shows a good qualitative agreement. The offset in the curves is motivated by the additional form drag influence of the wing surface and the more complex boundary-layer characteristics in general. In comparison to the flow along a flat plate, three-dimensional boundary-layer effects are much more distinct at the rounded leading edge of the diamond wing configuration. They influence the drag coefficient characteristics to some extent. The other carborundum grit cases W/T Forced Transition 190 μ m and 200 μ m show certain deviations from the overall trend, which can not be explained. The $C_{D,0}$ value of the trip-dot case W/T Forced Transition 150 μ m Dots is found to result in a zero-lift drag coefficient that is very close to that of case W/T Forced Transition 110 μ m. Despite different trip-strip approaches and roughness heights, comparable zero-lift drag coefficients are observed. The agreement is also valid for non-zero angles of attack, see Figure 5.2b. This further highlights the very similar drag coefficient characteristics of those two trip-strip cases.

Surface Pressure Coefficients

Next, the different trip-strip cases are examined with respect to the flow separation onset, as selected results of spanwise surface pressure coefficient distributions are discussed for the angle of attack of $\alpha = 12^\circ$. The smooth surface separation and the consecutive vortex formation was expected to occur at approximately mid-chord locations in this case. For this reason, the chordwise sections at $0.295 \leq x/c_r \leq 0.405$ are regarded in Figure 5.4. In addition to the results of the free transition measurements, all cases with forced transition are considered. Without any trip strip applied (case W/T Free Transition), the flow is already found as separated at this angle of attack and for the mentioned chordwise sections, and the leading-edge vortex has emerged. Typical distributions of the spanwise surface pressure coefficients are noticed, and the vortex core axis is indicated by suction peaks located inboard of the leading edge. The other cases with trip strips applied, in contrast, show diverse characteristics, which are discussed below.

As a result of a reasonable flow tripping and fixed turbulent boundary-layer characteristics compared to the free transition case, the onset of flow separation and the consecutive vortex formation is in general expected to be shifted more downstream and/or to higher angles of attack. This is due to more momentum present close to the wing surface, which prevents the flow from being separated up to higher angles of attack. This behavior is however not found for the cases with a total roughness height of $h_{ad} + k_s \geq 190 \mu\text{m}$, which at first were considered in the W/T experiments, see Figure 5.4. For the related cases (W/T Forced Transition 190 μ m / 200 μ m / 550 μ m), the vortex axis indicated by the suction peaks is located more inboard compared to the free transition case. Hence, vortex formation occurs even more upstream and for lower angles of attack, respectively. Consequently, these cases do not show the "expected" flow separation behavior of well-tripped boundary-layer flow. The total height of the adhesive layer and the surface

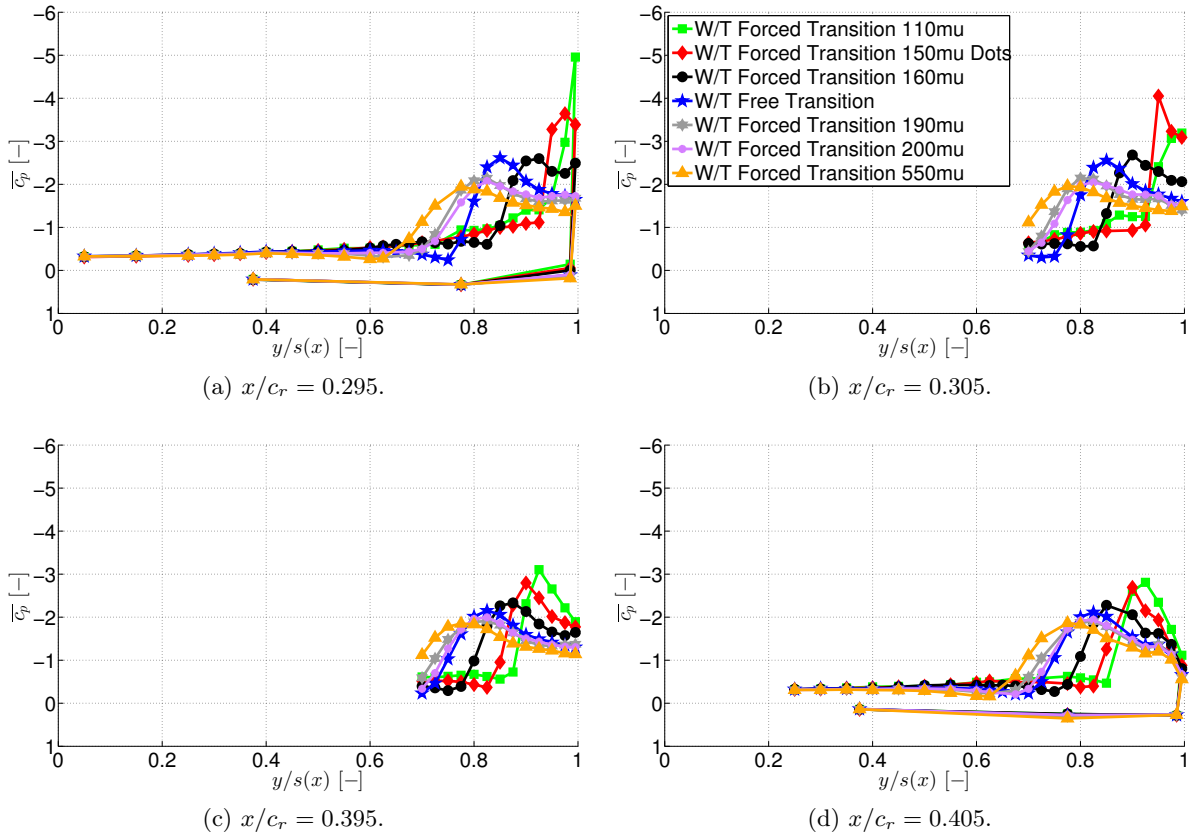


Figure 5.4: Leading-edge roughness effects at the AVT-183 configuration – Surface pressure coefficient \overline{c}_p versus semi-span $y/s(x)$ at $\alpha = 12^\circ$.

roughness is found to be too large. Therefore, the cases are characterized as "over-tripped". The result is a premature flow separation onset compared to the free transition case, which is directly induced by the trip strips itself. With respect to the requested turbulent boundary-layer conditions in the AVT-183 W/T investigations, these characteristics are not desired. Consequently, the target flow conditions are not met for those cases.

The other three trip-strip cases with reduced roughness height (W/T Forced Transition 110mu / 150mu Dots / 160mu), in contrast, lead to more useful characteristics, see Figure 5.4. The case W/T Forced Transition 110mu, for instance, shows attached flow with a large suction peak at the leading edge even for $\alpha = 12^\circ$ and $x/c_r = 0.295$, see Figure 5.4a. For the case W/T Forced Transition 150mu Dots, the flow separation currently takes place close to this chordwise section, as the suction peak is reduced and the vortex develops. Slightly more downstream at $x/c_r = 0.305$, see Figure 5.4b, the leading-edge vortex is formed with a suction peak located away from the leading edge. For the case W/T Forced Transition 110mu, the suction peak of the attached flow starts to decrease at this chordwise location, indicating the imminent appearance of the leading-edge vortex. More downstream at $x/c_r = 0.395$ and $x/c_r = 0.405$, both data sets then show a well-developed vortex flow, see Figure 5.4c and Figure 5.4d. Finally, the case W/T Forced Transition 160mu is regarded. At $x/c_r = 0.295$ and $x/c_r = 0.305$, the flow is

already separated, but compared to the free transition case, the suction peak is located more outboard. Subsequently, the separation point is delayed downstream as well. More downstream at $x/c_r = 0.395$ and $x/c_r = 0.405$, the grading corresponding to the roughness height can also be seen. The results of the case W/T Forced Transition 160mu fit between the free transition case and the above mentioned forced transition cases (110mu / 150mu Dots).

The analysis clearly points out the flow separation onset dependence on the roughness height. Figure 5.4 has demonstrated the effects of the different trip strips at $\alpha = 12^\circ$, but for other angles of attack, the same trends are observed accordingly. Therefore, a conclusion concerning the effects of varying leading-edge roughness at the AVT-183 configuration can be drawn. Focusing on the test cases with carborundum grit, a direct relation of flow separation and roughness height has been found. If the roughness height is chosen too large, however, the flow is threatened by over-tripping, which is associated with premature flow separation onsets. The trip-dot type, case W/T Forced Transition 150mu Dots, leads to results that are comparable to those of case W/T Forced Transition 110mu, despite the increased roughness height. The leading-edge contour, at which the application of surface roughness has been found to be crucial with regard to over-tripping, remains unchanged in this case. To adequately fulfill the requirement of reasonably-tripped, fixed turbulent boundary-layer flow at the wing surface of the AVT-183 W/T model, the two cases W/T Forced Transition 110mu and 150mu Dots are accordingly appropriate.

Figure 5.5 highlights the above discussed trends. For two chordwise sections, namely at $x/c_r = 0.295$ and $x/c_r = 0.395$, the minimum surface pressure coefficients of the corresponding sections and their spanwise positions are shown versus the angle of attack. In addition to the two appropriate cases (W/T Forced Transition 110mu / 150mu Dots), also the case W/T Free Transition and the over-tripped case W/T Forced Transition 550mu are considered for comparison. Attached flow is characterized in Figure 5.5b and Figure 5.5d by a value of $y/s(x)_{\overline{c_p, min}} \rightarrow 1$, which indicates the suction peak is located at the leading edge. For separated flow, this value decreases and shows the approximate spanwise position of the vortex core axis. Compared to the free transition case, the delayed flow separation onset of the reasonably-tripped cases is thereby emphasized. With increasing angle of attack, the location of the suction peak and hence, the vortex axis, moves further inboard, as the vortex grows in size and intensity. For the over-tripped case, in contrast, flow separation occurs at even lower angles of attack compared to the free transition case. The corresponding suction levels are shown in Figure 5.5a and Figure 5.5c, respectively. If an appropriate trip strip is applied, the suction peak of the attached flow increases with increasing angle of attack to considerably higher values, before the flow separation occurs. For even higher angles of attack, no distinct trend is observed, as three competing effects are present. On the one hand, the suction peak at the leading edge vanishes, which decreases the suction levels drastically. On the other hand, the suction peak of the emerged leading-edge vortex first increases with increasing angle of attack. Finally, vortex bursting effects move upstream, see Section 5.1.2, and the suction levels decrease again. The over-tripped case, in contrast, shows even more reduced suction levels for almost the entire angle-of-attack range.

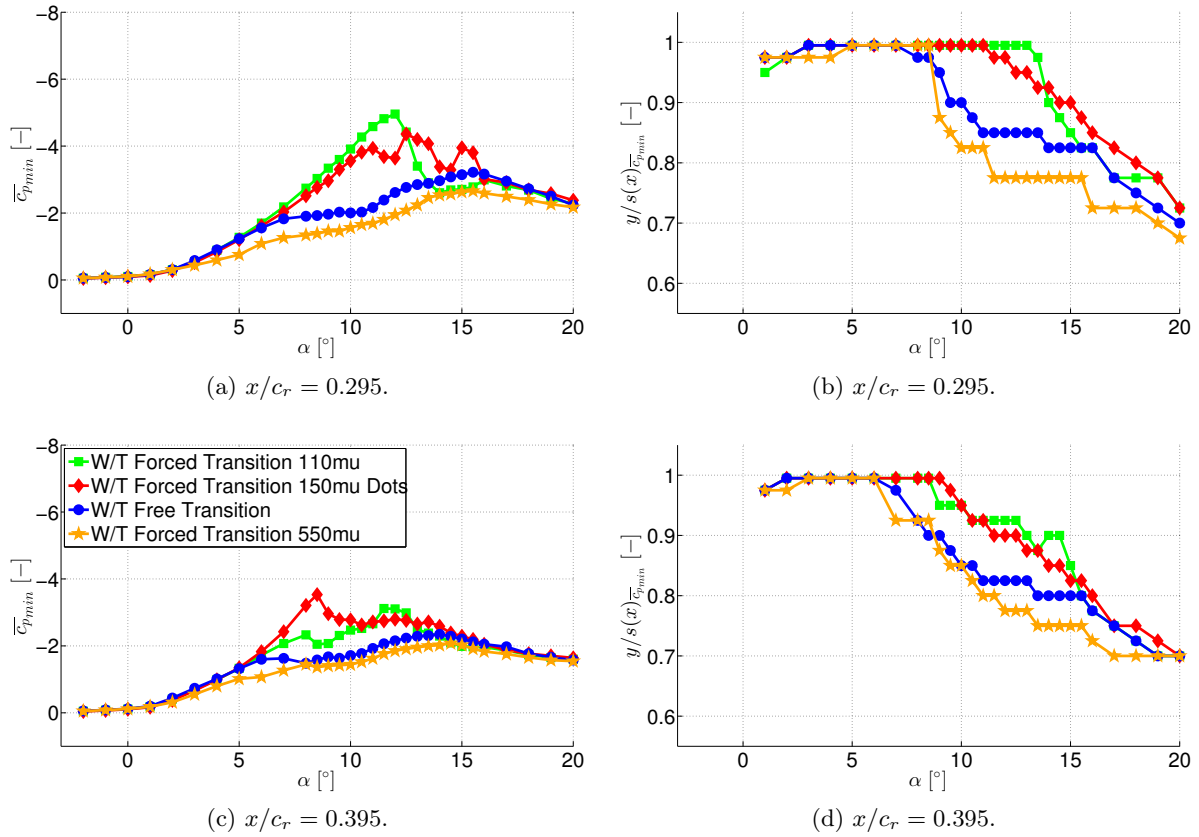


Figure 5.5: Leading-edge roughness effects at the AVT-183 configuration – Minimum surface pressure coefficient $\bar{c}_{p,min}$ and corresponding spanwise locations versus angle of attack α .

Short-Term Repeatability

The discussion of the longitudinal aerodynamic coefficients and the surface pressure coefficients as presented above rest upon mean data sets of several W/T runs. In each case, they were derived from three to four different measurements, which were conducted subsequently in one W/T campaign, respectively. Initial measurements on the AVT-183 configuration without any flow tripping showed a very good short-term repeatability in terms of aerodynamic coefficients and surface pressure coefficients. The results confirmed the overall validity of the measurement set-up and led to the mean data set of case W/T Free Transition, see Hövelmann et al. [68]. Due to the advent of trip strips at the leading edge to fix the boundary-layer transition, the analysis of the short-term repeatability becomes more relevant, as stable flow separation onset characteristics are desired. For this reason, the short-term repeatability of the AVT-183 W/T measurements is briefly evaluated and reviewed.

Figure 5.6 and Figure 5.7 present selected short-term repeatability results for the cases W/T Forced Transition 110mu and W/T Forced Transition 150mu Dots. The plots each depict the pitching-moment coefficient C_{my} versus the angle of attack, and the surface pressure coefficient distribution $c_p(y(s(x)))$ along the local semi-span at $\alpha = 14^\circ$ and $x/c_r = 0.405$. In case of the

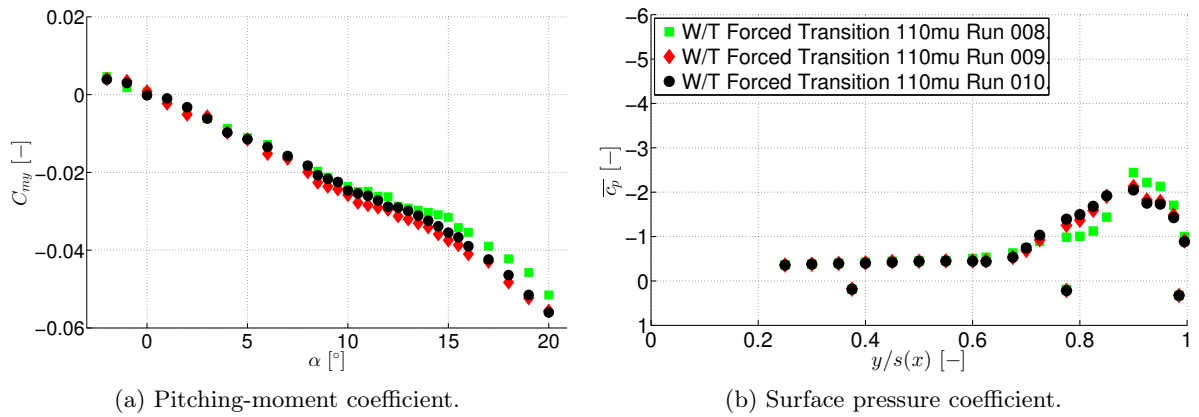


Figure 5.6: Short-term repeatability issues of case W/T Forced Transition 110mu — Pitching-moment coefficient C_{my} versus angle of attack α and surface pressure coefficient \bar{c}_p versus semi-span $y/s(x)$ at $\alpha = 14^\circ$ and $x/c_r = 0.405$.

single adhesive layer without additional carborundum particles (case W/T Forced Transition 110mu), the short-term repeatability of the W/T measurements becomes worse compared to the free transition case. In particular, the pitching-moment coefficient is influenced with increasing angle of attack, see Figure 5.6a. The surface pressure coefficients in Figure 5.6b also deviate from each other for subsequent W/T runs, thus showing a slightly different flow separation onset. The results indicate that the single adhesive layer changed its material properties, such as its characteristics in adhesion and elasticity, due to increasing ambient temperature in the W/T facility. Similar effects were also observed for the case W/T Forced Transition 190mu, which used the same type of a double-faced adhesive strip, but with carborundum particles. For this reason, the adhesive layer was modified for the related cases W/T Forced Transition 160mu and W/T Forced Transition 200mu, as a sprayed adhesive layer was applied instead. Then, the short-term repeatability again revealed very good results. Consequently, the short-term repeatability deficit of case W/T Forced Transition 110mu is directly linked to this observation. Especially at higher angles of attack, for which the trip strip is essential with respect to the flow separation onset, these characteristics are noted as disadvantageous.

Since for an appropriate flow tripping, however, the case W/T Forced Transition 110mu was rated "best" under the carborundum grit cases, another trip-strip method was sought for in the second campaign of the AVT-183 W/T investigations. It should improve the short-term repeatability and should show the same or similar vortex separation characteristics. Thereby, the trip dots came into focus of the experimental analyses. Similar flow separation onset characteristics have already been demonstrated above, and the effects on repeatability issues are highlighted in Figure 5.7. Compared to the latter case, the short-term repeatability of the W/T measurements is considerably improved. This time, the pitching-moment coefficient and the surface pressure coefficient distribution are reproduced very well by subsequent W/T polar runs. The flow separation onset is found to occur exactly at the same position for different measurements. The

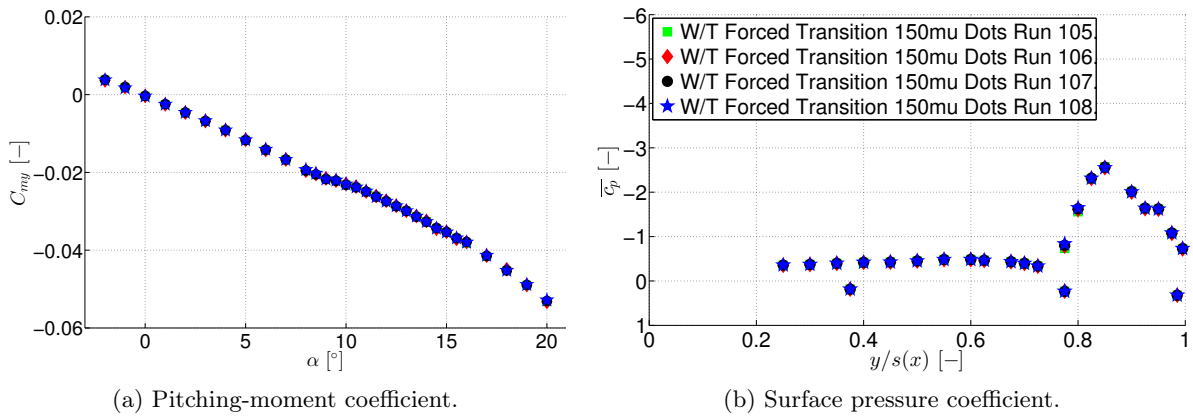


Figure 5.7: Short-term repeatability issues of case W/T Forced Transition 150mu Dots — Pitching-moment coefficient C_{my} versus angle of attack α and surface pressure coefficient \bar{c}_p versus semi-span $y/s(x)$ at $\alpha = 14^\circ$ and $x/c_r = 0.405$.

results thus emphasize the successful application of the trip dots at the AVT-183 W/T model. Based on the ordered structure, the definite position and the uncoated leading edge, much more reproducible characteristics are therefore observed. Overall, this leads to the conclusion that application of the trip dots (case W/T Forced Transition 150mu Dots) is preferable to the single adhesive layer (case W/T Forced Transition 110mu). Compared to the latter case, the short-term repeatability is extensively improved.

Long-Term Repeatability

In addition to the short-term analyses, the long-term measurement repeatability was also assessed within the AVT-183 W/T investigations. It is defined as the repeatability of the same test case, but measured within different W/T campaigns. In concordance with the preceding discussion of leading-edge roughness effects, this analysis again refers to mean data sets, which were averaged according to subsequent runs in the corresponding W/T campaigns. Needless to say, the model was dismounted at the end and remounted at the beginning of each W/T entry, respectively. Moreover, the trip strips were removed in each case and were reapplied in the following W/T campaign. Thereby, not only the long-term changes of the overall W/T facility set-up, but also model installation effects in the test section and trip-strip application differences can be assessed. The case W/T Free Transition was considered first in each W/T campaign, and the results showed a very good long-term repeatability of the measurements [68]. Overall, this again confirms the general validity of the present W/T experiments, also in terms of a long-term perspective.

Here, the discussion concentrates on the case W/T Forced Transition 150mu Dots, see Figure 5.8. Overall, the agreement between the results derived from different W/T entries is very satisfying. The pitching-moment coefficient curves in Figure 5.8a show an excellent agreement, and the spanwise pressure coefficient distributions almost coincide with each other, see Figure 5.8b. The agreement is also valid for other chordwise sections and angles of attack, respectively.

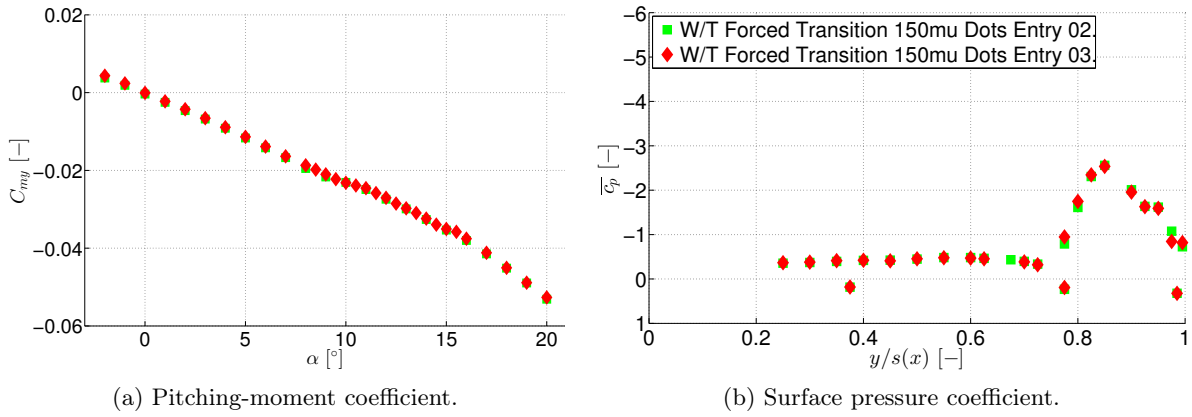


Figure 5.8: Long-term repeatability issues of case W/T Forced Transition 150mu Dots — Pitching-moment coefficient C_{my} versus angle of attack α and surface pressure coefficient \bar{c}_p versus semi-span $y/s(x)$ at $\alpha = 14^\circ$ and $x/c_r = 0.405$.

Moreover, the drag coefficient characteristics are predicted equally to each other. Consequently, the long-term repeatability of the longitudinal aerodynamic coefficients and the surface pressure coefficients is rated excellent for the case W/T Forced Transition 150mu Dots. Since the trip dots had to be removed between the second and the third W/T campaign due to test measurements with a coated W/T model for subsequent flow field analyses, the obtained results are valued even higher. They further indicate that the trip dots were applied very accurately in each W/T campaign, thus leading to equivalent boundary-layer characteristics over different W/T entries.

In summary, the entire analysis demonstrates that the trip dots represent the most reasonable trip-strip case that was tested in the experimental investigations. As a result of the excellent measurement repeatability and the desired flow separation onset characteristics, the case W/T Forced Transition 150mu Dots was therefore selected for the target flow conditions. For the subsequent flow field investigations, it was thus considered exclusively as flow tripping method. Furthermore, the same trip-strip layout was consequently chosen for the W/T experiments of the SAGITTA configuration, see Section 3.3.5.

5.1.2 Flow Physics Analysis

The near-wall flow field characteristics of the AVT-183 configuration are considered next. The angle of attack of $\alpha = 12^\circ$ and the target flow conditions (case W/T Forced Transition 150mu Dots) are relevant for the discussion. The focus is laid on the analysis of the leading-edge vortex formation and progression. In this context, both time-averaged values and fluctuating quantities are regarded, which originate from Stereo PIV and HWA measurements, and from surface pressure measurements. The unsteady surface pressures, however, refer to results of the case W/T Forced Transition 110mu, because the Kulite data is exclusively available for this trip-strip case. The approach is feasible, as very similar flow separation characteristics have been observed in comparison to the target flow conditions, see Section 5.1.1.

Mean Near-Wall Flow Field Characteristics

Figure 5.9 depicts an overview of the partly-developed leading-edge vortex, which is present on the AVT-183 configuration at $\alpha = 12^\circ$. Time-averaged results of the mean axial vorticity component $\bar{\omega}_x$ and the mean absolute velocity \bar{V} are shown as non-dimensional values for selected chordwise sections. The leading-edge vortex formation at approximately mid-chord locations and its progression on the diamond wing configuration are clearly noticed. The corresponding pressure distributions on the wing surface are summarized in Figure 5.10. In six selected chordwise sections of the surface pressure measurements, corresponding time-averaged results are plotted along the semi-span of the AVT-183 configuration. The colored circle symbols further highlight the mean values derived from the eight unsteady Kulite pressure transducers. Attached flow can be observed in the first two measurement sections at $x/c_r = 0.1$ and $x/c_r = 0.2$. The flow separation onset occurs slightly upstream of $x/c_r = 0.295$, where the leading-edge suction peak decreases and the minimum pressure coefficient starts to move slightly inboard. At $x/c_r = 0.405$, the leading-edge vortex is clearly noticed. The corresponding suction peak at the vortex core axis is about $c_{p,min} \approx -3$. Hence, the partly-developed leading-edge vortex is thereby emphasized. More downstream at $x/c_r = 0.5$ and $x/c_r = 0.6$, the vortex axis moves further inboard. The vortex considerably expands in spanwise direction and the suction levels drastically decrease. Consequently, this behavior indicates the existence of vortex breakdown, which is already relevant for the AVT-183 configuration at $\alpha = 12^\circ$.

To demonstrate the vortex breakdown characteristics in more detail, related sectional plots of the near-wall flow field data are discussed in the following, see Figure 5.11 and Figure 5.12. The axial vorticity component is considered first, see Figure 5.11a to Figure 5.11f. At $x/c_r = 0.1$ to $x/c_r = 0.295$, increased levels are mainly observed close to the wall in the attached boundary-layer region. By way of example, this shows the ability of the current Stereo PIV set-up to measure the flow field quantities in the vicinity of the diamond wing surface. Due to the proximity of the W/T floor, however, some imperfections are noticed in the flow field data of the most

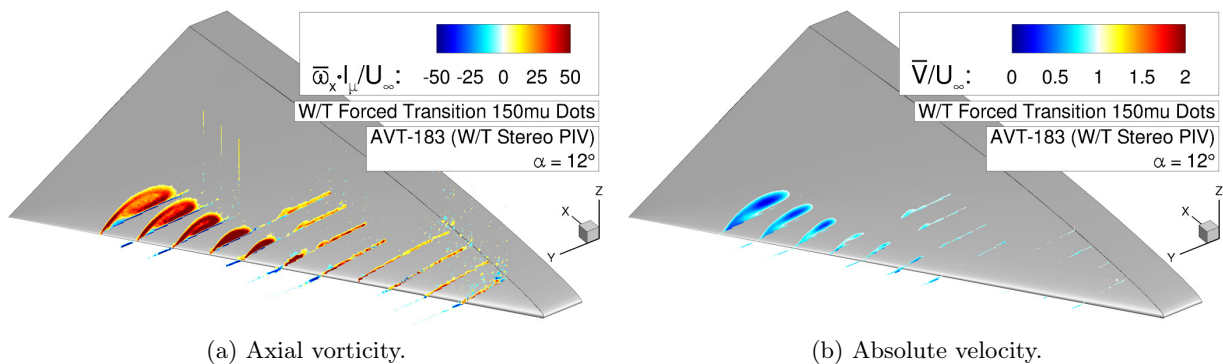


Figure 5.9: Flow physics analysis of the AVT-183 configuration – Axial vorticity contours $\bar{\omega}_x \cdot l_\mu / U_\infty$ and absolute velocity contours \bar{V} / U_∞ at $\alpha = 12^\circ$.

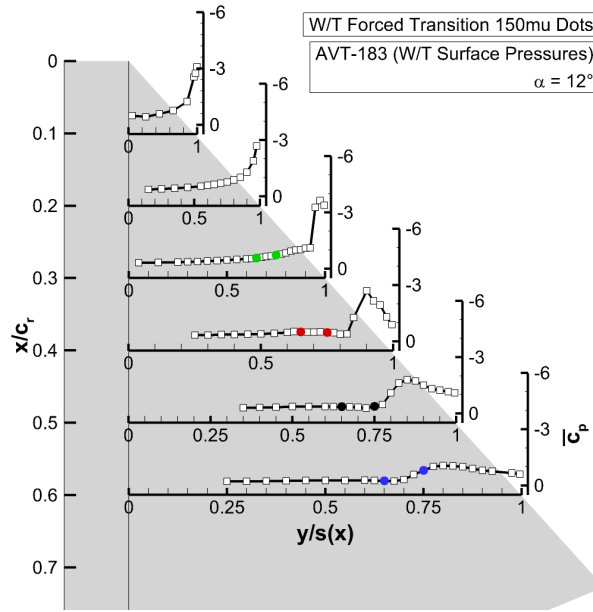


Figure 5.10: Flow physics analysis of the AVT-183 configuration – Surface pressure coefficient \bar{c}_p versus semi-span $y/s(x)$ at $\alpha = 12^\circ$.

upstream wing sections. They arise from reflections that could not be avoided, but considerably be minimized, see Section 3.4.3. The flow separation onset close to $x/c_r = 0.295$, as shown in Figure 5.10, is only hardly noticeable in the corresponding plot of the axial vorticity component, see Figure 5.11c, since the emanating vortex structure is still very small. At $x/c_r = 0.405$, the leading-edge vortex is then clearly visible as a large-scale structure, see Figure 5.11d. More downstream at $x/c_r = 0.5$ and $x/c_r = 0.6$, the axial vorticity component of the leading-edge vortex starts to decrease in the vortex core region, see Figure 5.11e and Figure 5.11f. The high vorticity levels of the separating shear layer close to the leading edge, in contrast, are even more pronounced. Due to the chosen measurement field of view, the vorticity content of the attached boundary layer inboard of the leading-edge vortex is only noticeable up to the chordwise section of $x/c_r = 0.405$. There, the boundary layer is slightly thickened at its outboard end, which results more downstream in a weak vortex structure. It is referred to as "inner vortex" and has the same rotation direction as the leading-edge vortex. Moreover, the structure is of similar type as observed in the VFE-2 investigations of the related research task group AVT-113 [43, 93]. In this thesis, the characteristics of the "inner vortex" are discussed in more detail in Section 5.2, where the numerical investigations of the AVT-183 configuration are presented.

The corresponding cross-section plots of the absolute velocity are shown in Figure 5.11g to Figure 5.11l. At $x/c_r = 0.405$, both the leading-edge vortex and the weak "inner vortex" are observed, see Figure 5.11j. Compared to the free stream velocity U_∞ , the vortex core velocities are already retarded and show a wake-type character. Above the leading-edge vortex, a region of accelerated flow is noticed, which is driven by the rotation energy of the vortical structure. More downstream at $x/c_r = 0.5$ and $x/c_r = 0.6$, the leading-edge vortex grows in size, and the

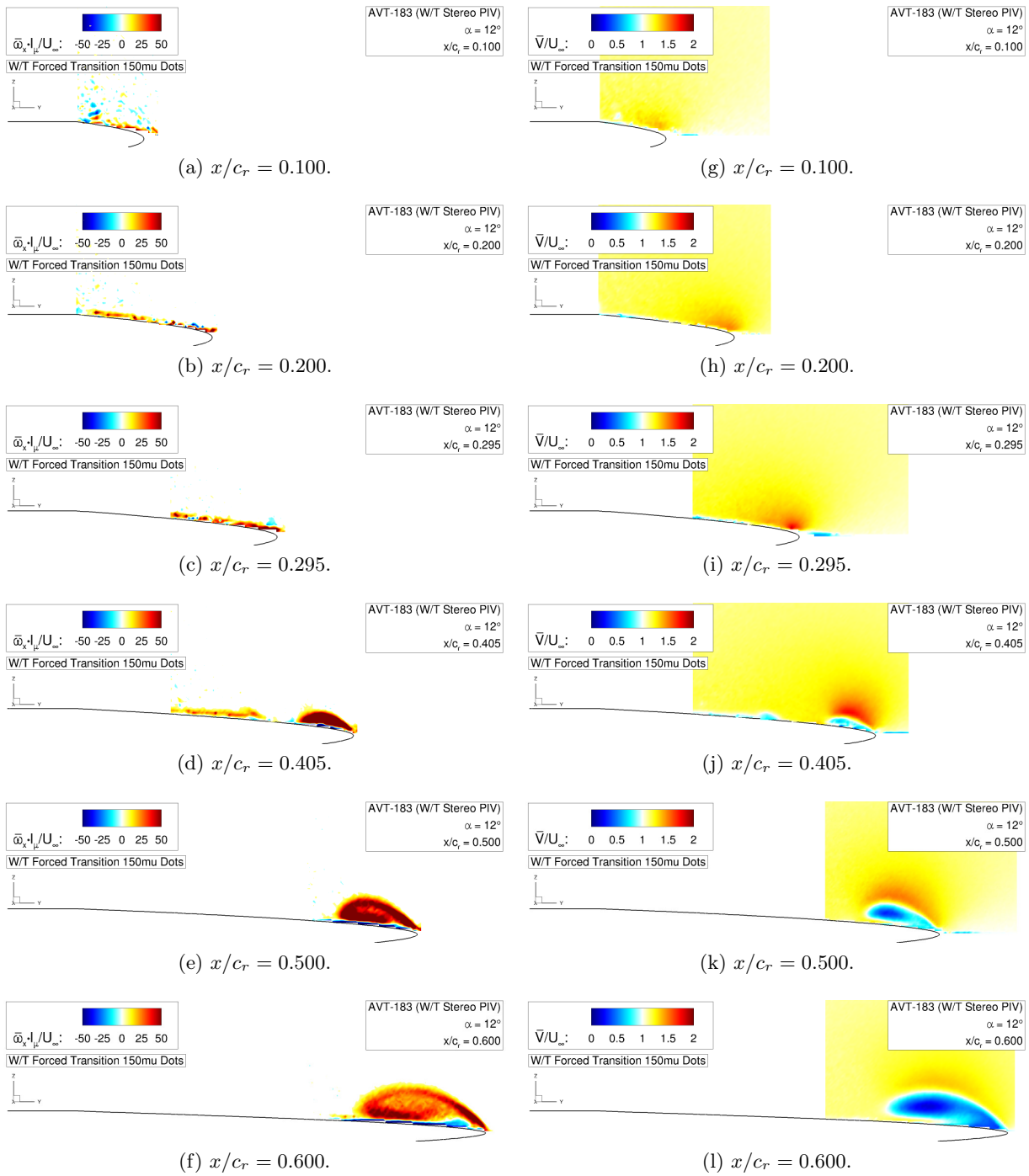


Figure 5.11: Flow physics analysis of the AVT-183 configuration – Axial vorticity contours $\bar{\omega}_x \cdot l_\mu / U_\infty$ and absolute velocity contours \bar{V} / U_∞ at $\alpha = 12^\circ$.

vortex axis moves inboard and upwards. Furthermore, the vortex core velocity is significantly reduced when moving downstream. This is directly linked to the phenomenon of vortex bursting as introduced above for the surface pressure coefficient distribution. At $x/c_r = 0.6$, almost the entire cross-section of the leading-edge vortex is dominated by a strong wake-type axial flow.

Analysis of Partly-Developed Leading-Edge Vortices

Figure 5.12 depicts the time-averaged lateral and normal velocity components gathered from the Stereo PIV measurements. The latter plots additionally contain information on the sectional contour (pseudo) streamlines. The location of the vortex axis in spanwise direction and normal to the diamond wing surface can thereby be analyzed. Figure 5.12a to Figure 5.12f emphasize

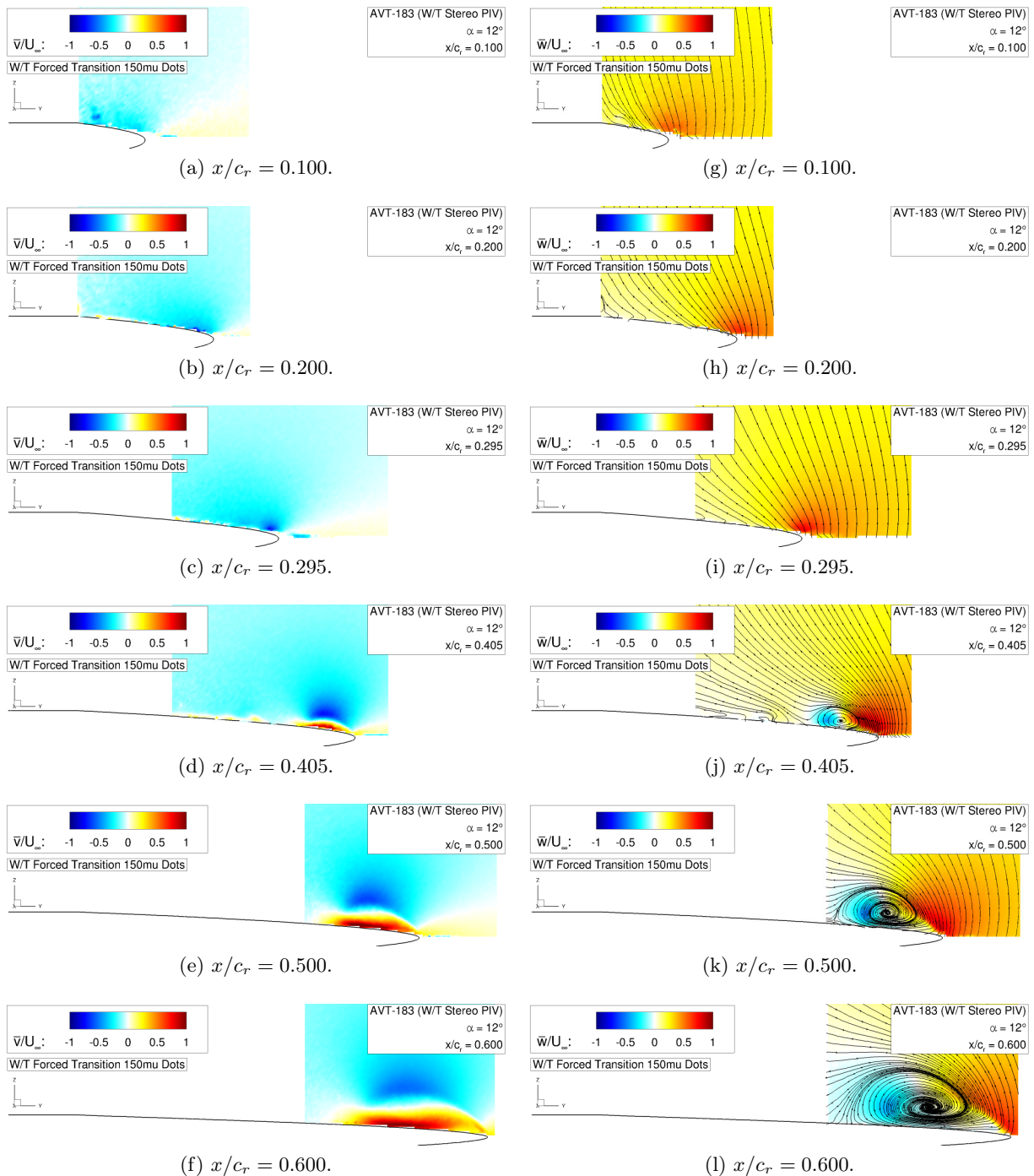


Figure 5.12: Flow physics analysis of the AVT-183 configuration – Lateral velocity component contours \bar{v}/U_∞ and normal velocity component contours \bar{w}/U_∞ at $\alpha = 12^\circ$.

that the flow is directed inboard above the vortex axis, and it points outboard towards the leading edge between the vortex axis and the diamond wing surface. Close to the wall, the lateral velocity component is increased up to approximately the free stream velocity, thus leading to the suction levels in the surface pressure coefficient distributions, see Figure 5.10. The normal velocity component shows a respective pattern for all considered chordwise sections, see Figure 5.12g to Figure 5.12l. The rotation of the flow is further highlighted by the contour streamlines. Upstream and in the vicinity of the flow separation onset at $x/c_r = 0.1$ to $x/c_r = 0.295$, the attached flow around the leading edge leads to increased normal velocity components in this region. Downstream of the flow separation onset, the leading-edge region is still dominated by increased normal velocity component values. This is due to the separating shear layer and the vortex induction close to the leading edge. The rotation of the vortical structure itself can explicitly be observed, and inboard of the vortex axis, negative normal velocity components are accordingly present.

Turbulent Near-Wall Flow Field Characteristics

The time-dependent quantities are examined in the following. Figure 5.13 depicts the power spectral densities of resulting pressure coefficient fluctuations versus the reduced frequency. The spectra were truncated at the low-pass cut-off frequency, which corresponds to a non-dimensional value of $k_{red} \approx 15$. Furthermore, a linear averaging over 1024 bands was applied in the spectral analyses. All unsteady pressure taps are regarded, and the respective line colors relate the curves to the chordwise locations on the W/T model, see Figure 5.10. Therein, one can notice that the Kulites are mostly located inboard of the leading-edge vortex trajectory. The influence of the vortical structure on the spectral characteristics is therefore significant only at certain pressure tap locations. The corresponding fluctuating results show in general higher levels of the power spectral density function at $y/s(x) = 0.750$ than more inboard at $y/s(x) = 0.650$, see Figure 5.13a and Figure 5.13b. The increased values are particularly noticed for the more downstream Kulite positions with $x/c_r \geq 0.405$, where the leading-edge vortex apparently impacts the spectral

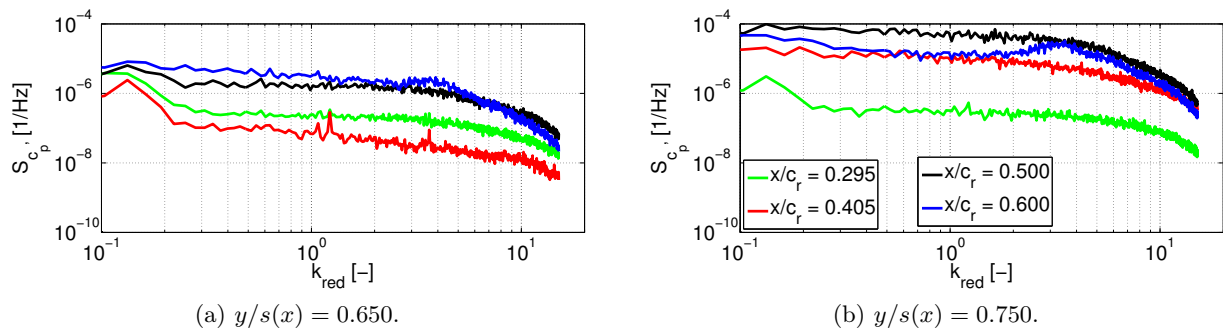


Figure 5.13: Flow physics analysis of the AVT-183 configuration – Power spectral densities of unsteady surface pressure fluctuations at $\alpha = 12^\circ$.

characteristics. The spectra at $x/c_r = 0.295$, in contrast, do not differ significantly, and the occurring flow separation onset is not relevant for the fluctuating surface pressures in this section. The most pronounced surface pressure fluctuations and the existence of a "dominant frequency" are observed for $x/c_r = 0.600$ and $y/s(x) = 0.750$, as increased levels are present around a reduced frequency of $k_{red} \approx 3.6$ ($f \approx 239 \text{ Hz}$). Since the pressure tap in this case is located directly under the leading-edge vortex trajectory, the spectral characteristics are attributed to the occurring vortex bursting. The corresponding energy concentration of the limited frequency band further gives indication that the "peak" is linked to the helical mode instability of the breakdown flow. This conclusion is made based on published data that focused on unsteady flow phenomena of leading-edge vortices. Gursul et al., for instance, classified the helical mode instability in this reduced frequency range [48], and Breitsamter showed respective results for a moderately-swept delta wing configuration [17]. In the present case, however, the energy concentration does not occur as narrow due to the relatively weak vortex structure emanating from the rounded leading-edge contour. Hence, the leading-edge radius does not only impact the vortex formation and progression, but also the resulting spectral characteristics of occurring unsteady flow phenomena.

Related results of the turbulent kinetic energy k in the near-wall flow field are shown in Figure 5.14. A logarithmic contour scale has been chosen for the plots, and three different chordwise sections are regarded, at which the leading-edge vortex has already emerged. This time, both the results obtained from the Stereo PIV measurements and the HWA measurements are presented, respectively. On the one hand, the Stereo PIV results provide a large measurement plane with high spatial discretization in each cross-section, but they are limited with respect to the number of PIV raw images available and the temporal resolution relevant for spectral analyses. On the other hand, the HWA measurements are limited with respect to the number of measurement points, but they provide an excellent time resolution with 19200 values per time series in the present analyses. For this reason, both data sources are used for the subsequent discussion. Considering the Stereo PIV results, the obtained contour fields appear to be slightly noisy. This is due to the aforementioned low time resolution and the rather few PIV raw images available, which results in a limited length of the time series. The leading-edge vortex, however, is still depicted down to the diamond wing surface, see Figure 5.14a to Figure 5.14c. The resulting values of the turbulent kinetic energy observed within the leading-edge vortex are up to two orders of magnitude larger than the corresponding values far off the wing surface. Moreover, the local turbulence maxima are found to decrease in downstream direction, which is consistent with corresponding numerical findings on the AVT-183 configuration by Frink [38]. This implies that vortex bursting has already become relevant at the chordwise position of $x/c_r = 0.405$, which is approximately $\Delta x/c_r \approx 0.1$ downstream of the first appearance of the leading-edge vortex in the surface pressure distributions. The instantaneous retardation of the axial vortex core flow as introduced in Figure 5.11j is thus consistent. Consequently, it seems that no typical developed leading-edge vortex emerges, but a vortical structure that immediately shows vortex bursting tendencies after its large-scale formation. Compared to the flow field characteristics of slender

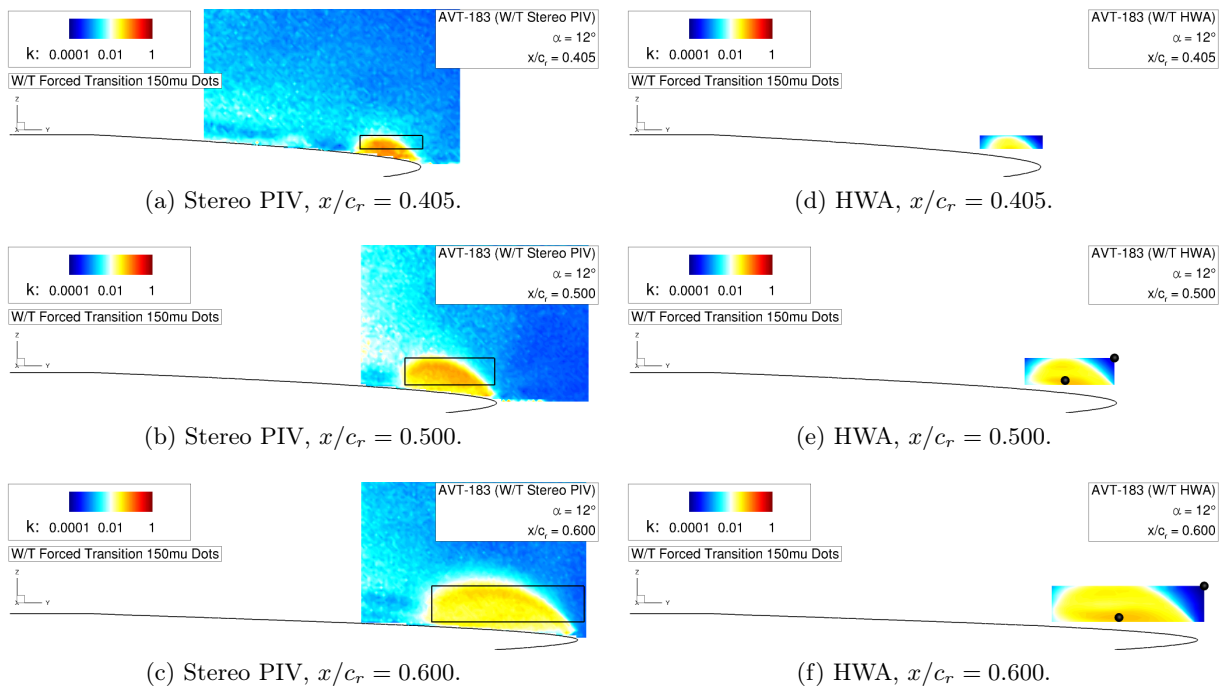


Figure 5.14: Flow physics analysis of the AVT-183 configuration – Turbulent kinetic energy contours k at $\alpha = 12^\circ$.

wings, vortex breakdown is thus observed to be less abrupt, but instantaneously present. The exact location of the vortex bursting is challenging to define. The present results thereby show agreement with observations for respective wing configurations with reduced wing sweep, see Gursul et al. [48]. Responsible for these phenomena are both the moderate leading-edge wing sweep and the rounded leading-edge contour. Based on the surface pressure distribution alone, as presented in Figure 5.10, the obtained flow field characteristics are not obvious at first sight.

The HWA measurements yield very similar turbulent near-wall flow field characteristics in comparison to the Stereo PIV results, see Figure 5.14d to Figure 5.14f. A good agreement is found with respect to the spatial extent of the leading-edge vortex and the increase of the turbulent kinetic energy around the separating shear layer. The effects of the increased length of the time series, the hot-wire measurements are based on, is immediately noticed in the results, as the contour plots show smooth but distinct gradients. Due to the size of the cross-wire probes, the HWA measurements were however not able to capture the flow field at the curved leading-edge contour down to the diamond wing surface. For this reason, the leading-edge vortex is not completely resolved at the chordwise location of $x/c_r = 0.405$, see Figure 5.14d. The local turbulence maximum is not displayed, and it is assumed to be located slightly closer to the wall. In the more downstream cross-sections at $x/c_r = 0.500$ and $x/c_r = 0.600$, in contrast, the local turbulence maxima are noticed, see Figure 5.14e and Figure 5.14f. Compared to the Stereo PIV results, see Figure 5.14b and Figure 5.14c, the peak values are slightly lower and their locations within the leading-edge vortex are different. The HWA results indicate turbulence maxima that

are closer to the diamond wing surface. In addition, typical annular structures of local maximum turbulent kinetic energy values are observed by the hot-wire measurements, which again reveal the existence of vortex bursting. The differences in turbulence maxima magnitude and location can be the result of several aspects. On the one hand, they may be a consequence of the limited Stereo PIV data and the reduced time resolution, for which the final results do not represent the local turbulence distribution in all details. On the other hand, slight probe mount interferences in the HWA measurements could also contribute to a minor shift of the leading-edge vortex trajectory. This would then affect the fluctuating quantities as well, finally leading to different local turbulence distributions in the considered chordwise sections.

Due to the low Stereo PIV sample rate, spectral analyses were therefore conducted for the HWA measurements only. Figure 5.15 and Figure 5.16 demonstrate selected results in two chordwise sections, namely at $x/c_r = 0.500$ and $x/c_r = 0.600$. The power spectral densities of the velocity fluctuation components are considered at locations close to the local turbulence maxima and outside of the leading-edge vortex, respectively. The exact positions can be observed by the bullets as shown in Figure 5.14e and Figure 5.14f. For the subsequent discussion, one should bear in mind that the logarithmic scale of the plots in Figure 5.15 and Figure 5.16 differs by two orders of magnitude, to provide a better plot scaling in each case. As it can be expected, the levels of the power spectral density function are much higher in the leading-edge vortex than outside of it. The levels of the axial velocity fluctuations are the highest, compared to the lateral and the normal components, see Figure 5.15. For a reduced frequency of $k_{red} \approx 0.3$, which corresponds to a frequency of $f \approx 20 \text{ Hz}$, peaks can be seen for all three velocity fluctuation components. Their origin, however, can not surely be attributed to a certain flow-physical phenomenon. At $x/c_r = 0.600$, increased levels are also noticed in the present spectra around a reduced frequency of $k_{red} \approx 4.3$ ($f \approx 285 \text{ Hz}$), but the three velocity components peak at slightly different reduced frequencies, see Figure 5.15b. Compared to the power spectral density analysis of the unsteady surface pressures, see Figure 5.13b, similar "dominant frequencies" are thus present. Consequently, the velocity fluctuation components again indicate the helical mode

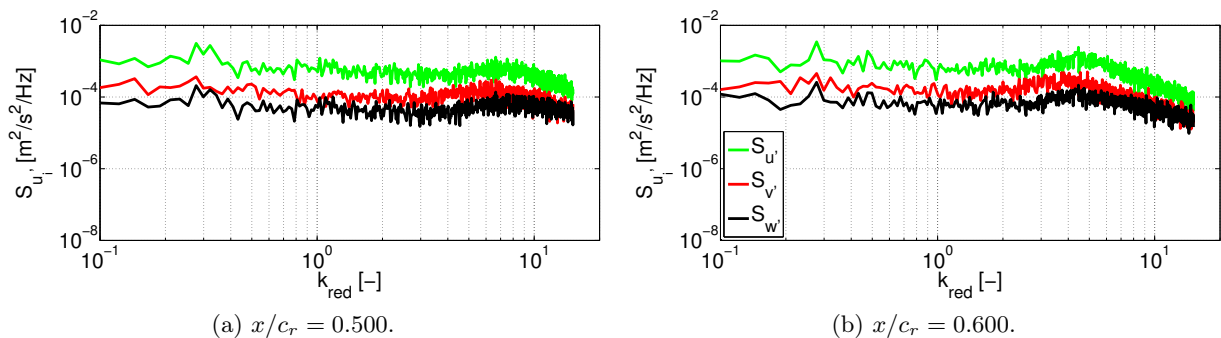


Figure 5.15: Flow physics analysis of the AVT-183 configuration – Power spectral densities of velocity fluctuations at $\alpha = 12^\circ$ close to local turbulence maxima. The locations can be observed from Figure 5.14e and Figure 5.14f.

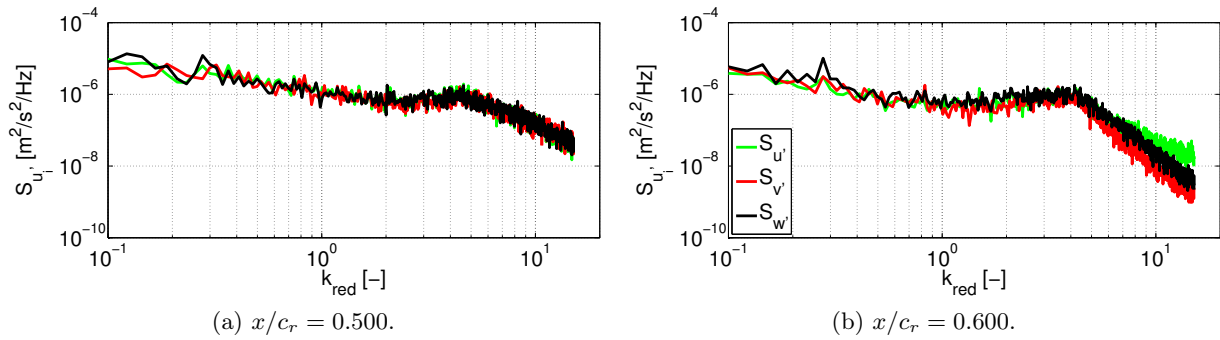


Figure 5.16: Flow physics analysis of the AVT-183 configuration – Power spectral densities of velocity fluctuations at $\alpha = 12^\circ$ outside of the leading-edge vortex. The locations can be observed from Figure 5.14e and Figure 5.14f.

instability of the breakdown flow. With increasing reduced frequencies, the spectral values in both chordwise sections decrease and are cut off at the low-pass filter frequency.

The spectral analyses of the other two probe positions, which are located outside of the leading-edge vortex, show considerably reduced levels of power spectral densities, see Figure 5.16. The velocity fluctuation components do not differ between each other as observed before, and the peak frequency at $k_{red} \approx 0.3$ is observed again in both chordwise sections. The reduction in the spectral energies with increasing reduced frequencies is more pronounced in this case, thus showing typical spectral characteristics of ordinary turbulent flow.

5.1.3 Longitudinal Aerodynamic Coefficients

Finally, the longitudinal aerodynamic coefficients associated with the target flow conditions are summarized. The lift, drag, and pitching-moment coefficient characteristics are considered for the entire angle-of-attack polar, which links the results to the preceding flow physics analysis. Therefore, the effects of the partly-developed leading-edge vortex on the overall aerodynamic characteristics are evaluated.

Lift Coefficient Characteristics

Figure 5.17a depicts the experimental lift coefficient curve versus the angle of attack. Linear lift coefficient characteristics are present, and the stall angle of attack is not reached before the measurement point at $\alpha = 20^\circ$. A distinct non-linear lift increase due to leading-edge vortex suction is not visible, which is typical of the present type of wing configuration. Due to the reduced wing sweep and the rounded leading-edge contour, the occurring partly-developed leading-edge vortex is relatively weak. In consequence, the integral lift coefficient characteristics are not impacted to a great extent. The flow-physical effects induced by the vortical structure become more obvious in the lift slope $C_{L,\alpha}$, see Figure 5.17b. For low positive angles of attack up to $\alpha = 7^\circ$, the lift slope slightly increases due to the increasing leading-edge suction levels of the

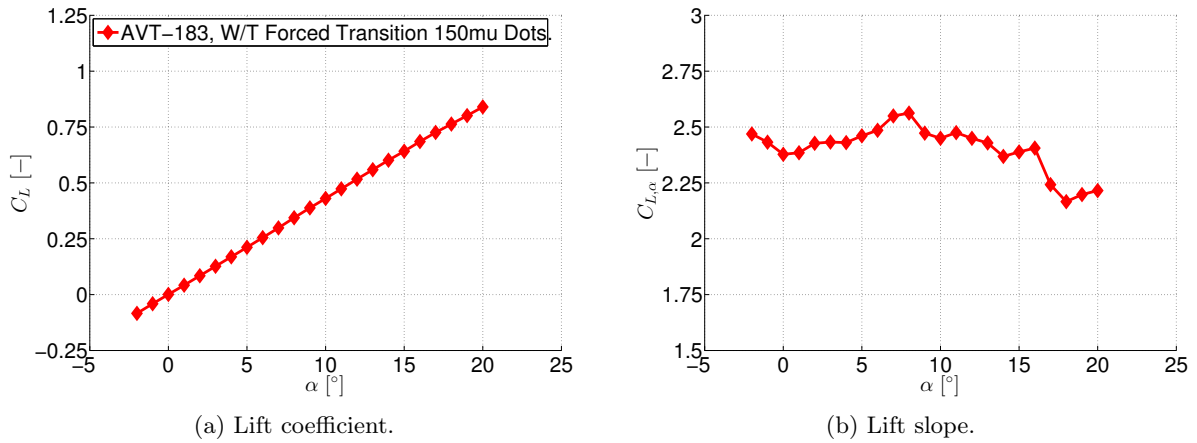


Figure 5.17: Longitudinal aerodynamic characteristics of the AVT-183 configuration — Lift coefficient C_L and derivative $C_{L,\alpha}$ versus angle of attack α .

initially-present attached flow. Then, the leading-edge vortex forms in the outboard wing section and moves upstream with increasing angle of attack. The lift slope slightly decreases again, since the contribution of the leading-edge vortex suction along the vortex axis cannot compensate the leading-edge suction of the disappearing attached flow regions. For higher angles of attack with $\alpha > 16^\circ$, this effect is strengthened, as the upstream-moving vortex breakdown phenomena, which have been introduced in the latter section, also contribute to the lift slope reduction. As a result, a lift slope value of approximately $C_{L,\alpha} \approx 2.2$ is finally observed at $\alpha = 20^\circ$.

Drag Coefficient Characteristics

The drag coefficient characteristics are summarized in Figure 5.18. Overall, the drag polar shows the typical appearance, see Figure 5.18a. The corresponding zero-lift drag coefficient results in $C_{D,0} = 0.0067$. With increasing angle of attack, the parabolic drag increase is noticeable. Figure 5.18b depicts the Lilienthal polar. Additionally, a reference line is plotted for comparison, which is tangential to the Lilienthal polar at the angle of attack of $\alpha = 4^\circ$. There, the maximum lift-to-drag ratio of $(C_L/C_D)_{max} = 14.28$ and the minimum glide angle of $\epsilon_{min} = 4.01^\circ$ are found. For the target flow conditions at $\alpha = 12^\circ$, the aerodynamic coefficients result in values of $C_L = 0.517$ and $C_D = 0.080$, respectively. This corresponds to a lift-to-drag ratio of $(C_L/C_D)_{\alpha=12^\circ} = 6.47$, and the respective value of k in the parabolic drag polar is $k_{\alpha=12^\circ} = 0.274$.

Pitching-Moment Coefficient Characteristics

The pitching-moment characteristics are finally reviewed in Figure 5.19a. With respect to the chosen pitching-moment reference point at the quarter section of the mean aerodynamic chord, the curve monotonically decreases for the considered angle-of-attack range. At $\alpha = 12^\circ$, a pitching-moment coefficient value of $C_{my} = -0.027$ is observed. In contrast to the lift coefficient curve, the C_{my} values visibly become non-linear with increasing angle of attack. This is highlighted

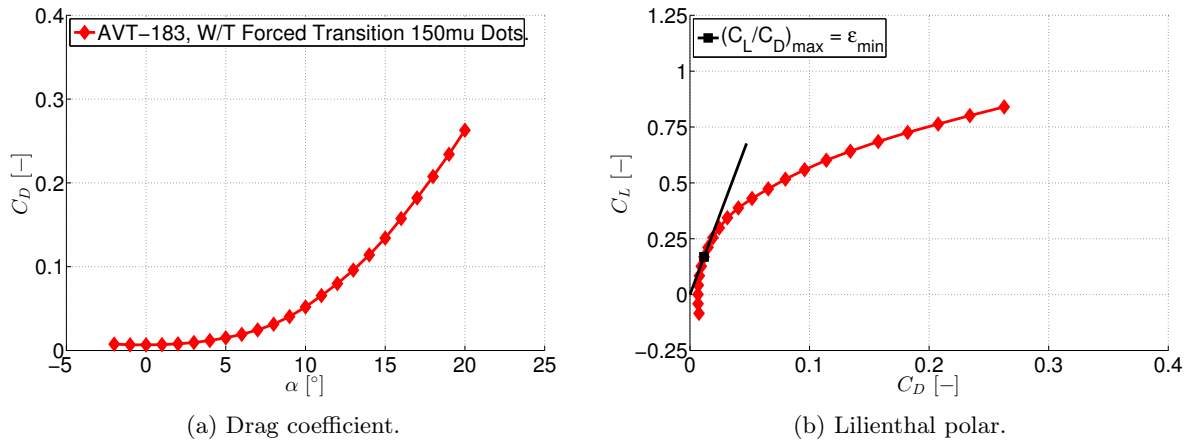


Figure 5.18: Longitudinal aerodynamic characteristics of the AVT-183 configuration — Drag coefficient C_D versus angle of attack α and Lilienthal polar C_L versus C_D .

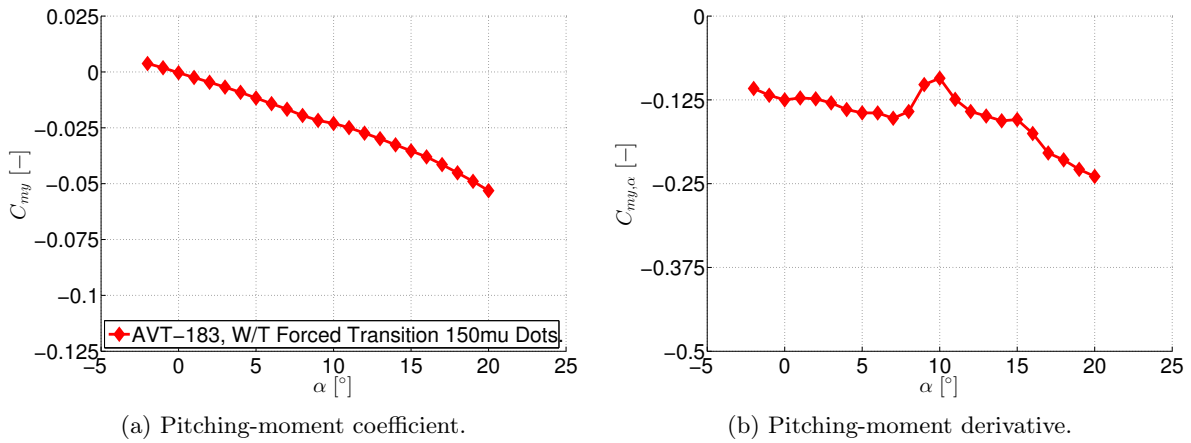


Figure 5.19: Longitudinal aerodynamic characteristics of the AVT-183 configuration — Pitching-moment coefficient C_{my} and derivative $C_{my,\alpha}$ versus angle of attack α .

in Figure 5.19b, which shows the pitching-moment derivative $C_{my,\alpha}$. In general, the derivative decreases over the angle-of-attack polar, but the trend is intercepted between $8^\circ \leq \alpha \leq 10^\circ$, for which a pronounced increase is noticed. Overall, the observed characteristics are the result of the occurring partly-developed leading-edge vortex. At the mentioned angles of attack, the surface pressure distributions on the wing surface change with areas of increased and decreased suction that are located up- and downstream of the pitching-moment reference point. When the vortical structure occurs in the outboard wing section at $\alpha \approx 8^\circ$, the derivative is temporarily influenced, since the outboard leading-edge suction is diminished and replaced by the emanating leading-edge vortex. For $\alpha \geq 10^\circ$, the derivative decreases again, since the flow separation onset moves upstream and the vortex suction along the core is intensified. For angles of attack of $\alpha \geq 16^\circ$, the derivative finally decreases more distinctly. Hence, not only the upstream-moving flow separation onset, but also the upstream-moving vortex breakdown influences the pitching-moment characteristics. With increasing angle of attack, this becomes particularly visible.

5.1.4 Synthesis

The leading-edge vortex formation and progression on the AVT-183 configuration have been presented in this section by experimental analyses. First, leading-edge roughness effects have been considered, from which reasonably-tripped boundary-layer characteristics have been derived. Then, the flow physics has been discussed for the occurring partly-developed leading-edge vortex, and the longitudinal aerodynamic coefficients have been evaluated. In sum, one can conclude:

Leading-Edge Roughness Effects

- The experimental results show that the flow separation onset and the partly-developed leading-edge vortex are very sensitive to the surface roughness and any contour modification at the diamond wing leading edge. Compared to the free transition case, both "over-tripped" and reasonably-tripped cases are identified, as varying flow separation onset characteristics are present, respectively.
- The case W/T Forced Transition 150mu Dots is selected as the baseline. Together with the free stream values ($Re_\infty = 2.7 \cdot 10^6$ and $Ma_\infty = 0.15$), it represents the target flow conditions, which were relevant for subsequent flow field investigations. With respect to the considered flow tripping cases, the trip dots show the most reasonable characteristics in terms of leading-edge vortex separation according to "fully"-turbulent boundary-layer flow, which was requested in the present W/T investigations. Moreover, this case shows excellent measurement repeatability, both in a short-term and a long-term perspective.

Flow Physics Analysis

- The flow field is characterized by a partly-developed leading-edge vortex, which originates from a smooth surface separation on the upper wing surface due to the rounded leading-edge contour. At $\alpha = 12^\circ$, the leading-edge vortex formation occurs at approximately $x/c_r \approx 0.300$, and more upstream, attached flow is present.
- The time-averaged results in the mean near-wall flow field demonstrate that the leading-edge vortex is mostly characterized by wake-type vortex core flow with $\bar{V}/U_\infty \leq 0.8$. Corresponding core values of the mean axial vorticity quickly decrease as well after the large-scale appearance of the leading-edge vortex ($\overline{\omega_x} \cdot l_\mu/U_\infty \leq 130$). Consequently, the vortical structure immediately shows vortex bursting tendencies. It is characteristic of this type of moderately-swept wing configuration with rounded leading-edge contour.
- The fluctuating quantities indicate that the highest local turbulence maxima are already observed close behind the leading-edge vortex formation. Respective values of the turbulent kinetic energy are in the order of $k \approx 0.1$. Further downstream and towards the trailing edge, the turbulent fluctuations then decrease. Unsteady flow phenomena occur, which can be attributed to the helical mode instability of the breakdown flow.

Longitudinal Aerodynamic Coefficients

- The partly-developed leading-edge vortex influences the lift and drag coefficient characteristics only to a small extent. A non-linear lift increase due to leading-edge vortex suction is not visible, as the vortical structure is rather weak. Overall, this results in lift slope values around $C_{L,\alpha} \approx 2.35$. The Lilienthal polar indicates a maximum lift-to-drag ratio of $(C_L/C_D)_{max} = 14.28$, which is observed at $\alpha = 4^\circ$. The zero-lift drag coefficient of the configuration is found at $C_{D,0} = 0.0067$.
- The pitching-moment coefficient characteristics are influenced more considerably. With increasing angle of attack, non-linear effects become obvious, which are caused by the upstream-moving leading-edge vortex. The derivative of the pitching-moment coefficient, however, is always negative over the angle-of-attack polar, and shows values of $-0.25 \leq C_{my,\alpha} \leq -0.1$.

5.2 Numerical Investigations

5.2.1 Validation of the Numerical Method

Grid Sensitivity Study

The validity of the numerical investigations on the AVT-183 configuration is proven first by a grid sensitivity study. For the subsequent analysis, three different grid resolutions are relevant, which have been introduced in Section 4.2.2. The corresponding grid parameters can be obtained from Table 4.1. The initial wall spacing was chosen equally for the different grids, and therefore the computed y^+ values are discussed on the medium grid resolution only, see Figure 5.20. The influence of the leading-edge vortex is clearly noticed, as increased y^+ values are observed in the corresponding region close to the wing leading edge. With increasing angle of attack, the flow separation onset moves upstream, but the maximum y^+ values always remain at $y^+_{Max} \approx 1.2$. In the inboard wing section and upstream of the leading-edge vortex formation, attached flow is present. The resulting y^+ values are lower and the criterion of $y^+_{Max} = 1$, which is desired due to the one-equation turbulence model applied in the present research, is completely fulfilled. Towards the trailing edge, the values decrease even more. Inboard of the leading-edge vortex, a thin strip of considerably reduced y^+ values is present on the diamond wing surface. This region depicts the footprint of the "inner vortex", which has already been introduced in the results of the experimental investigations, see Section 5.1.2. Its analysis is also part of the discussion in the following sections. Furthermore, this region separates the influence zones of the inboard attached and outboard vortex-dominated flow on the AVT-183 configuration. In summary, the results of Figure 5.20 demonstrate that the generated grids are well resolved in normal direction close to the diamond wing surface. With respect to the applied one-equation turbulence model, the initial wall spacing is thus chosen reasonably.

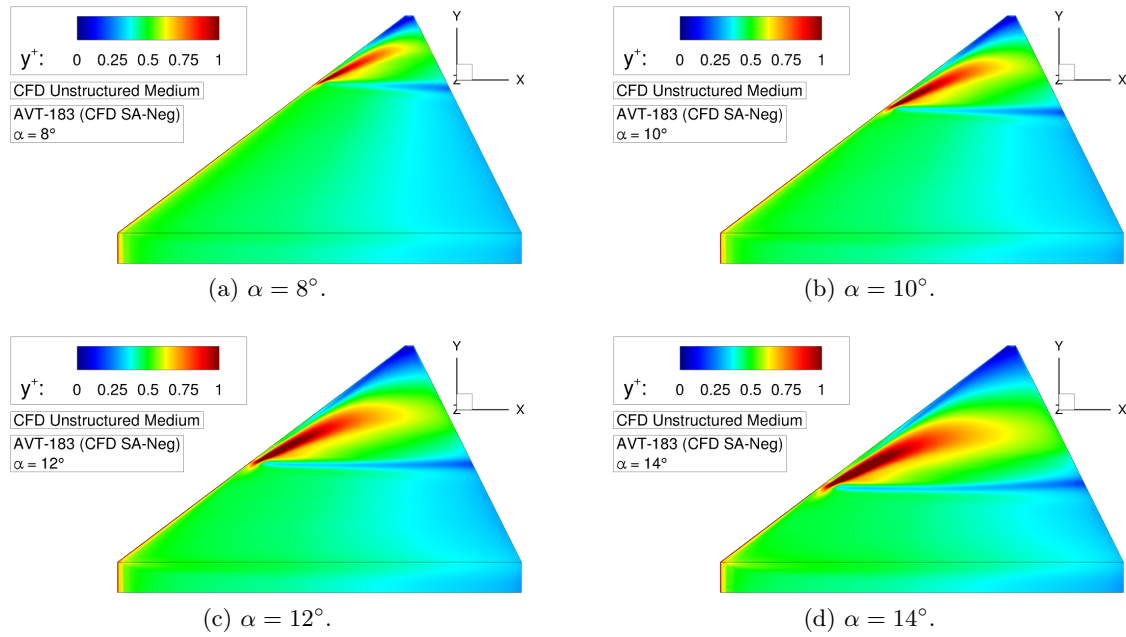


Figure 5.20: CFD validation of the AVT-183 configuration – Computed y^+ levels.

Next, the longitudinal aerodynamic coefficients are discussed with respect to grid convergence. For the angle of attack of $\alpha = 12^\circ$, the respective values are presented in Table 5.1 and Figure 5.21. The experimental results (target flow conditions, case W/T Forced Transition 150mu Dots) are given as a reference, as both uncorrected and corrected W/T data is stated. Among themselves, the different grid resolutions show satisfying results. Very similar values are observed in each case. Between the coarse and the medium grid resolution, differences are only slightly noticeable. For the fine grid resolution, almost no difference is left anymore, and the aerodynamic coefficients result in the same values compared to the medium grid resolution. This demonstrates that grid convergence has already been reached for the medium grid size. Corresponding results of surface pressures and near-wall flow field characteristics further confirm this conclusion, which is also valid for other angles of attack. The subsequent analyses in the present research are, for this reason, exclusively based on results computed for the medium grid resolution. With respect to the experimental reference data, the agreement between the CFD and the W/T results

	Coarse Grid Resolution	Medium Grid Resolution	Fine Grid Resolution	Experiment (Forced) Transition 150mu Dots	
				Uncorrected	Corrected
C_L	0.5573	0.5575	0.5577	0.5167	0.5589
C_D	0.0794	0.0800	0.0801	0.0798	0.0887
C_{my}	-0.0328	-0.0327	-0.0327	-0.0274	-0.0314

Table 5.1: CFD validation of the AVT-183 configuration – Longitudinal aerodynamic coefficients for different grid resolutions at $\alpha = 12^\circ$.

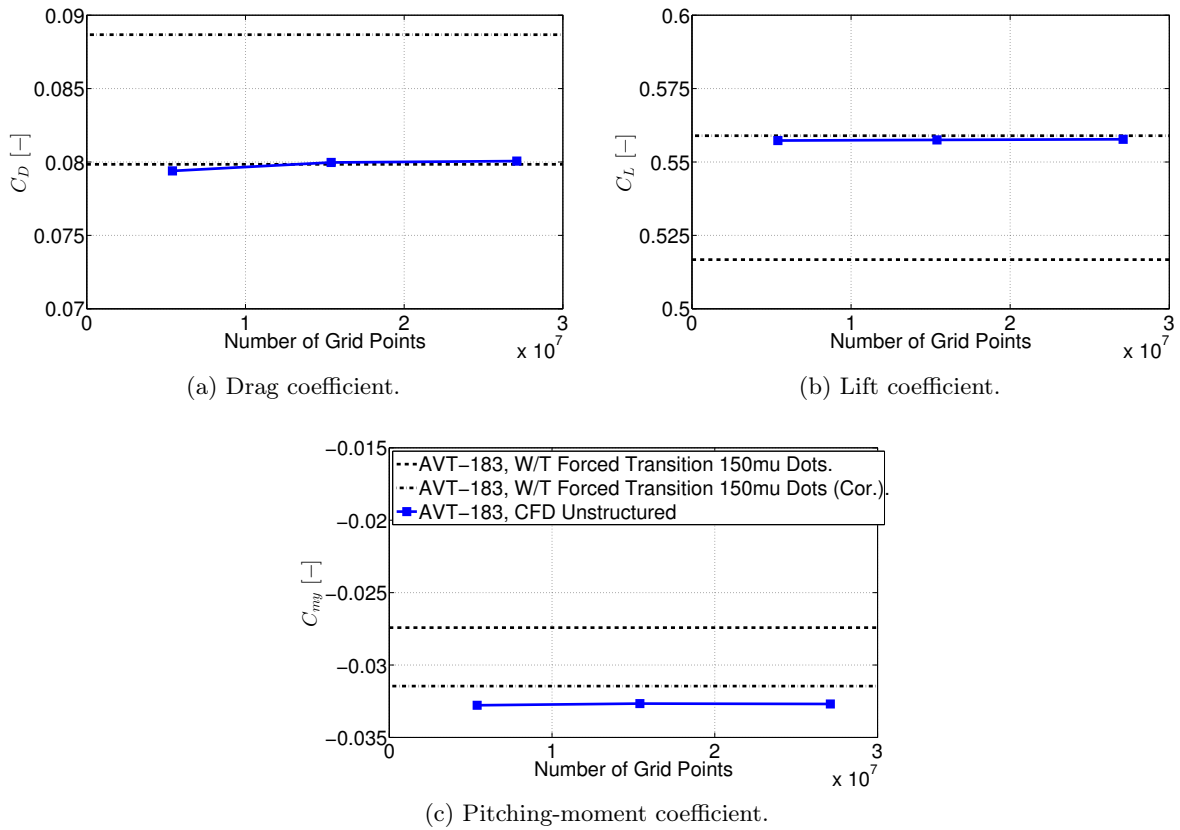


Figure 5.21: CFD validation of the AVT-183 configuration – Longitudinal aerodynamic coefficients for different grid resolutions at $\alpha = 12^\circ$.

at $\alpha = 12^\circ$ depends on whether W/T corrections are applied or not, see Figure 5.21. In this context, note also the comments on this issue in the following paragraph. Considering the uncorrected W/T data, the experimental drag coefficient value is almost matched by the numerical investigations. The computed lift coefficient, however, deviates by approximately 8% from the measured value, which is rather unusual as CFD can normally predict the lift coefficient quite accurately. Accordingly, the computed pitching-moment coefficient is also off with about 19% deviation. If W/T corrections are considered, the computed lift coefficient deviates from the experimental value by less than 0.5%. A much better agreement is thus observed. The maximum deviation of the pitching-moment coefficient is this time around 4%. The corrected experimental drag coefficient, however, is in this case underpredicted in the numerical solution by almost 10%.

Comparison to Experimental Data

The comparison of the computed CFD data and the experimental values is discussed in more detail for the entire angle-of-attack polar, which was considered in the numerical and experimental investigations, respectively. Figure 5.22 depicts the longitudinal aerodynamic coefficients versus the angle of attack, and the trends observed at $\alpha = 12^\circ$ are therefore highlighted. Considering the uncorrected W/T results, only the drag coefficient characteristics are predicted accurately with

Analysis of Partly-Developed Leading-Edge Vortices

increasing angle of attack, see Figure 5.22a. The computed lift and pitching-moment coefficient characteristics, in contrast, do not coincide with the corresponding experimental values for higher angles of attack, see Figure 5.22c and Figure 5.22d. The differences are specific for the AVT-183 semi-span model and do not occur in the analyses of the full-span SAGITTA configuration, see Section 6.1.1. Hence, they may be the result of the semi-span model and its test set-up combination with the open-jet W/T tunnel facility, which has not been modeled in the free air CFD computations. Apparently, this effect becomes more relevant for semi-span wing configurations due to the proximity of the W/T floor. In the context of the AVT-183 investigations, Coppin et al. presented ideas on corrections of the W/T data, which are motivated by lift interference effects between the W/T model and the open-jet boundary [35]. Appendix B summarizes the major points of the applied W/T correction for further information. Overall, a much better agreement between the numerical and the experimental results is thereby observed over the entire angle-of-attack polar. Both the lift coefficient and the pitching-moment characteristics are now predicted very accurately in CFD compared to the corrected experimental reference data, see Figure 5.22c and Figure 5.22d. Thus, the results are very satisfying. As already presented above for $\alpha = 12^\circ$, the drag coefficient characteristics then show some underprediction compared to the

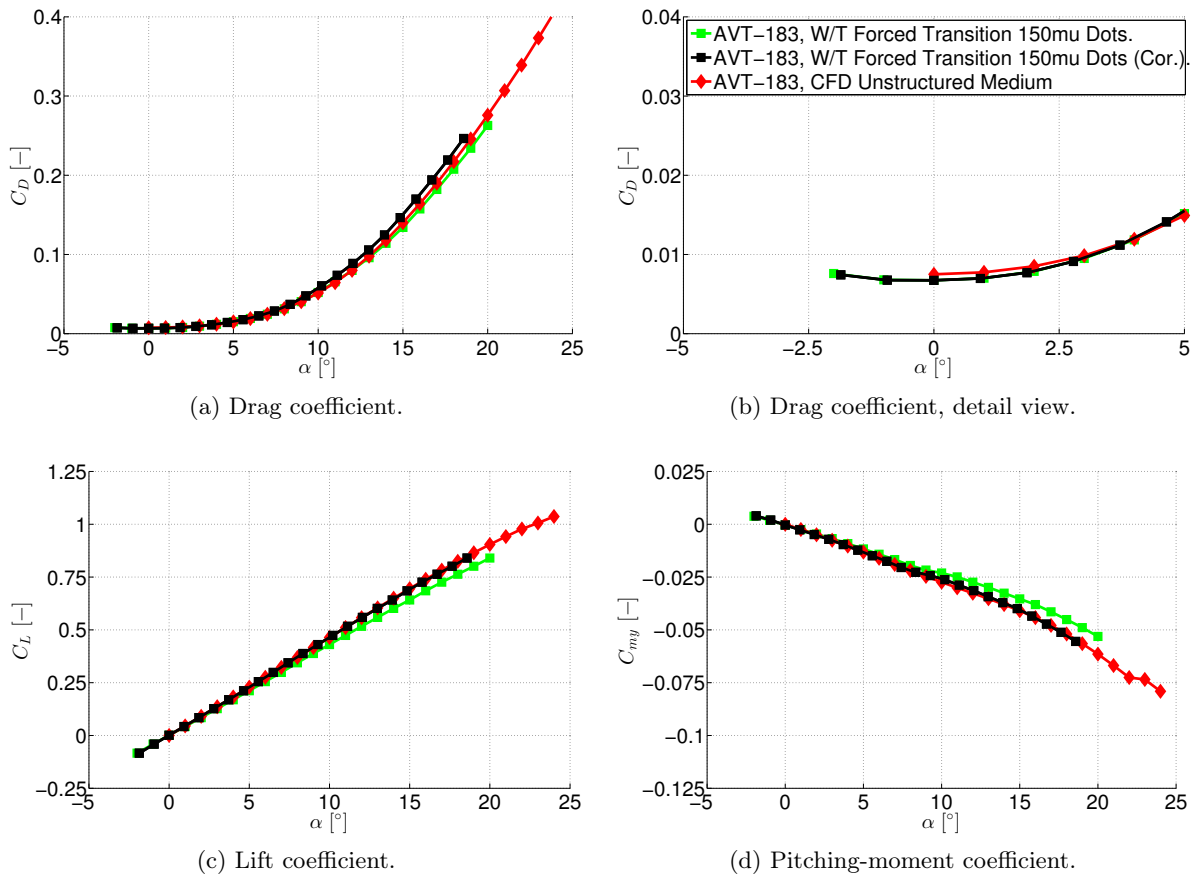


Figure 5.22: CFD validation of the AVT-183 configuration – Longitudinal aerodynamic coefficients versus angle of attack α .

corrected W/T data. However, this is only observed for higher angles of attack, but not close to the zero-lift drag coefficient $C_{D,0}$, see Figure 5.22b. The respective results are very close to each other and hence, the agreement once more confirms the selection of case W/T Forced Transition 150mu Dots as flow tripping method in the W/T experiments. Compared to fully-turbulent CFD computations, the applied trip dots lead to very similar drag coefficient characteristics, which supports the assumption of reasonably-tripped flow in the experimental investigations.

The prediction of the leading-edge vortex structure in the near-wall flow field is considered next. Figure 5.23 and Figure 5.24 present the axial vorticity component and the absolute velocity in several chordwise sections for two different angles of attack, namely $\alpha = 10^\circ$ and $\alpha = 12^\circ$. From now on, the uncorrected W/T data is considered again. The overall comparison of the CFD computations and the Stereo PIV investigations again demonstrates the agreement between the numerical and experimental approach. The size of the leading-edge vortex is predicted similarly to each other, and the associated contour levels are quite comparable. However, the results indicate a slightly upstream leading-edge vortex formation in the W/T experiments. Both the applied turbulence model and the used trip dots may contribute to occurring deviations, thus showing the sensitivity of the flow separation onset. Figure 5.23 further indicates similar levels of the axial vorticity contours towards the trailing edge in both the numerics and the experiments. The wake-type character of the leading-edge vortex is also predicted with comparable contour levels, see Figure 5.24. The "inner vortex", which is clearly noticed in the CFD computations by the respective footprint inboard of the leading-edge vortex, finally appears in the W/T experiments in similar size and strength. Especially at $\alpha = 10^\circ$, see Figure 5.23a and Figure 5.24a, the footprint

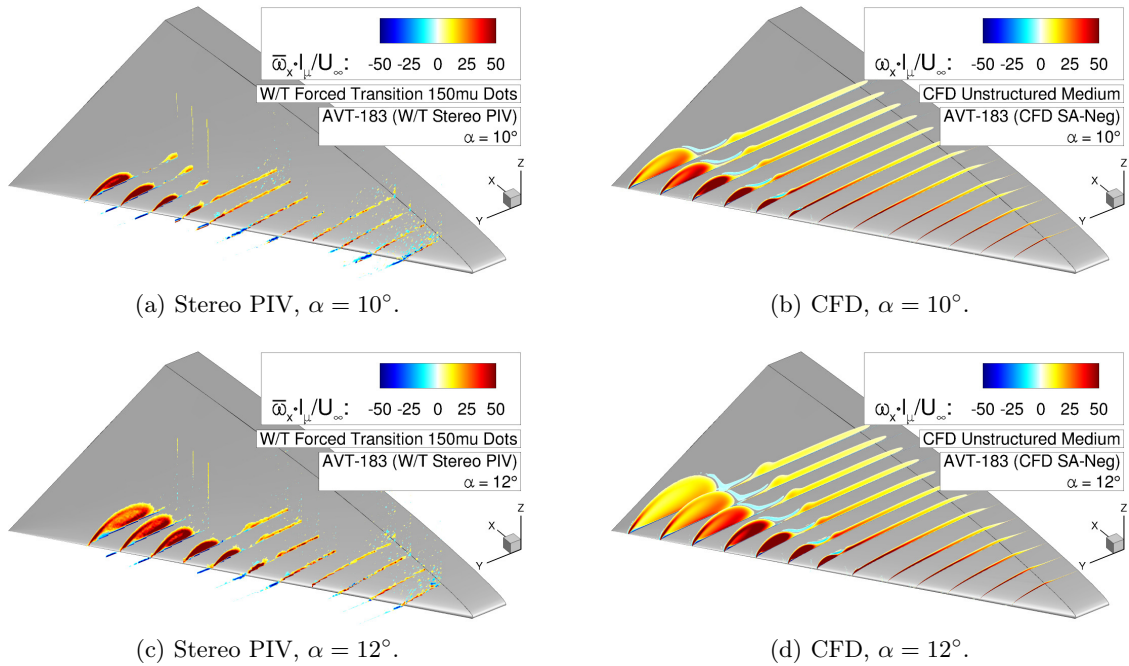


Figure 5.23: CFD validation of the AVT-183 configuration – Axial vorticity contours $\bar{\omega}_x \cdot l_\mu / U_\infty$.

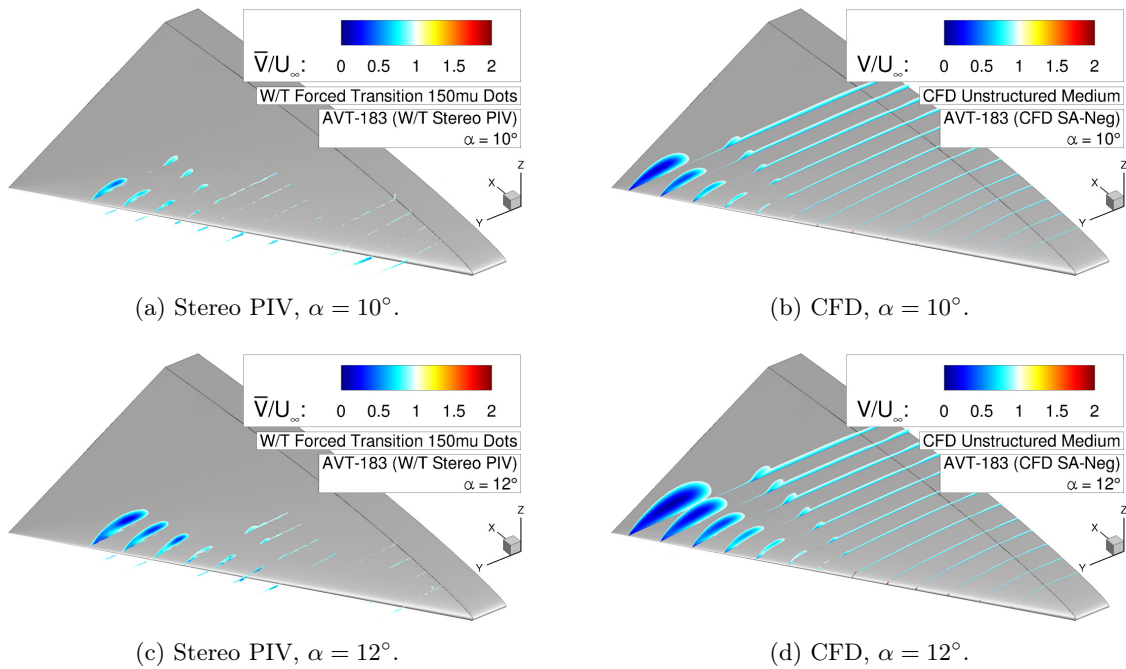


Figure 5.24: CFD validation of the AVT-183 configuration – Absolute velocity contours \bar{V}/U_∞ .

is observed up to the most downstream chordwise section that was measured with Stereo PIV. Due to the earlier leading-edge vortex formation in the experimental investigations, however, the trajectory of the "inner vortex" is consequently displaced as well.

Finally, the corresponding surface pressure distributions are compared to each other. Figure 5.25 depicts the results of the CFD computations and the W/T experiments in two chordwise sections and at three angles of attack, respectively. In the downstream section at $x/c_r = 0.5$, the delayed flow separation onset in the numerical investigations is noticed for all angles of attack, as the vortex axis is located more outboard and the suction levels of the leading-edge vortex are slightly more pronounced. The differences become less with increasing angle of attack, and the CFD and W/T results then match very well. More upstream at the chordwise section of $x/c_r = 0.295$, the sensitivity of the flow separation onset becomes obvious more considerably. At $\alpha = 12^\circ$, for instance, the leading-edge vortex formation immediately takes place in the W/T experiments, whereas the CFD data still shows attached flow, see Figure 5.25c. At $\alpha = 14^\circ$, the agreement is found again to be very good, see Figure 5.25e, as the spanwise position of the pressure reduction at the leading-edge vortex is predicted very accurately. Only the maximum suction level is different with some offset between the numerics and the experiments.

In summary, the presented plots demonstrate the validity of the numerical method that was applied in the CFD analyses of the AVT-183 configuration. Compared to the experimental reference data, the numerical investigations provide reliable results for the leading-edge vortex formation and progression as well as for the integral aerodynamic values. Depending on the consideration of W/T corrections and the applied flow tripping in the W/T experiments, however, slight deviations are noticed, which emphasize the difficulty of the analyzed flow phenomena.

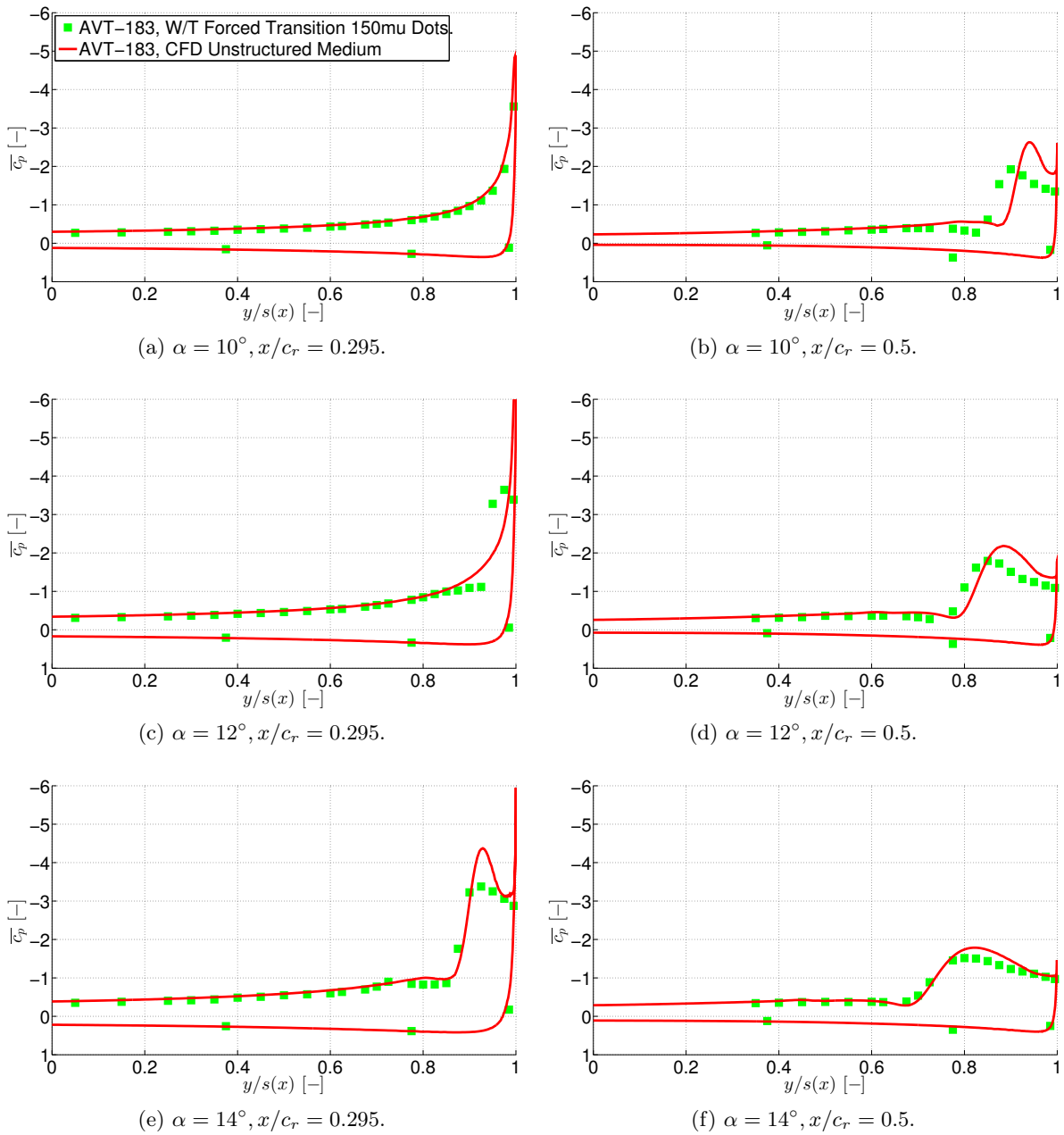


Figure 5.25: CFD validation of the AVT-183 configuration – Surface pressure coefficient \bar{c}_p versus semi-span $y/s(x)$.

5.2.2 Flow Physics Analysis

The analysis of the leading-edge vortex is extended based on numerical results. Since additional information in comparison to the W/T experiments is available from the CFD investigations, the experimental findings can substantially be expanded. Figure 5.26 presents the surface pressure coefficients including skin-friction lines for three different angles of attack, which range from $\alpha = 10^\circ$ to $\alpha = 14^\circ$. The variation of the surface pressure coefficient along the leading edge of

Analysis of Partly-Developed Leading-Edge Vortices

the semi-span wing is additionally given in each case. Considering the global characteristics, the existence of the partly-developed leading-edge vortex at the AVT-183 configuration is clearly seen in Figure 5.26a to Figure 5.26c. On the inboard portion of the diamond wing, the skin-friction lines show attached flow while the leading-edge vortex (LEV) emerges in the more outboard wing section. The flow separation moves considerably upstream with increasing angle of attack, and the leading-edge vortex size and intensity become stronger. A secondary vortex separation induced by the leading-edge vortex is also observed, see Figure 5.26d to Figure 5.26f. The designated skin-friction lines of the secondary separation line (SSL) and secondary attachment line (SAL) are exemplarily marked at $\alpha = 14^\circ$. Closely inboard of the primary attachment line (PAL), converging skin-friction patterns are further present. They arise from confluent boundary layers of the reattached leading-edge vortex flow and the inboard attached flow that is slightly directed outboard. The converging skin-friction lines are thus the origin of the "inner vortex" (IV) as introduced in Section 5.1.2. See also Figure 5.26a to Figure 5.26c for a global view. Contrary to the leading-edge vortex, however, no discernible pressure footprint is observed on the wing surface, which is due to the resulting flow topology, see Section 5.2.4.

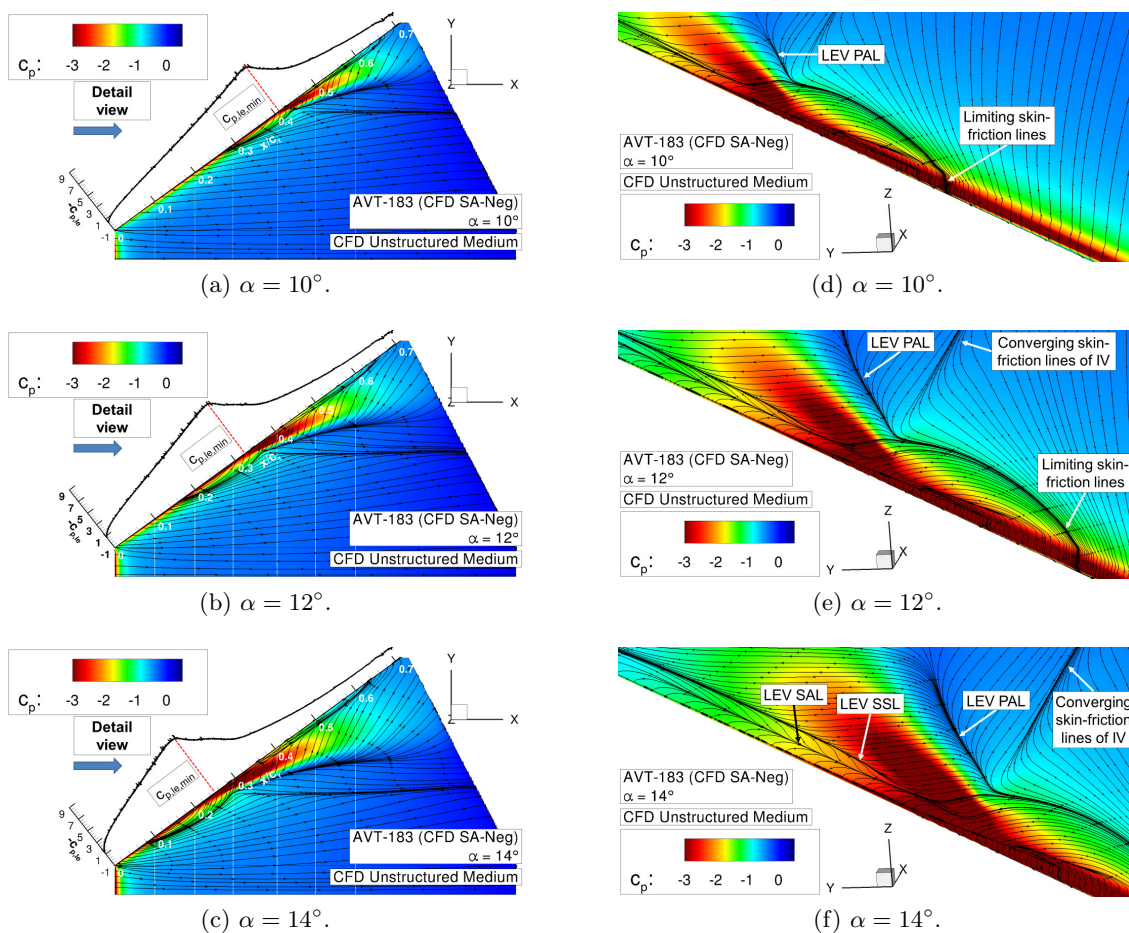


Figure 5.26: Flow physics analysis of the AVT-183 configuration – Surface pressure coefficient c_p including skin-friction lines.

Incipient to the large-scale appearance of the leading-edge vortex, distinct sets of curved skin-friction lines are observed in the leading-edge region, see Figure 5.26d to Figure 5.26f. In each case, the beginning of the respective region is marked by a condensed number of limiting skin-friction lines. The entire flow upstream of this location stays attached and exits the diamond wing surface at the trailing edge. The oncoming flow downstream of the limiting skin-friction lines is initially attached as well, but it returns more downstream to the leading edge and is thus relevant for the occurring leading-edge vortex as well as the respective secondary vortex separation. Therefore, this area is denoted by the incipient separation region of the partly-developed leading-edge vortex. At $\alpha = 12^\circ$, for instance, the limiting skin-friction lines are noticed at $x/c_r \approx 0.17$, see Figure 5.26b. This is considerably more upstream than the first appearance of the vortical structure in the surface patterns at $x/c_r \approx 0.34$. Within the region of incipient separation, the flow separation onset develops as a three-dimensional separation on boundary-layer level, before it significantly escapes from the wing surface more downstream. Section 5.2.3 focuses on this aspect in detail. The corresponding suction levels of the attached flow at the leading edge still increase along the semi-span in the incipient separation region, see Figure 5.26a to Figure 5.26c. Maximum leading-edge suction is reached right before the leading-edge vortex finally emanates in the global view. Thereafter, the leading-edge suction levels decrease again, and the main suction effect moves inboard to the leading-edge vortex axis.

The corresponding spanwise surface pressure coefficient distributions are highlighted in Figure 5.27. The plots recall the experimental results of Figure 5.10 and summarize the flow phenomena of the vortical flow field associated with the AVT-183 configuration. In the inboard wing section, attached flow is present, and more outboard, the upstream-moving leading-edge vortex occurs.

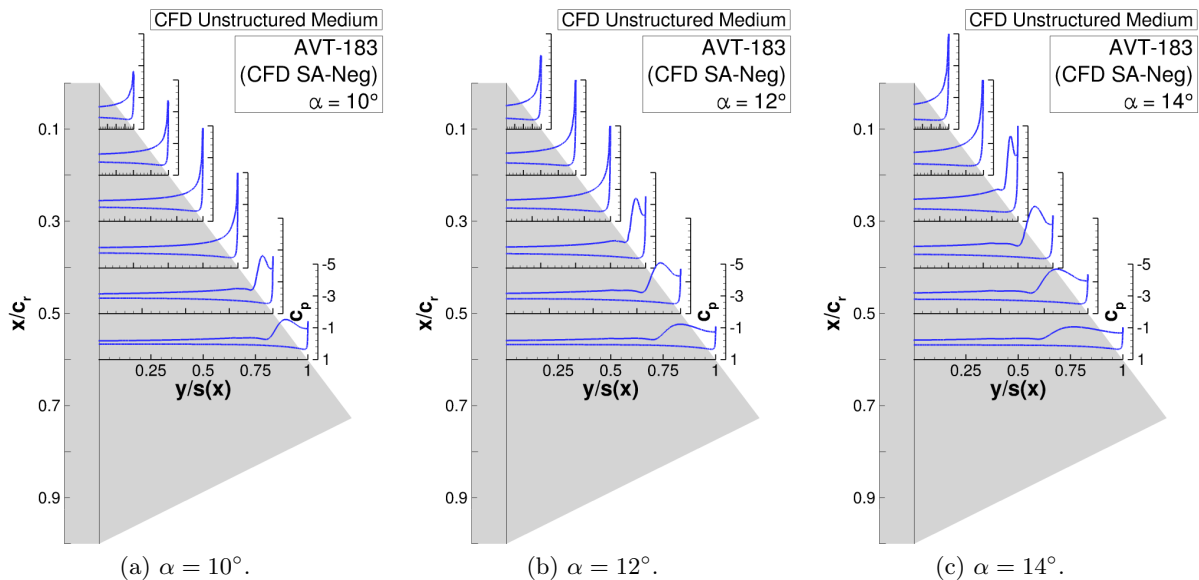


Figure 5.27: Flow physics analysis of the AVT-183 configuration – Surface pressure coefficient c_p versus semi-span $y/s(x)$.

Analysis of Partly-Developed Leading-Edge Vortices

The expanding footprints of the surface pressure coefficients with reduced suction levels in the more downstream wing sections indicate the occurring vortex breakdown, which has already been discussed by the experimental results at $\alpha = 12^\circ$. The plot sequence further shows that this phenomenon moves upstream with increasing angle of attack as well.

To further demonstrate the development of the vortex breakdown characteristics, related sectional plots of the absolute velocity contours are finally shown in Figure 5.28 and Figure 5.29. For the angle of attack of $\alpha = 12^\circ$, the axial vorticity contours are presented additionally. The results indicate in all regarded cases the instantaneous wake-type character of the leading-edge vortex and the continuous expansion of the vortex core region in downstream direction. Distinct occurrences of jet-type vortex core flow are not present, and vortex bursting tendencies are thus immediately relevant after the large-scale appearance of the leading-edge vortex. The global characteristics do not differ with varying angle of attack, but they are less or more distinct due to the location of the leading-edge vortex formation. Consequently, the results obtained from the experimental analyses are confirmed in all respects.

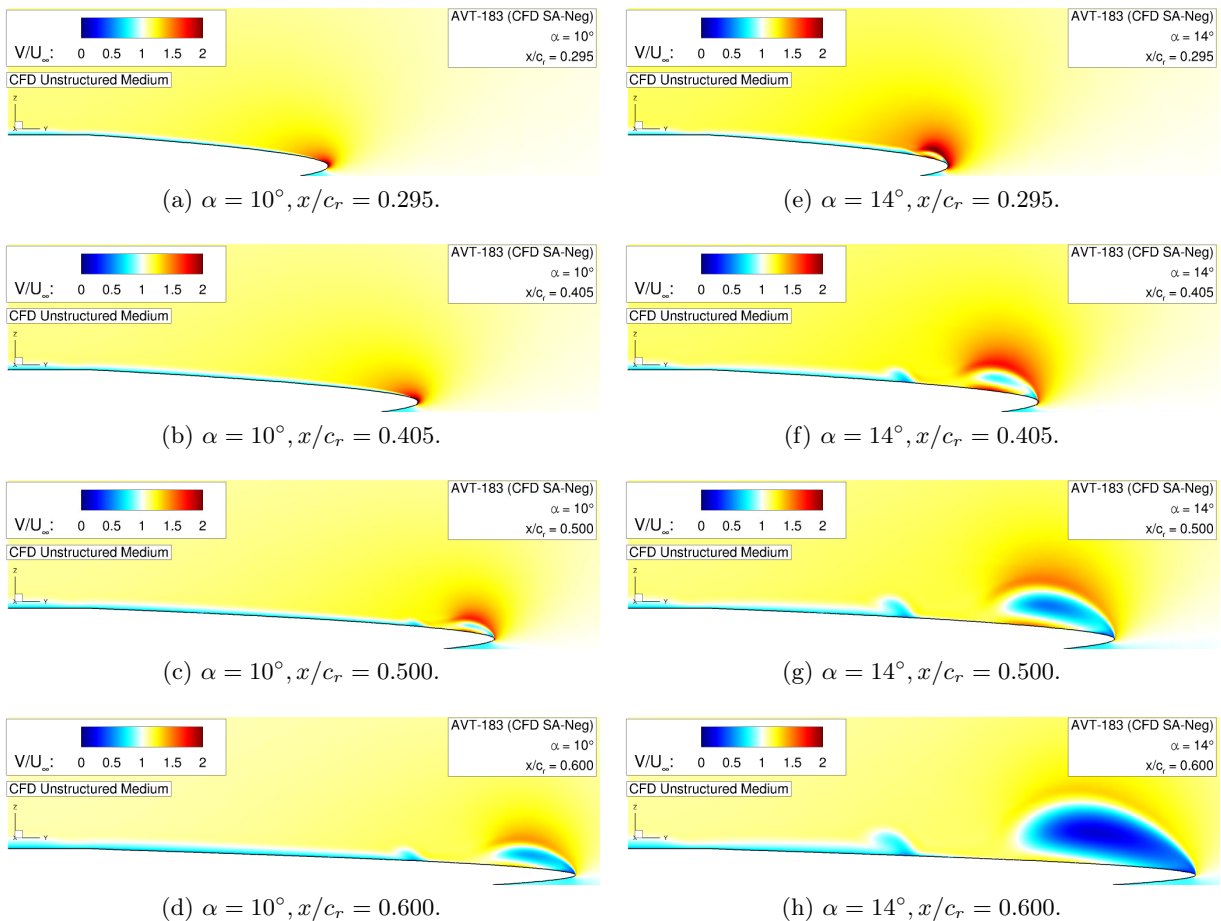


Figure 5.28: Flow physics analysis of the AVT-183 configuration – Absolute velocity contours V/U_∞ .

Finally, the "inner vortex" is considered again. Figure 5.29a to Figure 5.29d depict the axial vorticity contours at $\alpha = 12^\circ$ and thus refer to the experimental results of Figure 5.11c to Figure 5.11f. Thanks to the numerical investigations, the entire near-wall flow field information is accessible in this case. Overall, the sectional cuts show the split-up process of the continuous boundary layer along the semi-span wing in consequence of the large-scale appearance of the leading-edge vortex. More downstream, the development of the "inner vortex" structure is thereby observed. It is associated with a local increase of the inboard near-wall region with increased axial vorticity levels, see Figure 5.29c and Figure 5.29d. Outboard of the "inner vortex", the axial vorticity content close to the wing surface is first reduced. Then, the distinct leading-edge vortex is dominant. The corresponding plots of the absolute velocity contours also show the footprint of the "inner vortex" in the more downstream chordwise sections, as a wake-type vortex core flow is locally present close to the wing surface at the respective locations. At $\alpha = 14^\circ$, this is best noticeable, see Figure 5.28f to Figure 5.28h. Additional information on the flow phenomenon can also be found in Section 5.2.4. There, the formation of the "inner vortex" is discussed by a global flow topology interpretation of the resulting vortical flow field on the diamond wing configuration.

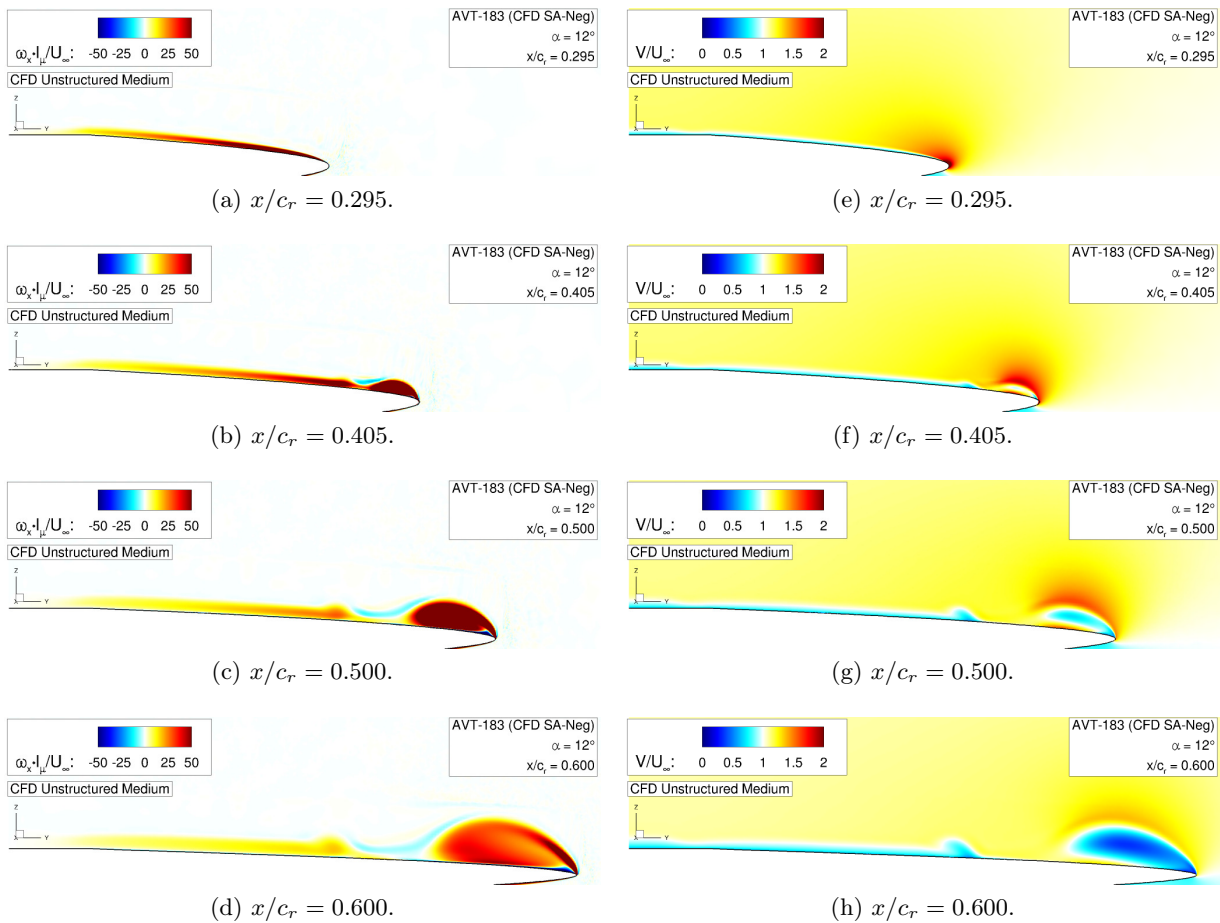


Figure 5.29: Flow physics analysis of the AVT-183 configuration – Axial vorticity contours $\omega_x \cdot l_\mu / U_\infty$ and absolute velocity contours V / U_∞ at $\alpha = 12^\circ$.

5.2.3 Flow Separation Onset Characteristics

Flow Physics Description

The flow separation onset characteristics in the incipient separation region are discussed for the angle of attack of $\alpha = 12^\circ$. The following analysis presents detail views that considerably zoom in on the respective wing region. For this reason, Figure 5.30 shows a global view of the flow field characteristics for comparison, thus highlighting the proportions of the incipient separation region and the extension of contour slices with increased axial vorticity levels. The flow phenomena on boundary-layer level, which are discussed below, are thereby set into context to the large-scale leading-edge vortex that emanates more downstream as a result of the flow separation onset.

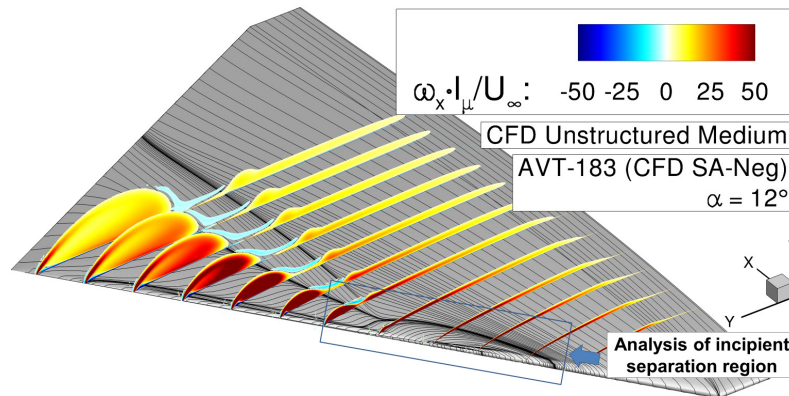


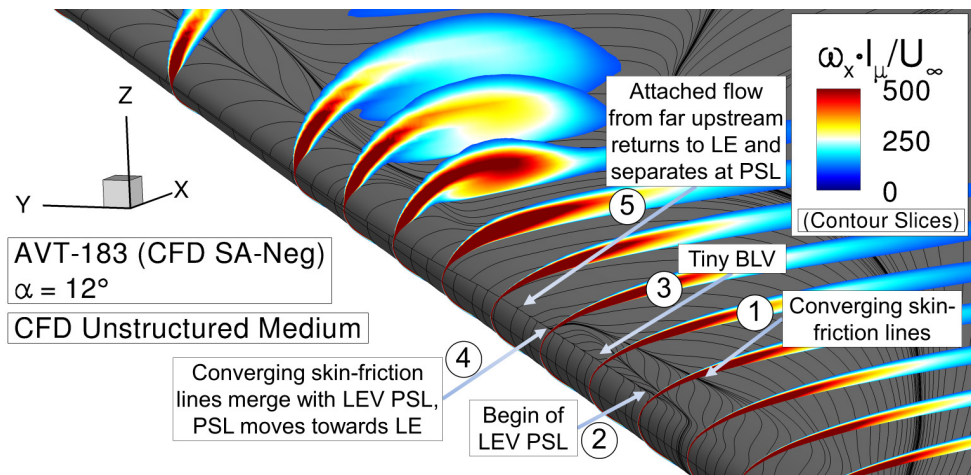
Figure 5.30: Flow separation onset characteristics of the AVT-183 configuration – Axial vorticity contours $\omega_x \cdot l_\mu / U_\infty$ including skin-friction lines at $\alpha = 12^\circ$.

Figure 5.31 depicts the skin-friction lines and additional information of the near-wall flow field in the incipient separation region. Considering the flow separation onset characteristics, two main flow phenomena are relevant, see Figure 5.31a. On the one hand, converging skin-friction lines are observed on the smooth wing surface (1), which indicate the origin of a three-dimensional separation. On the other hand, converging skin-friction lines are also present closer to (but not at) the wing leading edge (2). They form the beginning primary separation line (PSL) of the later occurring leading-edge vortex (LEV). Moreover, these skin-friction lines represent the separation line of an additional tiny vortex, which is established on boundary-layer level in consequence of the accelerated flow around the leading edge and the surface pressure gradient (BLV, 3). Between the primary attachment line of the boundary-layer vortex and the more inboard converging skin-friction lines, the flow is attached again on the wing surface. Moving downstream, the boundary-layer vortex is present only for a short run length. At a certain point (4), the converging skin-friction lines of the more inboard portion return to the leading edge (LE) and merge together with those of the primary separation line. Thereby, attached flow from far upstream, which was already located on the wing surface, is driven back to the leading edge, separates as well and escapes in normal direction similarly to the flow that comes around the leading edge at this chordwise location (5). From then on and in downstream direction, the

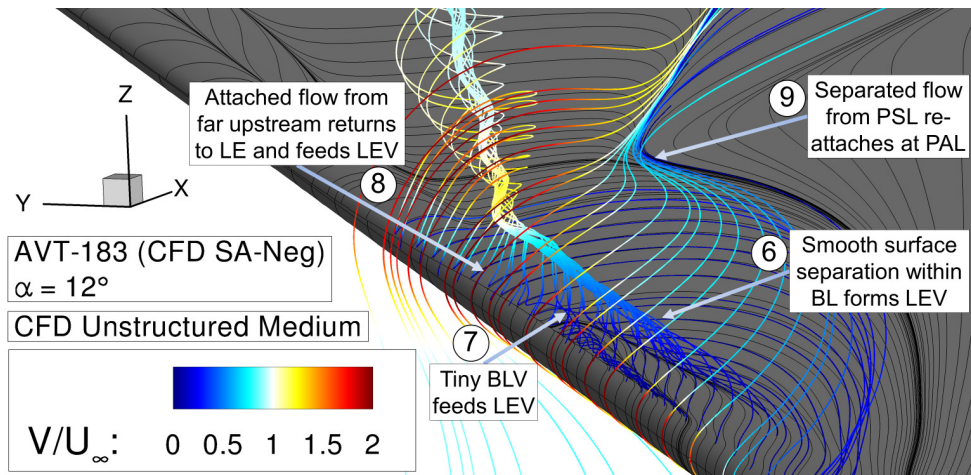
primary separation line is slightly shifted towards the leading edge, but it never reaches the nose coordinate due to the rounded leading-edge contour.

Figure 5.31b additionally highlights selected field streamlines that are associated with the relevant surface flow field characteristics in the incipient separation region. In each case, the streamlines have been released at appropriate locations that are displaced by only $d_{w,n} = 0.005 \text{ mm}$ to the wing surface in normal direction. Consequently, they represent the almost continuous extension of the skin-friction lines offside the wing surface. One can notice that the large-scale leading-edge vortex originates from the more inboard smooth surface separation, which forms the vortical structure by the three-dimensional flow separation on boundary-layer level (6). At this location, the boundary-layer height is approximately $\delta_{99} \approx 0.002 \text{ m}$. The tiny boundary-layer vortex is also noticeable and escapes from the wing surface at the location, where both converging skin-friction patterns merge together (4). Subsequently, the boundary-layer vortex is sucked into the incipient leading-edge vortex (7), which already shows at this development stage a concentrated vortex core. The distinct structure is continuously strengthened by fluid transport of the upstream attached flow that returns to the leading edge below the vortex core axis and separates at the primary separation line (8). Thereby, the leading-edge vortex escapes more downstream significantly from the wing surface and emerges as a visible large-scale vortical structure. The field streamlines above the emanating leading-edge vortex indicate the closure of the incipient separation region in normal direction (9). They are mostly aligned with the free stream and bend above the wing surface in the direction of the primary attachment line of the leading-edge vortex. Moreover, they do not return to the leading edge any longer. The limiting process towards the wing surface further shows that the locations of attachment move upstream along the primary attachment line. Thereby, the condensed skin-friction lines as introduced in Figure 5.26 are built, which define the beginning of the incipient separation region.

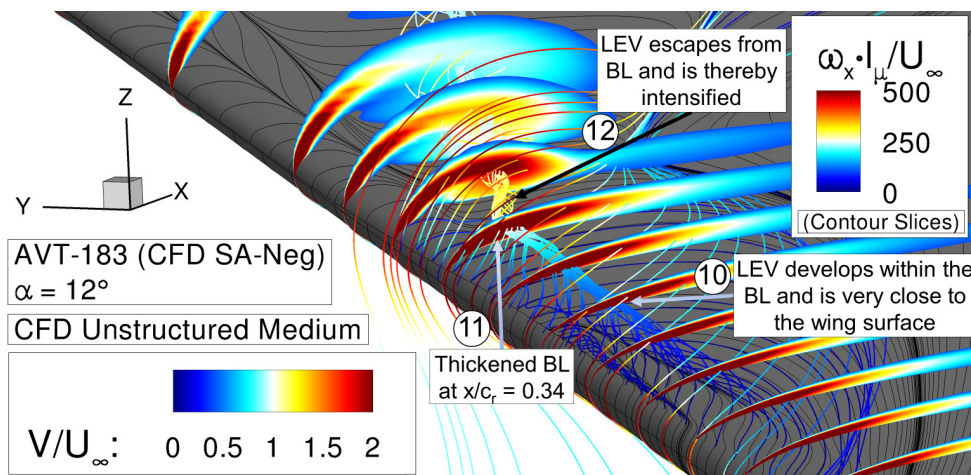
Figure 5.31c finally summarizes the wall-normal expansion of the incipient leading-edge vortex, as the corresponding axial vorticity contour slices are additionally shown. The comparison of field streamlines and contour slices demonstrates that the leading-edge vortex develops and mostly remains on boundary-layer level in the incipient separation region. The vortical structure appears very closely to the wing surface and even the limiting streamlines, which closure the incipient separation region in normal direction (9), are located within the "attached" boundary layer as pretended by the axial vorticity contour slices (10). The skin-friction patterns and field streamlines, however, clearly depict the three-dimensional flow separation in between, from which the incipient leading-edge vortex is formed. In sum, this proves that the flow separation onset of the partly-developed leading-edge vortex at the AVT-183 configuration is initiated upstream than noticeable in the axial contour slices, and it occurs in very close proximity to the wing surface. At the chordwise position of $x/c_r = 0.34$, a thickened boundary layer is observable for the first time in the axial vorticity contour slices (11). The absolute velocity in the vortex core is here intensified to levels of $V/U_\infty \approx 1.25$, which indicates the transition of the leading-edge vortex to a large-scale structure (12). The observed location of the first large-scale appearance of the lea-



(a) Skin-friction lines including axial vorticity contours $\omega_x \cdot l_\mu / U_\infty$. The contour levels have been adjusted for the following analysis.



(b) Skin-friction lines including field streamlines colored by absolute velocity V/U_∞ . The field streamlines have been released with $d_{w,n} = 0.005 \text{ mm}$.

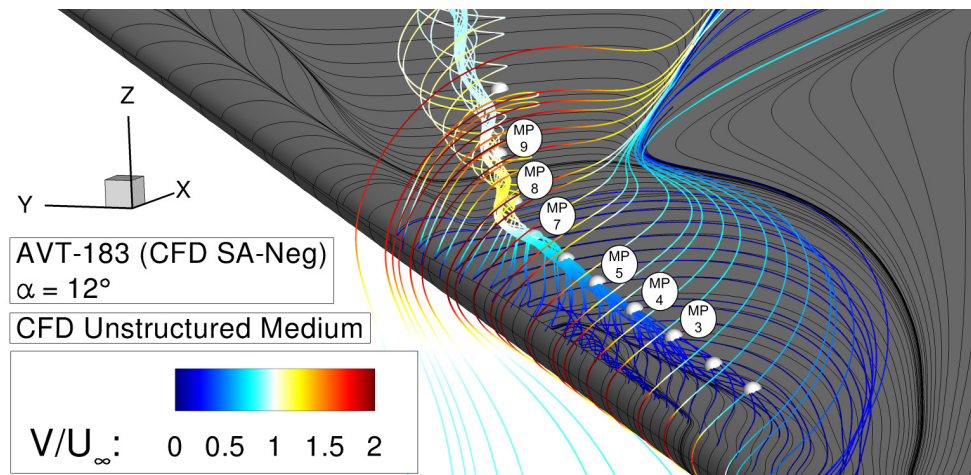


(c) Skin-friction lines including axial vorticity contours $\omega_x \cdot l_\mu / U_\infty$ and field streamlines colored by absolute velocity V/U_∞ .

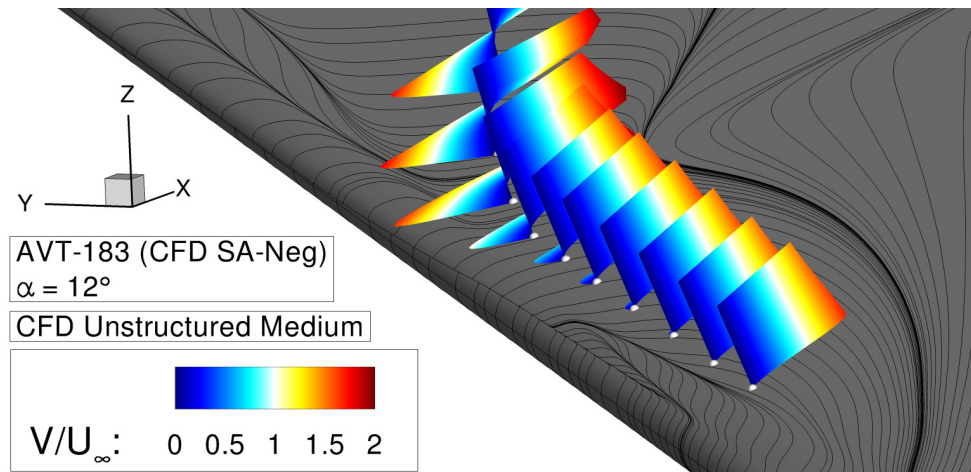
Figure 5.31: Flow separation onset characteristics of the AVT-183 configuration at $\alpha = 12^\circ$ (I).

ding-edge vortex is thus consistent with the result of the surface pressure footprint in Figure 5.26b. From then on, the leading-edge vortex grows on a large-scale basis. For instance, this is shown in the more downstream chordwise sections of Figure 5.31c, as the vortical structure including the separating shear layer is clearly covered by the axial vorticity contour slices. The leading-edge vortex, however, immediately shows decreasing axial vorticity levels and decreasing absolute velocities in the vortex core. The wake-type character of the partly-developed leading-edge vortex, as discussed before, is thus observed again.

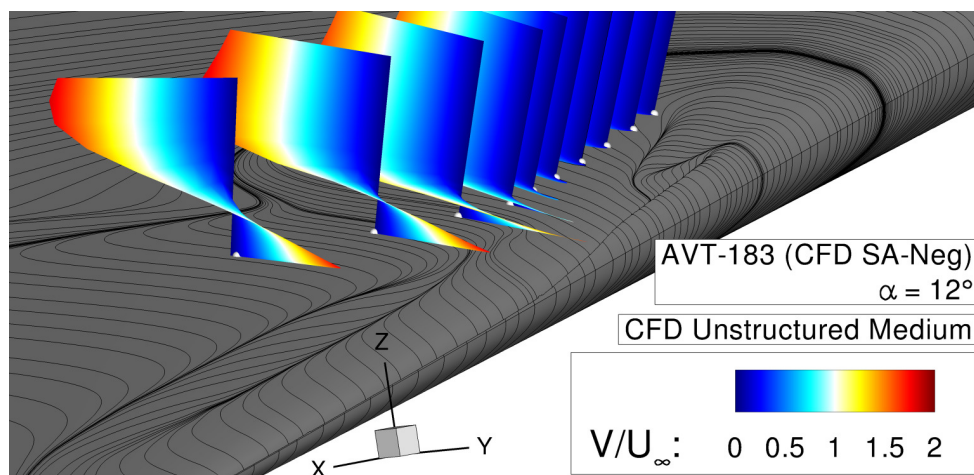
The distinct shear effects between the skin-friction lines and field streamlines in the incipient separation region are discussed next by near-wall velocity profiles. For this purpose, selected monitor points (MP) are evaluated. Figure 5.32 presents the corresponding results along the leading-edge vortex core in a three-dimensional view. For every monitor point, the full velocity profiles including streamwise and crossflow contributions are shown in the local skin-friction-line coordinate system, see Figure 5.32b and Figure 5.32c. Furthermore, the velocity profiles are each cut at $d_{w,n} = 0.015 m$, and they are colored by the respective absolute velocity. Going downstream, the velocity profiles precisely indicate the shear effects in the near-wall flow field. Close to the wing surface, the flow is directed towards the leading edge, whereas it points towards the almost opposite direction elsewhere. The wall-normal location of the leading-edge vortex core axis thereby becomes accessible, especially in the more downstream velocity profiles. For six selected monitor points as indicated in Figure 5.32a, the streamwise and crossflow components are therefore considered in more detail, see Figure 5.33. The corresponding plots depict the respective two-dimensional velocity profiles in the local skin-friction-line coordinate system separately. Considering monitor points 3-5, see Figure 5.33a to Figure 5.33c, the formation of the leading-edge vortex core is demonstrated, since the vortex core axis is aligned almost orthogonally to the respective local skin-friction-line coordinate systems. Especially for monitor points 4 and 5, the change of sign in the streamwise velocity profiles u_{sfl} indicates the vortex core axis, and it is located at only $d_{w,n} \approx 0.001 m$. Thus, the vortex only acts within the boundary layer, which height is approximately $\delta_{99} \approx 0.002 m$ at these locations. The corresponding crossflow velocity profiles do not differ significantly, but they show high values up to $v_{sfl}/U_\infty \approx 1.7$ in the near-wall flow field. Overall, this gives evidence for the strong shear in the region of the incipient leading-edge vortex. More downstream at monitor points 7-9, the development of the leading-edge vortex is highlighted, see Figure 5.33d to Figure 5.33f. The growing intensity of the vortical structure is demonstrated, as the values of the streamwise velocity profiles significantly increase in both directions close to the wing surface. As expected, the change-of-sign locations move in normal direction. At monitor point 8, for instance, the vortex core axis is located at $d_{w,n} \approx 0.003 m$, and the peak values of the streamwise velocity profile are in the range of $-1.1 \leq u_{sfl}/U_\infty \leq 1.6$. From this location on, also the crossflow velocity profiles change compared to the previous ones. The shear effects close to the wing surface are reduced, as the momentum is slightly displaced away from the wing surface. This shows the normal escape of the leading-edge vortex from the incipient separation region, which finally results in the large-scale vortical structure.



(a) Skin-friction lines including field streamlines colored by absolute velocity V/U_∞ and monitor points for near-wall velocity profile evaluation.



(b) Skin-friction lines including near-wall velocity profiles colored by absolute velocity V/U_∞ that are located along the leading-edge vortex core (front view).



(c) Skin-friction lines including near-wall velocity profiles colored by absolute velocity V/U_∞ that are located along the leading-edge vortex core (rear view).

Figure 5.32: Flow separation onset characteristics of the AVT-183 configuration at $\alpha = 12^\circ$ (II).

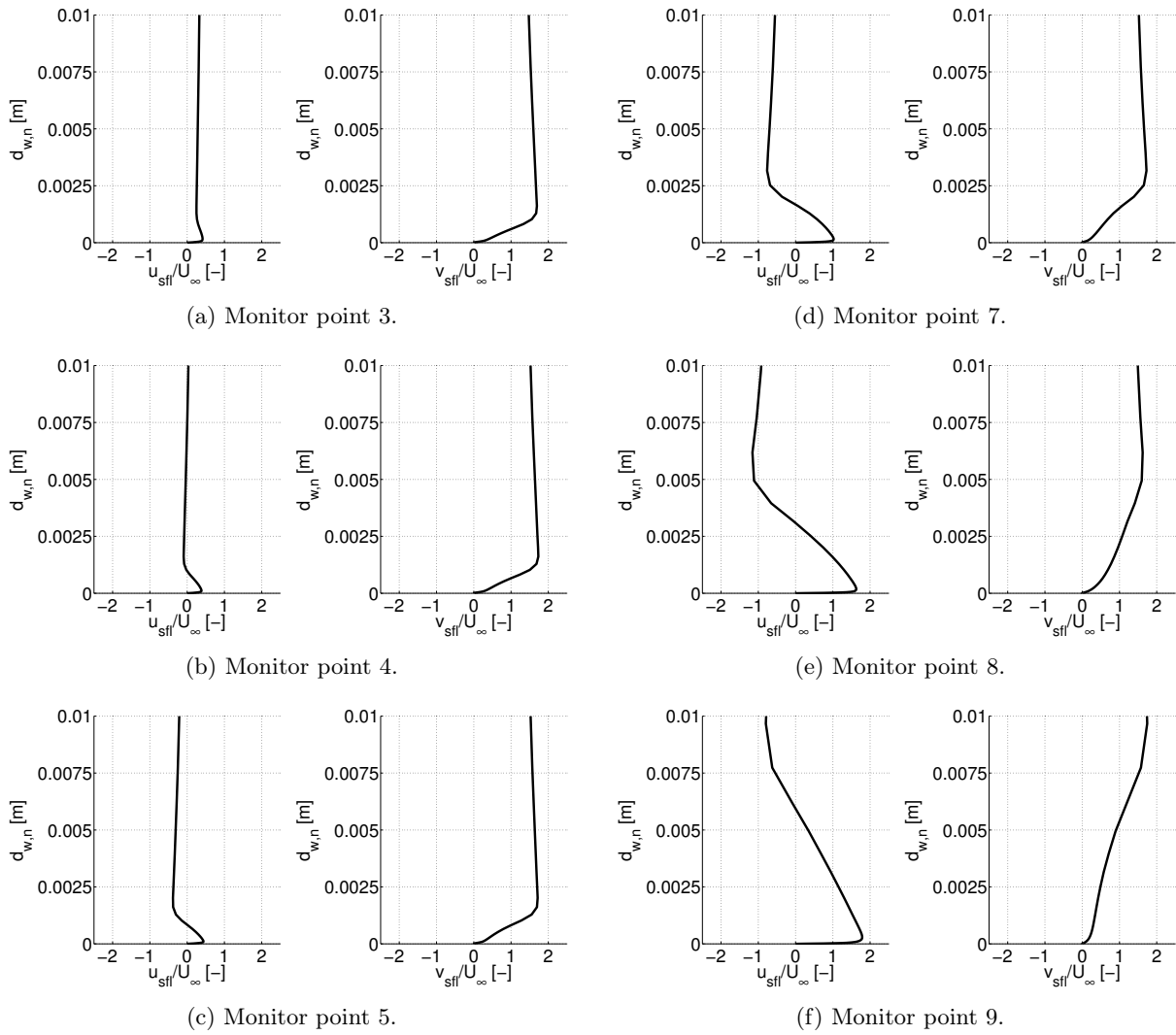
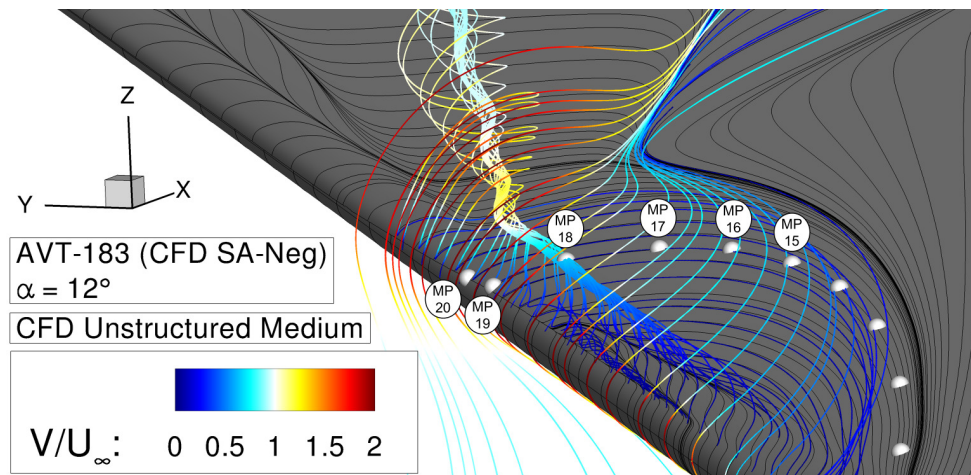
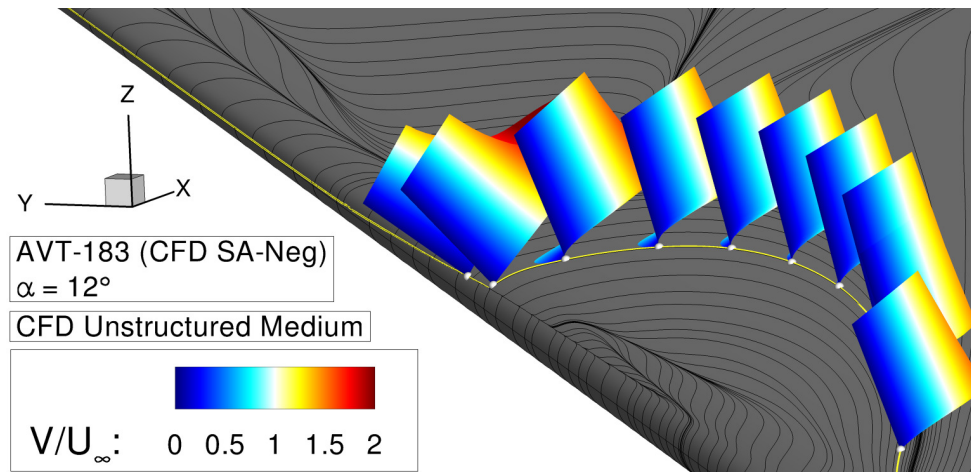


Figure 5.33: Flow separation onset characteristics of the AVT-183 configuration at $\alpha = 12^\circ$ – Near-wall velocity profiles in streamwise and crossflow direction along the leading-edge vortex core.

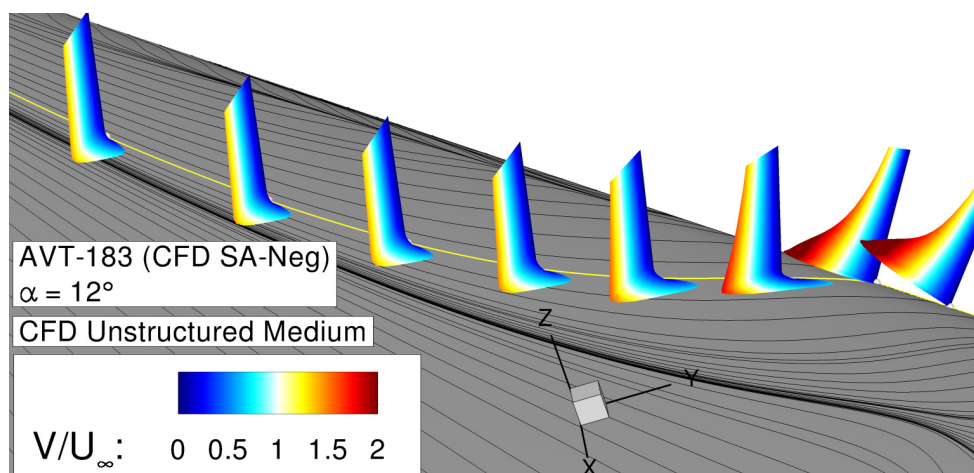
Figure 5.34 presents further near-wall velocity profiles along one particular skin-friction line, which passes the incipient separation region. Due to the induction of the leading-edge vortex, the shear effects in the near-wall flow field are noticed best in the proximity of the vortex core location around monitor point 18, see Figure 5.34b. More upstream along the skin-friction line, distorted velocity profiles are present as well close to the wing surface, but the shear effects occur not as obvious due to the global orientation of the local coordinate system at those locations, see Figure 5.34c. To obtain the corresponding velocity profiles more precisely, they are shown separately in two-dimensional plots for six selected monitor points, see Figure 5.35. At the first monitor point 15, this time both the streamwise and crossflow velocity profiles exhibit only positive values, since the global orientation of the skin-friction line just starts to turn back towards the leading edge. The boundary-layer height is approximately $\delta_{99} \approx 0.004 \text{ m}$ in this region. The streamwise velo-



(a) Skin-friction lines including field streamlines colored by absolute velocity V/U_∞ and monitor points for near-wall velocity profile evaluation.



(b) Skin-friction lines including near-wall velocity profiles colored by absolute velocity V/U_∞ that are located along one particular skin-friction line (front view).



(c) Skin-friction lines including near-wall velocity profiles colored by absolute velocity V/U_∞ that are located along one particular skin-friction line (rear view).

Figure 5.34: Flow separation onset characteristics of the AVT-183 configuration at $\alpha = 12^\circ$ (III).

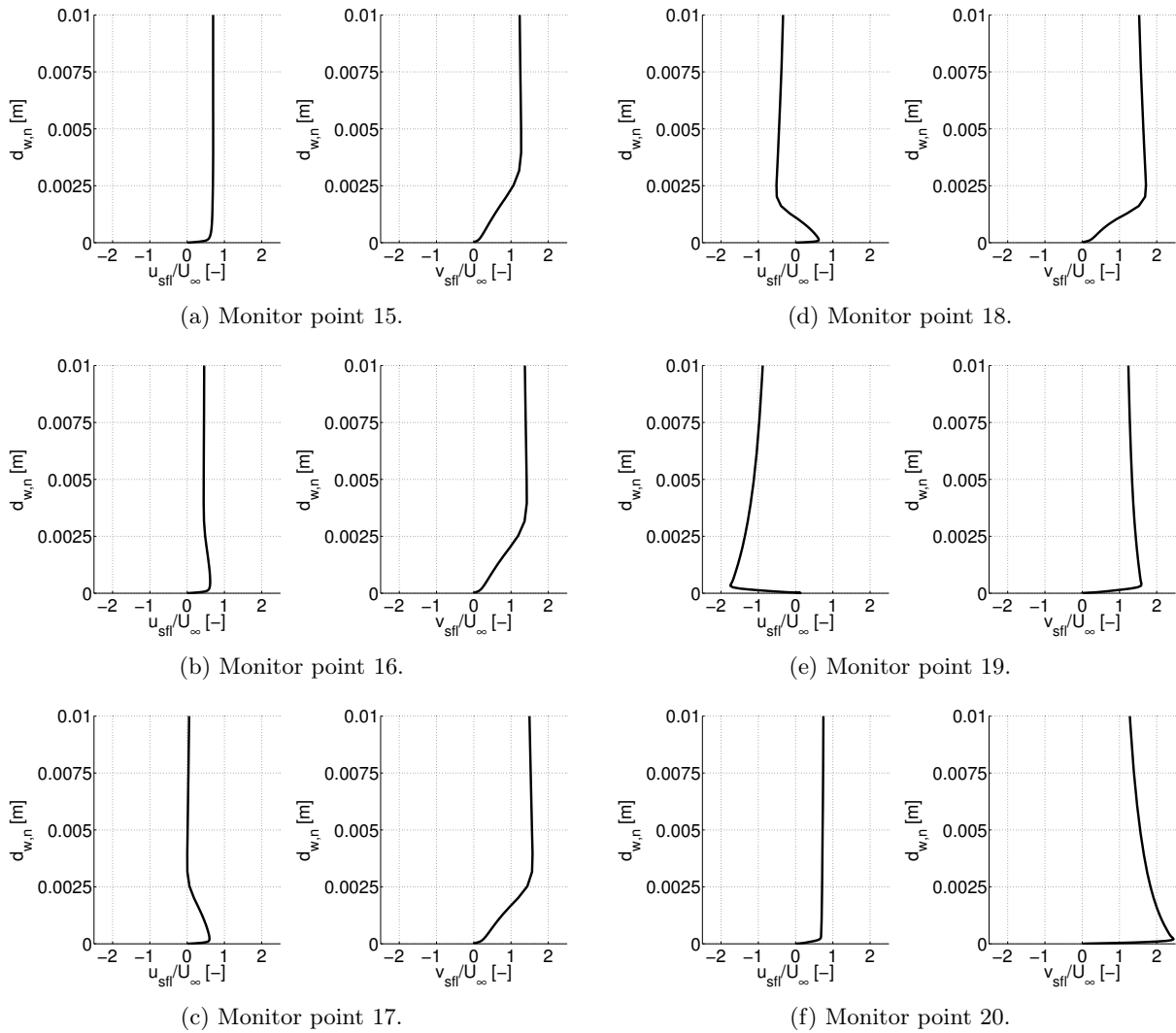


Figure 5.35: Flow separation onset characteristics of the AVT-183 configuration at $\alpha = 12^\circ$ – Near-wall velocity profiles in streamwise and crossflow direction along one particular skin-friction line.

city profiles of the next monitor points 16 and 17 show a local maximum close to the wing surface and locally-decreasing values in normal direction, see Figure 5.35b to Figure 5.35c. The change of sign is finally noticed at monitor point 18, see Figure 5.35d, as it is located close to the leading-edge vortex core and the orientation of the local coordinate system is almost orthogonal to the vortex axis. Moreover, the curve fits to those of the adjacent monitor points 5 and 7 as discussed in Figure 5.33. The crossflow velocity profile at monitor point 18 contains more momentum close to the wing surface than the previous ones, and this trend is amplified towards the location of the primary separation line close to monitor point 19, see Figure 5.35e. There, the positive streamwise component near the wing surface additionally drops out, as the flow separates at the primary separation line and changes almost the entire flow orientation in normal direction. This is also shown in the velocity profiles at monitor point 20, which is already located along the

primary separation line. Due to the reorientation of the skin-friction line and the local coordinate system, the crossflow component then describes the distinct flow deviation, which is induced by the flow separation at the primary separation line. At this location, the crossflow values increase up to $v_{sfl}/U_\infty \approx 2.4$ close to the wing surface. Further downstream, no significant changes are observed in the velocity profiles any longer, since the skin-friction line stays aligned with the primary separation line up to the wing-tip section.

Angle-of-Attack Development

The flow separation onset characteristics in the incipient separation region as observed at $\alpha = 12^\circ$ are likewise found for different angles of attack. There, the flow phenomena occur more up- and downstream, respectively. Consequently, they are characteristic of the AVT-183 configuration, and more generally for a moderately-swept wing configuration with rounded leading edge. In a detailed consideration, minor differences are however present over the angle-of-attack polar. For this reason, Figure 5.36 summarizes the locations of characteristic points on the diamond wing surface versus the angle of attack. On the one hand, designated locations as presented in Figure 5.31a are shown, namely the converging skin-friction lines (1), the origin of the primary separation line (2) and the merging point (4), where the lines (1) and (2) merge together. On the other hand, also the location of the limiting skin-friction lines at the leading edge as introduced in Figure 5.26d to Figure 5.26f is stated each, since it indicates the beginning of the incipient separation region. Considering the results of the chordwise and spanwise locations, the curves show the same trends, but they are slightly shifted. For this reason, the chordwise ratio x/c_r is referenced only in the continuing discussion. Overall, the curves demonstrate that the converging skin-friction lines on the smooth wing surface and the merging point move upstream more distinctly with increasing angle of attack than the origin of the primary separation line. In consequence, this implies a more pronounced role of the boundary-layer vortex at lower angles of attack and vice versa. At $\alpha = 8^\circ$, the beginning of the primary separation line is located at $x/c_r = 0.362$, which is upstream of the

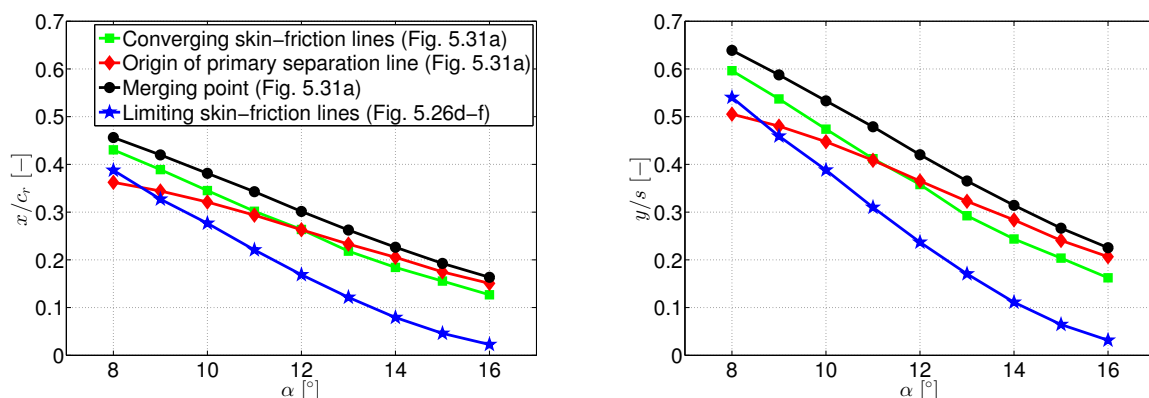


Figure 5.36: Flow separation onset characteristics of the AVT-183 configuration – Location of characteristic points versus angle of attack α .

more inboard converging skin-friction lines at $x/c_r = 0.431$. This is also noticeable from Figure 5.37a, which depicts the flow separation onset characteristics at $\alpha = 8^\circ$ in a three-dimensional view. With increasing angle of attack, the run length of the boundary-layer vortex is reduced, whereas the gap between the converging skin-friction lines on the smooth wing surface and the merging point remains rather constant with $\Delta x/c_r \approx 0.037$, see Figure 5.36. As a result, the curves intersect at $\alpha \approx 12^\circ$, where both characteristic points occur at $x/c_r = 0.263$. From then on, the converging skin-friction lines occur upstream of the origin of the primary separation line. At $\alpha = 16^\circ$, the converging skin-friction lines are observed at $x/c_r = 0.127$, and the primary separation line starts at $x/c_r = 0.151$. Overall, this results in the flow field characteristics as shown in Figure 5.37b.

At the angle of attack of $\alpha = 8^\circ$, the limiting skin-friction lines of the incipient separation region further start downstream of the boundary-layer vortex formation, see Figure 5.37a. Compared

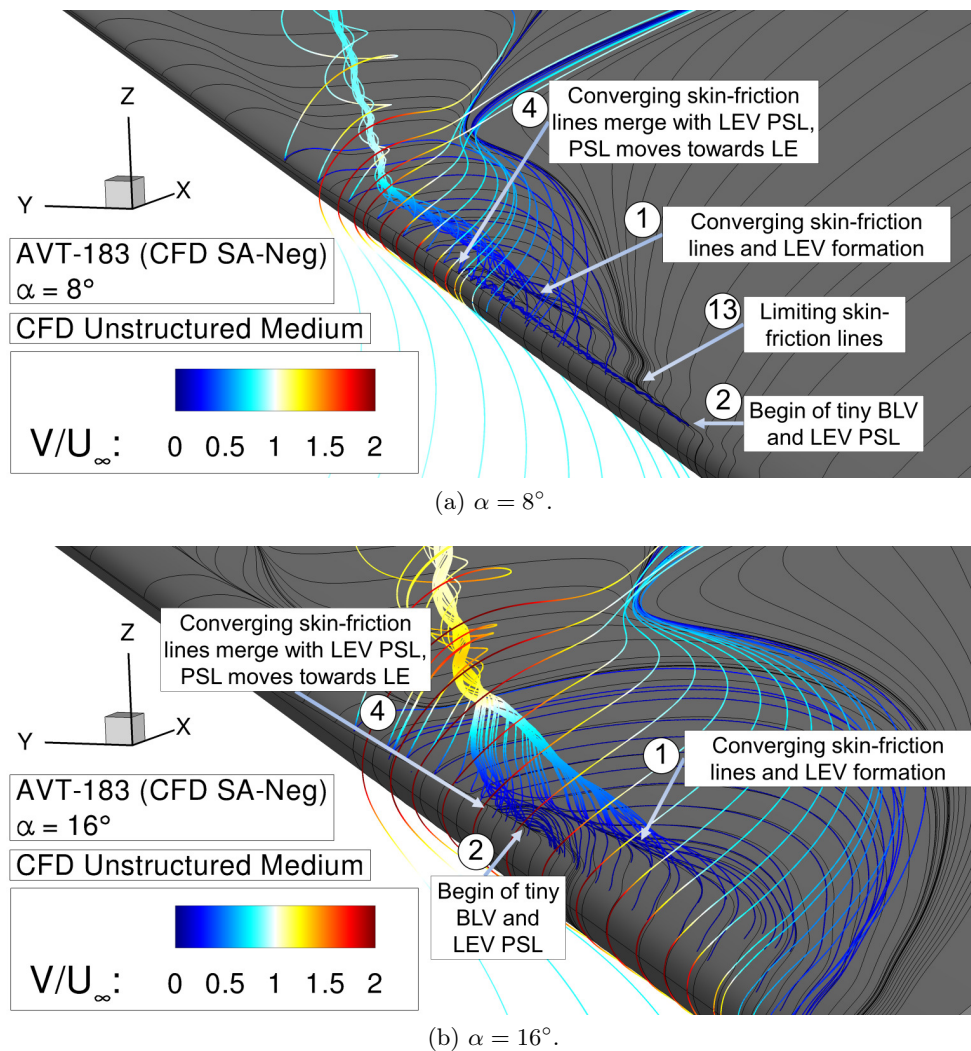


Figure 5.37: Flow separation onset characteristics of the AVT-183 configuration – Skin-friction lines including field streamlines colored by absolute velocity V/U_∞ .

to the resulting flow physics at $\alpha = 12^\circ$ and $\alpha = 16^\circ$, see Figure 5.31b and Figure 5.37b, the changed location of the limiting skin-friction lines is directly noticeable (13). In this case, the first occurrence of the incipient separation region is marked by the emerging boundary-layer vortex. With increasing angle of attack, the leading-edge location of the limiting skin-friction lines moves upstream with respect to the origin of the primary separation line, see Figure 5.36. Thus, the skin-friction patterns as observed in Figure 5.31b and Figure 5.37b are relevant again. The upstream movement of the limiting skin-friction lines is slightly more pronounced than that of the characteristic points (1) and (4). As a result, the incipient separation region grows in size with increasing angle of attack. For $\alpha \geq 14^\circ$, the gradient of the corresponding curves is finally reduced, since the beginning of the incipient separation region already reaches the peniche of the diamond wing configuration. Thereby, the upstream movement of the flow separation onset is attenuated.

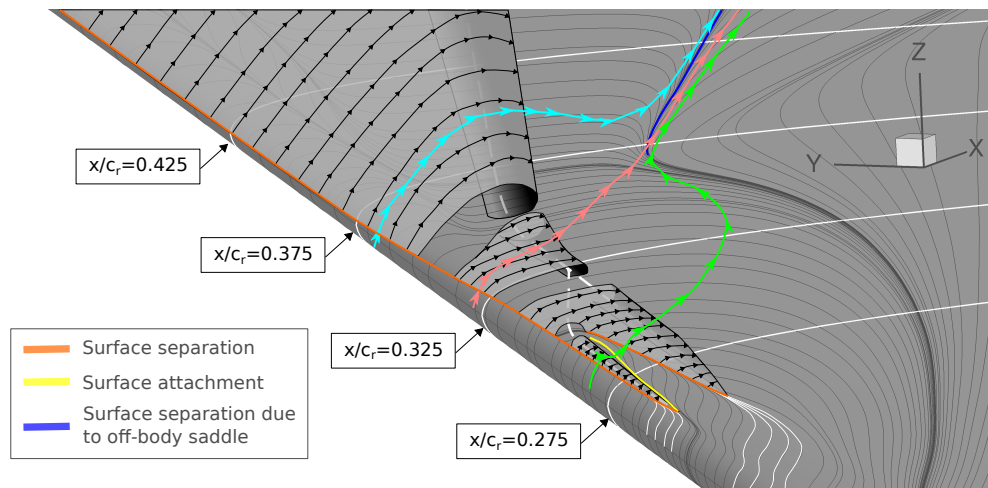
5.2.4 Flow Topology Interpretation

Subsequent to the flow physics analysis and the description of the flow separation onset characteristics, the flow topology associated with the flow field around the AVT-183 configuration is discussed. The results presented in the previous sections have shown the complex formation of the partly-developed leading-edge vortex, its progression as a large-scale structure on the diamond wing surface, and other occurring flow phenomena such as the "inner vortex". For a complete flow-physical interpretation of three-dimensional separation effects and attached flow regions, the topological rules as introduced in Section 2.2 must be valid. At this point, Equation 2.5 is recalled, which describes the topological rule for a cross-flow plane cutting a three-dimensional body. For the continuing discussion, it is rewritten as

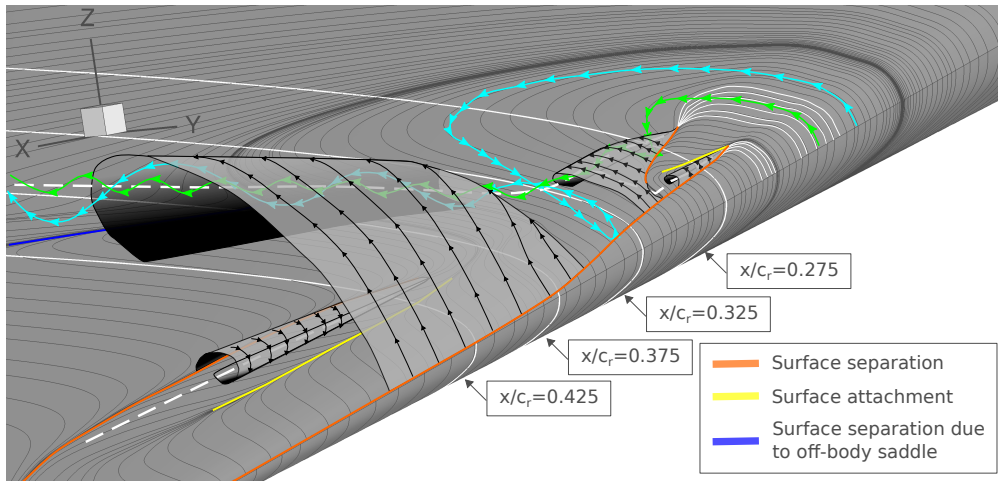
$$\sum N - \sum S + \frac{1}{2} \sum (N'_A + N'_S) - \frac{1}{2} \sum (S'_A + S'_S) = -1 . \quad (5.1)$$

Figure 5.38 to Figure 5.40 depict the final flow topology interpretation, which has been derived from the findings of the previous sections. The topological interpretation is further based on sectional contour streamline data, from which the flow direction around the diamond wing surface has been accessible at each location. The peniche is not accounted for in the evaluation of the topological rule, but the semi-span wing is theoretically mirrored to fulfill the equation. For a better representation of the associated flow phenomena, finally the sectional drawings are not true to scale, especially in the incipient separation region.

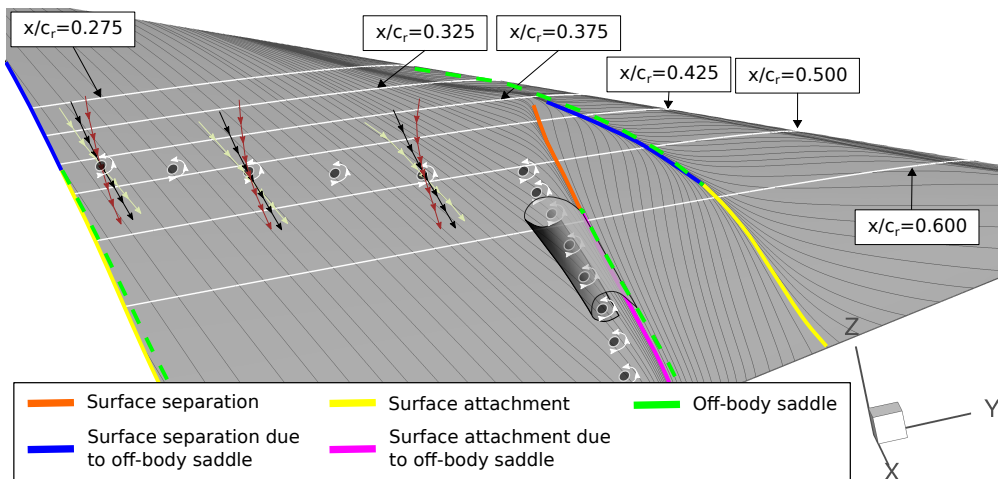
At first, the leading-edge vortex formation is considered, see Figure 5.38a. The sketch highlights the two characteristic structures for the vortex development, namely the tiny boundary-layer vortex and the more inboard three-dimensional flow separation that forms the leading-edge vortex core. Due to the rounded leading-edge contour, both structures occur on the wing surface as smooth surface separations. More downstream, they merge together and the leading-edge vortex finally appears as a continuously-growing large-scale structure. The corresponding flow topology



(a) Front view.



(b) Rear view (I).



(c) Rear view (II).

Figure 5.38: Flow topology interpretation of the AVT-183 configuration at $\alpha = 12^\circ$ – Three-dimensional views.

in two associated chordwise sections is presented in Figure 5.39a and Figure 5.39b. In the more upstream chordwise section at $x/c_r = 0.275$, the two smooth surface separations are noticeable. In between, the flow reattaches to the wing surface. Inboard of the inner vortical formation, however, the flow does not reattach again, but a saddle point is observed in the near-wall flow field. In consequence, the flow in the inboard wing section is directed outward close to the wing surface, and the plane of symmetry is represented by a half-node of separation. Due to the flow reorientation prescribed by the saddle point, the inboard flow further moves back towards the symmetry plane in normal direction offside the wing surface. The topological observation thus indicates a strong flow shear in this region. In the second chordwise section at $x/c_r = 0.325$, the two emanating vortices have merged and the point of separation slightly moves towards the leading edge. Apart from that, the same singular points as observed before are found. The saddle point and the separation half-nodes in the symmetry plane though attract attention, since they do not occur in classical singular-point arrangements associated with highly-swept delta wing configurations and sharp leading edges. Hence, they must be the result of the changed flow field characteristics induced by the rounded leading edge and the reduced wing sweep, which accumulates to the existence of the incipient separation region.

Next, the large-scale progression of the leading-edge vortex is discussed, see Figure 5.38b. The vortical structure grows in size and intensity, which comes along with a vertical and inward displacement of the vortex core axis in downstream direction. Furthermore, the secondary vortex is formed in consequence of the pressure gradient towards the primary separation line. It acts as a counter-rotating vortical structure close to the diamond wing surface. Figure 5.39c and Figure 5.39d depict the associated flow topology interpretation in additional chordwise sections. At $x/c_r = 0.375$, the singular-point arrangement does not change to the previous sectional cut, but the shape of the leading-edge vortex is different due to the large-scale appearance. At $x/c_r = 0.425$, the flow topology interpretation then becomes more complex. On the one hand, the secondary vortex is now present in the flow topology pattern. It involves an additional focus that is counted as a node, and a half-saddle of separation and attachment, respectively. On the other hand, the inboard flow field significantly changes in the sectional consideration, which leads to a modification of the singular points in the inboard wing section. In the plane of symmetry, the surface points on both the pressure and the suction side alter to attachment half-saddles. Moreover, a saddle point is present on the suction side, which is fed by the off-body saddle point located close to the leading-edge vortex. In consequence, the wing surface features additional singular points that represent separations of half-node and half-saddle type, respectively. Designated contour streamlines finally indicate a distinct rotation center close to the plane of symmetry, which is counted as a focus and is fed by the separation half-saddle. Altogether, the topological rule is valid and the flow directions of associated contour streamlines are considered to the full extent. Figure 5.38c resolves the singular points for a better consideration in a three-dimensional view. The connection to the skin-friction patterns at the wing surface is thereby highlighted. It turns out that the primary attachment line of the leading-edge vortex as introduced in Figure 5.26 is

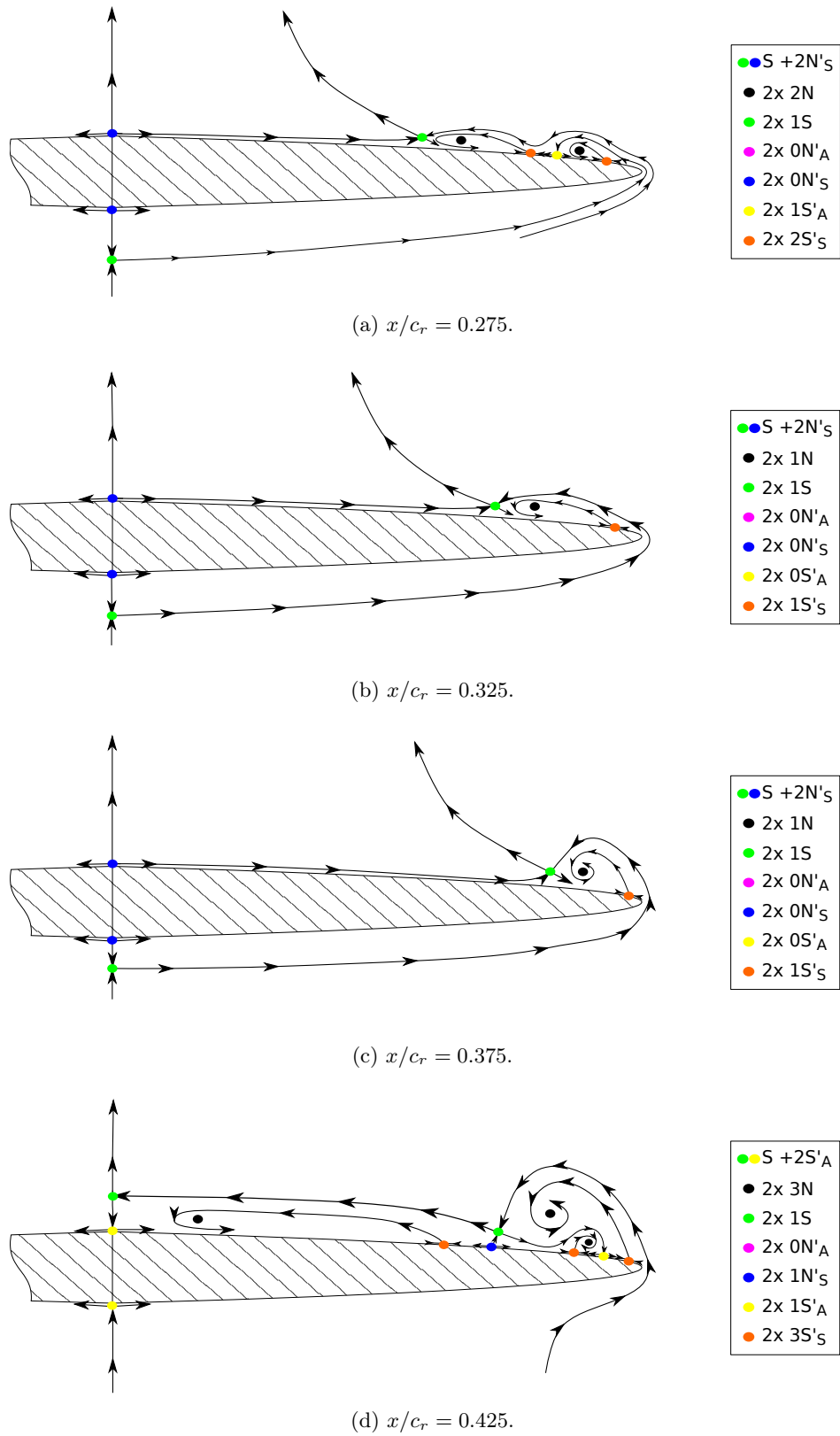


Figure 5.39: Flow topology interpretation of the AVT-183 configuration at $\alpha = 12^\circ$ – Sectional cuts (I).

in fact a separation line. The flow separation of half-node type thus links the wing surface with the saddle point in the near-wall flow field, where the leading-edge vortex in fact "reattaches". The more inboard separation half-saddle is connected to the converging skin-friction lines, at which the "inner vortex" finally develops more downstream. From a topological point of view, the flow does formally not attach before the plane of symmetry in this chordwise section. With respect to the actual flow field, however, the observed rotation in the sectional view just depicts the flow shear in the near-wall flow field of the inboard wing section. This is schematically indicated in Figure 5.38c by the near-wall field streamlines in various chordwise sections. In this context, the corresponding rotation centers define the locations, at which the passing streamlines do not feature any lateral and normal velocity component, either. As a result of the occurring flow shear and the wing surface curvature, the center of rotation moves outward in downstream direction. This is also noticeable in the sectional flow topology interpretation at $x/c_r = 0.500$, see Figure 5.40a. Compared to the previous sectional cut, the same singular points are relevant, but the vortical structures become more distinct and the rotation center of the inboard flow shear is shifted towards the separation half-saddle. Slightly more downstream, the center of rotation finally aligns with the converging skin-friction lines that are formed due to the confluent boundary layers, see Figure 5.38c. From then on, the rotation center is almost stable in spanwise direction.

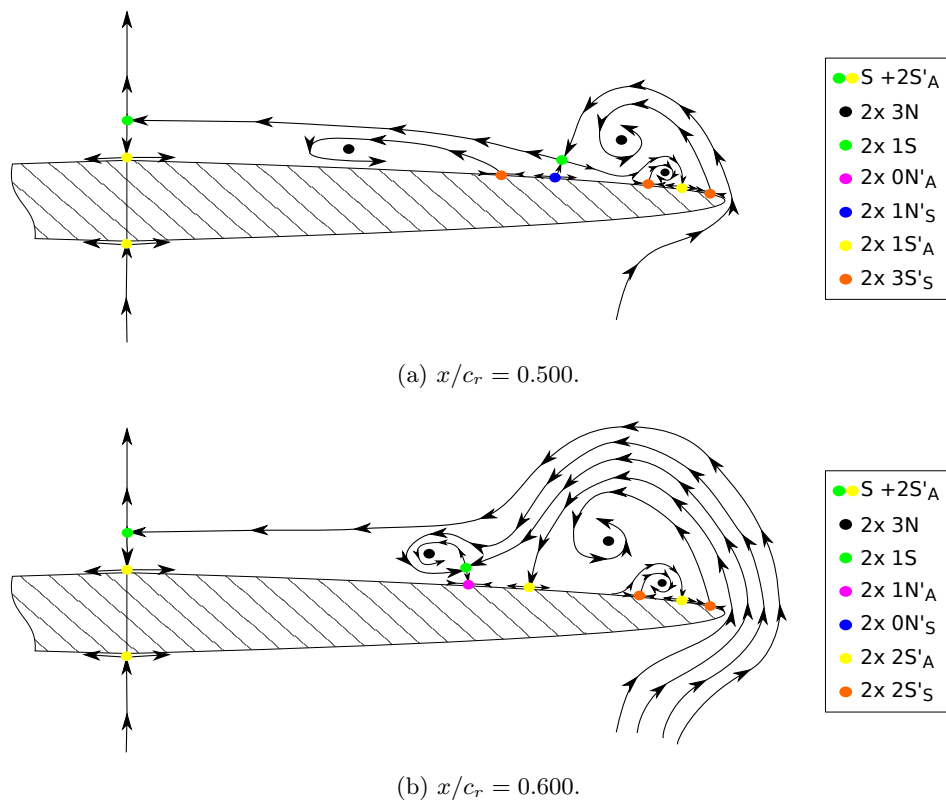


Figure 5.40: Flow topology interpretation of the AVT-183 configuration at $\alpha = 12^\circ$ – Sectional cuts (II).

At the chordwise position of $x/c_r = 0.600$, another change in the sectional flow topology is finally observed, see Figure 5.40b. The half-saddle separation of the inboard flow shear region alters to a combination of attachment half-node and off-body saddle point in the near-wall flow field. Consequently, the flow separation is displaced from the wing surface to the near-wall flow field and the converging skin-friction lines now define an attachment line. Simultaneously, this bears consequences to the flow topology of the leading-edge vortex. This time, the flow directly reattaches at the wing surface by an attachment half-saddle that replaces the off-body saddle point and the separation half-node. See in this context also the experimental PIV results of Figure 5.12k and Figure 5.12l, which show the same transformation and thus confirm the numerical findings. The contour streamlines that enclose the designated attachment streamline therefore feed the inboard off-body saddle point and restrict the region, in which the rotation center of the flow shear is concentrated. The "inner vortex" is thereby formed, but the structure does not feature increased axial fluid transport due to the off-body development, compare Figure 5.28 and Figure 5.29. Altogether, the topological interpretation is thus consistent with the observed flow field characteristics. Figure 5.38c summarizes the modified types of the singular points along the designated skin-friction lines in the downstream wing sections. The off-body separation and the vortex sheet of the "inner vortex" are also highlighted in this context.

5.2.5 Synthesis

This section has covered the numerical investigations of the AVT-183 configuration, and the discussion has mainly concentrated on the angle of attack of $\alpha = 12^\circ$. Based on the experimental results, the numerical method has been validated first. Then, a flow physics analysis has been presented, which supports the experimental findings of Section 5.1. Thereafter, the flow separation onset characteristics have been evaluated. The formation of the leading-edge vortex in the incipient separation region has thereby been characterized. Finally, a flow topology interpretation of the flow field characteristics has been derived, summarizing the findings on the partly-developed leading-edge vortex at the AVT-183 configuration. Altogether, the following conclusions can thus be drawn:

Validation of the Numerical Method

- The chosen numerical set-up results in reliable predictions of the flow field characteristics and the integral aerodynamic coefficients. The medium grid resolution ($15.4 \cdot 10^6$ grid points, initial wall-normal spacing of 0.003 mm) is sufficient to achieve grid independence.
- The corresponding numerical results are in very good agreement with experimental data, especially with respect to the flow field investigations. The integral values of the computed lift and pitching-moment coefficients slightly deviate from the experimental values. If appropriate W/T corrections are considered additionally, the agreement between the numerical and experimental results is significantly increased.

Flow Physics Analysis

- The numerical investigations expand the experimental results by additional information that is accessible at the wing surface and within the flow field. The skin-friction patterns on the diamond wing surface depict all relevant flow phenomena, such as the partly-developed leading-edge vortex, the secondary vortex separation, the inboard attached flow, and the "inner vortex" induced by confluent boundary layers in the inboard rear wing section.
- Upstream of the visible appearance of the leading-edge vortex, the vortical structure develops on boundary-layer level in the incipient separation region ($\delta_{99} \approx 0.002 \text{ m}$). The area is confined by limiting skin-friction lines, which define whether the flow remains in the inboard wing section or is relevant for the smooth surface separation with leading-edge vortex formation. At $\alpha = 12^\circ$, the incipient separation region begins at $x/c_r \approx 0.17$ while the first large-scale appearance of the vortical structure is at $x/c_r \approx 0.34$.
- The instantaneous wake-type character of the leading-edge vortex is confirmed by the numerical results. Closely downstream of the "visible" appearance of the vortical structure, the absolute velocity in the vortex core flow is already reduced and shows values of $V/U_\infty \leq 0.8$. The corresponding values of the axial vorticity further prove the vortex bursting tendencies, as they decrease significantly towards the more downstream wing sections.

Flow Separation Onset Characteristics

- Two main flow field phenomena are relevant for the leading-edge vortex formation in the incipient separation region. On the one hand, converging skin-friction lines on the smooth wing surface induce a three-dimensional flow separation, which is the origin of the leading-edge vortex core ($x/c_r \approx 0.26$). On the other hand, a tiny boundary-layer vortex is observed at approximately the same chordwise location, but closer to the wing leading edge. It is present only for a short run length and later feeds the emerging leading-edge vortex. Thereby, the origin of the primary separation line is defined.
- The leading-edge vortex remains within the incipient separation region on boundary-layer level. It is disconnected from the wing surface and is not discernible in the skin-friction patterns. At $\alpha = 12^\circ$, the expansion of the vortex core axis in normal direction is around $d_{w,n} \approx 0.003 \text{ m}$. At $x/c_r \approx 0.34$, the vortical structure finally appears as a large-scale leading-edge vortex and escapes significantly from the wing surface.
- The analysis of near-wall velocity profiles shows strongly distorted flow directions in the proximity of the wing surface. Attached flow from far upstream in the incipient separation region returns below the leading-edge vortex core axis to the wing leading edge and separates at the primary separation line. Thereby, the vortical structure is fed and grows in size and intensity.

- The flow separation onset characteristics do not differ with the angle of attack, but the relative location of the more inboard converging skin-friction lines alters compared to the beginning of the primary separation line. At lower angles of attack, the boundary-layer vortex is more distinct and occurs upstream of the converging skin-friction lines. With increasing angle of attack, the opposite case is noticed, as the run length of the boundary-layer vortex is significantly reduced.

Flow Topology Interpretation

- The evaluation of the corresponding topological rule in sectional cuts confirms the complex flow topology of the associated vortical flow field. All relevant flow phenomena are captured by respective singular points, but the observed arrangements change from upstream to downstream chordwise sections. To the author's information, this is beyond the state-of-the-art knowledge. The findings are characteristic of moderately-swept and vortex-dominated wing configurations with rounded leading-edge contour.
- After its formation, the leading-edge vortex does at first not reattach to the wing surface, but to an off-body saddle point within the near-wall flow field. Therefore, diverging skin-friction lines in this region mark a separation line of half-node type instead of an attachment line of half-saddle type.
- More downstream, the "inner vortex" is formed by confluent boundary layers, which diverge along an off-body line of saddle points. The converging skin-friction lines on the wing surface thus define an attachment line of half-node type, which is connected to the off-body saddle points. The flow topology of the leading-edge vortex thereby alters as well, and the flow reattaches again with an attachment half-saddle to the wing surface.

Chapter 6

Passive Flow Control by Leading-Edge Contour Modifications

This chapter presents the overall results that were derived for the SAGITTA configuration. First of all, the reference configuration SG Geo 1 is considered in detail, see Section 6.1. The numerical method is validated and the aerodynamic characteristics of the diamond wing configuration are discussed based on experimental and numerical results. Both the longitudinal and the lateral motion are regarded. The analysis includes aerodynamic forces and moments, surface pressures, and near-wall flow field data. The section thus constitutes the basis for the further analysis in the present chapter. The following sections concentrate on numerical results only. Section 6.2 depicts the flow physics of the diamond wing configurations with completely sharp and rounded leading edges, namely SG Geo 5 and SG Geo 6. The differences in the flow field characteristics and the aerodynamic coefficients compared to the reference configuration SG Geo 1 are assessed, especially with respect to the longitudinal stability behavior. In the context of the overall analysis, these leading-edge shape configurations represent comparison cases, which are used to identify and evaluate differences in the aerodynamic characteristics of wing configurations with spanwise-varying leading-edge contours. Three of them are treated in Section 6.3 and Section 6.4, namely the corresponding configurations SG Geo 2 to SG Geo 4. To some extent, they were already regarded in a pre-publication of the author [67]. The focus of the present discussion is laid on the detailed near-wall flow field analysis and the stability behavior in the longitudinal motion. The occurring flow phenomena associated with the spanwise-varying leading-edge contours are thereby investigated. In comparison to the reference configuration SG Geo 1, concepts of passive flow control by leading-edge contour modifications are thus assessed.

6.1 Reference Configuration

6.1.1 Validation of the Numerical Method

In accordance with the investigations on the AVT-183 configuration, a grid sensitivity study was carried out for the SAGITTA configuration to validate the accuracy of the computed results. Three different grid resolutions as introduced in Section 4.2.2 are considered for the reference configuration SG Geo 1. Subsequently, the computed data is compared to experimental values.

Grid Sensitivity Study

Figure 6.1 depicts the overall y^+ values for the medium grid resolution with increasing angle of attack. Since the different grids each share the same initial wall spacing, the y^+ values of the coarse and the fine grid resolution are not shown. The criterion of $y^+_{Max} = 1$ is matched quite well on the wing surface over the entire angle-of-attack polar. Close to the inboard sharp leading edge, increased y^+ values are noticed in the region of the emerging leading-edge vortex. With increasing angle of attack, the y^+ values reach the target value of $y^+_{Max} = 1$, but the maximum values do not exceed $y^+_{Max} \approx 1.2$. At the angle of attack of $\alpha = 24^\circ$, see Figure 6.1d, the increased y^+ values in the midboard wing section additionally give indication for a second vortex separation, which occurs on the smooth surface offside the leading edge. In the wing-tip region, considerably decreased y^+ values are observed, which is due to occurring flow separation effects. In sum, Figure 6.1 confirms that the desired wall resolution of $y^+_{Max} = 1$ is mostly ensured for the entire angle-of-attack polar. This demonstrates a reasonable choice of the initial wall spacing that was applied in the grid generation process of the SAGITTA configuration.

Next, the CFD computations of the different grid resolutions are discussed with respect to the aerodynamic coefficients. For the angle of attack of $\alpha = 12^\circ$, the longitudinal force and moment coefficients are exemplarily presented, see Table 6.1 and Figure 6.2. The corresponding experimental results of the case W/T Forced Transition 150mu Dots are stated as well. This time, the uncorrected W/T data is presented exclusively, since W/T corrections are not needed in this case. Considering the numerical results, the values of the aerodynamic coefficients C_D and C_L vary only slightly between the coarse and the medium grid resolution. For the fine grid resolution, even the same values are derived. The pitching-moment coefficient C_{my} is predicted almost

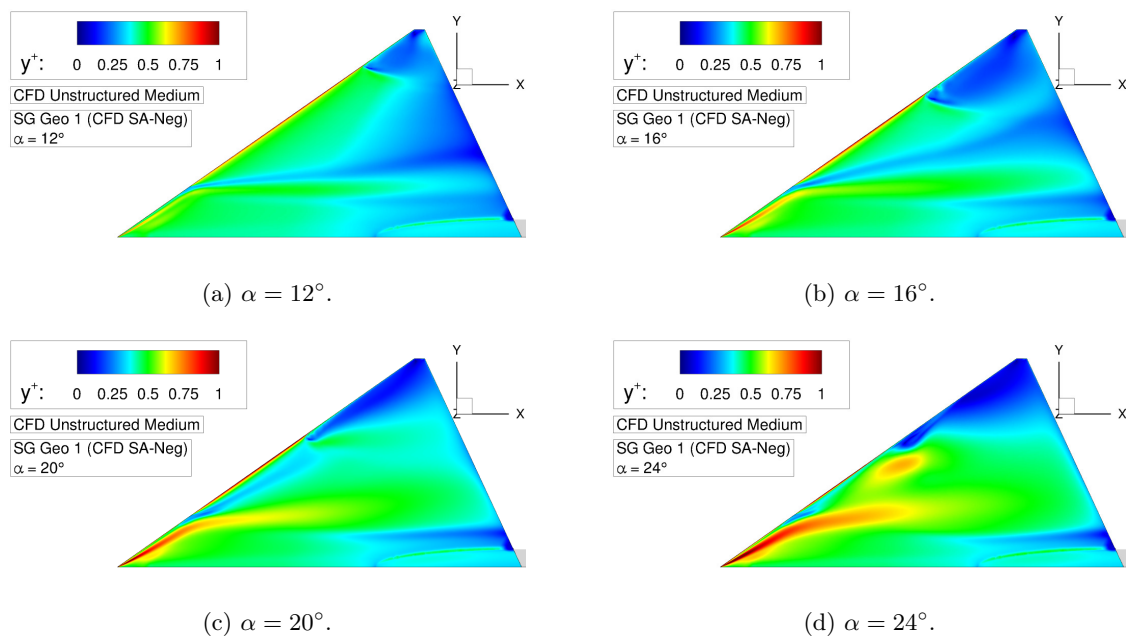


Figure 6.1: CFD validation of configuration SG Geo 1 – Computed y^+ levels.

identically by all the different grid resolutions. Compared to the experimental reference data, the three grid resolutions provide similar values, respectively. Overall, the agreement between the CFD and the W/T results is thus very satisfying. The lift coefficient C_L deviates from the W/T experiment at $\alpha = 12^\circ$ by only 0.5%, and the maximum deviation of the drag coefficient C_D is less than 3%. The pitching-moment coefficient C_{my} shows a deviation of approximately 8% to the W/T experiment at $\alpha = 12^\circ$. Due to the small absolute value and the known sensitivity of the pitching-moment coefficient, however, the result is still sufficiently accurate. Further analyses of the aerodynamic coefficients, the surface pressures, and the near-wall flow field characteristics

	Coarse Grid Resolution	Medium Grid Resolution	Fine Grid Resolution	Experiment (Forced Transition 150mu Dots)
C_L	0.4743	0.4739	0.4739	0.4761
C_D	0.0611	0.0620	0.0620	0.0603
C_{my}	-0.0363	-0.0363	-0.0362	-0.0335

Table 6.1: CFD validation of configuration SG Geo 1 – Longitudinal aerodynamic coefficients for different grid resolutions at $\alpha = 12^\circ$.

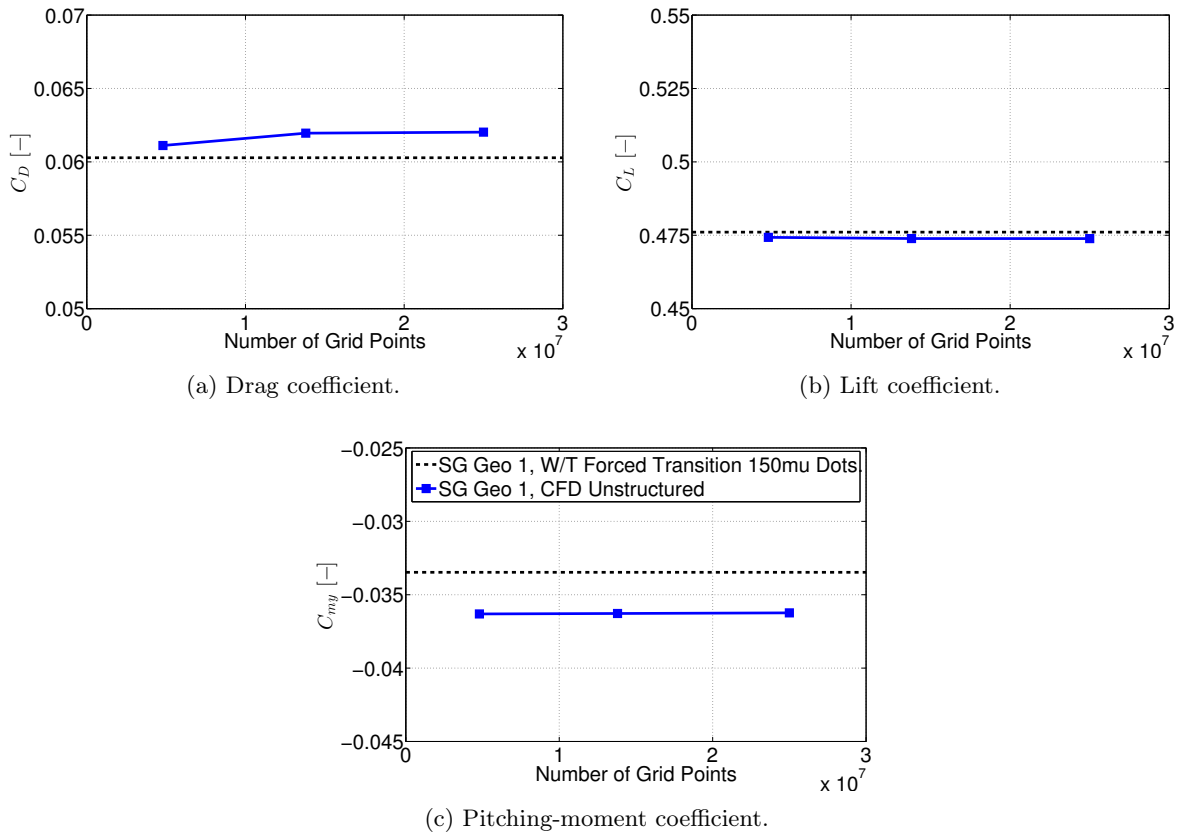


Figure 6.2: CFD validation of configuration SG Geo 1 – Longitudinal aerodynamic coefficients for different grid resolutions at $\alpha = 12^\circ$.

confirm the grid independence of the CFD computations for different angles of attack, at least for the medium and the fine grid resolution. Based on the comparison of the resulting differences and the required computational effort, the medium grid resolution was therefore selected as the baseline grid for the further CFD computations. For this reason, the grids of the other regarded configurations SG Geo 2 to SG Geo 6 were generated with the parameter set of the medium grid resolution of configuration SG Geo 1, see Section 4.2.2. In this context, Table 4.3 summarizes the resulting total number of grid points for all considered cases of the SAGITTA configuration.

Comparison to Experimental Data

To expand the comparisons of numerical results and experimental reference data, further investigations are presented. At first, the longitudinal force and moment coefficients of the reference configuration SG Geo 1 are shown for both the CFD and the W/T results versus the angle of attack, see Figure 6.3. The experimental data corresponds to the case with flow tripping (case W/T Forced Transition 150 μ Dots), and the numerical results are given for the medium grid resolution. The overall agreement between both data sets is found to be very good. For the lift

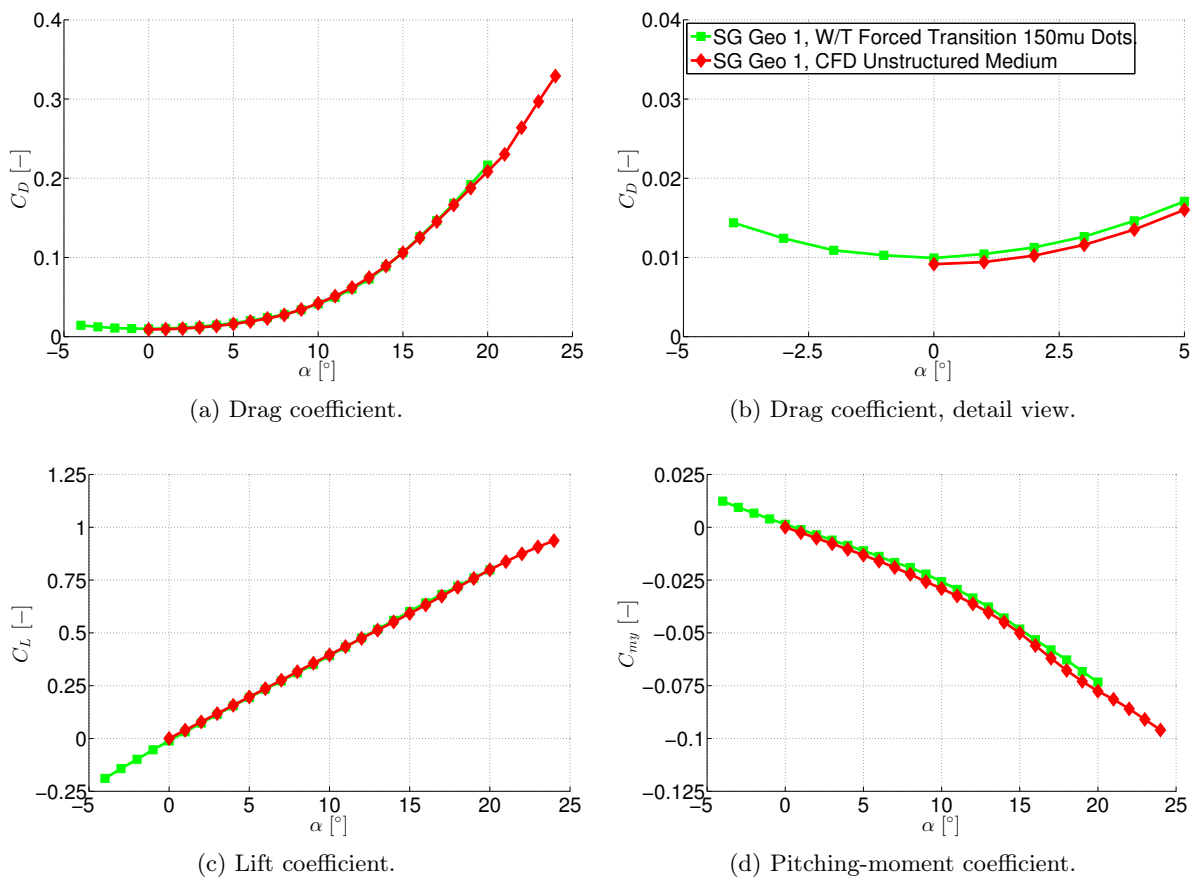


Figure 6.3: CFD validation of configuration SG Geo 1 – Longitudinal aerodynamic coefficients versus angle of attack α .

coefficient, an excellent match is observed over the entire angle-of-attack polar, see Figure 6.3c. The corresponding lift slope is about $C_{L,\alpha} \approx 2.3$, but beginning with $\alpha \approx 20^\circ$, it slightly decreases. The stall angle of attack is however not reached before $\alpha_{max} = 36^\circ$, which was observed in preliminary numerical analyses of the SAGITTA configuration. For comparison, Figure 6.4 depicts the associated results, and the maximum lift coefficient is obtained at $C_{L,max} \approx 1.17$. The drag coefficient characteristics are also predicted very accurately by the CFD investigations, see Figure 6.3a. With regard to low angles of attack, only small deviations are noticed, see Figure 6.3b. Moreover, the zero-lift drag coefficient is computed very similarly to the experimental value, which was obtained due to the application of the trip dots ($C_{D,0,W/T} = 0.0099, C_{D,0,CFD} = 0.0091$). The general effect of flow tripping at the SAGITTA configuration compared to the free transition case can be found in Reference [67]. The pitching-moment coefficient exhibits a small offset between both data sets as introduced above. However, the deviations remain constant over the entire angle-of-attack polar, see Figure 6.3d. A sufficient accurate match is thereby obtained. The corresponding pitching-moment slope ranges between $-0.35 \leq C_{my,\alpha} \leq -0.15$. The lower values are observed with increasing angle of attack. In sum, the generated grids and the applied numerical parameters thus lead to very reliable predictions of the longitudinal aerodynamic coefficients. For the lateral motion, this holds likewise, especially for low to medium angles of attack. In this context, Appendix C presents the lateral aerodynamic coefficients for a sideslip angle of $\beta = -10^\circ$. Up to $\alpha \approx 10^\circ$, very good correlations are found. With increasing angle of attack, deviations between the CFD and the W/T results become obvious, thus showing differences in the prediction of the occurring asymmetric flow phenomena. The reliability of the numerical method, however, is therefore not impaired.

Next, the longitudinal flow field characteristics are considered. Figure 6.5 and Figure 6.6 depict them for three different angles of attack. The experimental data is shown on the left-hand side and originates from the conducted Stereo PIV investigations. The right-hand side depicts the numerical results. Similar to the prediction of the longitudinal aerodynamic coefficients, the agreement between the CFD and the W/T results is found to be very good. With increasing angle of attack, the flow field is characterized by an inboard leading-edge vortex, which originates from

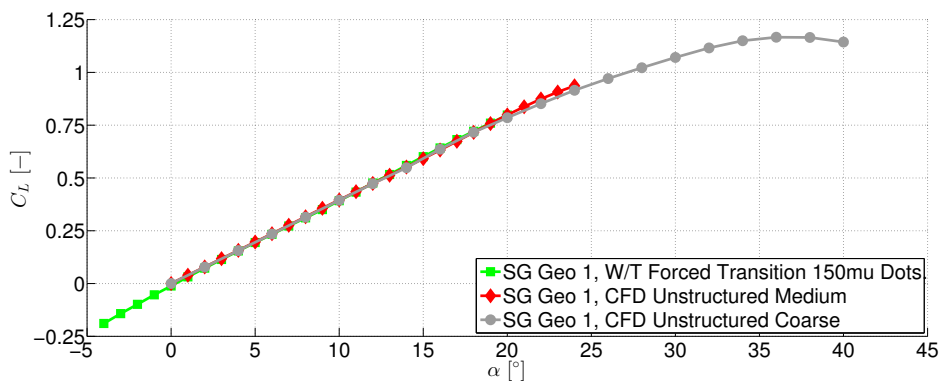


Figure 6.4: CFD validation of configuration SG Geo 1 – Lift coefficient versus angle of attack α .

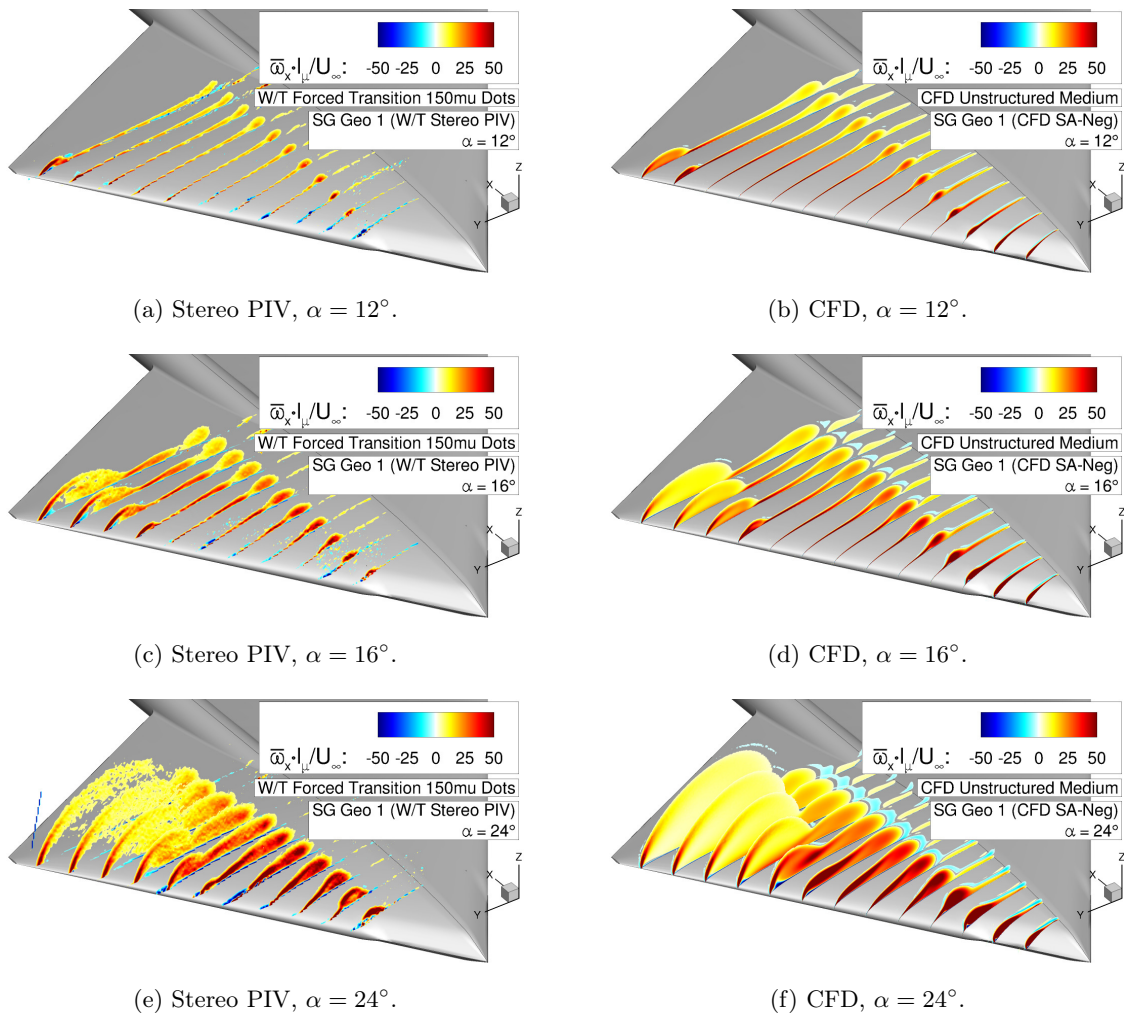


Figure 6.5: CFD validation of configuration SG Geo 1 – Axial vorticity contours $\overline{\omega}_x \cdot l_\mu / U_\infty$.

the inboard sharp leading edge, and an outboard region of irregular separated flow, which finally alters to a midboard leading-edge vortex. In this context, Section 6.1.2 presents a detailed flow physics analysis for configuration SG Geo 1. The two flow phenomena are predicted very similarly in both the numerics and the experiments. The intensity levels of the axial vorticity component in Figure 6.5 and the absolute velocity in Figure 6.6 further highlight the good agreement of the CFD analyses in comparison to the W/T investigations. Just for the inboard leading-edge vortex core flow, less distinct velocity deficits are observed in the numerical predictions. Furthermore, the CFD analyses show a slightly larger midboard and outboard separation region.

Finally, the surface pressure coefficients are compared to each other. Figure 6.7 depicts experimental and numerical results for the three angles of attack as considered above. On the left-hand side, the chordwise section of $x/c_r = 0.2$ is regarded. On the right-hand side, the results obtained at $x/c_r = 0.5$ can be found. Overall, the plots again indicate the good agreement between the CFD and the W/T results. At the chordwise section of $x/c_r = 0.2$, one can notice the pressure peak of the inboard leading-edge vortex at approximately $y/s(x) \approx 0.8$. Due to the transition

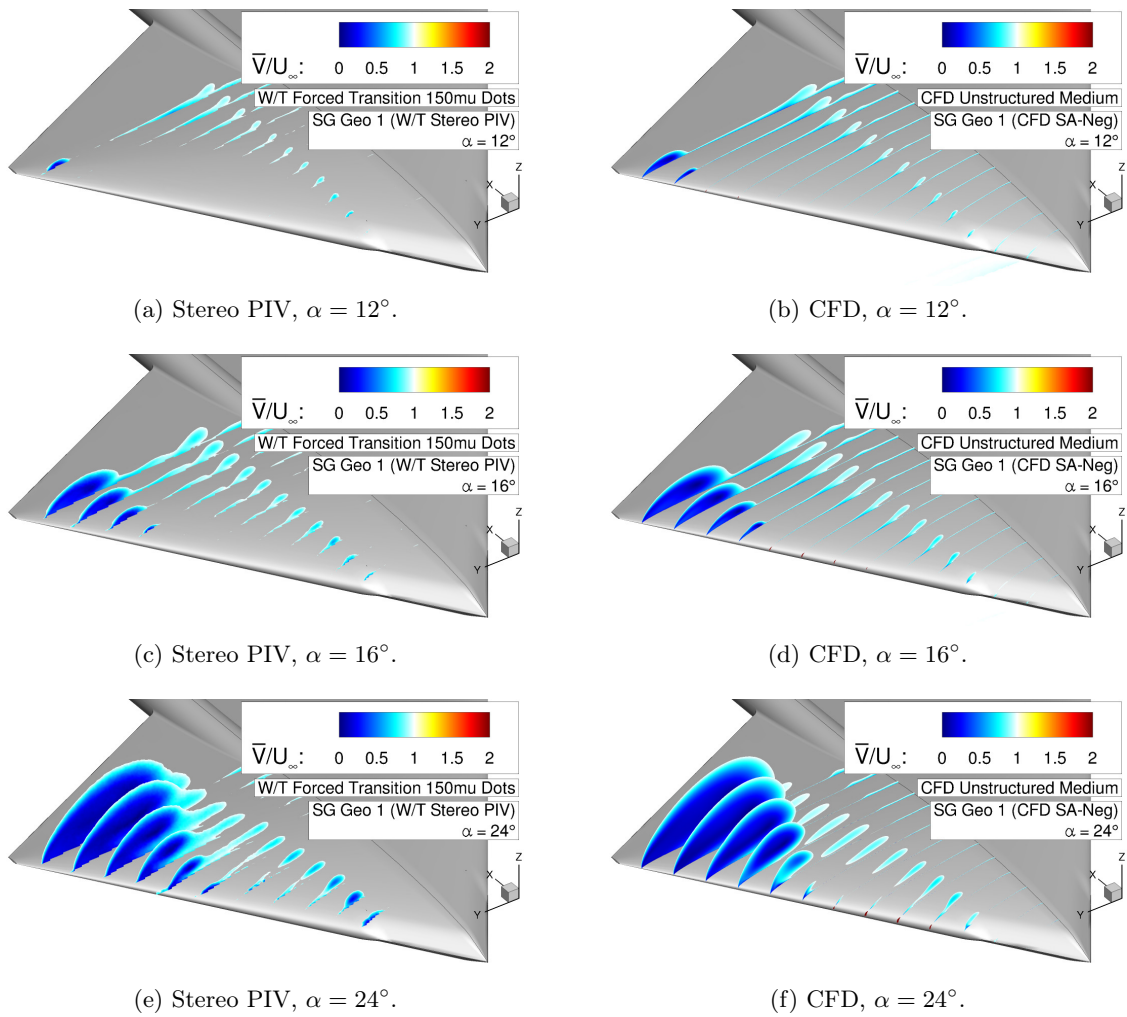


Figure 6.6: CFD validation of configuration SG Geo 1 – Absolute velocity contours \bar{V}/U_∞ .

from the sharp to the rounded leading-edge shape, the structure has detached from the leading edge. See also Section 6.1.2 for a more detailed analysis. The position and the strength of the inboard leading-edge vortex are predicted quite comparably by both approaches. Moreover, the leading-edge suction peaks fit well together. In particular, this is noticed for the more downstream chordwise section at $x/c_r = 0.5$. Only for higher angles of attack, at which the outboard flow separation moves upstream, small deviations can be observed between the results of the CFD investigations and the W/T experiments. To emphasize the agreement of the surface pressure predictions even more, Appendix C states additional results with present sideslip angle. With increasing angle of attack, slight differences become obvious in the computed and measured results while otherwise the agreement is satisfying.

In summary, the present section proves the overall validity of the numerical method that was applied in the CFD analyses. Compared to the W/T results, the occurring vortical structures in the flow field are predicted well. Consequently, the numerical set-up used for the reference configuration SG Geo 1 was also applied to the other considered cases of the SAGITTA configuration.

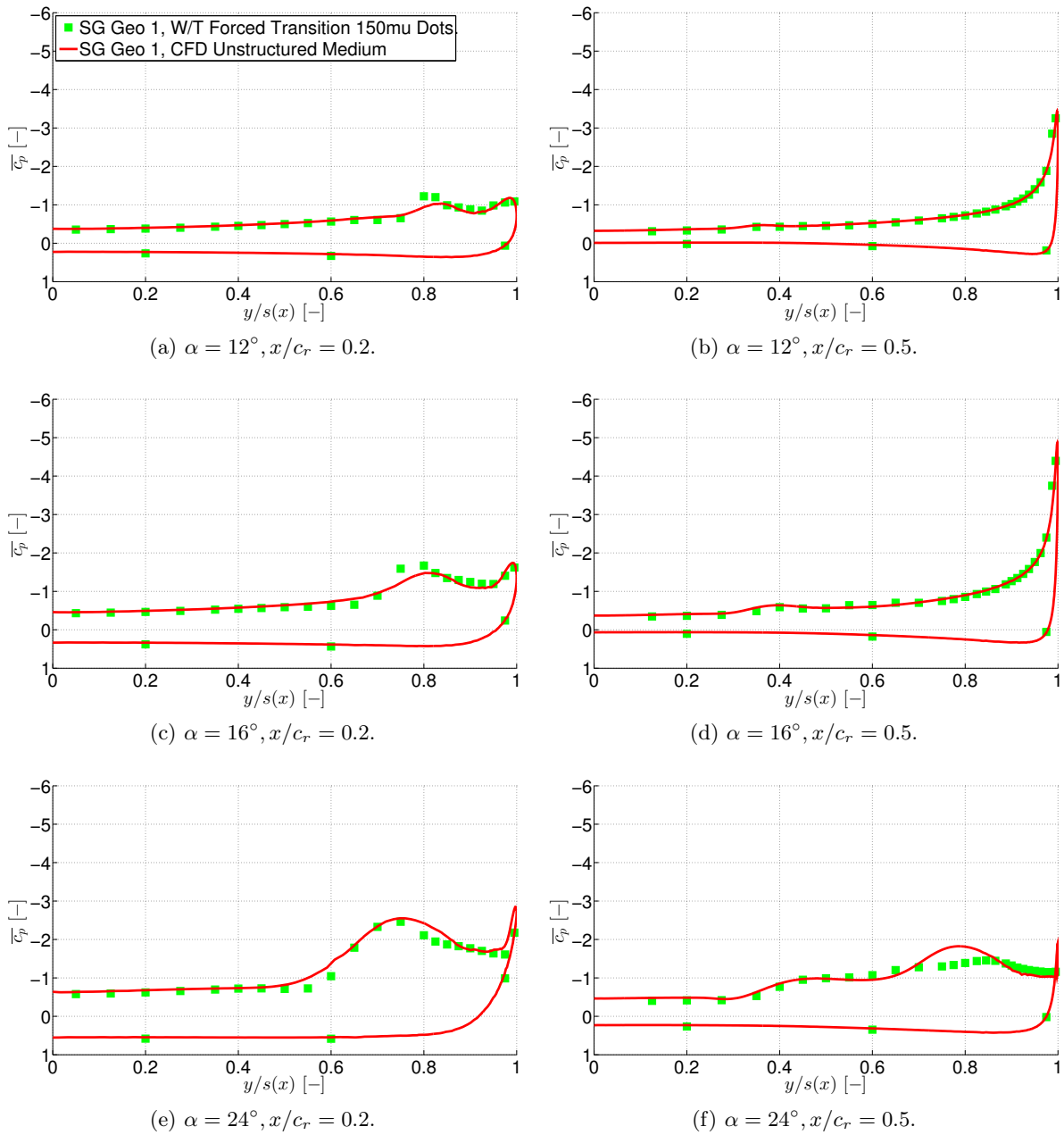


Figure 6.7: CFD validation of configuration SG Geo 1 – Surface pressure coefficient $\overline{c_p}$ versus semi-span $y/s(x)$.

6.1.2 Flow Physics Analysis

Longitudinal Motion

The overall flow phenomena associated with the reference configuration SG Geo 1 are presented for the longitudinal motion. Figure 6.8 depicts the surface pressure coefficient distributions and axial vorticity contours in different chordwise sections. In addition, field streamlines are shown, which were released close to the leading edge. The flow physics is evaluated for the angles of attack

of $\alpha = 8^\circ$ to $\alpha = 24^\circ$. According to the four different leading-edge (LE) segments in spanwise direction as introduced in Figure 1.10, the occurring flow phenomena are each discussed. In the most inboard (IB) wing section, namely LE segment I, the leading-edge contour is of sharp type. Already at $\alpha = 8^\circ$, a leading-edge vortex is thereby present. In the further analysis, this vortex is termed IB LE vortex. At the transition from the sharp leading edge to the rounded leading-edge contour of LE segment II, see for instance Figure 6.8f, the IB LE vortex detaches from the leading edge and the vortex axis is shifted in chordwise direction. This is caused by the attached flow in LE segment II as indicated in Figure 6.8a. With increasing angle of attack, the IB LE vortex grows in size and intensity. Close to the sharp leading edge, the corresponding suction levels rise considerably in this context, see Figure 6.8a to Figure 6.8e. The associated axial vorticity contours show high values, especially in the vortex core region close to the sharp leading edge. Once the IB LE vortex moves downstream on the diamond wing surface, the axial vorticity decreases in the vortex core region, see Figure 6.8f to Figure 6.8j.

The other leading-edge segments of configuration SG Geo 1 exclusively feature rounded leading-edge contours. Consequently, attached flow is present in these wing sections at the moderate angle of attack of $\alpha = 8^\circ$. The large leading-edge radius of the 12% relative thickness NACA airfoil does not promote any vortex formation. In the outboard wing section, a beginning leading-edge separation is noticed, see Figure 6.8a. However, it is attributed to the short wing-tip section and the resulting adverse pressure gradient. With increasing angle of attack, this separation region grows in size and forms an irregular recirculation area with flow reversal, see Figure 6.8b and Figure 6.8c. Due to the large bluntness of the airfoil sections, a leading-edge vortex as observed on the AVT-183 configuration is not formed at the respective angles of attack. Beginning with $\alpha = 16^\circ$, Figure 6.9 additionally highlights the corresponding skin-friction lines. At this angle of attack, the flow reversal in the outboard wing sections is clearly noticed, see Figure 6.9a. More inboard, attached flow is still present, and the skin-friction lines converge on the diamond wing surface with the skin-friction pattern of the downstream-moving inboard vortical structure. Figure 6.9b depicts the converging skin-friction lines in detail.

At the angle of attack of $\alpha = 20^\circ$, the flow structure in the outboard and the midboard (MB) wing sections change, see Figure 6.8d. The field streamline pattern and the pressure coefficient footprint indicate an incipient smooth surface separation, which leads to the formation of a MB LE vortex close to the rounded leading edge. The outboard wing section is influenced by the emerging vortical structure, and the flow reversal is significantly reduced, see Figure 6.9c. The converging skin-friction lines of the IB LE vortex and the attached flow in LE segment II and III move, compared to $\alpha = 16^\circ$, considerably upstream and align almost parallel to the leading edge, see Figure 6.9d. Subsequently, the attached flow is deviated and finally escapes from the wing surface in the MB LE vortex. In the skin-friction pattern, this is noticed by the singular point of focus-type. Therefore, the IB LE vortex considerably influences the flow separation onset of the MB LE vortex at the reference configuration SG Geo 1. If the angle of attack is further increased, the flow physics becomes thereby more complex. It is explained for $\alpha = 24^\circ$, see Figure 6.8e and

Passive Flow Control by Leading-Edge Contour Modifications

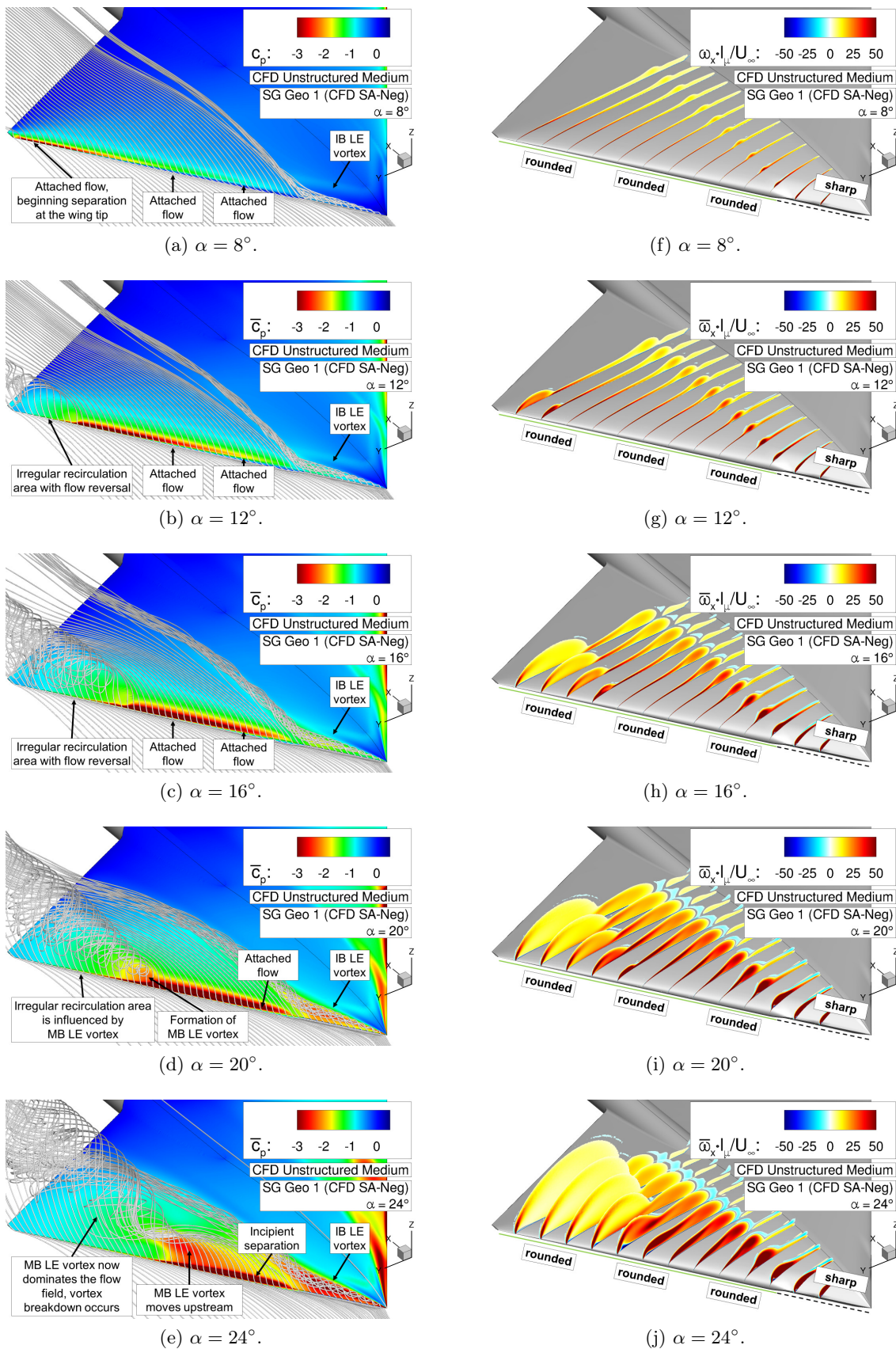


Figure 6.8: Flow physics analysis of configuration SG Geo 1 – Surface pressure coefficient \bar{c}_p including field streamlines, and axial vorticity contours $\bar{\omega}_x \cdot l_\mu / U_\infty$.

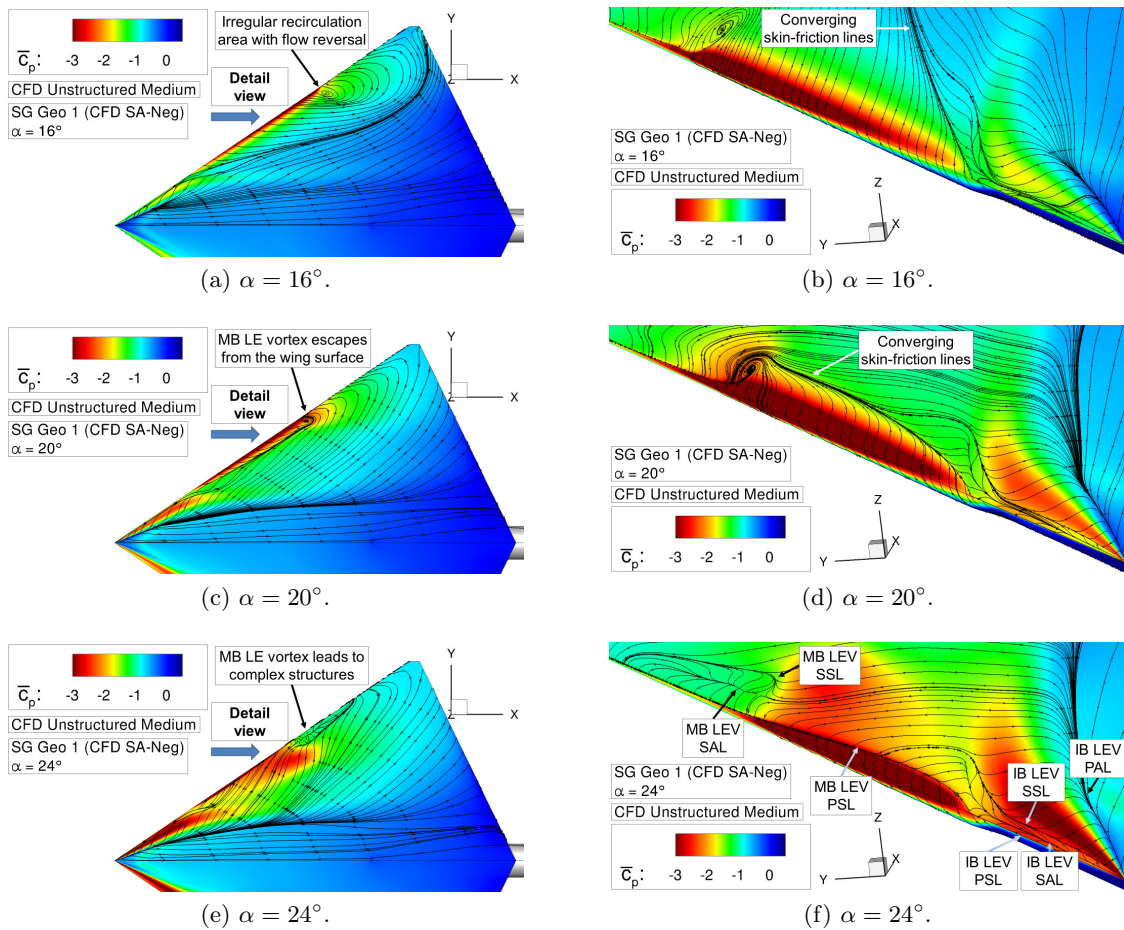


Figure 6.9: Flow physics analysis of configuration SG Geo 1 – Surface pressure coefficient \bar{c}_p including skin-friction lines.

Figure 6.8j. Overall, the MB LE vortex becomes stronger, and it moves upstream and more inboard. The associated skin-friction patterns now show a primary separation line (PSL) for the MB leading-edge vortex (MB LEV) along the entire rounded wing section, see Figure 6.9f. It is located completely offside the leading edge, which highlights the associated smooth surface separation of the midboard vortical structure. Consequently, this region defines the incipient flow separation. Next to the primary vortex structure, additional secondary separation and attachment lines (SSL, SAL) are also found for the MB LE vortex at $\alpha = 24^\circ$. Compared to the corresponding secondary effects of the IB LE vortex (IB LEV), they are more distinct. Overall, the IB LE vortex already features a secondary vortex separation at lower angles of attack. When the IB LE vortex is displaced from the sharp leading edge in succession of the leading-edge contour transition, the secondary structure is locally intensified, but vanishes shortly after. At the angle of attack of $\alpha = 24^\circ$, this effect is most visible, see Figure 6.9f.

In accordance with the observations on the AVT-183 configuration, the vortex structures occurring at the SAGITTA configuration instantly show vortex bursting tendencies after their formation. Figure 6.10 exemplarily demonstrates this in selected chordwise sections for the angle

Passive Flow Control by Leading-Edge Contour Modifications

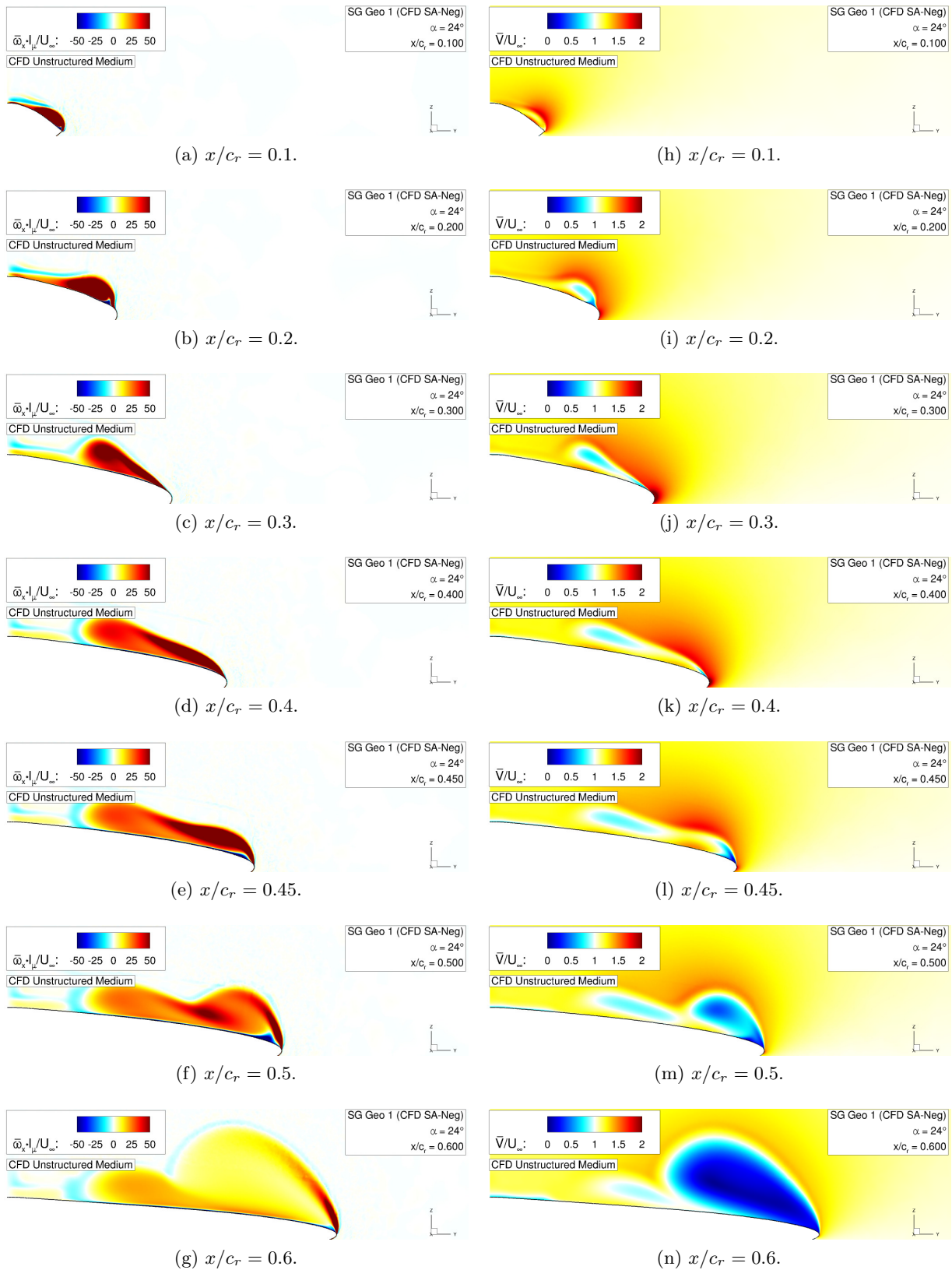


Figure 6.10: Flow physics analysis of configuration SG Geo 1 – Axial vorticity contours $\overline{\omega}_x \cdot l_\mu / U_\infty$ and absolute velocity contours \overline{V} / U_∞ at $\alpha = 24^\circ$.

of attack of $\alpha = 24^\circ$. Shortly after its formation, the IB LE vortex already features reduced absolute velocities in the vortex core, see Figure 6.10h and Figure 6.10i. Distinct increased velocities are not observed. The MB LE vortex almost immediately results in vortex core flow velocity deficits, see Figure 6.10l. Thus, the vortex core flow of the occurring LE vortices is dominated by a wake-type character, which indicates vortex bursting tendencies. The corresponding pressure coefficients along the vortex axes support this observation, since the high suction levels are only maintained close to the vortex formation. The MB LE vortex exhibits, in addition, drastically increased cross-sections and decreased axial vorticity contour levels downstream, see Figure 6.10f and Figure 6.10g. The occurring vortex breakdown thus becomes further obvious.

The sectional plots of Figure 6.10 also highlight the interaction between both vortex structures at high angles of attack. In the midboard wing section, the IB and MB LE vortex form a continuous sheet of axial vorticity. The dependence of the midboard flow separation associated with rounded leading edges on the IB LE vortex occurring from the sharp leading-edge contour is thus demonstrated for the reference configuration SG Geo 1. In addition, the above discussed secondary vortex structures of both LE vortices can be observed. At $x/c_r = 0.2$ and $x/c_r = 0.5$, respectively, the corresponding counter-rotating secondary structures associated with the IB and MB LE vortex are noticed, see Figure 6.10b and Figure 6.10f.

Lateral Motion

Next, the flow field characteristics occurring in the lateral motion with present sideslip angle are regarded. The flow physics analysis concentrates on the angle of sideslip of $\beta = -10^\circ$, for which the effective sweep angle of the right semi-span wing is increased to $\varphi_{le,eff} = 65^\circ$. Therefore, vortex separation effects due to rounded leading edges are expected to occur already at lower angles of attack. In line with the analysis of the longitudinal motion, the same angle-of-attack range of $\alpha = 8^\circ$ to $\alpha = 24^\circ$ is considered. Corresponding results with $\beta = 10^\circ$, for which the effective sweep angle of the right semi-span wing is reduced, are stated in Appendix C. In this case, the outboard recirculation area of irregular separated flow is even more dominant with increasing angle of attack. Compared to the flow physics associated with the longitudinal motion, vortex separation effects are only present due to the inboard sharp leading edge, and thus not as relevant for the discussion of partly-developed leading-edge vortices in this research.

Figure 6.11 depicts the surface pressure coefficient distributions and axial vorticity contours in different chordwise sections at $\beta = -10^\circ$. Due to the sideslip angle, the IB LE vortex is generally more aligned with the free stream direction. Already at $\alpha = 8^\circ$ and $\alpha = 12^\circ$, the increased effective leading-edge sweep angle leads to modified flow physics in the wing-tip section. The region of irregular separated flow is replaced by an outboard (OB) LE vortex, see Figure 6.11a and Figure 6.11b. However, the vortical structure breaks up instantly. This is caused by the proximity to the trailing edge, where the pressure recovery must be fulfilled. Thereby, the leading-edge pressure coefficient is immediately increased. In the midboard wing section, attached flow is relevant and no difference to the longitudinal motion is present. Beginning with the angle of

Passive Flow Control by Leading-Edge Contour Modifications

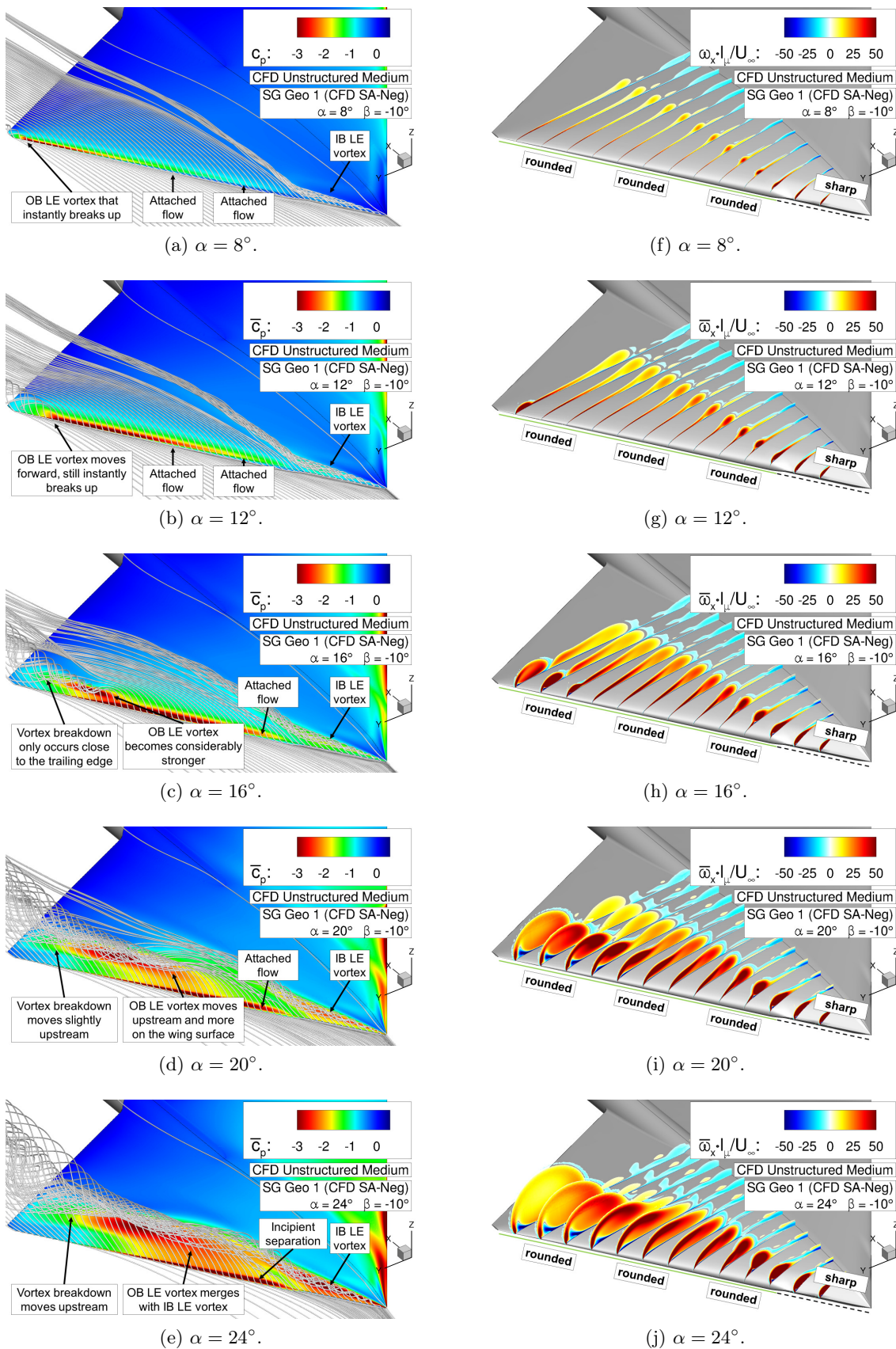


Figure 6.11: Flow physics analysis of configuration SG Geo 1 – Surface pressure coefficient \bar{c}_p including field streamlines, and axial vorticity contours $\bar{\omega}_x \cdot l_\mu / U_\infty$ at $\beta = -10^\circ$.

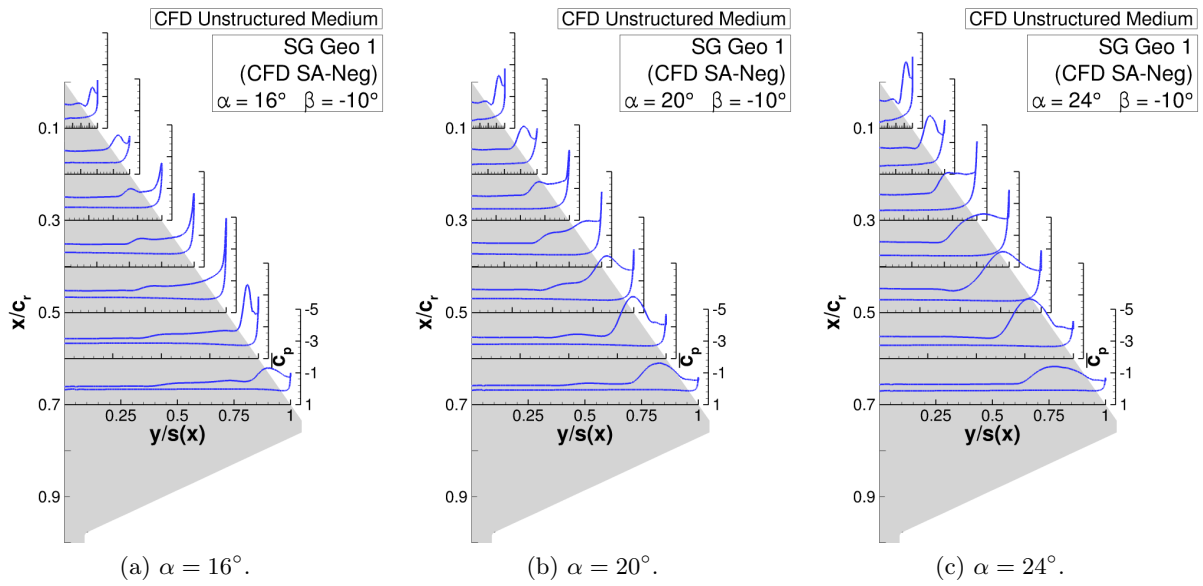


Figure 6.12: Flow physics analysis of configuration SG Geo 1 – Surface pressure coefficient $\overline{c_p}$ versus semi-span $y/s(x)$ at $\beta = -10^\circ$.

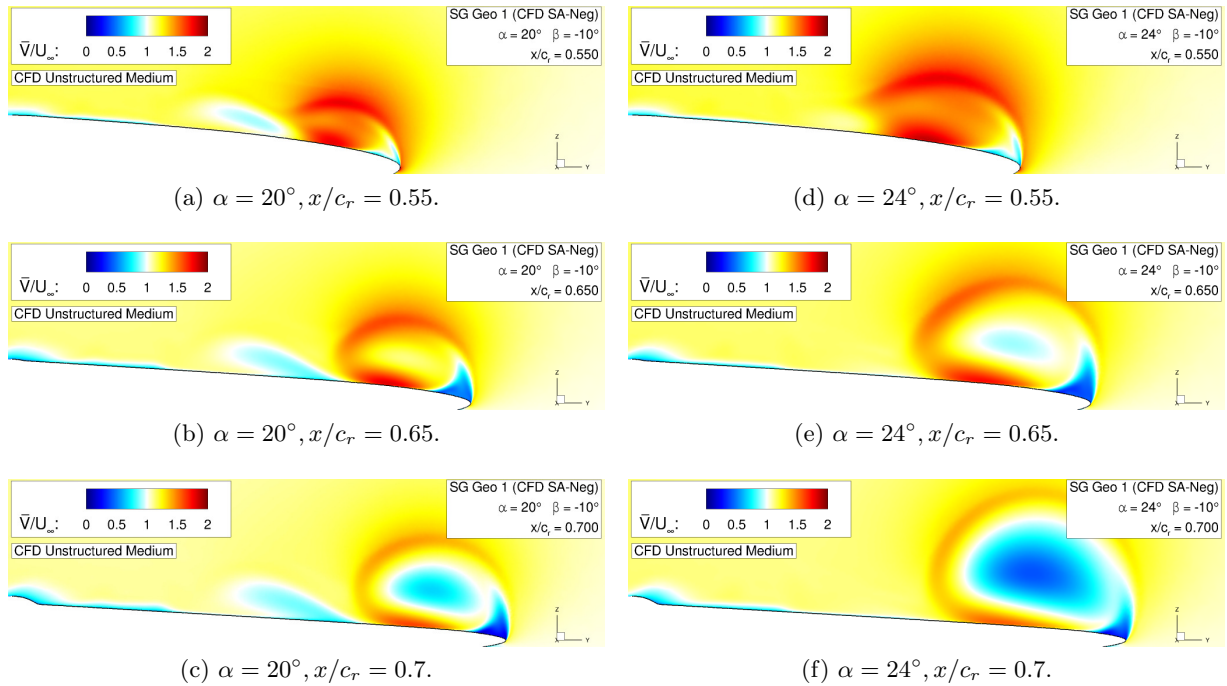


Figure 6.13: Flow physics analysis of configuration SG Geo 1 – Absolute velocity contours \overline{V}/U_∞ at $\beta = -10^\circ$.

attack of $\alpha = 16^\circ$, remarkable differences to the case without sideslip angle are observed in the resulting flow physics. To support the further analysis, Figure 6.12 and Figure 6.13 are introduced. They depict the chordwise surface pressure coefficient distributions along the right semi-span wing and sectional contour plots of the absolute velocity at selected chordwise sections.

Overall, the OB LE vortex becomes considerably stronger at $\alpha = 16^\circ$ and moves upstream along the rounded leading-edge contour, see Figure 6.11c and Figure 6.11h. The suction of the OB LE vortex is substantially intensified, as it is shown in Figure 6.12a by the distinct pressure peak at $x/c_r = 0.6$. More downstream, the pressure coefficient distribution still indicates the existence of vortex breakdown. At $\alpha = 20^\circ$, the smooth surface separation moves further upstream and more inboard on the diamond wing surface, see Figure 6.11d. The OB LE vortex is strengthened, which can be observed by the increased axial vorticity levels in Figure 6.11i and the surface pressure coefficient distributions in Figure 6.12b. In contrast to the MB LE vortex in the longitudinal motion, this time the OB LE vortex does not immediately show wake-type flow in the vortex core after its formation, but a jet-type character with an increased velocity component along the vortex axis. This is highlighted in Figure 6.13a. The process of vortex breakdown is then noticed in the subsequent chordwise sections, see Figure 6.13b and Figure 6.13c, as the core flow velocity continuously reduces and the cross-section of the OB LE vortex expands. With increasing angle of attack, this trend remains, see Figure 6.13d to Figure 6.13f. Moreover, the flow separation onset is further promoted, and at the angle of attack of $\alpha = 24^\circ$, the IB and OB LE vortex merge together. Subsequently, they build one dominant leading-edge vortex structure at the right semi-span wing of the reference configuration SG Geo 1, see Figure 6.11e. The axial vorticity contour levels in Figure 6.11j support this observation. In the midboard wing section, a combined vortical structure is present, which exclusively feeds the OB LE vortex in the more downstream wing sections. Two separate vortex structures in the rear wing sections, as obtained in Figure 6.8j for the flow field associated with the longitudinal motion, are not seen any longer for this case with $\beta = -10^\circ$.

6.1.3 Synthesis

The overall aerodynamic characteristics of the reference configuration SG Geo 1 have been presented in this section. First, the validity of the numerical method has been proven. Then, the flow physics of the occurring vortex structures has been discussed in both the longitudinal and the lateral motion. In total, this leads to the following synthesis:

Validation of the Numerical Method

- The numerical set-up applied to the CFD analyses of the SAGITTA configuration results in reliable predictions of the aerodynamic characteristics including vortex separation effects. The medium grid resolution ($13.8 \cdot 10^6$ grid points, initial wall-normal spacing of 0.003 mm) is sufficient to achieve grid independence. The numerical results of the reference configuration SG Geo 1 are in very good agreement with respective experimental data.
- The effects of the further discussed leading-edge contour modifications can consequently be assessed based on CFD analyses. For the computations associated with the other regarded SAGITTA configurations, the validated numerical set-up has therefore been applied.

Flow Physics Analysis

- Due to the sharp inboard leading-edge contour, the flow field of the reference configuration SG Geo 1 is characterized by an inboard leading-edge vortex. With increasing angle of attack, the structure grows in size and intensity up to values of $\overline{\omega}_x \cdot l_\mu / U_\infty \approx 200$ and $\overline{V} / U_\infty \approx 1.2$ in the inboard wing section, respectively.
- In the outboard wing section with rounded leading-edge contour, a recirculation area with flow reversal occurs at $\alpha = 8^\circ$. It expands upstream with increasing angle of attack. Compared to the AVT-183 configuration, different flow phenomena are therefore present at moderate angles of attack. They are the direct consequence of the increased leading-edge bluntness and airfoil thickness, respectively. At the angle of attack of $\alpha = 20^\circ$, the outboard structure of irregular separated flow finally alters to a midboard leading-edge vortex. It occurs offside the leading edge at the upper wing surface and dominates the outboard wing section. The existence of the midboard leading-edge vortex is particularly caused by the influence of the inboard leading-edge vortex.
- The midboard leading-edge vortex is characterized by wake-type vortex core flow with $\overline{V} / U_\infty \leq 0.8$. It thus immediately shows vortex bursting tendencies. As earlier concluded for the AVT-183 configuration as well, this is typical of smooth surface separations associated with non-slender wing configurations.
- With present sideslip angle, asymmetric flow phenomena are present and influence the aerodynamic characteristics. In the context of the present research, in particular the flow physics of the semi-span wing with increased effective leading-edge sweep angle attracts the attention. Here, an additional leading-edge vortex occurs in the outboard wing section at low angles of attack. Irregular separated flow is not relevant any longer in this case.
- For $\beta = -10^\circ$, the outboard leading-edge vortex on the right semi-span wing is already present at $\alpha = 8^\circ$. With increasing angle of attack, it becomes considerably stronger and exhibits jet-type vortex core flow with values up to $\overline{V} / U_\infty \approx 1.6$. Downstream-occurring vortex breakdown with decreased velocity components is thereby more evident. At $\alpha = 24^\circ$, the inboard and the outboard leading-edge vortex completely merge in the midboard wing section. Subsequently, they highly influence each other and form one dominant leading-edge vortex on the right semi-span wing.

6.2 Sharp and Rounded Leading-Edge Contour

The flow field characteristics of configurations SG Geo 5 and SG Geo 6 are considered in the following. The regarded cases each feature a constant leading-edge contour, as the leading edge of configuration SG Geo 5 is sharp and the leading edge of configuration SG Geo 6 is round, see Figure 1.10. For the subsequent investigations, the longitudinal motion is regarded only.

6.2.1 Flow Physics Analysis

Configuration SG Geo 5

Figure 6.14 presents the resulting flow phenomena with varying angle of attack for configuration SG Geo 5. In line with the previous analyses, the surface pressure coefficient distributions are shown together with field streamlines and axial vorticity contours. Due to the sharp leading-edge contour along the entire span of the diamond wing configuration, the vortical flow field differs considerably in comparison to the flow phenomena associated with the reference configuration SG Geo 1. Already at $\alpha = 8^\circ$, a full-span leading-edge vortex is present, see Figure 6.14a. It is aligned closely to the leading edge and continues almost parallel to it. With increasing angle of attack, the full-span LE vortex becomes stronger, including increased suction levels on the upper wing surface. As known from classical vortex theory, the vortex axis additionally moves further inboard. In the downstream wing section close to the trailing edge, vortex breakdown occurs, which can be observed by the radial expansion of the field streamlines, see Figure 6.14b to Figure 6.14d. For higher angles of attack, the vortex bursting phenomena move upstream. At the angle of attack of $\alpha = 24^\circ$, they have reached the chordwise location of $x/c_r \approx 0.35$.

To highlight the vortex breakdown, Figure 6.15 depicts selected sectional contour plots of the absolute velocity at $\alpha = 20^\circ$ and $\alpha = 24^\circ$. Overall, the plots show the transition of the vortex core flow velocity from a slight jet-type character in the more upstream chordwise sections to a downstream wake-type character with considerably decreased velocity components. The upstream movement of the vortex breakdown with increasing angle of attack is also demonstrated. The general shape of the full-span leading-edge vortex of configuration SG Geo 5 is of oval type, see also Figure 6.14f to Figure 6.14j. Comparable vortex shapes have already been observed for the midboard leading-edge vortex of the reference configuration SG Geo 1 at $\beta = 0^\circ$ and the leading-edge vortex of the AVT-183 configuration, which both occur from rounded leading edges. In summary, this proves that the oval type of the leading-edge vortex is more a result of the moderate leading-edge sweep angle than of the leading-edge shape. The outboard leading-edge vortex of the reference configuration SG Geo 1 at $\beta = -10^\circ$, in turn, leads to a more circular shape. One can thus conclude that this is a direct consequence of the increased effective leading-edge sweep angle. In this case, a strengthened leading-edge vortex with higher axial vorticity contour levels is present, see Figure 6.11, and a more developed jet-type vortex core flow is observed, see Figure 6.13. Altogether, this delays the vortex breakdown downstream and to higher angles of attack. In case of configuration SG Geo 5 and the associated full-span leading-edge vortex, in contrast, the jet-type vortex core flow is considerably less developed, and vortex bursting phenomena are more relevant. They do not occur as apparent compared to the other case, see Figure 6.15. Due to the oval shape of the leading-edge vortex, the typical "doughnut-shape" is not present any longer in the vortex breakdown process of configuration SG Geo 5, before the wake-type character of the vortex core flow becomes dominant. To conclude, this behavior is characteristic of non-slender wing configurations, and regardless of the leading-edge shape. In the context of the AVT-183 in-

6.2 Sharp and Rounded Leading-Edge Contour

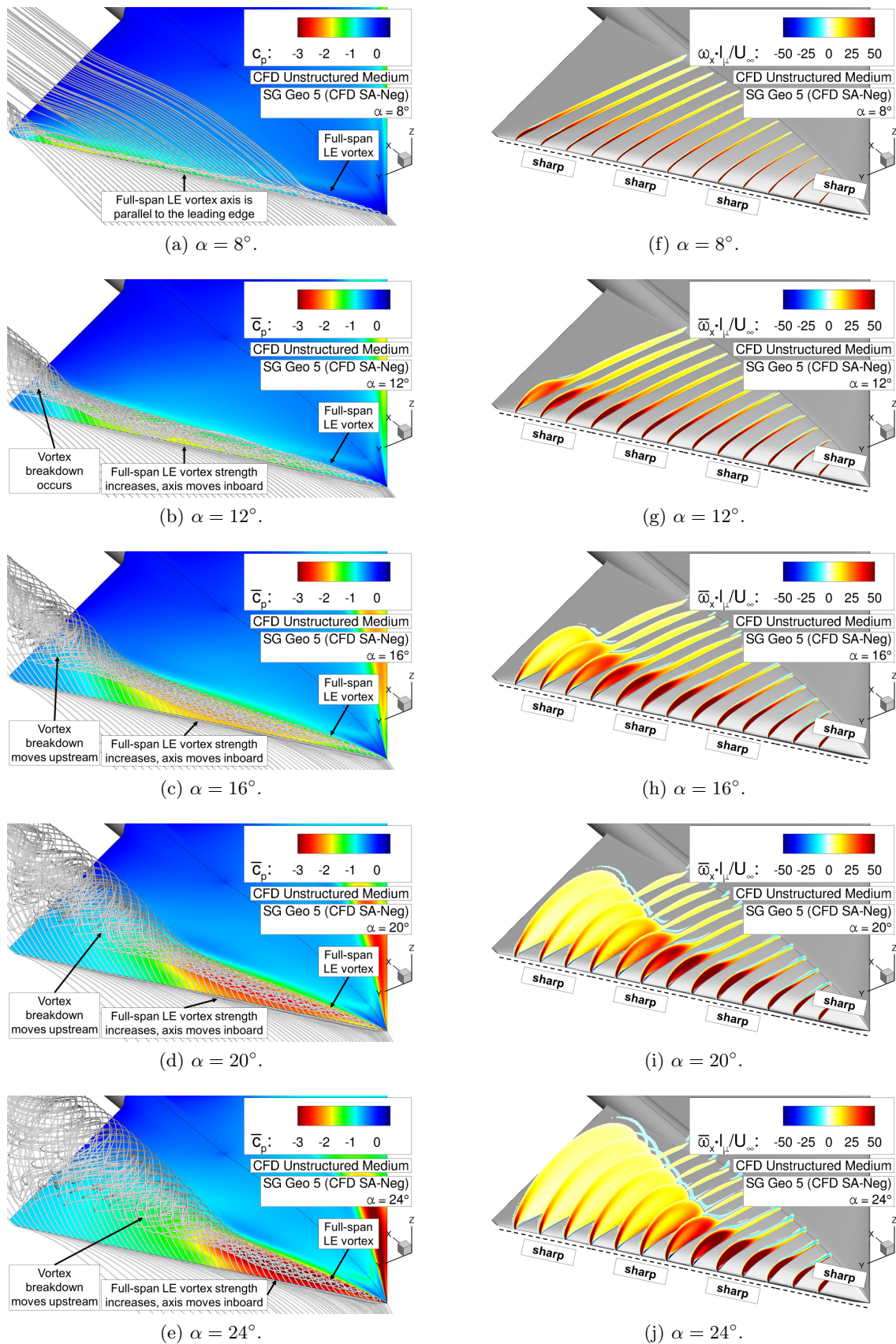


Figure 6.14: Flow physics analysis of configuration SG Geo 5 – Surface pressure coefficient \bar{C}_p including field streamlines, and axial vorticity contours $\bar{\omega}_x \cdot l_\mu / U_\infty$.

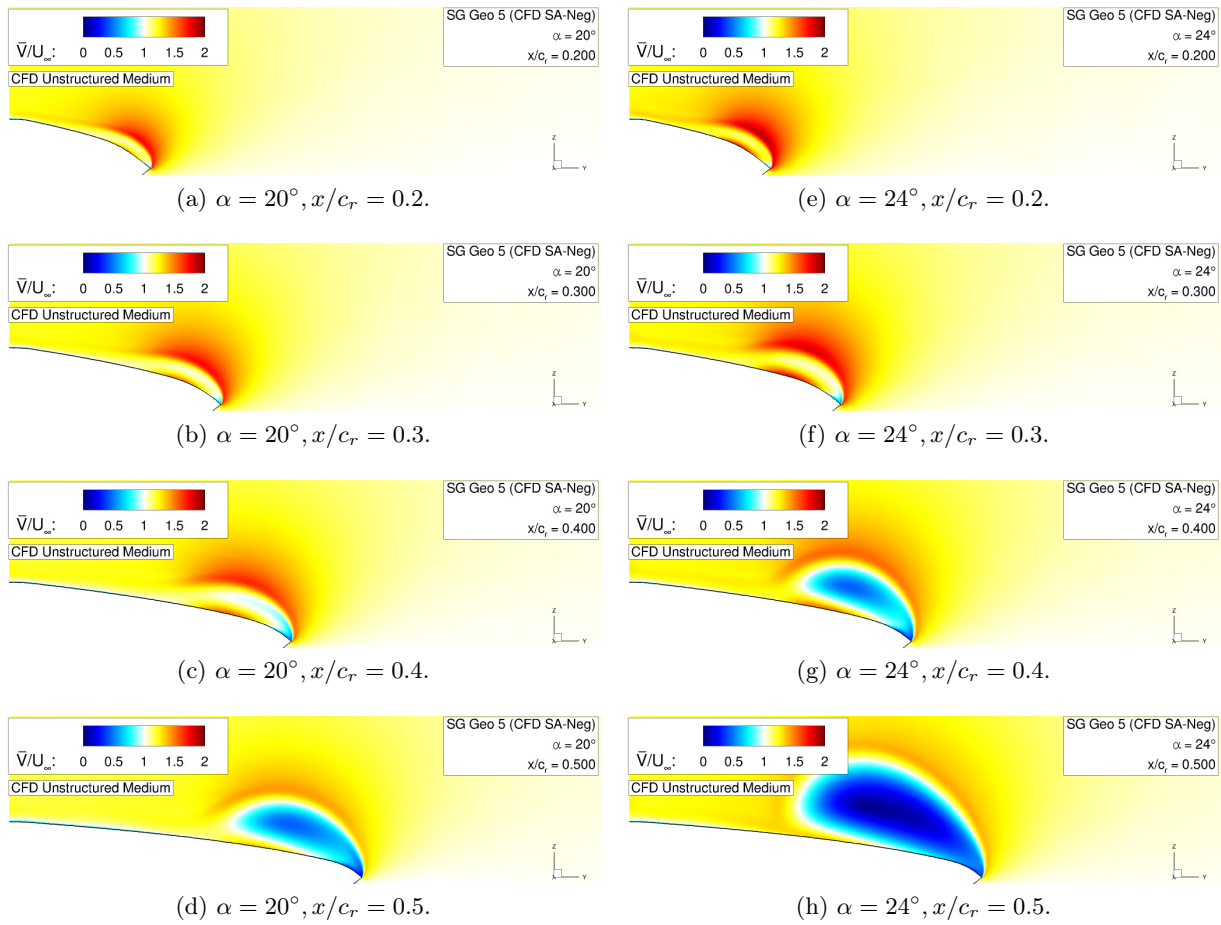


Figure 6.15: Flow physics analysis of configuration SG Geo 5 – Absolute velocity contours \bar{V}/U_∞ .

vestigations, Hitzel et al. demonstrated this effect as well, as a modified configuration with a leading-edge sweep angle of $\varphi_{le} = 65^\circ$ was considered [55]. The results were compared to those of the original AVT-183 configuration and in total, the same trends were discovered.

Configuration SG Geo 6

Next, the flow physics of configuration SG Geo 6 including a completely rounded leading-edge contour is discussed. Figure 6.16 introduces the corresponding plots for the considered angles of attack. Due to the absence of a sharp leading-edge contour compared to the reference configuration SG Geo 1, attached flow is dominant in the inboard wing section as well. This holds up to the angle of attack of $\alpha = 24^\circ$, see Figure 6.16e. As a result of the large leading-edge radius, flow separation is not relevant in this wing segment. In the midboard and outboard wing section, the flow field characteristics of configuration SG Geo 6 match the flow physics of the reference configuration SG Geo 1 up to $\alpha = 16^\circ$. The outboard-occurring irregular recirculation area with flow reversal is predicted very similarly and expands upstream with increasing angle of attack, see Figure 6.16a to Figure 6.16c. In the midboard wing section, attached flow is still present.

6.2 Sharp and Rounded Leading-Edge Contour

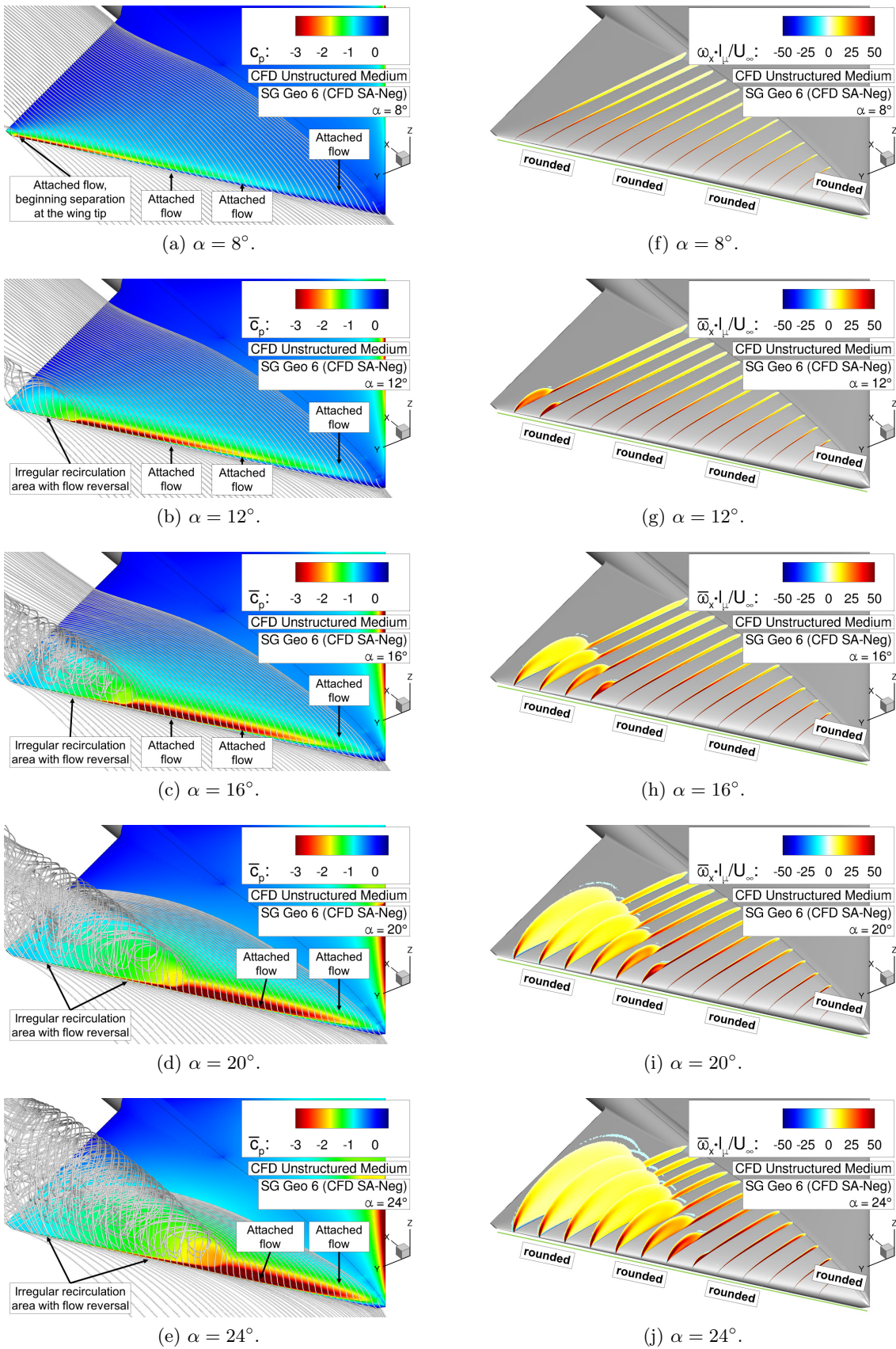


Figure 6.16: Flow physics analysis of configuration SG Geo 6 – Surface pressure coefficient \bar{c}_p including field streamlines, and axial vorticity contours $\bar{\omega}_x \cdot l_\mu / U_\infty$.

For higher angles of attack, the outboard and midboard flow phenomena become different between configurations SG Geo 6 and SG Geo 1. This is directly caused by the absence of the IB LE vortex. To support the further discussion, Figure 6.17 therefore shows the skin-friction patterns of configuration SG Geo 6 at $\alpha = 20^\circ$ and $\alpha = 24^\circ$. This time, no distinct MB LE vortex is established on the upper wing surface, but the region of irregular separated flow including flow reversal remains up to the angle of attack of $\alpha = 24^\circ$. Compared to the skin-friction pattern of the reference configuration SG Geo 1 as shown in Figure 6.9, different flow physics is present. Overall, this result confirms that the existence of the MB LE vortex at the SAGITTA configuration is mainly dependent on the presence of the IB LE vortex. Without sharp leading-edge segments, flow separation with subsequent leading-edge vortex formation does not occur, at least not until the maximum angle of attack considered in this research.

In comparison to the flow field characteristics of the AVT-183 configuration, the results further demonstrate the general effect of increased leading-edge bluntness and airfoil thickness on the leading-edge vortex formation and progression. For the AVT-183 configuration with a 6% relative thickness airfoil ($r_{le}/c = 0.23\%$) and a leading-edge sweep angle of $\varphi_{le} = 53^\circ$, a partly-developed leading-edge vortex is already present for moderate angles of attack around $\alpha = 12^\circ$, see Figure 5.26. Configuration SG Geo 6 with a 12% relative thickness airfoil ($r_{le}/c = 0.99\%$) and $\varphi_{le} = 55^\circ$, in contrast, does not feature any leading-edge vortex structure up to $\alpha = 24^\circ$. To study the effects of partly-developed leading-edge vortices at the SAGITTA configuration and to exploit them for passive flow control concepts, sharp leading-edge segments are thus required. For this reason, the reference configuration SG Geo 1 and the derived versions SG Geo 2 to SG Geo 4 feature spanwise-varying leading-edge contours.

6.2.2 Longitudinal Aerodynamic Coefficients

As a result of the different flow field characteristics that arise from various leading-edge shapes, the aerodynamic force and moment coefficients and the respective derivatives are influenced. In the course of the present research, they are discussed for configurations SG Geo 2 to SG Geo 6. The resulting values are each compared to the baseline data of the reference configuration SG Geo 1. The corresponding analyses concentrate on the longitudinal motion, thus showing the lift,

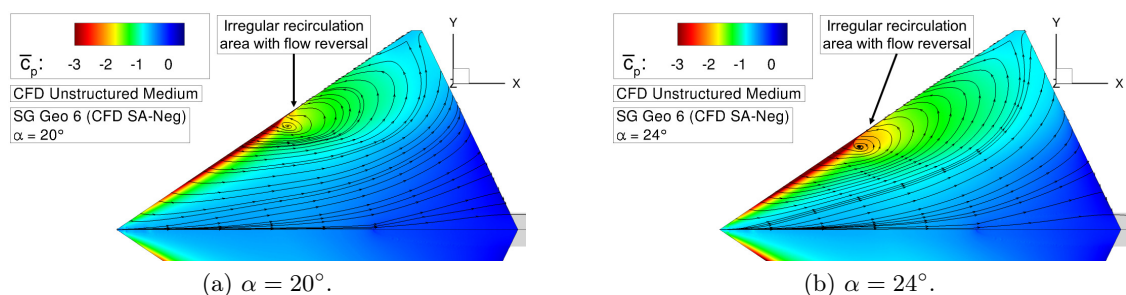


Figure 6.17: Flow physics analysis of configuration SG Geo 6 – Surface pressure coefficient \overline{C}_p including skin-friction lines.

drag and pitching-moment coefficient characteristics for the entire angle-of-attack polar. With respect to the stability characteristics of the SAGITTA configuration, the longitudinal stability derivative $C_{m_y, \alpha}$ and derived quantities such as the local center of pressure x_d/c_r or a derived longitudinal stability value $|(x_{m_{rp}} - x_n)/l_\mu|$ are of central concern. Based on varying vortex flow phenomena of the regarded wing configurations, which are caused by the leading-edge contour modifications, differences in the longitudinal stability behavior are expected. Hence, this analysis overall summarizes the outcome of the proposed passive flow control concepts in comparison to the reference configuration SG Geo 1.

The present section covers the discussion of the longitudinal aerodynamic coefficients of configurations SG Geo 5 and SG Geo 6. Thereby, the characteristics of the reference configuration SG Geo 1 are initially explained as well. Furthermore, numerical results of a low-fidelity numerical method are once presented for comparison. For this purpose, the program AVL (Athena Vortex Lattice) was used, employing an extended vortex lattice model for the lifting surfaces of the wing planform. Sectional properties, such as camberline effects of the NACA64A012 airfoil, are considered as well in this approach¹. Therefore, the high-fidelity CFD results of the SAGITTA configuration are set into context to common handbook methods.

Lift Coefficient Characteristics

In Figure 6.18, the lift coefficient C_L and the lift slope $C_{L, \alpha}$ are regarded. Although the flow field characteristics differ considerably for the three wing configurations, the resulting lift coefficients are very similar. At low to moderate angles of attack, they almost match each other. With increasing angle of attack, only small deviations are noticed, see Figure 6.18a. Moreover, the AVL result of the reference configuration SG Geo 1 does not show significant differences over the entire angle-of-attack polar. Consequently, the lift coefficients of the SAGITTA configuration

¹<http://web.mit.edu/drela/Public/web/avl>, retrieved February 2016

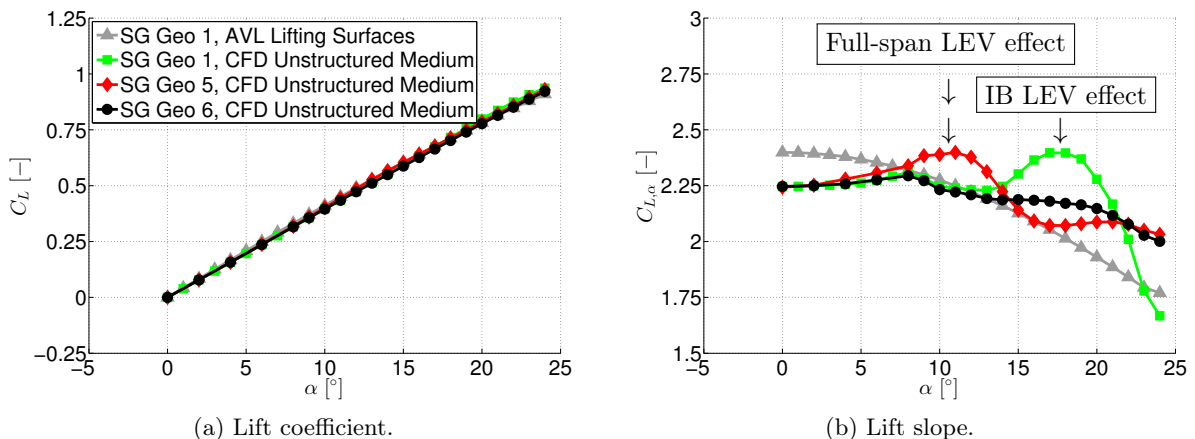


Figure 6.18: Longitudinal aerodynamic coefficients of configurations SG Geo 5 and SG Geo 6 – Lift coefficient C_L and derivative $C_{L, \alpha}$ versus angle of attack α .

are mostly determined by the wing planform. Additional non-linear lift due to leading-edge vortex suction is hardly observable, neither for configuration SG Geo 5 with the completely sharp leading-edge contour. To highlight the effects of the different flow physics, the lift slope $C_{L,\alpha}$ is considered instead, see Figure 6.18b. The lift-slope characteristics of configuration SG Geo 5 result in slightly increasing values up to the angle of attack of $\alpha = 11^\circ$, since the full-span leading-edge vortex becomes stronger, including increased suction levels along the vortex axis. Thereby, a weak trend of non-linear lift increase is noticeable. Then, vortex breakdown occurs close to the trailing edge, and decreasing lift-slope values are observed. These characteristics hold up to $\alpha = 17^\circ$. For even higher angles of attack, the lift slope finally remains rather constant. Thus, the lift-slope-decreasing trend of the upstream-moving vortex breakdown and the lift-slope-increasing trend of the leading-edge vortex suction in the more upstream wing regions roughly balance each other.

Regarding configuration SG Geo 6 with completely rounded leading edges, the lift slope $C_{L,\alpha}$ slightly increases up to the angle of attack of $\alpha = 8^\circ$, for which attached flow is present exclusively. It is a result of the increasing leading-edge suction peaks, but compared to the lift-slope values of configuration SG Geo 5, the increase is less pronounced. Then, the flow separates at the wing tip and the outboard region of irregular separated flow emerges. The recirculation region, which grows upstream with increasing angle of attack, thus leads to a continuous decrease of the lift-slope values, see Figure 6.18b. In sum, this effect is stronger than the lift-slope increase due to the attached flow in the more inboard wing sections, which remains up to $\alpha = 24^\circ$.

The reference configuration SG Geo 1 shows more complex lift-slope characteristics due to the spanwise-varying leading-edge contour. Both lift-slope-increasing and -decreasing trends occurring from attached flow, irregular separated flow, and separated vortex flow are present for different angles of attack. In consequence, the lift slope varies more considerably, especially at higher angles of attack, see Figure 6.18b. The corresponding results of the lifting surface method, in contrast, do not show these variations. They indicate a continuously-decreasing lift slope, which is caused by the camberline effect of the considered NACA 64A012 airfoil. Considering the high-fidelity RANS computations, the lift-slope values are very close to those of configuration SG Geo 6 up to $\alpha = 13^\circ$. The flow physics of the rounded leading-edge segments is dominant and the existence of the IB LE vortex does not have a significant effect so far. This is changed with increasing angle of attack. Up to approximately $\alpha = 18^\circ$, a slight non-linear lift increase is observed, which is attributed to the growing strength of the IB LE vortex. Then, a local maximum is reached in the lift-slope characteristics of configuration SG Geo 1, and the values considerably decrease. On the one hand, this is due to vortex bursting effects of the IB LE vortex on the rear wing surface. On the other hand, the trend is amplified by the formation of the MB LE vortex. With increasing angle of attack, the respective flow separation onset moves upstream on the upper wing surface and replaces the attached flow region in the midboard wing section. This reduces the $C_{L,\alpha}$ values. Since vortex breakdown occurs instantly for the MB LE vortex as well, the lift slope is further reduced.

Drag Coefficient Characteristics

Next, the drag coefficient characteristics are assessed. Figure 6.19 presents the corresponding curves for the studied wing configurations versus the angle of attack α and as Lilienthal polar C_L versus C_D . As expected, the results show the highest drag coefficient values for configuration SG Geo 5 with the full-span leading-edge vortex. The maximum lift-to-drag ratio is obtained at $\alpha = 6^\circ$ with $(C_L/C_D)_{max,SG\ Geo\ 5} = 11.33$, which corresponds to a minimum glide angle of $\epsilon_{min,SG\ Geo\ 5} = 5.04^\circ$. Compared to the other configurations, the deviations become more remarkable at higher angles of attack, since the vortex size and strength continuously increase. In general, this shows that vortex-dominated configurations always lead to increased drag coefficient values compared to configurations featuring attached flow regions.

The drag coefficient characteristics of configurations SG Geo 1 and SG Geo 6 are very similar to each other over the entire angle-of-attack polar. Only at certain angles of attack, the reference configuration SG Geo 1 results in slightly increased values compared to those of configuration SG Geo 6. Overall, this is due to the IB and MB LE vortex. This time, also the low-fidelity AVL result is far off with increasing angle of attack, and the parabolic drag increase is not described correctly. Altogether, the observed characteristics of configuration SG Geo 1 and SG Geo 6 lead to the corresponding Lilienthal polars as shown in Figure 6.19b. The maximum lift-to-drag ratio is still observed at $\alpha = 6^\circ$ with $(C_L/C_D)_{max,SG\ Geo\ 1} = 12.34$ and $(C_L/C_D)_{max,SG\ Geo\ 6} = 12.41$. Hence, it is nearly constant and increased by approximately 9% to the corresponding value of configuration SG Geo 5. In consequence, this also lowers the minimum glide angle to $\epsilon_{min,SG\ Geo\ 1} = 4.63^\circ$ and $\epsilon_{min,SG\ Geo\ 6} = 4.61^\circ$, respectively.

Pitching-Moment Coefficient Characteristics

Finally, the pitching-moment characteristics are discussed for configurations SG Geo 5, SG Geo 6, and the reference configuration SG Geo 1. The results of the pitching-moment coefficient C_{my}

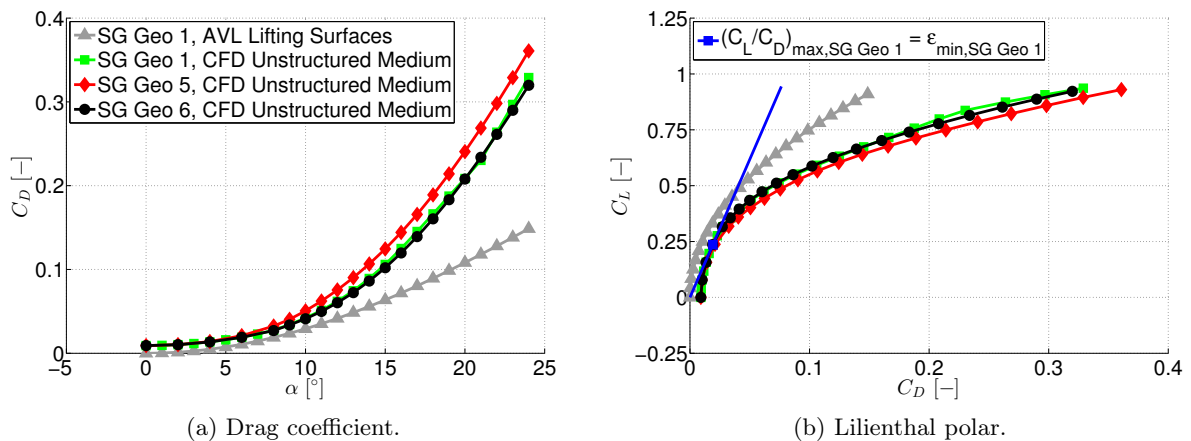


Figure 6.19: Longitudinal aerodynamic coefficients of configurations SG Geo 5 and SG Geo 6 – Drag coefficient C_D versus angle of attack α and Lilienthal polar C_L versus C_D .

and the derivative $C_{my,\alpha}$ versus angle of attack α are plotted in Figure 6.20. With respect to the chosen pitching-moment reference point, the SAGITTA configuration is found to be stable in pitch, regardless of the leading-edge contour. This is indicated by the negative slope of the curves in Figure 6.20a, and it holds for the entire angle-of-attack polar considered in this research. As a result of the symmetric airfoil, the pitching-moment coefficient becomes zero at $\alpha = 0^\circ$. With any present angle of attack, nose-down moments occur for the regarded wing configurations. The AVL analysis of the reference configuration SG Geo 1 provides accurate predictions of the pitching-moment coefficient up to approximately $\alpha \approx 13^\circ$. Thereafter, remarkable deviations are observed compared to the CFD results, as the slope of the respective curve is computed incorrectly. The pitching-moment derivative exhibits negative values only, see Figure 6.20b. In general, this parameter is relevant for stability investigations in the longitudinal motion. Figure 6.21a additionally highlights the resulting local center of pressure x_d/c_r versus the angle of attack. For all considered cases, it is located downstream of the pitching-moment reference point x_{mrp} ,

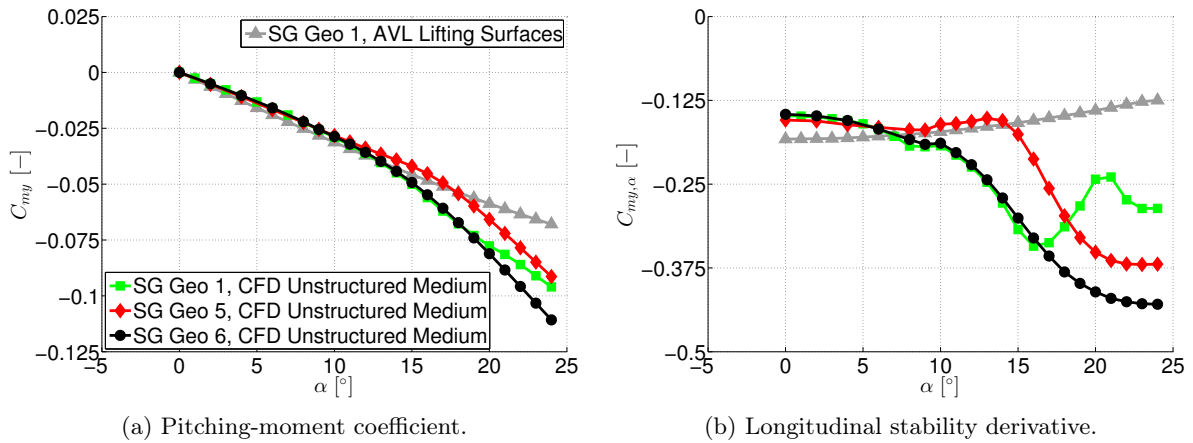


Figure 6.20: Longitudinal aerodynamic coefficients of configurations SG Geo 5 and SG Geo 6 – Pitching-moment coefficient C_{my} and derivative $C_{my,\alpha}$ versus angle of attack α .

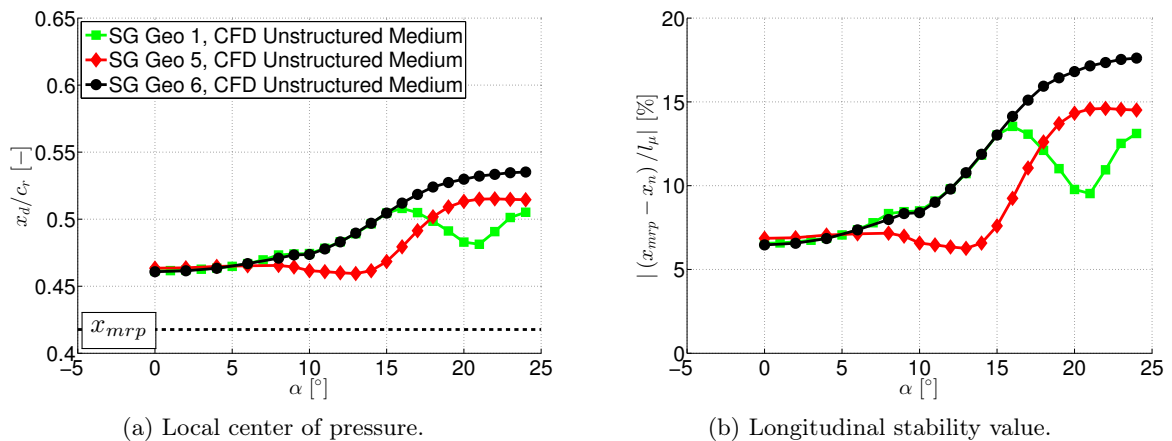


Figure 6.21: Longitudinal stability investigation of configurations SG Geo 5 and SG Geo 6 – Local center of pressure x_d/c_r and stability value $|(x_{mrp} - x_n)/l_\mu|$ vs. angle of attack α .

and it varies with increasing angle of attack. The position of x_{mrp} is plotted as a reference as well, see the dashed line in Figure 6.21a. Figure 6.21b finally depicts the derived longitudinal stability value $|(x_{mrp} - x_n)/l_\mu|$, which is considered in this thesis for the overall stability assessment. Since mass effects are not regarded in this research, the gravity center x_{cg} is replaced by the pitching-moment reference point as the decisive reference position.

Based on the diverse flow phenomena of the configurations considered in this section, the pitching-moment characteristics differ with increasing angle of attack. Configuration SG Geo 5 exhibits an almost constant longitudinal stability derivative up to the angle of attack of $\alpha = 14^\circ$, see Figure 6.20b. Subsequent to slightly-decreasing values, a small increase is noticed between $\alpha = 8^\circ$ and $\alpha = 14^\circ$. It is attributed to the incipient vortex breakdown and the rather low suction levels of the full-span leading-edge vortex. The resulting local center of pressure is thus nearly constant, see Figure 6.21a. With increasing angle of attack, the stability derivative then increases considerably in its absolute value and reaches a plateau with $C_{my,\alpha} \approx -0.375$ at $\alpha = 24^\circ$. Thereby, the local center of pressure is moved downstream for higher angles of attack, including a final stability value of almost 15%, see Figure 6.21b. The comparison of the surface pressure coefficient distributions at $\alpha = 14^\circ$ and $\alpha = 20^\circ$ in Figure 6.22a and Figure 6.22b highlights the effects of the full-span leading-edge vortex that are relevant for this behavior. Although the most distinct suction levels along the vortex axis increase considerably at $\alpha = 20^\circ$ and appear more upstream of the pitching-moment reference point (1), the size of the midboard and outboard wing region, that is influenced by the vortex structure, is decisive for the increased stability value (2). The upstream-moving vortex breakdown indeed reduces the high suction levels downstream of x_{mrp} , but negative pressure coefficient values are still noticeable for the corresponding wing region. Moreover, the reattached flow in the inboard wing section is accelerated with increasing angle of attack due to the leading-edge vortex induction, which also leads to reduced pressure coefficients downstream of the pitching-moment reference point (3). In sum, this further contributes to the increased nose-down moment of configuration SG Geo 5.

The longitudinal stability derivative of configuration SG Geo 6 with the rounded leading edges is discussed next, see Figure 6.20b. Compared to the characteristics of configuration SG Geo 5, the slight increase at moderate angles of attack is less pronounced and the drop in the $C_{my,\alpha}$ values occurs at lower angles of attack. From then on, both curves are roughly displaced parallel, which results in a stability value of approximately 17.5% at $\alpha = 24^\circ$, see Figure 6.21b. With respect to the pitching-moment coefficient at the final angle of attack, this corresponds to an increase of approximately 21% in the absolute C_{my} value, see Figure 6.20a. Due to the absence of the leading-edge vortex, the reasons for the pitching-moment characteristics are different. This time, the increase of the longitudinal stability derivative at $\alpha = 9^\circ$ and $\alpha = 10^\circ$ is a result of the emerging irregular flow separation at the wing tip. Due to the very short chord length, the flow separation moves quickly upstream and diminishes the distinct leading-edge suction peaks in the outboard wing section. In consequence, this slightly reduces the longitudinal stability. Beginning with the angle of attack of $\alpha = 11^\circ$, decreasing $C_{my,\alpha}$ values are dominant again. The increasing

suction levels of the attached flow in the outboard and midboard wing sections downstream of the pitching-moment reference point (4) have more impact on the stability derivative than the growing wing-tip separation region (5) and the rather low leading-edge suction levels upstream of x_{mnp} . For the angle of attack of $\alpha = 14^\circ$, this is shown in Figure 6.22c. With increasing angle of attack, the trend attenuates, since the distinct leading-edge suction peaks are shifted upstream of the pitching-moment reference point (4), see Figure 6.22d. The wing region influenced by the irregular separated flow (5) and the inboard rear wing section with attached flow (6), however, still contributes with reduced pressure coefficient values along with the associated influence region to the pronounced longitudinal stability of configuration SG Geo 6 at high angles of attack.

Based on the foregoing investigations of the configurations with constant leading-edge contour, the pitching-moment characteristics of the reference configuration SG Geo 1 are finally discussed. Up to the angle of attack of $\alpha = 15^\circ$, almost no differences are observable in the results with respect to configuration SG Geo 6, see Figure 6.20 and Figure 6.21. The outcome is thus consistent with the findings presented above for the lift coefficient characteristics. The low impact of the

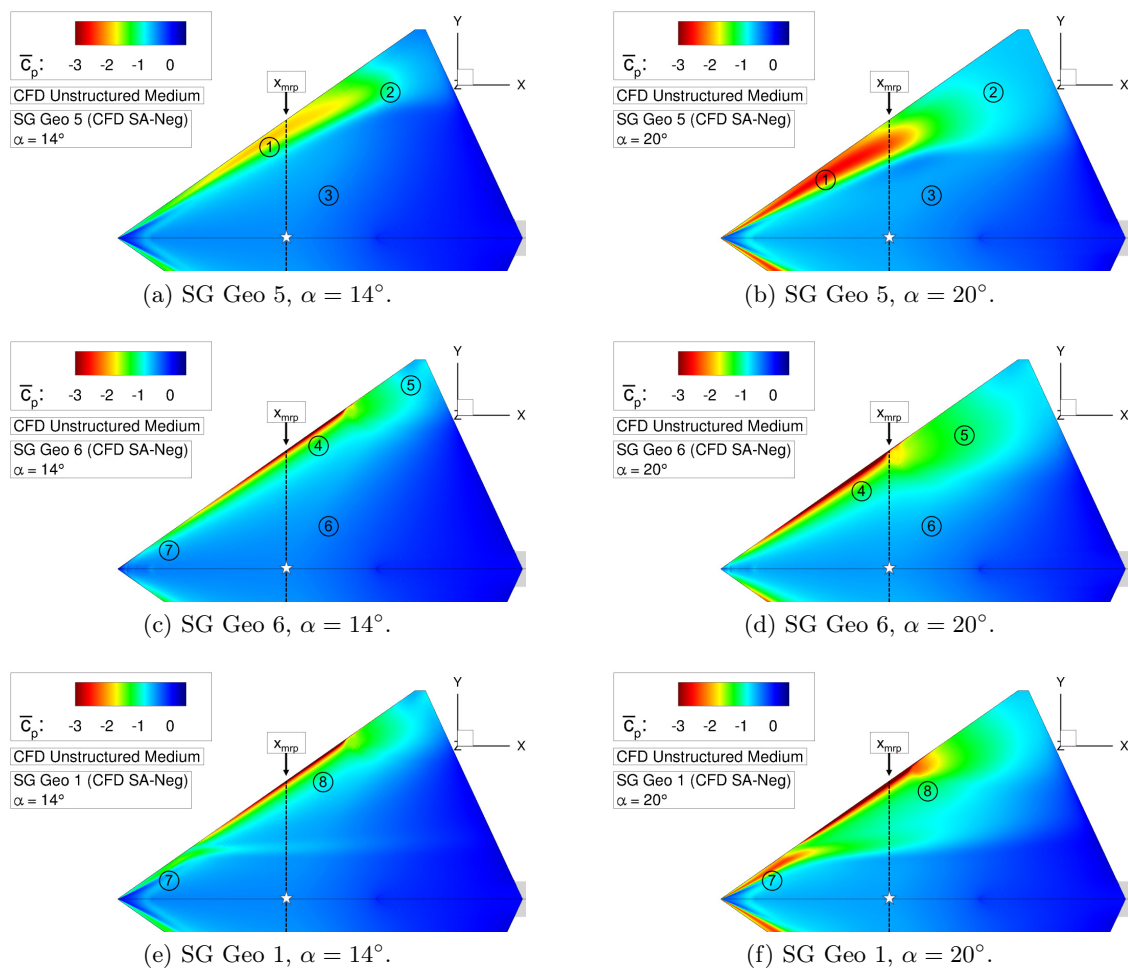


Figure 6.22: Longitudinal stability investigation of configurations SG Geo 5 and SG Geo 6 – Surface pressure coefficient \bar{c}_p .

IB LE vortex at low to moderate angles of attack is further highlighted by the comparison of the surface pressure coefficient distributions, see Figure 6.22c and Figure 6.22e, as only weak suction levels are present close to the inboard sharp leading-edge contour (7). With increasing angle of attack, however, the IB LE vortex becomes considerably stronger (7) and influences the pitching-moment characteristics, see Figure 6.22f. Due to the distance of the inboard sharp leading-edge section to the pitching-moment reference point, the longitudinal stability derivative is substantially increased, which lowers the longitudinal stability. This can be noticed from Figure 6.20b and Figure 6.21b. The values of the pitching-moment coefficient are thus displaced towards those of configuration SG Geo 5, see Figure 6.20a. At $\alpha = 20^\circ$, the MB LE vortex emerges in consequence of the IB LE vortex induction on the upper wing surface. With respect to x_{mrp} , the flow separation onset is located downstream (8), see Figure 6.22f. This leads to a local "maximum" of the $C_{my,\alpha}$ curve at $\alpha = 21^\circ$ and decreasing values. The increase in stability, however, is directly attenuated with increasing angle of attack, see Figure 6.20b, since the MB LE vortex moves upstream of the pitching-moment reference point. The corresponding pitching-moment coefficient of configuration SG Geo 1 at $\alpha = 24^\circ$ thus results in a value that deviates by only 5% from the C_{my} value of configuration SG Geo 5. Altogether, the discussion emphasizes the complex flow physics of the reference configuration SG Geo 1 and its effect on the pitching-moment characteristics at higher angles of attack. In summary, a varying longitudinal stability value is observed for $\alpha \geq 15^\circ$, which mainly depends on the vortex flow phenomena induced by the spanwise-varying leading-edge contour.

6.2.3 Synthesis

The discussion of configurations SG Geo 5 (entirely sharp LE) and SG Geo 6 (entirely round LE) in this section has provided valuable information with respect to the general influence of the leading-edge shape at the SAGITTA configuration. To understand and explain the flow physics of wing configurations with spanwise-varying leading-edge contours, this is of great importance. The analysis of the longitudinal aerodynamic coefficients has further demonstrated, which of the local flow phenomena, that occur for the reference configuration SG Geo 1 with spanwise-varying leading-edge contour, are relevant for the varying aerodynamic coefficients at different angles of attack. For the further analysis, an improved assessment of the cases with leading-edge contour modifications, compared to the reference configuration SG Geo 1, is thus feasible. In summary, one can conclude:

Flow Physics Analysis

- Configuration SG Geo 5 with the sharp leading-edge contour shows typical leading-edge vortex flow along the entire semi-span of the diamond wing. Due to the non-slender wing configuration, the leading-edge vortex shape is of oval type and only exhibits weak jet-type vortex core flow with $\bar{V}/U_\infty \leq 1.2$, despite the completely sharp leading edge. Vortex

breakdown is already relevant at low to moderate angles of attack ($\alpha_{burst} \approx 12^\circ$), which mostly leads to wake-type vortex core flow on the diamond wing configuration.

- Configuration SG Geo 6 with the rounded leading-edge contour features attached flow in the inboard wing section up to $\alpha = 24^\circ$. In the midboard and outboard wing sections, no differences are observed to the flow field characteristics of the reference configuration SG Geo 1 up to $\alpha = 16^\circ$. For higher angles of attack, however, the region of irregular separated flow with flow reversal continuously grows and is preserved. A midboard leading-edge vortex does not arise, at least not until the angle of attack of $\alpha = 24^\circ$.
- The finding regarding the existence of the midboard leading-edge vortex at reference configuration SG Geo 1, which has been stated in Section 6.1.3, is therefore proved. The growing strength of the inboard leading-edge vortex determines the flow separation characteristics in the midboard and outboard wing sections with increasing angle of attack. The formation of the midboard leading-edge vortex due to the rounded leading-edge contour of the reference configuration SG Geo 1 is thus a result of the inboard leading-edge vortex induction.

Longitudinal Aerodynamic Coefficients

- Despite diverse flow field characteristics of the regarded configurations, the lift coefficients only slightly differ at the SAGITTA configuration, regardless of the leading-edge contour. Hence, they are mainly determined by the diamond wing planform. Deviations become more remarkable in the drag and the pitching-moment coefficients, especially with increasing angle of attack. The resulting maximum lift-to-drag ratios, for example, differ between $11.3 \leq (C_L/C_D)_{max} \leq 12.4$, and the pitching-moment derivatives alter at $\alpha = 24^\circ$ between $-0.42 \leq C_{my,\alpha} \leq -0.29$.
- The analysis of the aerodynamic coefficients for configurations SG Geo 5 and SG Geo 6 show the basic effects of separated vortex flow, attached flow, and irregular separated flow on the integral forces and moments of the SAGITTA configuration. This further allows for the differentiation of the local flow phenomena that occur for the reference configuration SG Geo 1 with spanwise-varying leading-edge contour. Their effects can therefore be assigned to the resulting aerodynamic coefficients at different angles of attack.
- With regard to the aerodynamic coefficient characteristics of the reference configuration SG Geo 1, one can conclude: For low to moderate angles of attack up to $\alpha = 16^\circ$, the existence of the inboard sharp leading-edge contour is of minor importance with respect to the longitudinal aerodynamic coefficients. For higher angles of attack, however, at which the presence of the inboard leading-edge vortex is decisive for the midboard and outboard flow phenomena, remarkable differences occur. Then, the inboard leading-edge shape is crucial and considerably determines the longitudinal aerodynamic characteristics, including the corresponding stability behavior.

6.3 Leading-Edge Shape Modifications

This section deals with the flow physics of configurations SG Geo 2 and SG Geo 3, which also feature sharp leading-edge segments in the outboard and midboard wing sections. As introduced in Figure 1.10, configuration SG Geo 2 exhibits sharp leading edges in LE segment I+IV, whereas for configuration SG Geo 3 the LE segments I+III are sharp. In comparison to the reference configuration SG Geo 1, the modifications thus result in more varying leading-edge contours along the semi-span of the diamond wing configuration. Differences in the occurring flow phenomena and the aerodynamic coefficients are therefore expected. In line with the previous section, the longitudinal motion is regarded exclusively.

6.3.1 Flow Physics Analysis

Configuration SG Geo 2

The flow field characteristics of configuration SG Geo 2 are shown in Figure 6.24 for different angles of attack. Already at $\alpha = 8^\circ$, the sharp leading-edge contour in the outboard wing section leads to an additional OB LE vortex, see Figure 6.24a. The vortex axis is located close to the leading edge, and the suction levels are rather low. Figure 6.23a highlights the corresponding spanwise surface pressure coefficient distributions. At $x/c_r = 0.6$, the OB LE vortex suction peak is clearly noticed. More downstream and close to the wing tip, however, vortex bursting effects are already relevant as well. The expansion of the field streamlines and the reduction of the suction levels at $x/c_r = 0.7$ give evidence for the phenomenon. In the more inboard wing sections, the flow field characteristics are equal to those of the reference configuration SG Geo 1.

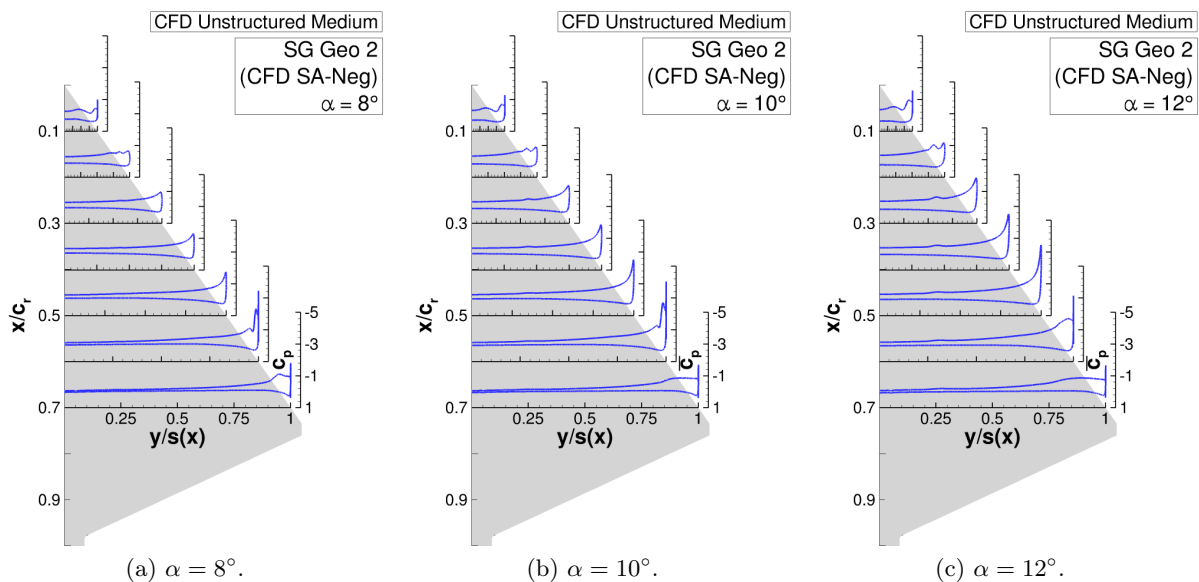


Figure 6.23: Flow physics analysis of configuration SG Geo 2 – Surface pressure coefficient $\overline{c_p}$ versus semi-span $y/s(x)$.

Passive Flow Control by Leading-Edge Contour Modifications

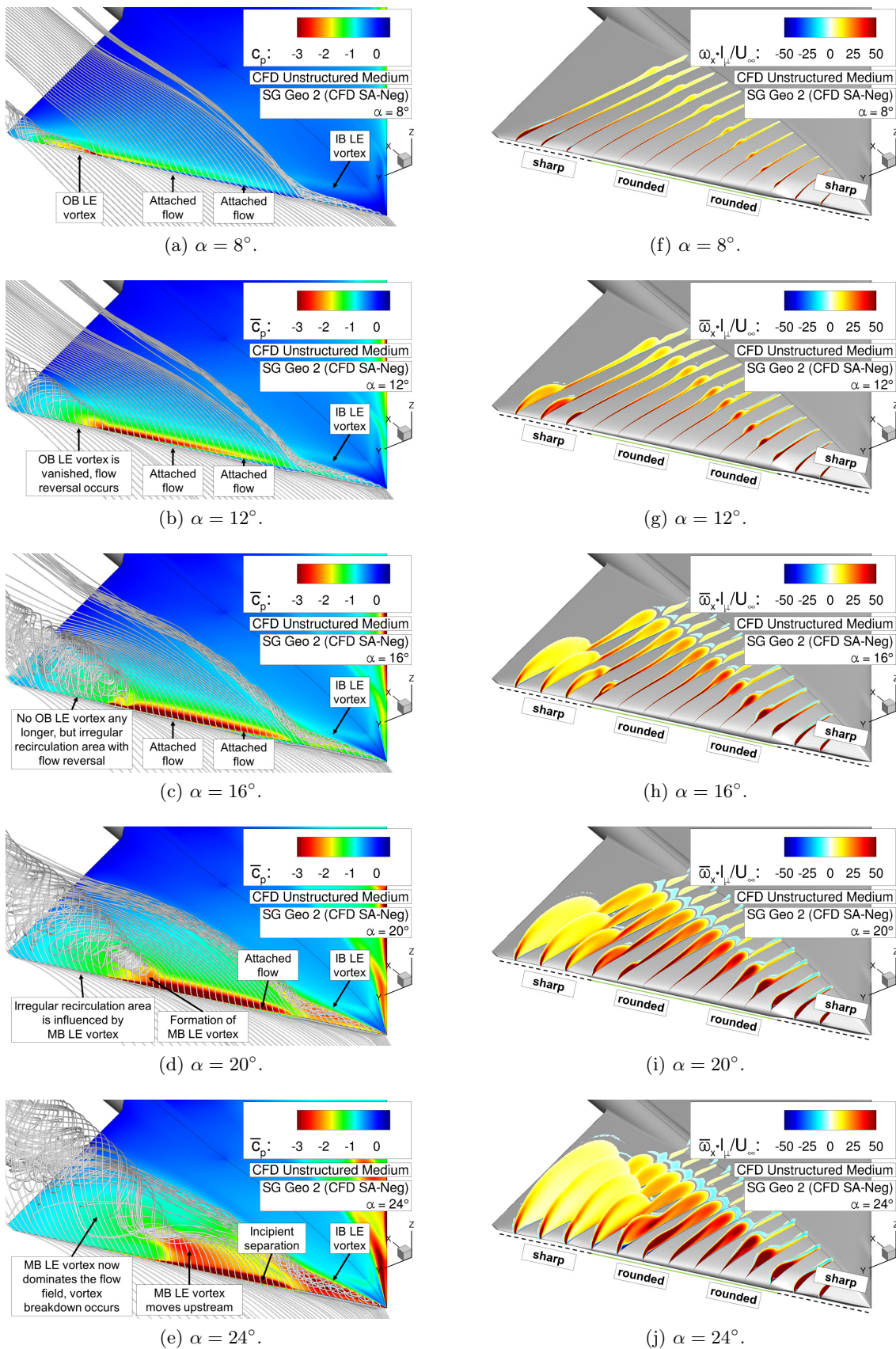


Figure 6.24: Flow physics analysis of configuration SG Geo 2 – Surface pressure coefficient \bar{c}_p including field streamlines, and axial vorticity contours $\bar{\omega}_x \cdot l_\mu / U_\infty$.

Between $\alpha = 8^\circ$ and $\alpha = 12^\circ$, the outboard flow phenomena change fundamentally for configuration SG Geo 2. Dominated by the upstream-moving vortex breakdown, the OB LE vortex has completely vanished at $\alpha = 12^\circ$, see Figure 6.24b. The skin-friction lines in Figure 6.25 depict the differences in the outboard wing section in more detail. This time, a region of irregular separated flow including flow reversal is present, which is comparable to the outboard recirculation area of the reference configuration SG Geo 1. Moreover, the spanwise surface pressure coefficient distributions in Figure 6.23 show the disappearance of the OB LE vortex with increasing angle of attack. As a result, the flow field of configuration SG Geo 2 at $\alpha = 12^\circ$ equals the occurring flow phenomena of the reference configuration SG Geo 1 along the entire semi-span.

For higher angles of attack, no remarkable differences are present any longer when comparing the flow physics of configurations SG Geo 2 and SG Geo 1. The flow field characteristics match each other at the considered angles of attack, including the growing recirculation area, the IB LE vortex induction, and the formation of the MB LE vortex, see Figure 6.24c to Figure 6.24e. The corresponding skin-friction patterns look alike those of the reference configuration SG Geo 1. Once the OB LE vortex at the outboard sharp leading edge has vanished, the leading-edge shape in LE segment IV is of less importance. Only the size of the outboard separation region is found to be slightly larger for configuration SG Geo 2 compared to SG Geo 1, see Figure 6.24h and Figure 6.8h. At the angle of attack of $\alpha = 16^\circ$, this is shown by the related axial vorticity contour levels, which are more pronounced at the inboard edge of the separation region for configuration SG Geo 2. The formation of the MB LE vortex at $\alpha = 20^\circ$, however, is therefore not displaced.

Configuration SG Geo 3

Next, the flow physics analysis is presented for configuration SG Geo 3. Figure 6.26 depicts the corresponding plots at $\alpha = 8^\circ$ to $\alpha = 24^\circ$. Already at low angles of attack, the sharp leading-edge contour in LE segment III leads to a second vortex structure that is referred to as MB LE vortex. At $\alpha = 8^\circ$, the flow field exhibits four different segments with alternating vortex flow and attached flow regions, see Figure 6.26a. At the wing tip, the incipient flow separation is present as explained before, and the outboard recirculation area arises with increasing angle of attack. The separation region, however, is only momentarily of importance for the flow field characteristics

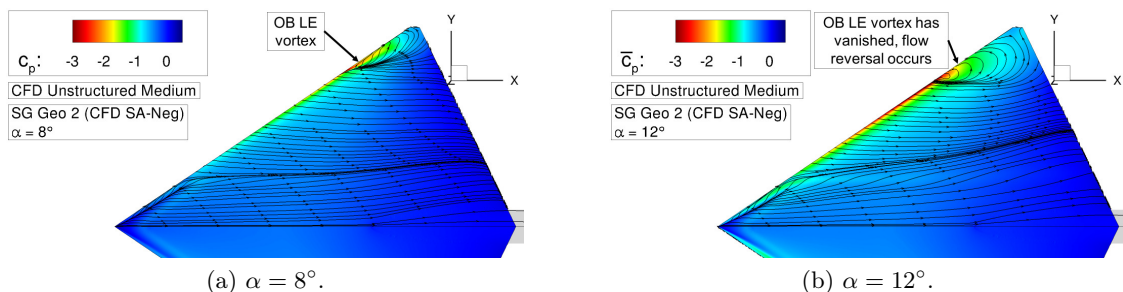


Figure 6.25: Flow physics analysis of configuration SG Geo 2 – Surface pressure coefficient $\overline{c_p}$ including skin-friction lines.

Passive Flow Control by Leading-Edge Contour Modifications

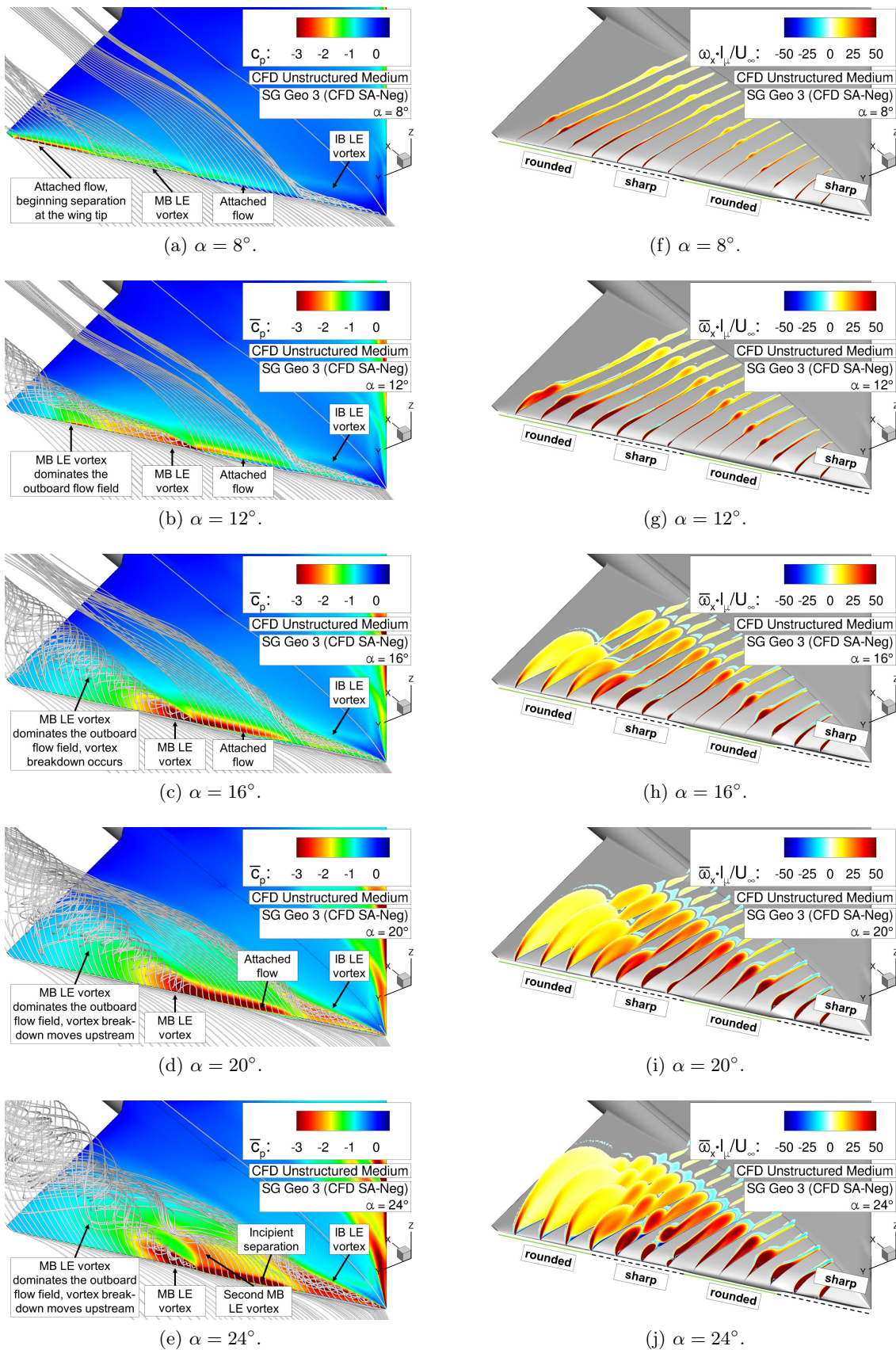


Figure 6.26: Flow physics analysis of configuration SG Geo 3 – Surface pressure coefficient \bar{c}_p including field streamlines, and axial vorticity contours $\bar{\omega}_x \cdot l_\mu / U_\infty$.

of configuration SG Geo 3. Instead, the MB LE vortex of LE segment III takes control over the entire outboard wing section at $\alpha = 12^\circ$, see Figure 6.26b. The resulting differences in the skin-friction patterns compared to the reference configuration SG Geo 1 are highlighted in Figure 6.27. Flow reversal is not relevant any longer, and typical vortex flow is observed for the MB LE vortex along the sharp leading edge of LE segment III and the rounded leading edge of LE segment IV. Despite the rounded leading-edge contour, the flow also rolls up in LE segment IV and feeds the MB LE vortex. In consequence, the vortex strength is increased, and high axial vorticity contour levels are noticed for the MB LE vortex, see Figure 6.26g.

To support the continuing analysis of configuration SG Geo 3, the resulting skin-friction patterns are considered likewise for higher angles of attack, see Figure 6.28. Overall, the MB LE vortex becomes stronger at $\alpha = 16^\circ$, see Figure 6.26c. The flow separation onset, however, does not move further upstream. This is caused by the contour transition from sharp to round and the rounded leading-edge contour in LE segment II. Instead, the vortex axis slightly inclines more inboard. The corresponding skin-friction lines in Figure 6.28b emphasize the different flow phenomena that are induced by the varying leading-edge contour. In the midboard wing section, attached flow with high leading-edge suction levels is present. More outboard, the flow then separates at the sharp leading edge of LE segment III and forms the MB LE vortex. The primary and secondary separation and attachment lines are also indicated in this context. The high suction levels of the MB LE vortex are not maintained very long on the wing surface, which again indicates the existence of vortex breakdown. The expanding streamlines in the outboard flow field support this fact, see Figure 6.26c.

Beginning with the angle of attack of $\alpha = 20^\circ$, the flow field characteristics of configuration SG Geo 3 become more complex. In line with the observations for the reference configuration SG Geo 1, converging skin-friction lines are observed in Figure 6.28d close to the leading edge in LE segment II, where the flow is still attached. In case of the reference configuration SG Geo 1, this results in a smooth surface separation including the formation of a MB LE vortex, compare Figure 6.9d and Figure 6.9f. For the present case with configuration SG Geo 3, the converging skin-friction pattern comes together with the MB LE vortex originating from the sharp leading-edge contour, see Figure 6.28d. The primary attachment line of the MB LE vortex observed before is

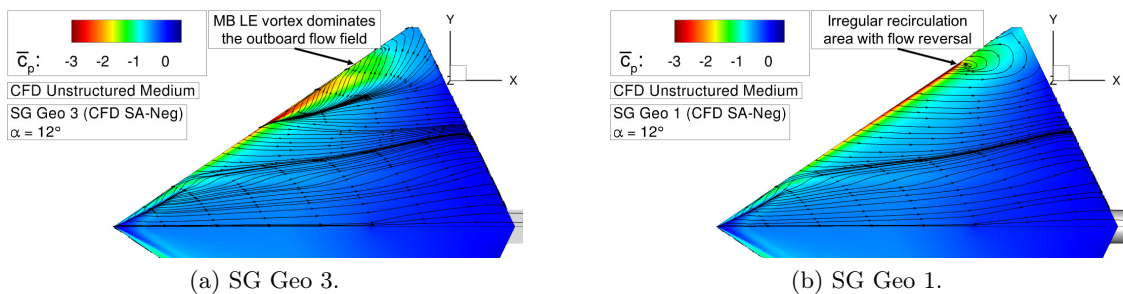


Figure 6.27: Flow physics analysis of configuration SG Geo 3 – Surface pressure coefficient $\overline{c_p}$ including skin-friction lines at $\alpha = 12^\circ$.

omitted and coincides with that of the IB LE vortex as a common primary attachment line. The flow separation onset close to the rounded midboard leading-edge contour is thus initiated for configuration SG Geo 3 as well, and it additionally joins the present MB LE vortex at $\alpha = 20^\circ$. With increasing angle of attack, the smooth surface separation is promoted upstream and splits up the combined vortical structure. Thus, two different leading-edge vortices are observed in the midboard wing section, see Figure 6.26e and Figure 6.26j. For differentiation, the occurring MB LE vortices are referred to as MB LE vortex I and MB LE vortex II. At $\alpha = 24^\circ$, in total three partly-developed leading-edge vortices are finally present for configuration SG Geo 3. The IB LE vortex and the MB LE vortex I originate from the sharp leading-edge segments I+III. The MB LE vortex II is a result of the smooth surface separation on the upper wing surface in LE segment II. Due to the local disjunction of the vortical structures at $\alpha = 24^\circ$, the MB LE vortex I features a primary attachment line again. Figure 6.28f further demonstrates that this is a result of a secondary vortex separation occurring for the MB LE vortex II, which is present on the wing surface between the two midboard vortical structures. The primary attachment line of the MB LE vortex I coincides with the secondary attachment line of the MB LE vortex II.

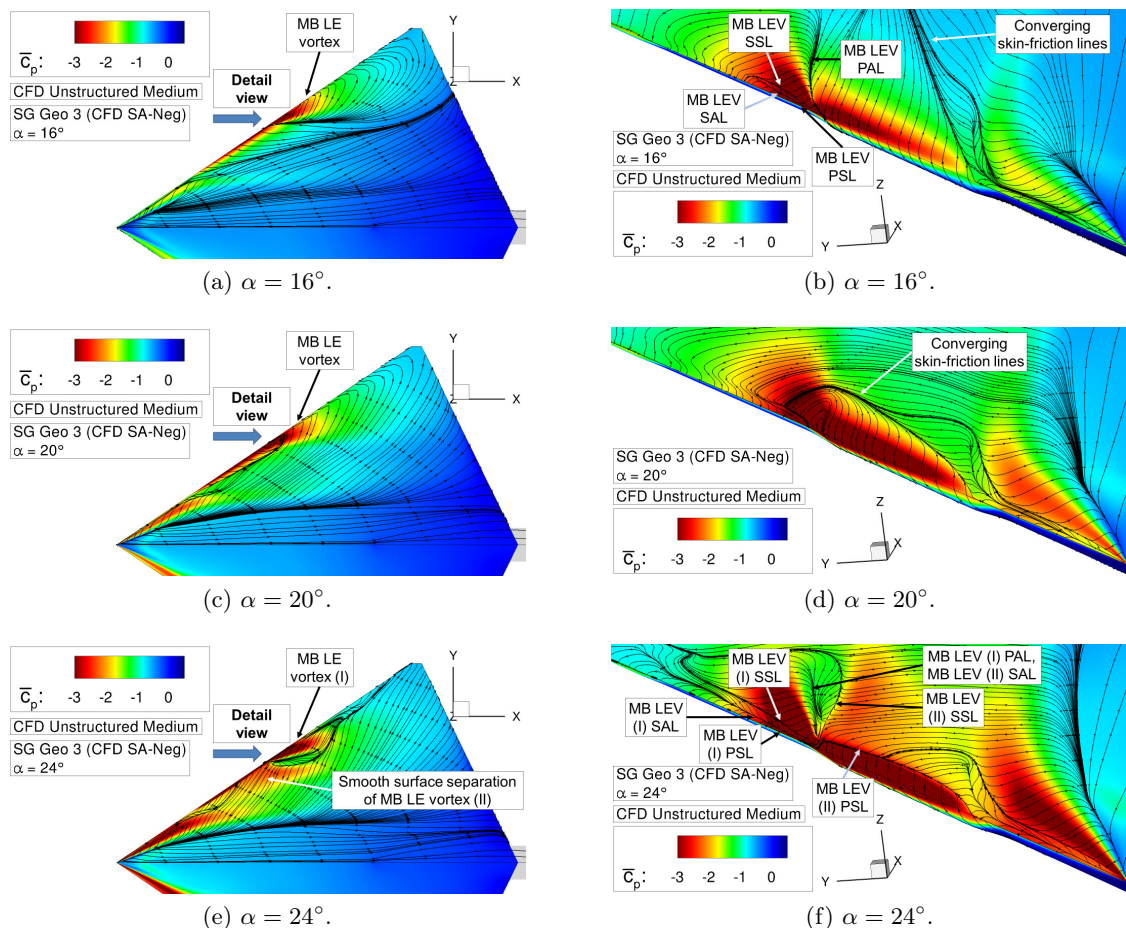


Figure 6.28: Flow physics analysis of configuration SG Geo 3 – Surface pressure coefficient \bar{C}_p including skin-friction lines.

6.3 Leading-Edge Shape Modifications

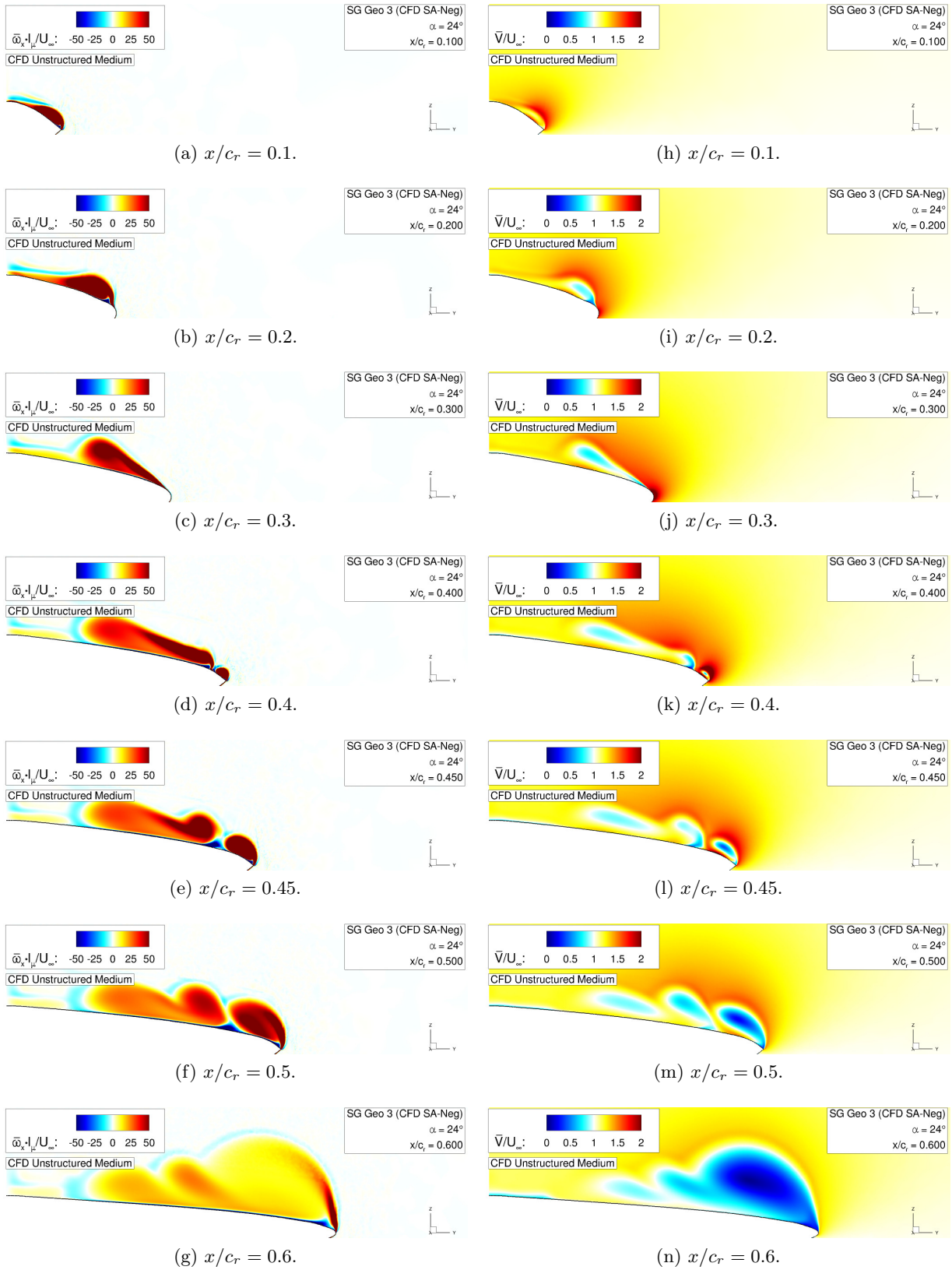


Figure 6.29: Flow physics analysis of configuration SG Geo 3 – Axial vorticity contours $\bar{\omega}_x \cdot l_\mu / U_\infty$ and absolute velocity contours \bar{V} / U_∞ at $\alpha = 24^\circ$.

To highlight the vortex formation and progression of configuration SG Geo 3 at $\alpha = 24^\circ$, Figure 6.29 additionally depicts corresponding sectional contour plots. Both the axial vorticity component and the absolute velocity are considered in selected chordwise sections on the diamond wing surface. The IB LE vortex is already observed in the most upstream wing section at $x/c_r = 0.1$. Due to the contour transition from sharp to round, it is then displaced from the leading edge to the upper wing surface and moves downstream on the inboard wing section, see Figure 6.29a to Figure 6.29c. Between $x/c_r = 0.4$ and $x/c_r = 0.5$, the vortex formation of both MB LE vortices occurs, see Figure 6.29d to Figure 6.29f. In total, three dominant structures with high axial vorticity contour levels are finally noticeable. The associated secondary effects become also obvious, as remarkable counter-rotating structures are present between both MB LE vortices. The contour plots of the absolute velocity further demonstrate the instantaneous wake-type character of each MB LE vortex core flow, see Figure 6.29k to Figure 6.29m. For the MB LE vortex I, the reduced speeds are much more distinct, since vortex breakdown has already moved upstream for quite a while. In summary, this shows the complex flow field characteristics that are present for configuration SG Geo 3 with increasing angle of attack. In comparison to configuration SG Geo 2, the flow physics is thus more influenced by the leading-edge contour modification of LE segment III. With respect to the aerodynamic coefficients of the reference configuration SG Geo 1, more distinct differences are therefore expected.

6.3.2 Longitudinal Aerodynamic Coefficients

Lift Coefficient Characteristics

Figure 6.30 shows the lift coefficient characteristics of configurations SG Geo 2 and SG Geo 3 versus the angle of attack. Compared to the reference configuration SG Geo 1, both cases nearly result in the same lift coefficient curves. Significant differences are only noticeable in the lift slope $C_{L,\alpha}$ for configuration SG Geo 3, see Figure 6.30b. Configuration SG Geo 2 shows rather

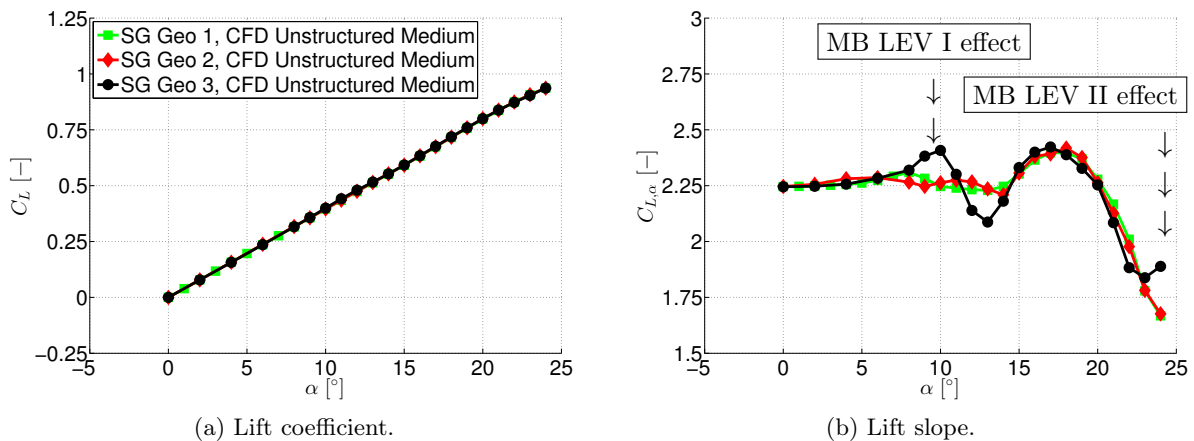


Figure 6.30: Longitudinal aerodynamic coefficients of configurations SG Geo 2 and SG Geo 3 – Lift coefficient C_L and derivative $C_{L,\alpha}$ versus angle of attack α .

insignificant deviations in the $C_{L,\alpha}$ values at low to medium angles of attack. They are the result of the OB LE vortex, which is only present up to $\alpha = 12^\circ$. From then on, the flow field characteristics are equal to those of the reference configuration SG Geo 1, which leads to the same lift-slope characteristics with increasing angle of attack.

With respect to configuration SG Geo 3, the occurring deviations are caused by the midboard leading-edge vortices. Increasing $C_{L,\alpha}$ values are noticed first up to $\alpha = 10^\circ$, since the MB LE vortex I becomes continuously stronger. As soon as the MB LE vortex I also controls the outboard wing region, a lift-slope-decreasing trend becomes dominant, since the attached flow region in between of the MB LE vortex I and the recirculation area is suddenly diminished. In addition, the incipient and upstream-moving vortex breakdown amplifies this trend. For angles of attack of $\alpha > 14^\circ$, the lift slope increases again, as the IB and MB LE vortex become stronger and more dominant. With increasing angle of attack, the lift-slope characteristics are then comparable to those of the reference configuration SG Geo 1. At the angles of attack of $\alpha = 23^\circ$ and $\alpha = 24^\circ$, the effect of the MB LE vortex II is finally observed, and increasing values are present again. For even higher angles of attack, remarkable deviations can thus be expected in comparison to the reference configuration SG Geo 1.

Drag Coefficient Characteristics

Next, the drag coefficient characteristics are compared to each other. The results are presented in Figure 6.31. Between configurations SG Geo 2 and SG Geo 1, no relevant differences are present. The low impact of this leading-edge contour modification thus becomes visible for the entire angle-of-attack polar. Configuration SG Geo 3, in contrast, results in increased drag coefficient values compared to the reference configuration SG Geo 1. This is due to the additional MB LE vortex I. Overall, higher drag coefficients are present, especially with increasing angle of attack. Together with the slightly different lift coefficients, this shifts the resulting Lilienthal polar to the right.

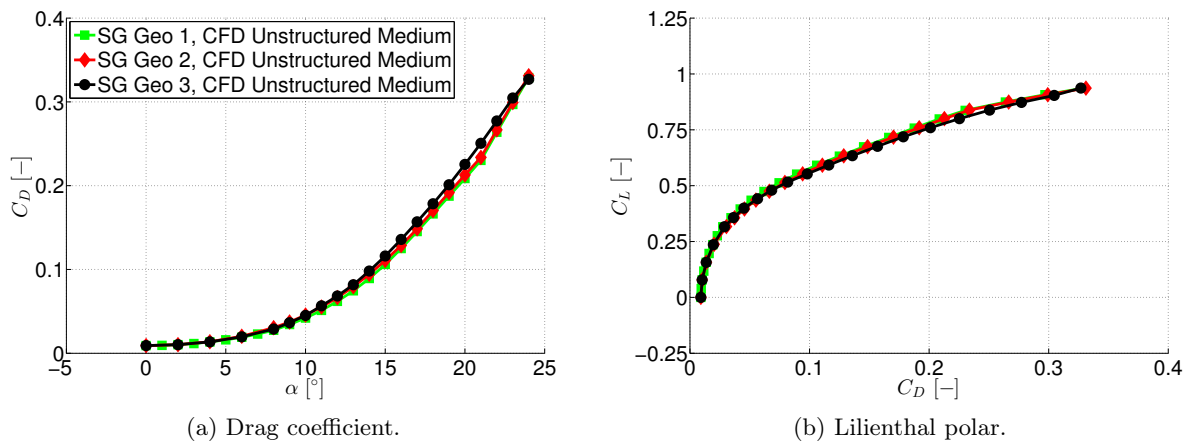


Figure 6.31: Longitudinal aerodynamic coefficients of configurations SG Geo 2 and SG Geo 3 – Drag coefficient C_D versus angle of attack α and Lilienthal polar C_L versus C_D .

The associated maximum lift-to-drag ratio at $\alpha = 6^\circ$ alters to $(C_L/C_D)_{max,SG\ Geo\ 3} = 12.06$. At $\alpha \geq 23^\circ$, the deviations attenuate, which again leads to comparable drag coefficient values.

Pitching-Moment Coefficient Characteristics

Finally, the pitching-moment characteristics are assessed for configurations SG Geo 2 and SG Geo 3. In Figure 6.32, the corresponding curves are opposed to those of the reference configuration SG Geo 1. In line with the findings of the lift coefficient characteristics, configuration SG Geo 2 does not show decisive differences in the pitching-moment characteristics over the entire angle-of-attack polar. The results of the local center of pressure and the derived stability value prove this observation, see Figure 6.33. Therefore, the longitudinal stability behavior is almost equal in comparison to the reference configuration SG Geo 1. The outboard leading-edge contour modification of configuration SG Geo 2 is thus of only minor importance for general application as passive flow control concept.

The continuing discussion concentrates on the results of configuration SG Geo 3. Compared to the pitching-moment characteristics of configuration SG Geo 1, the MB LE vortex I influences the longitudinal stability derivative for the first time at moderate angles of attack, see Figure 6.32b. At $\alpha = 11^\circ$ and $\alpha = 12^\circ$, the derivative considerably decreases in its absolute value, which is not seen for the other two cases. The effect is caused by the changing flow field characteristics in the outboard wing section as explained before. For the angle of attack of $\alpha = 12^\circ$, the underlying reasons are emphasized by the surface pressure distributions shown in Figure 6.34a and Figure 6.34b. On the one hand, the MB LE vortex I formation for configuration SG Geo 3 begins upstream of the longitudinal pitching-moment reference point $x_{mrp}(1)$. As a result, increased suction levels are noticed compared to configuration SG Geo 1. On the other hand, the vortical flow replaces the high leading-edge suction peaks of configuration SG Geo 1 downstream of $x_{mrp}(2)$. The upstream-moving vortex breakdown of configuration SG Geo 3 additionally decreases

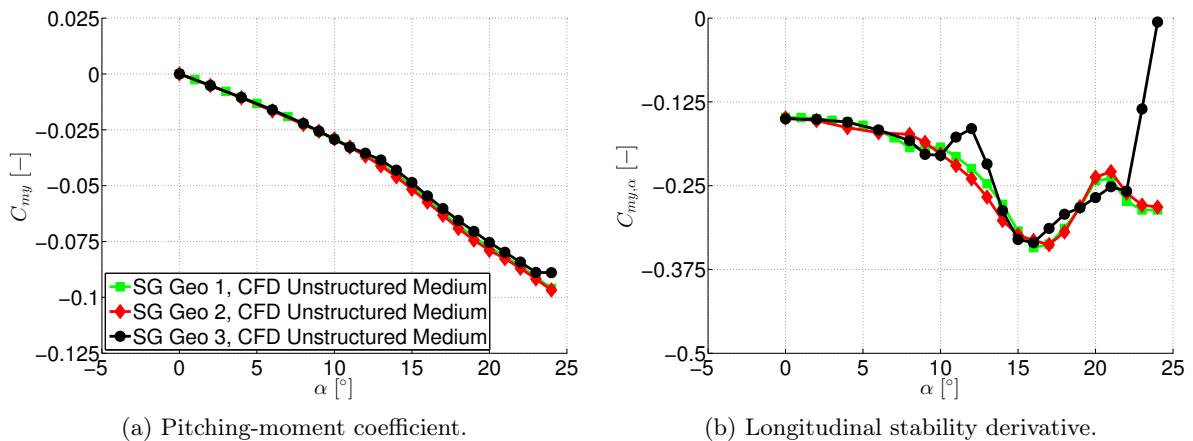


Figure 6.32: Longitudinal aerodynamic coefficients of configurations SG Geo 2 and SG Geo 3 – Pitching-moment coefficient C_{my} and derivative $C_{my,\alpha}$ versus angle of attack α .

the wing-tip suction levels (3). In total, this together leads to the noticeable deviation in the pitching-moment characteristics. The longitudinal stability value is thereby slightly reduced at the respective angles of attack, see Figure 6.33b.

With increasing angle of attack, the pitching-moment characteristics of configuration SG Geo 3 approximate to those of the reference configuration SG Geo 1, see Figure 6.32b. It is a consequence of the strengthened IB LE vortex, which becomes the dominant factor for the overall trend. For the angles of attack of $17^\circ \leq \alpha \leq 21^\circ$, small deviations are noticed again between both configurations due to the existence of the MB LE vortex I. Finally, a pronounced change is

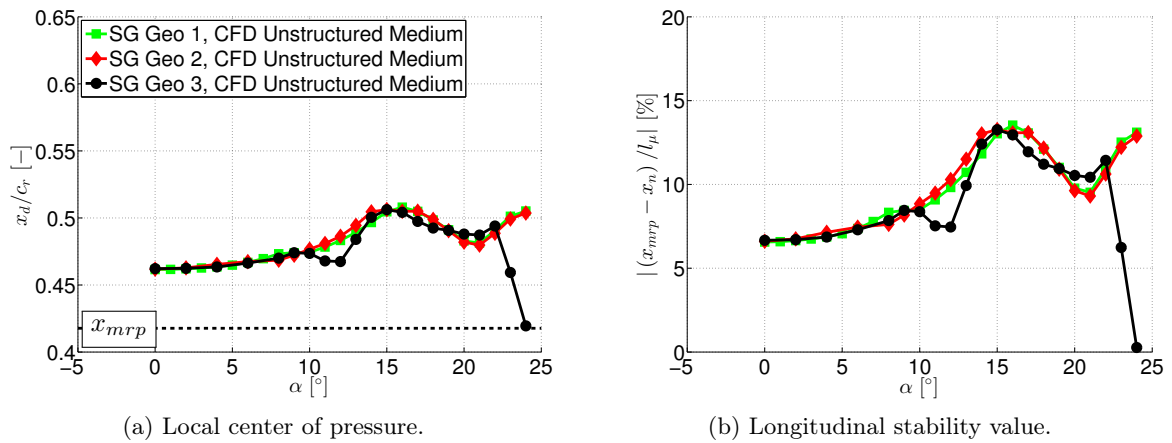


Figure 6.33: Longitudinal stability investigation of configurations SG Geo 2 and SG Geo 3 – Local center of pressure x_d/c_r and stability value $|(x_{mrp} - x_n)/l_\mu|$ vs. angle of attack α .

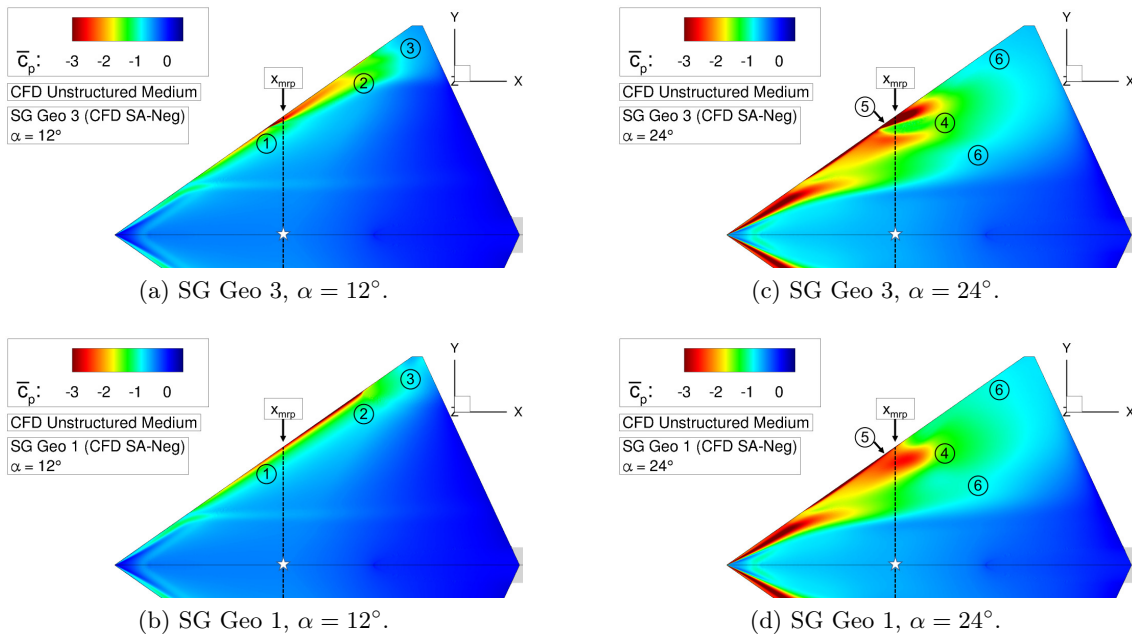


Figure 6.34: Longitudinal stability investigation of configuration SG Geo 3 – Surface pressure coefficient \bar{c}_p .

observed in the characteristics of configuration SG Geo 3 at $\alpha = 23^\circ$ and $\alpha = 24^\circ$. Due to the advent of the MB LE vortex II, the longitudinal stability derivative shows a distinct pitch-up tendency, see Figure 6.32b. The pitching-moment coefficient curve results in a remarkable deflection, see Figure 6.32a, and the derived stability value is almost reduced to 0%, see Figure 6.33b. The reasons for this behavior are demonstrated by the pressure coefficient distribution comparison at $\alpha = 24^\circ$, which is shown in Figure 6.34c and Figure 6.34d. Due to the split-up of both MB LE vortices, the overall size of the immediate suction region downstream of x_{mrp} is reduced for configuration SG Geo 3 compared to the reference configuration SG Geo 1 (4). The MB LE vortex I indeed exhibits decreased pressure coefficient values along the vortex axis downstream of x_{mrp} , but this also holds upstream of the pitching-moment reference point (5). The combination of the two MB LE vortices further impacts the size of the extended suction region downstream of x_{mrp} as well (6), and it is reduced for configuration SG Geo 3. Altogether, this particularly influences the resulting pitching-moment coefficients, and pitch-up characteristics are almost present at $\alpha = 24^\circ$. For higher angles of attack, unstable characteristics are consequently expected for configuration SG Geo 3. Hence, this demonstrates the impact of the applied leading-edge contour modification on the longitudinal stability behavior. Especially at higher angles of attack, the integral forces and moments are therefore controlled. In sum, configuration SG Geo 3 represents an example for passive flow control by leading-edge contour modification.

6.3.3 Synthesis

Two configurations with modified leading-edge contours have been considered in this section, namely configurations SG Geo 2 and SG Geo 3. Due to additional sharp leading-edge segments in the outboard and midboard wing sections, respectively, differences in the flow physics have been identified compared to the reference configuration SG Geo 1. The impact on the longitudinal aerodynamic coefficients is rated differently, which leads to the following conclusions:

Configuration SG Geo 2

- The additional sharp leading-edge contour in the outboard wing section of configuration SG Geo 2 influences the flow physics only up to the angle of attack of $\alpha = 12^\circ$. The emerging outboard leading-edge vortex is not stable, since vortex breakdown instantly becomes dominant.
- Beginning with $\alpha = 12^\circ$, the outboard leading-edge vortex has completely vanished and is replaced by a recirculation area with flow reversal, which is almost equal to the outboard separation region of the reference configuration SG Geo 1. Despite the modified leading-edge contour, no significant differences compared to the flow physics of configuration SG Geo 1 are thus present any longer.
- The longitudinal aerodynamic coefficients are hardly influenced by the leading-edge contour modification of configuration SG Geo 2. Consequently, the outboard leading-edge shape

can not control the integral forces and moments with increasing angle of attack. In the context of passive flow control concepts, this finally shows the low impact of the outboard leading-edge contour on the aerodynamic characteristics of the SAGITTA configuration.

Configuration SG Geo 3

- Due to the sharp leading-edge contour in the midboard leading-edge segment III, the flow physics associated with configuration SG Geo 3 is influenced more considerably. As a result, a midboard leading-edge vortex is present over the entire angle-of-attack polar.
- The midboard leading-edge vortex, which occurs at $\alpha = 20^\circ$ for the reference configuration SG Geo 1 due to a smooth surface separation, is still relevant for configuration SG Geo 3. It complicates the overall flow field characteristics with increasing angle of attack. In consequence, three different partly-developed leading-edge vortices are present at $\alpha = 24^\circ$, namely the inboard and two midboard leading-edge vortices.
- The longitudinal aerodynamic coefficients of configuration SG Geo 3 are influenced by the additional sharp leading-edge contour over the entire angle-of-attack polar. In particular, the pitching-moment coefficient characteristics are changed. As a result of the complex vortex flow phenomena with increasing angle of attack, pitch-up characteristics are almost present at $\alpha = 24^\circ$. Hence, this proves the general ability of leading-edge contour modifications to affect the aerodynamic characteristics and to control the overall stability behavior. In case of the SAGITTA configuration, the midboard wing section is appropriate for this purpose. Due to the decreased longitudinal stability at higher angles of attack, the agility of the diamond wing configuration is thereby improved.

6.4 Leading-Edge Twist Modification

The last configuration considered in this research, namely configuration SG Geo 4, is characterized by a leading-edge twist modification of the reference configuration SG Geo 1. The leading-edge nose coordinate is twisted along the semi-span in z-direction. The corresponding local distribution can be observed from Figure 1.11. At the wing tip, the entire airfoil section is twisted versus the root chord airfoil. Overall, the applied leading-edge twist modification results in increased effective angles of attack, especially in the midboard wing section. In consequence, the smooth surface separation in the midboard wing region with the MB LE vortex formation is expected to occur already at lower angles of attack.

6.4.1 Flow Physics Analysis

Figure 6.35 shows the resulting flow phenomena for the considered angle-of-attack polar. Up to $\alpha = 12^\circ$, only minor differences can be observed in the overall flow field characteristics compared to the reference configuration SG Geo 1. Because of the modified leading-edge nose position at

Passive Flow Control by Leading-Edge Contour Modifications

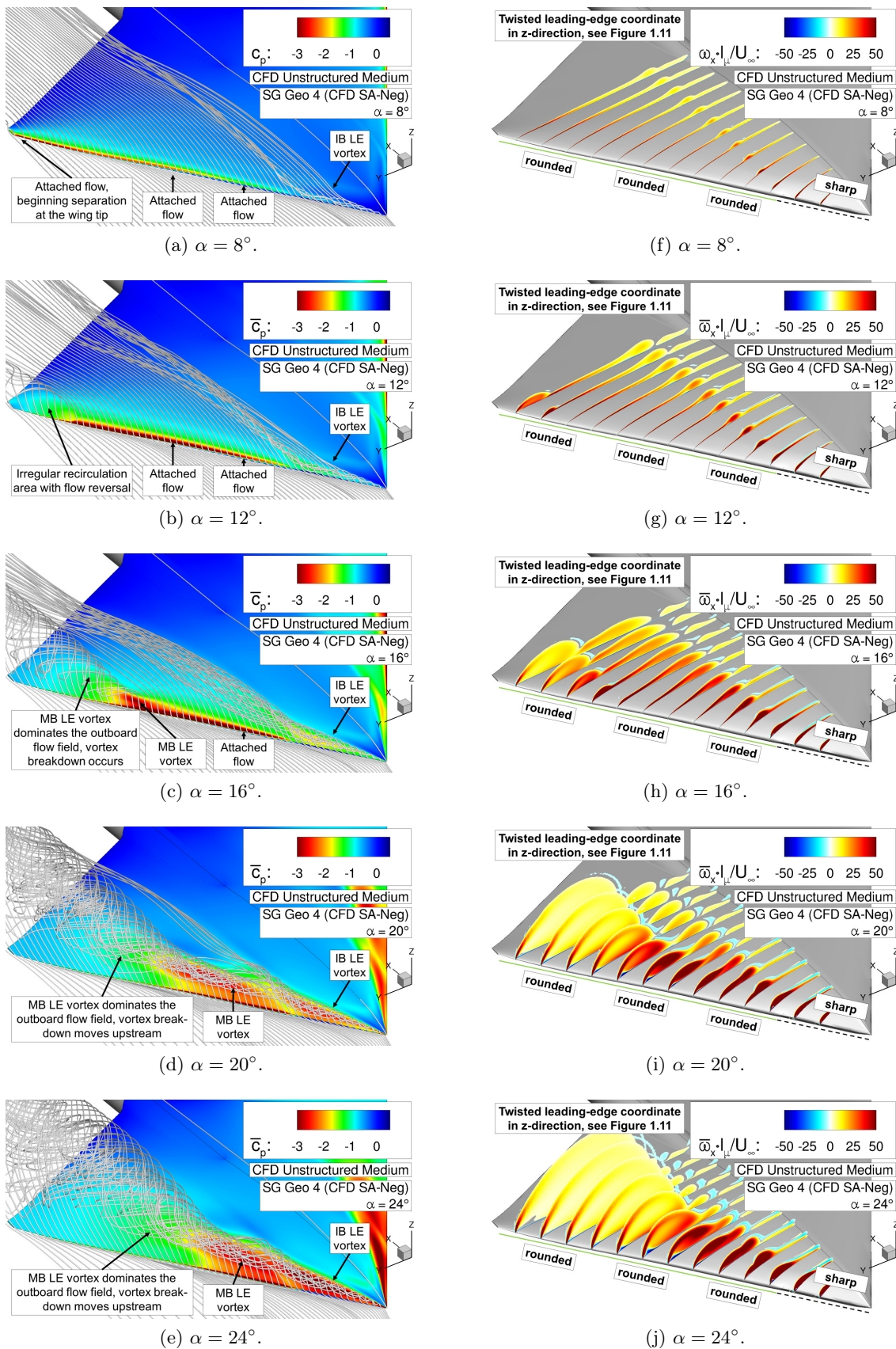


Figure 6.35: Flow physics analysis of configuration SG Geo 4 – Surface pressure coefficient \bar{c}_p including field streamlines, and axial vorticity contours $\bar{\omega}_x \cdot l_\mu / U_\infty$.

the inboard transition from sharp to round, the IB LE vortex strength is slightly decreased at first, compare Figure 6.35a and Figure 6.8a. The high leading-edge suction levels in the midboard attached flow region, in contrast, are promoted upstream and are more pronounced for configuration SG Geo 4, see Figure 6.35b and Figure 6.8b.

At the angle of attack of $\alpha = 16^\circ$, the flow physics shown in Figure 6.35c indicates a fundamental change in the outboard and midboard flow field characteristics, since a distinct MB LE vortex is present in this case. It controls the outboard flow field and the recirculation area is no longer relevant. To emphasize the flow separation onset in more detail, additional skin-friction patterns are presented in Figure 6.36. In particular, the flow physics progression is considered from $\alpha = 15^\circ$ to $\alpha = 18^\circ$. Figure 6.36a and Figure 6.36b depict the situation at $\alpha = 15^\circ$. Converging skin-friction lines occur close to the leading edge and direct towards a focus point, where the incipient MB LE vortex escapes from the wing surface. The local skin-friction structure is very similar to the corresponding one of the reference configuration SG Geo 1 at $\alpha = 20^\circ$, see Figure 6.9d. Hence, this proves the assumption of a premature MB LE vortex formation at configuration SG Geo 4 in consequence of the increased effective angle of attack. More inboard on the upper wing surface, additional converging skin-friction lines are noticed in Figure 6.36b. This structure is quite comparable to the corresponding skin-friction lines of configuration SG Geo 1 at $\alpha = 16^\circ$, compare Figure 6.9b. The particular skin-friction line, which divides the IB LE vortex flow and the midboard attached flow, directly starts at the contour transition from sharp to round (1). If the angle of attack is only slightly increased, the MB LE vortex strongly develops and a primary separation line is suddenly present along the entire midboard wing section, see Figure 6.36d. Beginning with the contour transition point (1), it is located offside the leading edge on the upper wing surface, thus defining the incipient separation region. The MB LE vortex footprint is observed further outboard, and distinct vortex suction levels occur. From then on towards the wing tip, the primary separation line is displaced to the wing leading edge. At $\alpha = 17^\circ$, the MB LE vortex is massively promoted upstream and the vortex axis moves considerably inboard on the upper wing surface, see Figure 6.36e. Compared to the reference configuration SG Geo 1, the progression of the MB LE vortex happens more abruptly and with increased intensity. This is a result of the leading-edge twist modification. In addition, the primary separation line slightly moves back towards the leading edge, see Figure 6.36f, but with increasing angle of attack, it still remains on the upper wing surface. The outboard flow between the MB LE vortex and the leading edge is fed by fluid transport of the IB LE vortex, which is concluded from the condensed skin-friction lines in this area (2). With increasing MB LE vortex strength, this leads to secondary separation effects in the midboard wing region (3), see Figure 6.36h and Figure 6.36j. For the angle of attack of $\alpha = 24^\circ$, the associated separation and attachment lines are highlighted.

Figure 6.35d and Figure 6.35e globally demonstrate the upstream progression of the MB LE vortex with increasing of attack. At $\alpha = 24^\circ$, the IB LE vortex and the MB LE vortex merge together and form one dominant vortex structure. The axial vorticity contour levels support this observation, since the downstream IB LE vortex footprints on the wing surface become less dis-

Passive Flow Control by Leading-Edge Contour Modifications

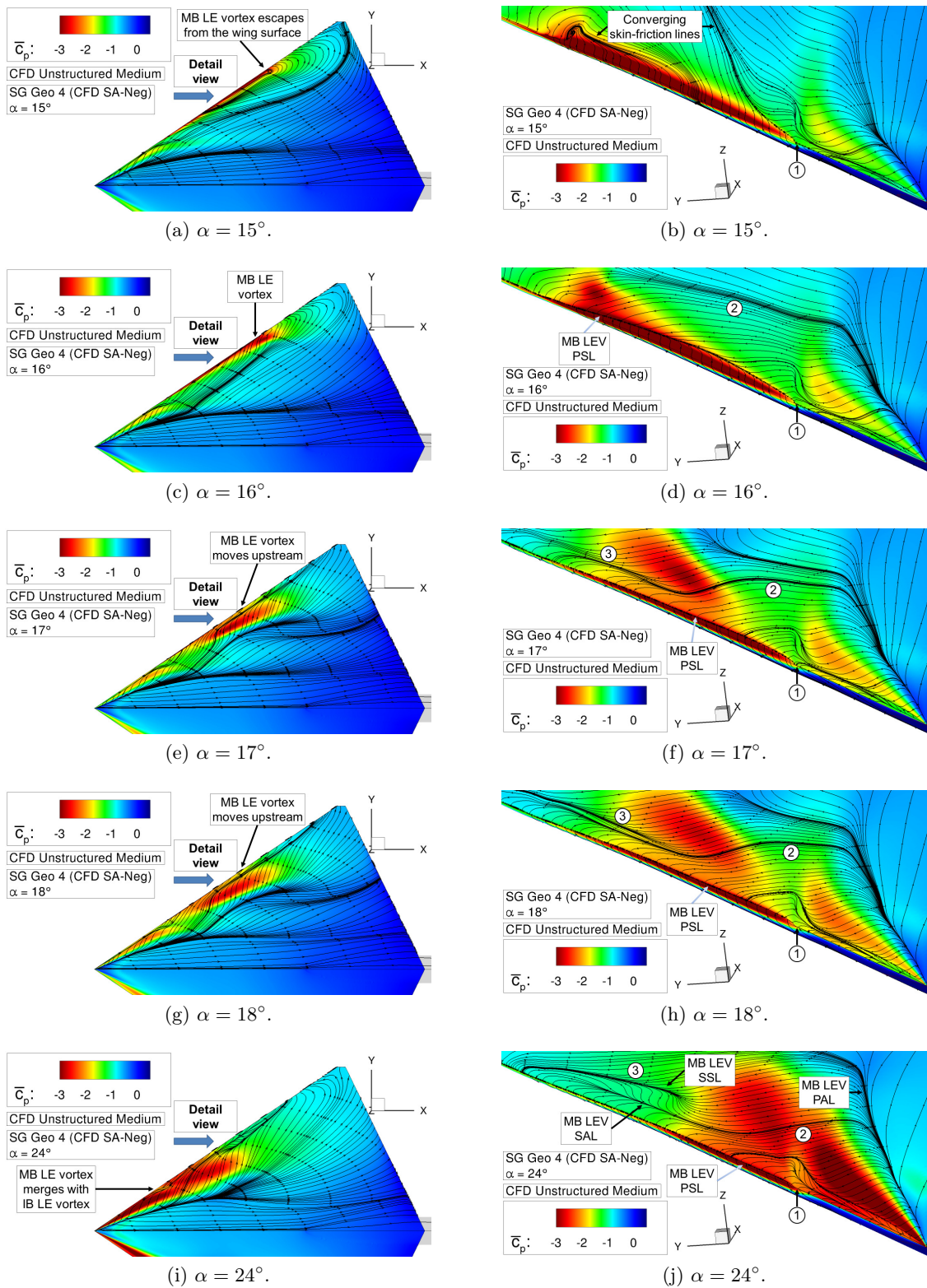


Figure 6.36: Flow physics analysis of configuration SG Geo 4 – Surface pressure coefficient \bar{c}_p including skin-friction lines.

6.4 Leading-Edge Twist Modification

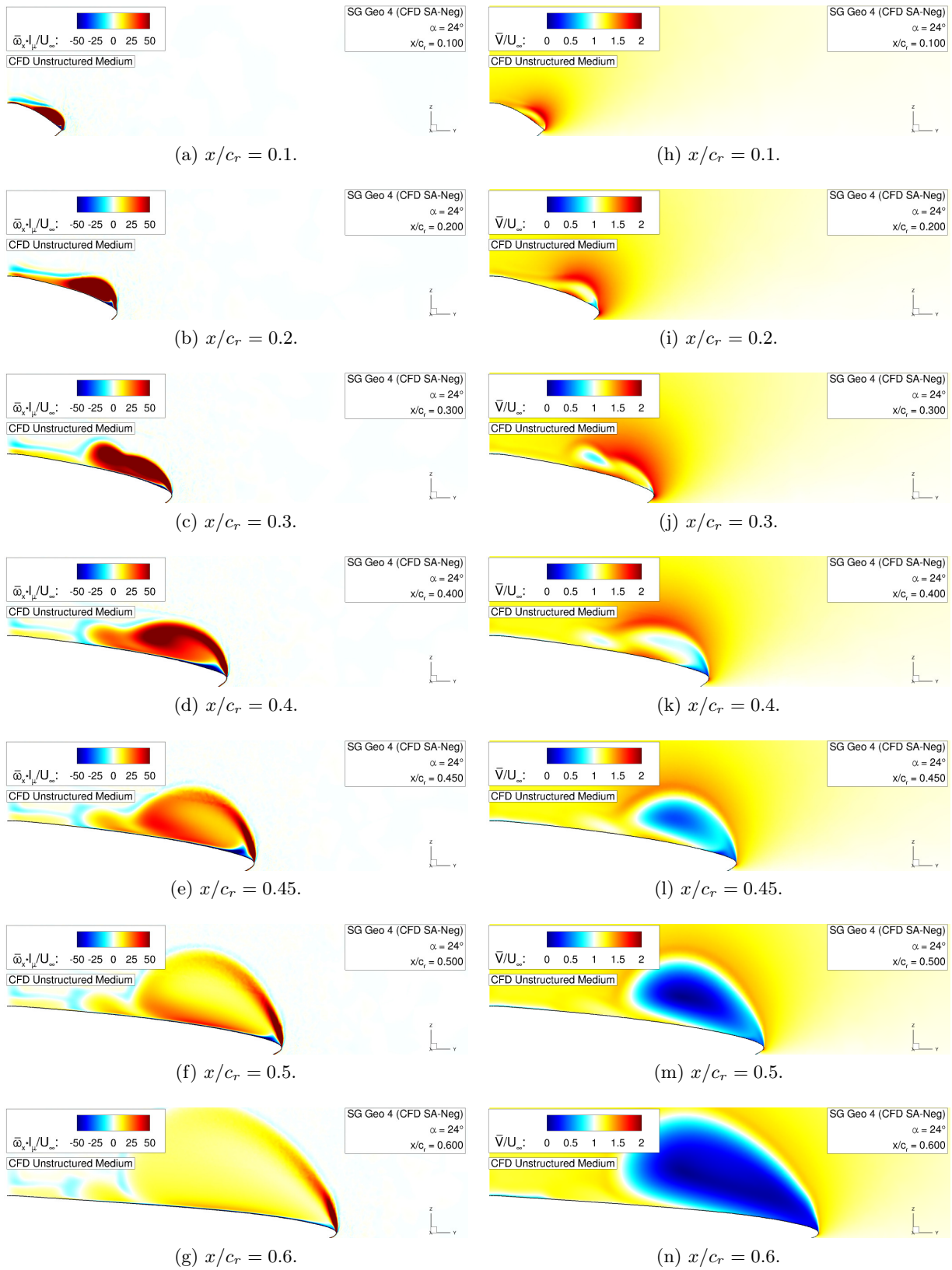


Figure 6.37: Flow physics analysis of configuration SG Geo 4 – Axial vorticity contours $\bar{\omega}_x \cdot l_\mu / U_\infty$ and absolute velocity contours \bar{V} / U_∞ at $\alpha = 24^\circ$.

tinct due to the feeding of the MB LE vortex, see Figure 6.35j. For selected chordwise sections, Figure 6.37 highlights this trend in sectional contour plots. Compared to the corresponding characteristics of the reference configuration SG Geo 1, see Figure 6.10, the IB LE vortex is less intense in the downstream chordwise sections. The MB LE vortex, in contrast, is much more developed in the upstream wing sections. Already at $x/c_r = 0.3$, the MB LE vortex is observed due to the premature flow separation onset, see Figure 6.37c. Pronounced axial vorticity contour levels are then noticed up to $x/c_r = 0.45$, before decreased $\overline{\omega_x}$ values become dominantly. Moreover, the area with low axial vorticity levels of the MB LE vortex is increased, which demonstrates the occurring vortex bursting phenomena. The dominant role of the MB LE vortex at higher angles of attack is thus emphasized for configuration SG Geo 4. The absolute velocity development of the MB LE vortex furthermore confirms the vortex breakdown process in the downstream wing sections, as the wake-type character in the vortex core flow is clearly seen in Figure 6.37k to Figure 6.37n. In comparison to the reference configuration SG Geo 1, the plots also show the upstream-shifted vortex breakdown for configuration SG Geo 4 in consequence of the earlier MB LE vortex formation. The vortex core flow of the IB LE vortex in the most upstream wing sections, in contrast, is stabilized by the combined vortex structure. The comparison at $x/c_r = 0.2$ indicates a reduced wake-type character of the IB LE vortex core flow for configuration SG Geo 4, see Figure 6.37i and Figure 6.10i. This is again caused by the nearby existence of the MB LE vortex and the associated fluid transport to feed the additional leading-edge vortex. As a result, this also leads to more pronounced suction levels along the IB LE vortex axis in the most upstream wing region, compare Figure 6.36j and Figure 6.9f.

6.4.2 Longitudinal Aerodynamic Coefficients

Lift Coefficient Characteristics

The effects of the leading-edge twist modification on the lift coefficient characteristics are presented in Figure 6.38. With respect to the integral values of the lift coefficient, differences to the reference configuration SG Geo 1 are hardly noticeable over the angle-of-attack polar. The corresponding lift slope, in contrast, emphasizes the deviations, which are present for configuration SG Geo 4 by the premature MB LE vortex formation and its progression. They become obvious for $\alpha > 12^\circ$, as the intensified leading-edge suction levels in the attached midboard wing section first lead to a more pronounced lift-slope increase, see Figure 6.38b. As soon as the MB LE vortex strongly develops and the flow separates close to the midboard leading edge, the $C_{L,\alpha}$ values remarkably decrease for $\alpha > 15^\circ$. This effect is however attenuated shortly after, since the abrupt upstream promotion of the MB LE vortex is damped with increasing angle of attack and both LE vortices are continuously strengthened. In total, this leads to a slight and constant reduction of the lift-slope values at higher angles of attack, which is less distinct than the lift-slope reduction of configuration SG Geo 1. In summary, this shows that the increasing vortex strength of the IB and MB LE vortex can not compensate the effects of the upstream-moving vortex breakdown up

to $\alpha = 24^\circ$. Compared to the results of the reference configuration SG Geo 1, however, higher lift-slope values are observed for $\alpha > 22^\circ$.

Drag Coefficient Characteristics

Next, the drag coefficient characteristics of configuration SG Geo 4 are discussed, see Figure 6.39. Due to the earlier formation of the MB LE vortex compared to configuration SG Geo 1, a significant drag increase is noticeable for angles of attack of $\alpha > 16^\circ$. The abrupt formation of the MB LE vortex contributes to the occurring deviations, which are observed up to $\alpha = 24^\circ$. In sum, configuration SG Geo 4 thus results in increased drag coefficient values at higher angles of attack. The Lilienthal polar in Figure 6.39b further highlights this finding. In comparison to the results associated with the leading-edge shape modifications of configurations SG Geo 2 and SG Geo 3, see Figure 6.31b, more remarkable differences are therefore present.

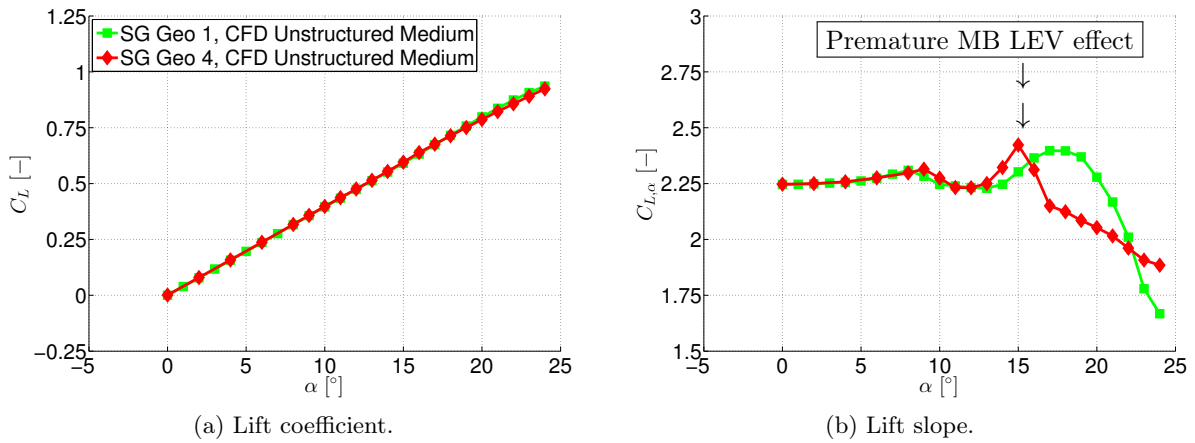


Figure 6.38: Longitudinal aerodynamic coefficients of configuration SG Geo 4 – Lift coefficient C_L and derivative $C_{L,\alpha}$ versus angle of attack α .

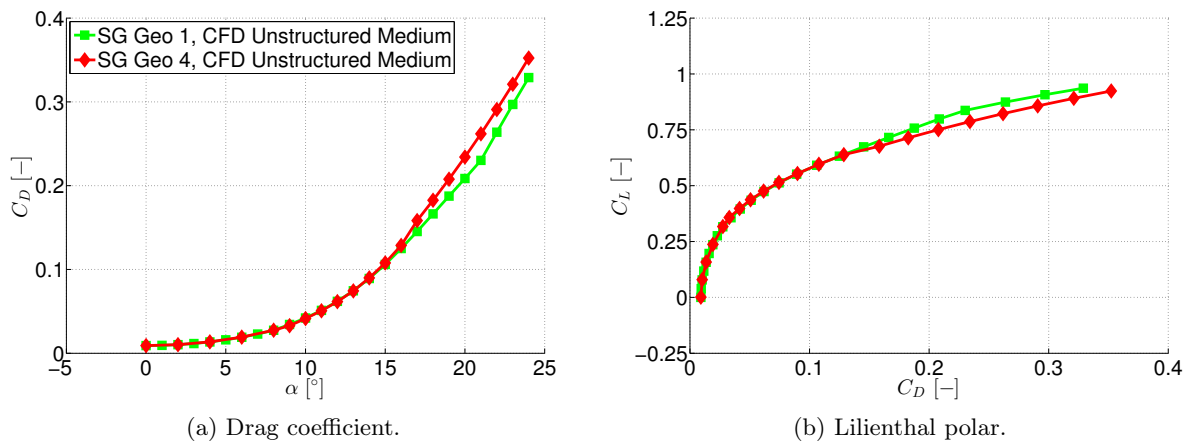


Figure 6.39: Longitudinal aerodynamic coefficients of configuration SG Geo 4 – Drag coefficient C_D versus angle of attack α and Lilienthal polar C_L versus C_D .

Pitching-Moment Coefficient Characteristics

The pitching-moment characteristics of configuration SG Geo 4 are finally considered. Figure 6.40 presents the corresponding coefficient and the longitudinal stability derivative versus the angle of attack. Figure 6.41 highlights the resulting local center of pressure and the derived stability value. Up to the angle of attack of $\alpha = 14^\circ$, the pitching-moment characteristics of configuration SG Geo 4 are equal to those of the reference configuration SG Geo 1. Then, remarkable differences are present with increasing angle of attack. They are caused by the premature MB LE vortex formation and the mutual interaction with the IB LE vortex. Overall, the effects are much more distinct than those occurring for configuration SG Geo 2 and SG Geo 3. At $\alpha = 16^\circ$ and $\alpha = 17^\circ$, the pitching-moment coefficient of configuration SG Geo 4 is momentarily displaced to higher values, see Figure 6.40a. In consequence, the longitudinal stability derivative drastically decreases in its absolute value, and the stability value is reduced to less than 4%, see Figure

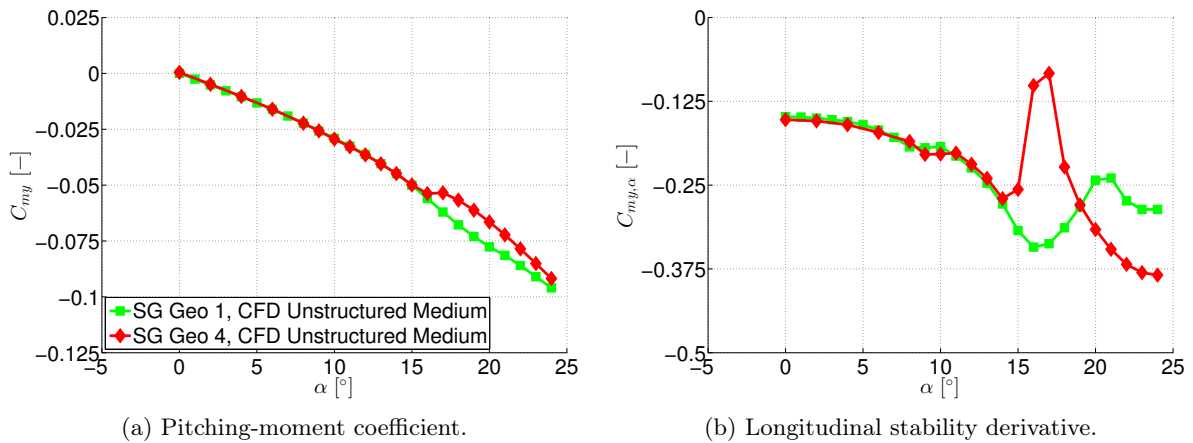


Figure 6.40: Longitudinal aerodynamic coefficients of configuration SG Geo 4 – Pitching-moment coefficient C_{my} and derivative $C_{my,\alpha}$ versus angle of attack α .

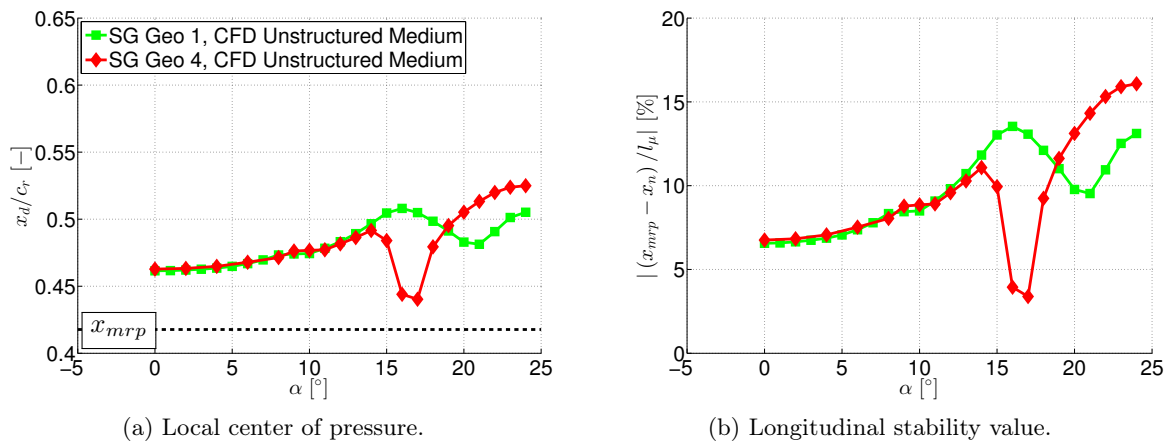


Figure 6.41: Longitudinal stability investigation of configuration SG Geo 4 – Local center of pressure x_d/c_r and stability value $|(x_{mrp} - x_n)/l_\mu|$ vs. angle of attack α .

6.40b and Figure 6.41b. The relevant reasons for this behavior are emphasized in Figure 6.42a and Figure 6.42b. The comparison of the surface pressure coefficients shows the diverse flow field characteristics of configurations SG Geo 4 and SG Geo 1 at $\alpha = 17^\circ$. The upstream-moving MB LE vortex instantly results in a flow separation onset located upstream of the pitching-moment reference point x_{mrrp} (1), which in summary leads to a destabilizing effect compared to the attached flow in the midboard wing section of configuration SG Geo 1. The suction levels of the IB LE vortex are thereby increased for configuration SG Geo 4 (2), which also contributes to the immediate stability loss. Finally, the interaction between the two vortical structures of configuration SG Geo 4 further results in a region of reduced surface pressures upstream of x_{mrrp} (3), and increased \bar{c}_p values downstream of the pitching-moment reference point (4). Altogether, this ends up in the displacement of the C_{my} values as shown in Figure 6.40a.

For $\alpha > 17^\circ$, decreasing pitching-moment coefficients are noticed again for configuration SG Geo 4. With increasing angle of attack, the negative slope increases and the pitching-moment coefficients approximate to those of the reference configuration SG Geo 1. At $\alpha = 24^\circ$, a difference of only 4% is left in the final C_{my} value. The corresponding stability derivative thus exhibits decreasing values as well, see Figure 6.40b, but the overall trend attenuates. For $\alpha > 19^\circ$, the $C_{my,\alpha}$ values are found to be smaller for configuration SG Geo 4 than for configuration SG Geo 1. In summary, the local center of pressure is shifted downstream with increasing angle of attack, and the derived stability value is increased, see Figure 6.41. At $\alpha = 24^\circ$, a value of $|(x_{mrrp} - x_n)/l_\mu| \approx 16\%$ is observed for configuration SG Geo 4, which roughly corresponds to a 21% increase compared to the reference configuration SG Geo 1. Overall, this is the result of

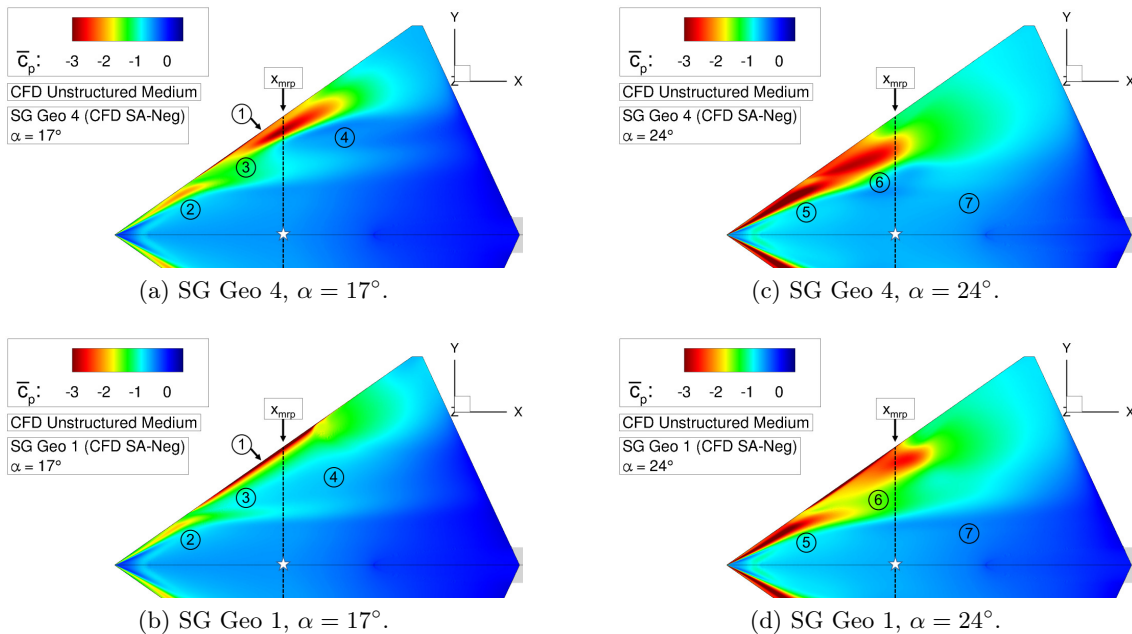


Figure 6.42: Longitudinal stability investigation of configuration SG Geo 4 – Surface pressure coefficient \bar{c}_p .

the modified pressure distribution on the wing surface in consequence of the leading-edge twist modification. By way of example, Figure 6.42c and Figure 6.42d demonstrate the corresponding characteristics at $\alpha = 24^\circ$. On the one hand, the combined vortex structure of the IB and the MB LE vortex dominates the flow field upstream of the pitching-moment reference point to a larger extent than in case of the reference configuration SG Geo 1 (5,6). The higher suction levels along the vortex axes are rather disadvantageous with respect to the longitudinal stability behavior. On the other hand, however, the increased vortex strength feeds the inboard attached flow region downstream of x_{mrp} more intensively in case of configuration SG Geo 4. It results in reduced pressure coefficient values for a large inboard and downstream wing region (7). In total, this is the key factor for the increased longitudinal stability value compared to configuration SG Geo 1. With respect to the pitching-moment characteristics of configuration SG Geo 5 as discussed in Section 6.2.2, the same trends thus dominate the derived stability value of configuration SG Geo 4 at high angles of attack. Once the IB and MB LE vortex have merged for configuration SG Geo 4, one can further show the similarity of the corresponding surface pressure distributions with those of configuration SG Geo 5. Despite the differences in the midboard and outboard leading-edge contour, comparable $\overline{c_p}$ values are observed on the diamond wing surface, apart from slight deviations in the LE vortex suction levels upstream of x_{mrp} . Compared to the reference configuration SG Geo 1, this results in the increased stability value of configuration SG Geo 4 for the angles of attack of $19^\circ < \alpha < 24^\circ$. In summary, the present analysis thus shows the significance of the leading-edge twist modification for the pitching-moment characteristics at the SAGITTA configuration. The changed flow field characteristics influence the longitudinal stability behavior at high angles of attack in a positive manner, which proves configuration SG Geo 4 as a successful concept of passive flow control. For even higher angles of attack not considered in this thesis, the stability gain is still expected to remain, as the strength of the merged IB and MB LE vortex increases and the downstream induction on the inboard attached flow regions is maintained.

6.4.3 Synthesis

This section has discussed the flow physics and the aerodynamic coefficients of configuration SG Geo 4, which features a leading-edge twist modification compared to the reference configuration SG Geo 1. The results demonstrate that the overall flow field characteristics are changed for the considered angle-of-attack polar. The longitudinal stability behavior is therefore influenced as well. In comparison to the aerodynamic characteristics of the reference configuration SG Geo 1, one can conclude:

Configuration SG Geo 4

- The formation of the midboard leading-edge vortex already becomes relevant at the angle of attack of $\alpha = 15^\circ$, since the effective angle of attack is increased in the rounded midboard wing section due to the modified leading-edge nose coordinate. The vortex formation and

progression based on the rounded leading-edge contour occurs more abruptly and more intensively, which especially influences the pitching-moment characteristics of configuration SG Geo 4.

- With increasing angle of attack, the upstream-moving midboard leading-edge vortex highly interacts with the inboard leading-edge vortex. Both structures finally merge together and impact the overall pressure distribution on the wing surface. The results indicate that this fact is decisive with respect to the resulting stability characteristics in pitch, as the inboard wing region with attached flow is also influenced to some extent.
- The premature flow separation onset of the midboard leading-edge vortex temporarily reduces the longitudinal stability of configuration SG Geo 4 at $\alpha = 16^\circ$ and $\alpha = 17^\circ$. For higher angles of attack, in contrast, the pitching-moment characteristics then feature an increased stability value compared to the reference configuration SG Geo 1. Consequently, the leading-edge twist modification of configuration SG Geo 4 demonstrates a successful passive flow control concept with regard to increased longitudinal stability at high angle of attack.

Chapter 7

Conclusion and Outlook

The analysis and control of partly-developed leading-edge vortices on moderately-swept, low-aspect-ratio wing configurations are challenging in many aspects. Amongst others, occurring leading-edge vortex separations strongly depend in this case on the airfoil shape including rounded or spanwise-varying leading-edge contours, and on the boundary-layer characteristics due to Reynolds number effects. Consequently, complex flow separation onset characteristics are usually present for this type of wing configuration, and vortex-vortex interactions may occur with increasing angle of attack or sideslip conditions.

The present thesis has examined these issues in detail, as two different diamond wing configurations have been considered in experimental and numerical investigations at low-speed wind tunnel (W/T) conditions. On the one hand, the flow separation onset characteristics associated with rounded leading edges as well as the leading-edge vortex progression have been discussed on the AVT-183 configuration. The wing design refers to analyses of an international research task group within the community of NATO's Science and Technology Organization. In particular, a consistent flow-physical description of the leading-edge vortex formation from a smooth surface separation on boundary-layer level in the incipient separation region has been provided in this thesis for the first time. On the other hand, leading-edge contour modifications have been considered on the SAGITTA configuration, which relies on a research project associated with Airbus Defence and Space. Generally, the application of a spanwise-varying leading-edge geometry is motivated by mission requirements of typical unmanned (combat) aerial vehicle (U(C)AV) configurations. Moreover, leading-edge contour modifications demonstrate concepts of passive flow control. Some of them have therefore been reviewed and assessed in this thesis. They result in various flow physics with regard to occurring partly-developed leading-edge vortices and integral aerodynamic coefficients. The outcome of this study demonstrates improvements in the stability, controllability and agility characteristics of the considered wing configurations. They are thus of major relevance for practical wing designs of future low-observable U(C)AV applications, which likewise need to consider optimized aerodynamic characteristics and radar cross-section issues defined by wing planform and airfoil shape parameters.

The following paragraphs summarize the analyses that have been conducted in the course of this thesis. Key results of each diamond wing configuration are highlighted and major findings are emphasized. Thereafter, the overall outcome of both studies is combined and placed into context.

This provides a final assessment of the conducted research. Lastly, an outlook is given on the potential and need for future investigations, which are of central concern for further improvements in the respective field of research.

Analysis of Partly-Developed Leading-Edge Vortices

The investigation of the AVT-183 configuration has provided valuable insights into the leading-edge vortex formation and progression on a moderately-swept diamond wing configuration ($\varphi_{le} = 53^\circ$) with rounded leading-edge contour (NACA 64A006 airfoil). For the analyses, fully-turbulent flow has been considered by a fixed transition location with corresponding low-speed free stream conditions of $Re_\infty = 2.7 \cdot 10^6$ and $Ma_\infty = 0.15$. Generally, the observed flow physics is characteristic of the regarded type of vortex-dominated wing configuration. The derived findings therefore contribute to an improved understanding of smooth surface separations with consecutive leading-edge vortex formation. Essentially, the following conclusions can be stated:

- The flow field characteristics are represented by a partly-developed leading-edge vortex and other relevant flow field phenomena such as upstream attached flow, a secondary vortex separation close to the wing leading edge, and the "inner vortex" in the rear wing section. Both W/T experiments and CFD investigations identify the flow field phenomena very similarly. Hence, the results overall show a satisfying agreement between each other. In the experimental analyses, the flow separation onset characteristics are very sensitive to flow tripping by the applied leading-edge surface roughness. Specific target flow conditions have been defined for this reason, which show reasonably-tripped flow and are thus comparable to fully-turbulent CFD investigations.
- Upstream of the visible appearance of the leading-edge vortex, the vortical structure develops on boundary-layer level in the incipient separation region ($\delta_{99} \approx 0.002 \text{ m}$). The area is confined by limiting skin-friction lines, which define whether the flow remains in the inboard wing section or is relevant for the smooth surface separation with leading-edge vortex formation. At $\alpha = 12^\circ$, the incipient separation region begins at $x/c_r \approx 0.17$ while the first large-scale appearance of the vortical structure is at $x/c_r \approx 0.34$.
- The partly-developed leading-edge vortex is mostly characterized by wake-type vortex core flow with $\bar{V}/U_\infty \leq 0.8$ and quickly-decreasing axial vorticity levels of $\bar{\omega}_x \cdot l_\mu/U_\infty \leq 130$. Consequently, vortex bursting is immediately relevant after the large-scale appearance of the leading-edge vortex. Moreover, local maxima of turbulent kinetic energy with $k \approx 0.1$ are observed closely downstream at $x/c_r \approx 0.40$. They decrease towards the trailing edge.
- Two flow field phenomena are involved in the leading-edge vortex formation within the incipient separation region. First, the leading-edge vortex core is formed by converging skin-friction lines on the upper wing surface, which induce a three-dimensional flow separation at $x/c_r \approx 0.26$. Second, a tiny boundary-layer vortex is present closer to the wing leading

edge, which defines the origin of the primary separation line and later feeds the emerging leading-edge vortex.

- The evaluation of the corresponding topological rule in sectional cuts demonstrates changing arrangements of the singular points from upstream to downstream chordwise sections. Off-body saddle points are present within the near-wall flow field, which indicates that the partly-developed leading-edge vortex does locally not reattach to the wing surface. The "inner vortex" is formed further downstream along an off-body line of saddle points within the near-wall flow field. It is thereby not discernible in the corresponding skin-friction patterns.
- The integral lift and drag coefficient characteristics are influenced only to a small extent by the partly-developed leading-edge vortex. A non-linear lift increase due to leading-edge vortex suction is not visible. The pitching-moment characteristics are affected more considerably. As a result of the upstream-moving vortex breakdown characteristics, non-linearities are observed with increasing angle of attack.

Passive Flow Control by Leading-Edge Contour Modifications

The effects of leading-edge contour modifications have been analyzed on the SAGITTA diamond wing configuration. The respective leading-edge sweep angle is $\varphi_{le} = 55^\circ$ and the basic airfoil shape is of NACA 64A012 type. In addition to the reference configuration SG Geo 1, which features an inboard sharp leading-edge contour, and two cases with constant sharp and rounded leading edges (SG Geo 5 / SG Geo 6), three different configurations with modified spanwise-varying leading-edge contour (SG Geo 2 to SG Geo 4) have been investigated at low-speed W/T conditions of $Re_\infty = 2.3 \cdot 10^6$ and $Ma_\infty = 0.13$. In sum, the analyzed leading-edge contour modifications successfully demonstrate concepts of passive flow control, which are representative for application on typical U(C)AV designs. Therefore, one can conclude:

- The numerical results of the reference configuration SG Geo 1 are in very good agreement with respective experimental data. In consequence, the effects of the further discussed leading-edge contour modifications have been assessed exclusively based on CFD analyses.
- The flow field of the reference configuration SG Geo 1 is characterized by an inboard leading-edge vortex with core flow velocities of $\bar{V}/U_\infty \leq 1.2$. It is present due to the inboard sharp leading-edge contour. In the outboard wing section with rounded leading-edge contour, a recirculation area with flow reversal occurs with increasing angle of attack. At $\alpha = 20^\circ$, the outboard structure of irregular separated flow finally alters to a midboard leading-edge vortex, which emerges from a smooth surface separation. It is characterized by wake-type vortex core flow with $\bar{V}/U_\infty \leq 0.8$ and immediately shows vortex bursting tendencies.
- Configuration SG Geo 5 with an entirely sharp leading-edge contour features a full-span leading-edge vortex, which is of oval type and exhibits weak jet-type vortex core flow with

$\bar{V}/U_\infty \leq 1.2$ in the upstream wing sections. Vortex breakdown close to the trailing edge already occurs at low to moderate angles of attack ($\alpha_{burst} \approx 12^\circ$). This mostly leads to wake-type vortex core flow in the rear wing sections. The results thereby prove that the weak appearance of the leading-edge vortex and the vortex breakdown affinity is rather a consequence of the moderately-swept wing planform than of the leading-edge shape.

- The analysis of configuration SG Geo 6 with entirely rounded leading edges demonstrates that the midboard leading-edge vortex formation depends on the existence of the inboard leading-edge vortex. In case of configuration SG Geo 6, no leading-edge vortex occurs on the SAGITTA configuration up to $\alpha = 24^\circ$, but the outboard region of irregular separated flow continuously expands upstream. Compared to the results of the AVT-183 configuration, the observations prove the delay in leading-edge vortex formation with increased airfoil thickness at moderately-swept wing configurations featuring rounded leading edges.
- With regard to the aerodynamic characteristics of the reference configuration SG Geo 1, one can conclude: For low to moderate angles of attack up to $\alpha = 16^\circ$, the existence of the inboard sharp leading-edge contour is of minor importance with respect to the longitudinal aerodynamic coefficients. For higher angles of attack, in contrast, remarkable differences occur. Then, the inboard leading-edge shape is crucial for the midboard leading-edge vortex formation. The aerodynamic characteristics are thereby controlled, including the corresponding longitudinal stability behavior. The effects are most pronounced in the drag and the pitching-moment coefficients, whereas the lift coefficients are mostly determined by the wing planform only. With respect to the chosen pitching-moment reference point, longitudinal stability is further assured over the entire angle-of-attack polar.
- The additional sharp leading-edge contour in the outboard wing section of configuration SG Geo 2 influences the aerodynamic characteristics up to $\alpha = 12^\circ$ only. With increasing angle of attack, the flow physics does not differ any longer to those of the reference configuration SG Geo 1. In the context of passive flow control concepts, this ultimately shows the low impact of the outboard leading-edge contour on the aerodynamic characteristics of the SAGITTA configuration.
- Due to the additional sharp leading-edge contour in the midboard wing section, the flow physics associated with configuration SG Geo 3 is influenced more considerably. This time, a further midboard leading-edge vortex is present over the entire angle-of-attack polar. For $\alpha \geq 20^\circ$, in total three different partly-developed leading-edge vortices are observed, which interact with each other and complicate the flow field characteristics. In consequence, the aerodynamic coefficients are influenced with increasing angle of attack, especially the pitching-moment coefficient characteristics. At $\alpha = 24^\circ$, pitch-up tendencies are nearly reached on the SAGITTA configuration, which increases the response characteristics in terms of flight control inputs. Hence, the applied leading-edge contour modification in the midboard wing section is appropriate to control the overall stability behavior.

-
- The leading-edge twist modification of configuration SG Geo 4 lowers the formation of the midboard leading-edge vortex from a smooth surface separation to the angle of attack of $\alpha = 15^\circ$. The flow separation onset and progression occurs more abruptly and more intensively in this case, which in particular influences the pitching-moment characteristics. With increasing angle of attack, distinct vortex-vortex interactions are present between the inboard and the midboard leading-edge vortex, before both structures finally merge. For $\alpha \geq 19^\circ$, the pitching-moment characteristics result in an increased longitudinal stability compared to the reference configuration SG Geo 1. Overall, the leading-edge twist modification of configuration SG Geo 4 demonstrates a successful passive flow control concept with regard to enhanced longitudinal stability at high angle of attack.

Final Assessment

In combination, the investigation of the two diamond wing configurations in this thesis has significantly increased the level of knowledge on partly-developed leading-edge vortices occurring from smooth surface separations and spanwise-varying leading-edge contours. By the detailed analysis of the AVT-183 configuration, a fundamentally important contribution has been provided with regard to the overall understanding of the associated flow physics. The consistent flow-physical description of the flow separation onset and the leading-edge vortex progression including vortex breakdown effects adds to the fundamentals in this field of research. Moreover, the observed flow field phenomena are characteristic of moderately-swept wing configurations with rounded leading edges. The influence of airfoil thickness and leading-edge radius on the leading-edge vortex formation has also been demonstrated in this context by a comparison of the respective results to the corresponding ones of the SAGITTA configuration SG Geo 6.

In general, the key findings on the flow field characteristics of the AVT-183 configuration likewise apply to the flow physics of the SAGITTA configuration. This holds particularly for the weak appearance of occurring leading-edge vortices with mostly wake-type vortex core flow, instantaneous vortex bursting tendencies, and leading-edge vortex core shapes of oval type. The underlying reasons for the observed flow physics, however, are in this case not obvious at first sight. This is due to the increased airfoil thickness and the spanwise-varying leading-edge contour, from which vortex-vortex interactions arise with increasing angle of attack. This altogether complicates the flow physics of the considered SAGITTA configurations with modified leading-edge contours. In consequence, partly-developed leading-edge vortices occurring from smooth surface separations are considerably delayed and shifted to higher angles of attack. Moreover, they are only provoked by the existence of an inboard leading-edge vortex occurring from inboard sharp leading edges, or by a leading-edge twist modification of the midboard rounded leading-edge contour.

The fundamental effects of the flow field phenomena, which are present for configurations SG Geo 1 to SG Geo 4, have thus been accessible by the flow field characteristics of the AVT-183 configuration and the SAGITTA configurations SG Geo 5 and SG Geo 6 with entirely sharp and rounded leading-edge contours. Therefore, the aerodynamic characteristics of those configurations

with a spanwise-varying leading-edge contour have been understood and valued with regard to flight performance issues as well as stability concerns in the longitudinal motion. In sum, the lift coefficients have been found to vary only slightly by the leading-edge contour modifications, whereas drag and pitching-moment coefficients alter more significantly. Overall, the considered passive flow control concepts can therefore be regarded as examples for application on U(C)AV-related wing configurations. Due to the spanwise-varying leading-edge contours, relevant mission requirements such as low-observability criteria are accounted for while improvements on the longitudinal stability characteristics can also be achieved.

Outlook

The key findings of this thesis underline the significance of the AVT-183 configuration for the study of smooth surface separations. Furthermore, they have confirmed the potentials of passive flow control concepts on the SAGITTA configuration with regard to practical U(C)AV applications. Future investigations should now strive to extend the present research to other regimes within the flight envelope of related low-aspect-ratio wing designs. In particular, additional analyses with increased Mach and Reynolds numbers are essential in this context. At low-speed W/T conditions, the foundations have been laid by this thesis, but the knowledge on partly-developed leading-edge vortices at real-scale flight conditions of respective U(C)AV applications must further be improved. Since such low-aspect-ratio wing configurations commonly operate up to high subsonic Mach numbers, transonic effects will be present that also determine the overall aerodynamic shaping. Thus, the competing mission requirements concerning aerodynamic performance and radar cross-section issues are influenced even more by other parameters. The rather low impact of the leading-edge contour modifications on the lift coefficient characteristics, as demonstrated in this thesis, presents further options that allow for more rigorous leading-edge geometry changes in order to optimize the aerodynamic performance with increasing angle of attack by separated leading-edge vortex flow. The resulting effects on the pitching-moment coefficient characteristics, including the associated stability behavior, however, can not be foreseen to the full extent, especially in other regimes of the flight envelope.

As a result of the extensive experimental investigations conducted for this research, comprehensive data sets have further been derived for the AVT-183 and the SAGITTA configuration. They provide high-quality data bases suitable for overall CFD validation, which focuses on relevant flow fields of vortex-dominated wing configurations with reduced wing sweep and rounded or spanwise-varying leading-edge contours. With respect to a larger time horizon, the obtained data could therefore lead to an improved predictability of corresponding flow physics in present CFD codes, as current turbulence models could be tuned according to the experimental findings. The outcome of this research could thereby directly contribute to corresponding U(C)AV design and development, which is commonly undertaken by numerical analyses and mostly focuses on flight-relevant Mach and Reynolds numbers.

References

- [1] AGARD (ed.); **“Boundary Layer Simulation and Control in Wind Tunnels”**; AGARD Advisory Report 224; Advisory Group for Aeronautical Research and Development, 1988.
- [2] Allmaras, S. R., Johnson, F. T., and Spalart, P. R.; **“Modifications and Clarifications for the Implementation of the Spalart-Allmaras Turbulence Model”**; *7th International Conference on Computational Fluid Dynamics (ICCFD7)*, Big Island (HI), United States, July 9–13, 2012.
- [3] Alrutz, T.; **“Hybrid Grid Adaptation in TAU”**; *MEGAFLOW - Numerical Flow Simulation for Aircraft Design*, Vol. 89 of Notes on Numerical Fluid Mechanics and Multidisciplinary Design, Springer Verlag, 2005, pp. 109–115.
- [4] Arthur, M. T. and Petterson, K.; **“A Computational Study of the Low-Speed Flow Over the 1303 UCAV Configuration”**; *25th AIAA Applied Aerodynamics Conference, Miami (FL), United States, June 25–28, 2007*; No. 4568 in AIAA 2007.
- [5] Aupoix, B. and Spalart, P.; **“Extensions of the Spalart–Allmaras turbulence model to account for wall roughness”**; *International Journal of Heat and Fluid Flow*, Vol. 24, No. 4, 2003, pp. 454–462.
- [6] Barlow, J. B., Rae, W. H., and Pope, A.; **“Low-Speed Wind Tunnel Testing”**; 3rd Edition; Springer Verlag, ISBN 978-0-471-55774-6, 1999.
- [7] Blazek, J.; **“Computational Fluid Dynamics: Principles and Applications”**; 2nd Edition; Elsevier, ISBN 978-0-08-044506-9, 2005.
- [8] Boelens, O. J.; **“CFD Analysis of the Flow Around the X-31 Aircraft at High Angle of Attack”**; *Aerospace Science and Technology*, Vol. 20, No. 1, 2012, pp. 38–51.
- [9] Boelens, O. J.; Personal communication; 2015.
- [10] Boelens, O. J., Luckring, J. M., Breitsamter, C., Hövelmann, A., Knoth, F., Malloy, D., and Deck, S.; **“Numerical and Theoretical Considerations for the Design of the AVT-183 Diamond-Wing Experimental Investigations”**; *53rd AIAA Aerospace Sciences Meeting, Kissimmee (FL), United States, January 5–9, 2015*; No. 0062 in AIAA 2015.
- [11] Boelens, O. J., Badcock, K. J., Elmilgui, A., Abdol-Hamid, K. S., and Massey, S. J.; **“Comparison of Measured and Block Structured Simulation Results for the F-16XL Aircraft”**; *Journal of Aircraft*, Vol. 46, No. 2, 2009, pp. 377–384.

References

- [12] Boelens, O. J., Badcock, K. J., Görtz, S., Morton, S., Fritz, W., Karman, S. L., Michal, T., and Lamar, J. E.; “**F-16XL Geometry and Computational Grids Used in Cranked-Arrow Wing Aerodynamics Project International**”; *Journal of Aircraft*, Vol. 46, No. 2, 2009, pp. 369–376.
- [13] Braslow, A. L.; “**Review of the Effect of Distributed Surface Roughness on Boundary-Layer Transition**”; AGARD Report 254; Advisory Group for Aeronautical Research and Development, 1960.
- [14] Braslow, A. L. and Knox, E. C.; “**Simplified Method for Determination of Critical Height of Distributed Roughness Particles for Boundary-Layer Transition at Mach Numbers from 0 to 5**”; NACA Technical Note 4363; National Advisory Committee for Aeronautics, 1958.
- [15] Breitsamter, C.; “**Aerodynamic Efficiency of High Maneuverable Aircraft Applying Adaptive Wing Trailing Edge Section**”; *24th Congress of the International Council of the Aeronautical Sciences, Yokohama, Japan, August 29 – September 3, 2004*; No. 4.3.2 in ICAS 2004.
- [16] Breitsamter, C.; “**Turbulente Strömungsstrukturen an Flugzeugkonfigurationen mit Vorderkantenwirbeln**”; Dissertation, Technische Universität München; Herbert Utz Verlag, ISBN 3-89675-201-4, 1997.
- [17] Breitsamter, C.; “**Unsteady Flow Phenomena Associated with Leading-Edge Vortices**”; *Progress in Aerospace Sciences*, Vol. 44, No. 1, 2008, pp. 48–65.
- [18] Breitsamter, C.; “**Strömungsphysik und Modellgesetze**”; Lecture Notes; Technische Universität München, 2012.
- [19] Breitsamter, C.; Personal communication; 2015.
- [20] Breitsamter, C. and Laschka, B.; “**Vortical Flowfield Structure at Forward Swept-Wing Configurations**”; *Journal of Aircraft*, Vol. 38, No. 2, 2001, pp. 193–207.
- [21] Chu, J. and Luckring, J. M.; “**Experimental Surface Pressure Data Obtained on 65° Delta Wing Across Reynolds Number and Mach Number Ranges**”; NASA Technical Memorandum 4645; National Aeronautics and Space Administration, 1996.
- [22] Courant, R., Friedrichs, K., and Lewy, H.; “**On the Partial Difference Equations of Mathematical Physics**”; *IBM Journal of Research and Development*, Vol. 11, No. 2, 1967, pp. 215–237.
- [23] Cummings, R. M. and Schütte, A.; “**Integrated Computational/Experimental Approach to Unmanned Combat Air Vehicle Stability and Control Estimation**”; *Journal of Aircraft*, Vol. 49, No. 6, 2012, pp. 1542–1557.
- [24] Cummings, R. M. and Schütte, A.; “**Detached-Eddy Simulation of the vortical flow field about the VFE-2 delta wing**”; *Aerospace Science and Technology*, Vol. 24, No. 1, 2013, pp. 66–77.

-
- [25] Davey, A.; “**Boundary-layer flow at a saddle point of attachment**”; *Journal of Fluid Mechanics*, Vol. 10, No. 4, 1961, pp. 593–610.
- [26] DFVLR (ed.); “**Grenzschichtsteuerung durch Transitionsfixierung**”; DFVLR-Mitteilung 84-17; Institut für Experimentelle Strömungsmechanik der DFVLR, 1984.
- [27] Déleury, J. M.; “**Physics of Vortical Flows**”; *Journal of Aircraft*, Vol. 29, No. 5, 1992, pp. 856–876.
- [28] Déleury, J. M.; “**Robert Legendre and Henri Werlé: Toward the Elucidation of Three-Dimensional Separation**”; *Annual Review of Fluid Mechanics*, Vol. 33, No. 1, 2001, pp. 129–154.
- [29] DLR (ed.); “**TAU-Code User Guide Release 2015.1.0**”; Technical Report; DLR Institute of Aerodynamics and Flow Technology, 2015.
- [30] DLR (ed.); “**Technical Documentation of the DLR TAU-Code Release 2015.1.0**”; Technical Report; DLR Institute of Aerodynamics and Flow Technology, 2015.
- [31] Drougge, G.; “**The International Vortex Flow Experiment for Computer Code Validation**”; *16th Congress of the International Council of the Aeronautical Sciences, Jerusalem, Israel, August 28 – September 2, 1988*; No. 0.5, in ICAS 1988.
- [32] Dryden, H. D.; “**Review of Published Data on the Effect of Roughness on Transition from Laminar to Turbulent Flow**”; *Journal of the Aeronautical Sciences*, Vol. 20, No. 7, 1953, pp. 477–482.
- [33] Dwight, R. P.; “**Efficiency Improvements of RANS-Based Analysis and Optimization Using Implicit and Adjoint Methods on Unstructured Grids**”; PhD Thesis, University of Manchester; Deutsches Zentrum für Luft- und Raumfahrt (DLR), ISRN DLR-FB–2006-11, 2006.
- [34] Dwight, R. P., Lucas, P., and Bijl, H.; “**Solution Methods and Acceleration Techniques in CFD**”; *Encyclopedia of Aerospace Engineering*, 2010.
- [35] Edefur, H., Tormalm, M., Coppin, J., Birch, T., and Nangia, R. K.; “**Numerical study of blunt leading edge separation on a 53 degree swept diamond wing (STO AVT-183) using the Edge and Cobalt flow solver**”; *53rd AIAA Aerospace Sciences Meeting, Kissimmee (FL), United States, January 5–9, 2015*; No. 0290 in AIAA 2015.
- [36] Elsenaar, A., Hjelmberg, L., Bütetfisch, K., and Bannik, W. J.; “**The International Vortex Flow Experiment**”; *AGARD Fluid Dynamics Panel Symposium on "Validation of Computational Fluid Dynamics - Volume 1", Lisbon, Portugal, May 2–5, 1988*; No. 437 in AGARD Conference Proceedings.
- [37] Ferziger, J. H. and Perić, M.; “**Computational Methods for Fluid Dynamics**”; 3rd, rev. Edition; Springer Verlag, ISBN 978-3-540-42074-3, 2002.

References

- [38] Frink, N. T.; “**Numerical Analysis of Incipient Separation on 53° Swept Diamond Wing**”; *53rd AIAA Aerospace Sciences Meeting, Kissimmee (FL), United States, January 5–9, 2015*; No. 0288 in AIAA 2015.
- [39] Frink, N. T., Tormalm, M., and Schmidt, S.; “**Three Unstructured Computational Fluid Dynamics Studies on Generic Uninhabited Combat Air Vehicle**”; *Journal of Aircraft*, Vol. 49, No. 6, 2012, pp. 1619–1637.
- [40] Fritz, W.; “**Numerical Simulation of the Peculiar Subsonic Flow-Field About the VFE-2 Delta Wing With Rounded Leading Edge**”; *Aerospace Science and Technology*, Vol. 24, No. 1, 2013, pp. 45–55.
- [41] Fritz, W., Davis, M. B., Karman, S. L., and Michal, T.; “**Reynolds-Averaged Navier–Stokes Solutions for the CAWAPI F-16XL Using Different Hybrid Grids**”; *Journal of Aircraft*, Vol. 46, No. 2, 2009, pp. 409–422.
- [42] Furman, A. and Breitsamter, C.; “**Stereo-PIV and Hot-Wire Investigations on Delta Wing with Sharp and Rounded Leading Edge**”; *1st CEAS European Air and Space Conference, Berlin, Germany, September 10 – 13, 2007*; No. 430 in CEAS 2007.
- [43] Furman, A. and Breitsamter, C.; “**Turbulent and Unsteady Flow Characteristics of Delta Wing Vortex Systems**”; *Aerospace Science and Technology*, Vol. 24, No. 1, 2013, pp. 32–44.
- [44] Galle, M.; “**Ein Verfahren zur numerischen Simulation kompressibler, reibungsbehafteter Strömungen auf hybriden Netzen**”; Dissertation, Universität Stuttgart; Deutsches Zentrum für Luft- und Raumfahrt (DLR), ISRN DLR-FB–1999-04, 1999.
- [45] Garner, H. C., Rogers, E. W. E., Acum, W. E. A., and Maskell, E. C.; “**Subsonic Wind Tunnel Wall Corrections**”; AGARDograph 109; Advisory Group for Aeronautical Research and Development, 1966.
- [46] Gerhold, T.; “**Overview of the Hybrid RANS Code TAU**”; *MEGAFLOW - Numerical Flow Simulation for Aircraft Design*, Vol. 89 of Notes on Numerical Fluid Mechanics and Multidisciplinary Design, Springer Verlag, 2005, pp. 81–92.
- [47] Görtz, S., Jirásek, A., Morton, S. A., McDaniel, D. R., Cummings, R. M., Lamar, J. E., and Abdol-Hamid, K. S.; “**Standard Unstructured Grid Solutions for Cranked Arrow Wing Aerodynamics Project International F-16XL**”; *Journal of Aircraft*, Vol. 46, No. 2, 2009, pp. 385–408.
- [48] Gursul, I., Gordnier, R., and Visbal, M.; “**Unsteady Aerodynamics of Non-Slender Delta Wings**”; *Progress in Aerospace Sciences*, Vol. 41, No. 1, 2005, pp. 515–557.
- [49] Gursul, U.; “**Unsteady Flow Phenomena over Delta Wings at High Angle of Attack**”; *AIAA Journal*, Vol. 32, No. 2, 1994, pp. 225–231.

-
- [50] Gursul, U.; **“Review of Unsteady Vortex Flows over Slender Delta Wings”**; *Journal of Aircraft*, Vol. 42, No. 2, 2005, pp. 299–319.
- [51] Hirschel, E. H., Cousteix, J., and W.Kordulla; **“Three-Dimensional Attached Viscous Flow - Basic Principles and Theoretical Foundations”**; 1st Edition; Springer Verlag, ISBN 978-3-642-41377-3, 2014.
- [52] Hitzel, S. M.; **“Flightphysical Aspects and Methods of Future Military Aircraft Designs”**; *63rd Deutscher Luft- und Raumfahrtkongress, Augsburg, Germany, September 16–18, 2014*; Not published.
- [53] Hitzel, S. M.; **“Perform and Survive - Evolution of Some U(M)CAV Platform Requirements”**; *STO AVT Workshop on "Innovative Control Effectors for Military Vehicles"*, Stockholm, Sweden, May 20–22, 2013; No. 1 in STO-MP-AVT-215.
- [54] Hitzel, S. M., Boelens, O. J., van Rooij, M., and Hövelmann, A.; **“Vortex Development on the AVT-183 Diamond Wing Configuration - Numerical and Experimental Findings”**; *53rd AIAA Aerospace Sciences Meeting, Kissimmee (FL), United States, January 5–9, 2015*; No. 0289 in AIAA 2015.
- [55] Hitzel, S. M., Boelens, O. J., van Rooij, M., and Hövelmann, A.; **“Vortex development on the AVT-183 diamond wing configuration - numerical and experimental findings”**; *Aerospace Science and Technology*, 2015, Article in press, pp. 1–13; DOI: 10.1016/j.ast.2015.12.007.
- [56] Hummel, D.; **“Documentation of Separated Flows for Computational Fluid Dynamics Validation”**; *AGARD Fluid Dynamics Panel Symposium on "Validation of Computational Fluid Dynamics - Volume 2"*, Lisbon, Portugal, May 2–5, 1988; No. 437 in AGARD Conference Proceedings.
- [57] Hummel, D.; **“Effects of Boundary Layer Formation on the Vortical Flow above Slender Delta Wings”**; *RTO AVT Specialists' Meeting on "Enhancement of NATO Military Flight Vehicle Performance by Management of Interacting Boundary Layer Transition and Separation"*, Prague, Czech Republic, October 4–7, 2004; No. 30 in RTO-MP-AVT-111.
- [58] Hummel, D.; **“On the Vortex Formation Over a Slender Wing at Large Angles of Incidence”**; *AGARD Fluid Dynamics Panel Symposium on "High Angle of Attack Aerodynamics"*, Sandefjord, Norway, October 4–6, 1978; No. 247 in AGARD Conference Proceedings.
- [59] Hummel, D.; **“Experimentelle Untersuchung der Strömung auf der Saugseite eines schlanken Deltaflügels”**; *Zeitschrift für Flugwissenschaften*, Vol. 13, No. 7, 1965, pp. 247–252.
- [60] Hummel, D.; **“Untersuchungen über das Aufplatzen der Wirbel an schlanken Deltaflügeln”**; *Zeitschrift für Flugwissenschaften*, Vol. 13, No. 5, 1965, pp. 158–168.

References

- [61] Hummel, D.; “**Experimentelle Untersuchung dreidimensionaler laminarer Grenzschichten an einem schlanken Deltaflügel**”; *Zeitschrift für Flugwissenschaften und Weltraumforschung*, Vol. 10, No. 1, 1986, pp. 133–145.
- [62] Hummel, D.; “**The International Vortex Flow Experiment 2 (VFE-2) Background Objectives and Organization**”; *Aerospace Science and Technology*, Vol. 24, No. 1, 2013, pp. 1–9.
- [63] Hummel, D.; Personal communication; 2014.
- [64] Hunt, J. C. R., Abell, C. J., Peterka, J. A., and Woo, H.; “**Kinematical studies of the flows around free or surface-mounted obstacles; applying topology to flow visualization**”; *Journal of Fluid Mechanics*, Vol. 86, No. 1, 1978, pp. 179–200.
- [65] Hövelmann, A. and Breitsamter, C.; “**Experimental Investigations on Vortex Flow Phenomena of a Diamond Wing Configuration**”; *29th Congress of the International Council of the Aeronautical Sciences, St. Petersburg, Russia, September 7 – 12, 2014*; No. 4.1.1 in ICAS 2014.
- [66] Hövelmann, A. and Breitsamter, C.; “**Leading-Edge Geometry Effects on the Vortex System Formation of a Diamond Wing Configuration**”; *31st AIAA Applied Aerodynamics Conference, San Diego (CA), United States, June 24–27, 2013*; No. 3187 in AIAA 2013.
- [67] Hövelmann, A. and Breitsamter, C.; “**Leading-Edge Geometry Effects on the Vortex Formation of a Diamond-Wing Configuration**”; *Journal of Aircraft*, Vol. 52, No. 5, 2015, pp. 1596–1610.
- [68] Hövelmann, A., Knoth, F., and Breitsamter, C.; “**Leading-Edge Roughness Effects on the Flow Separation Onset of the AVT-183 Diamond Wing Configuration**”; *5^{3rd} AIAA Aerospace Sciences Meeting, Kissimmee (FL), United States, January 5–9, 2015*; No. 0063 in AIAA 2015.
- [69] Hövelmann, A., Knoth, F., and Breitsamter, C.; “**AVT-183 diamond wing flow field characteristics Part 1: Varying leading-edge roughness and the effects on flow separation onset**”; *Aerospace Science and Technology*, 2016, Article in press, pp. 1–13; DOI: 10.1016/j.ast.2016.01.002.
- [70] Hövelmann, A., Pfnür, S., and Breitsamter, C.; “**Flap Efficiency Analysis for the SAGITTA Diamond Wing Demonstrator Configuration**”; *CEAS Aeronautical Journal*, Vol. 6, No. 4, 2015, pp. 497–514.
- [71] Hövelmann, A., Grawunder, M., Buzica, A., and Breitsamter, C.; “**Experimental Analyses on the Flow Field Characteristics of the AVT-183 Diamond Wing Configuration**”; *5^{3rd} AIAA Aerospace Sciences Meeting, Kissimmee (FL), United States, January 5–9, 2015*; No. 0064 in AIAA 2015.

-
- [72] Hövelmann, A., Grawunder, M., Buzica, A., and Breitsamter, C.; “**AVT-183 diamond wing flow field characteristics Part 2: Experimental analysis of leading-edge vortex formation and progression**”; *Aerospace Science and Technology*, 2015, Article in press, pp. 1–12; DOI: 10.1016/j.ast.2015.12.023.
- [73] Jameson, A.; “**Time Dependent Calculations Using Multigrid, with Applications to Unsteady Flows Past Airfoils and Wings**”; *10th AIAA Computational Fluid Dynamics Conference, Honolulu (HI), United States, June 24–26, 1991*; No. 1596 in AIAA 1991.
- [74] Jameson, A.; “**Solution of the Euler Equations for Two Dimensional Transonic Flow by a Multigrid Method**”; *Applied Mathematics and Computation*, Vol. 13, No. 3–4, 1983, pp. 327–355.
- [75] Jameson, A.; “**Transonic Flow Calculations for Aircraft**”; *Numerical Methods in Fluid Dynamics*, Vol. 1127 of Lecture Notes in Mathematics, Springer Verlag, 1985, pp. 156–242.
- [76] Jameson, A., Schmidt, W., and Turkel, E.; “**Numerical Solutions of the Euler Equations by Finite Volume Methods Using Runge-Kutta Time-Stepping Schemes**”; *14th AIAA Fluid and Plasma Dynamics Conference, Palo Alto (CA), United States, June 23–25, 1981*; No. 1259 in AIAA 1981.
- [77] Jameson, A. and Yoon, S.; “**Lower-Upper Implicit Schemes with Multiple Grids for the Euler Equations**”; *AIAA Journal*, Vol. 25, No. 7, 1987, pp. 929–935.
- [78] Jirásek, A. and Cummings, R. M.; “**Reduced Order Modeling of X-31 Wind Tunnel Model Aerodynamic Loads**”; *Aerospace Science and Technology*, Vol. 20, No. 1, 2012, pp. 52–60.
- [79] Konrath, R., Klein, C., and Schröder, A.; “**PSP and PIV investigations on the VFE-2 configuration in sub- and transonic flow**”; *Aerospace Science and Technology*, Vol. 24, No. 1, 2013, pp. 22–31.
- [80] Konrath, R., Klein, C., Schröder, A., and Kompenhans, J.; “**Combined Application of Pressure Sensitive Paint and Particle Image Velocimetry to the Flow Above a Delta Wing**”; *Experiments in Fluids*, Vol. 44, No. 3, 2008, pp. 357–366.
- [81] Lachmann (ed.), G. V.; “**Boundary Layer and Flow Control - Its Principles and Application, Volume 2**”; Pergamon Press, ISBN 978-1-4832-1323-1, 1961.
- [82] Lambourne, N. C. and Dryer, D. W.; “**Some Measurements in the Vortex Flow Generated by a Sharp Leading Edge Having 65 Degrees Sweep**”; ARC Current Papers 477; Aeronautical Research Council, 1960.
- [83] Lambourne, N. C. and Dryer, D. W.; “**The Bursting of Leading-Edge Vortices. Some Observations and Disussions of the Phenomenon**”; ARC Reports and Memoranda 3282; Aeronautical Research Council, 1962.

References

- [84] Legendre, R.; “**Separation de l’écoulement laminaire tridimensionnel (Separation of a Laminar Three-Dimensional Flow)**”; *La Recherche Aeronautique*, Vol. 54, No. 1, 1956, pp. 3–8.
- [85] Lighthill, M. J.; “**Attachment and Separation in Three-Dimensional Flow**”; pp. 72 –82 in *Laminar Boundary Layers*, L. Rosenhead (ed.); Oxford University Press, ISBN 978-0-1985-6315-0, 1963.
- [86] Luckring, J. M.; “**A Survey of Factors Affecting Blunt Leading-Edge Separation for Swept and Semi-Slender Wings**”; *28th AIAA Applied Aerodynamics Conference, Chicago (IL), United States, June 28 – July 01, 2010*; No. 4820 in AIAA 2010.
- [87] Luckring, J. M.; “**Compressibility and Leading-Edge Bluntness Effects for a 65° Delta Wing**”; *42nd AIAA Aerospace Sciences Meeting and Exhibit, Reno (NV), United States, January 5–8, 2004*; No. 765 in AIAA 2004.
- [88] Luckring, J. M.; “**Reynolds Number and Leading-Edge Bluntness Effects on a 65° Delta Wing**”; *40th AIAA Aerospace Sciences Meeting and Exhibit, Reno (NV), United States, January 14–17, 2002*; No. 419 in AIAA 2002.
- [89] Luckring, J. M.; “**Reynolds Number, Compressibility, and Leading-Edge Bluntness Effects on Delta-Wing Aerodynamics**”; *24th Congress of the International Council of the Aeronautical Sciences, Yokohama, Japan, August 29 – September 3, 2004*; No. 4.1.4 in ICAS 2004.
- [90] Luckring, J. M.; “**Transonic Reynolds Number and Leading-Edge Bluntness Effects on a 65° Delta Wing**”; *41st AIAA Aerospace Sciences Meeting and Exhibit, Reno (NV), United States, January 6–9, 2003*; No. 753 in AIAA 2003.
- [91] Luckring, J. M.; “**Initial experiments and analysis of blunt-edge vortex flows for VFE-2 configurations at NASA Langley, USA**”; *Aerospace Science and Technology*, Vol. 24, No. 1, 2013, pp. 10–21.
- [92] Luckring, J. M. and Boelens, O. J.; “**A Reduced-Complexity Investigation of Blunt Leading-Edge Separation Motivated by UCAV Aerodynamics**”; *53rd AIAA Aerospace Sciences Meeting, Kissimmee (FL), United States, January 5–9, 2015*; No. 0061 in AIAA 2015.
- [93] Luckring, J. M. and Hummel, D.; “**What was learned from the new VFE-2 experiments**”; *Aerospace Science and Technology*, Vol. 24, No. 1, 2013, pp. 77–88.
- [94] Mavriplis, D. J. and Jameson, A.; “**Multigrid Solution of the Navier-Stokes Equations on Triangular Meshes**”; *AIAA Journal*, Vol. 28, No. 8, 1990, pp. 1415–1425.
- [95] Melber-Wilkending, S., Brodersen, O., Kallinderis, Y., Wilhelm, R., Sutcliffe, M., Wild, J., and Ronzheimer, A.; “**Hybrid unstructured Grid Generation in MEGAFLOW**”; *MEGAFLOW - Numerical Flow Simulation for Aircraft Design*, Vol. 89 of Notes on Numerical Fluid Mechanics and Multidisciplinary Design, Springer Verlag, 2005, pp. 3–24.

-
- [96] Mendenhall, M. R., Perkins Jr., S. C., Tomac, M., Rizzi, A., and Nangia, R. K.; “**Comparing and Benchmarking Engineering Methods for the Prediction of X-31 Aerodynamics**”; *Aerospace Science and Technology*, Vol. 20, No. 1, 2012, pp. 12–20.
- [97] Nikuradse, J.; “**Strömungsgesetze in rauhen Rohren**”; VDI-Forschungsheft; 361. Beilage zu Forschung auf dem Gebiete des Ingenieurwesens, 1933.
- [98] Obara, C. J. and Lamar, J. E.; “**Overview of the Cranked-Arrow Wing Aerodynamics Project International**”; *Journal of Aircraft*, Vol. 46, No. 2, 2009, pp. 355–368.
- [99] Osterhuber, R.; “**FCS-Requirements for Combat Aircraft – Lessons Learned for Future Designs**”; *STO AVT Workshop on "Innovative Control Effectors for Military Vehicles"*, Stockholm, Sweden, May 20–22, 2013; No. KN-5 in STO-MP-AVT-215.
- [100] Peake, D. J.; “**Controlled and Uncontrolled Flow Separation in Three Dimensions**”; NRCC Aeronautical Report LR-591; National Research Council Canada, 1976.
- [101] Raffel, M., Willert, C. E., Wereley, S. T., and Kompenhans, J.; “**Particle Image Velocimetry – A Practical Guide**”; 2nd Edition; Springer Verlag, ISBN 978-3-540-72307-3, 2007.
- [102] Rivers, M. B. and Dittberner, A.; “**Experimental Investigations of the NASA Common Research Model**”; *Journal of Aircraft*, Vol. 51, No. 4, 2014, pp. 1183–1193.
- [103] Rizzi, A., Jirásek, A., Lamar, J. E., Crippa, S., Badcock, K. J., and Boelens, O. J.; “**Lessons Learned from Numerical Simulations of the F-16XL Aircraft at Flight Conditions**”; *Journal of Aircraft*, Vol. 46, No. 2, 2009, pp. 423–441.
- [104] Rohlf, D., Schmidt, S., and Irving, J.; “**Stability and Control Analysis for an Unmanned Aircraft Configuration Using System-Identification Techniques**”; *Journal of Aircraft*, Vol. 49, No. 6, 2012, pp. 1597–1609.
- [105] Roosenboom, E. W. M., Konrath, R., Schröder, A., Pallek, D., and Otter, D.; “**Stereoscopic Particle Image Velocimetry Flowfield Investigation of an Unmanned Combat Air Vehicle**”; *Journal of Aircraft*, Vol. 49, No. 6, 2012, pp. 1584–1596.
- [106] RTO (ed.); “**Understanding and Modeling Vortical Flows to Improve the Technology Readiness Level for Military Aircraft**”; Final Report TR-AVT-113; NATO Research and Technology Organization, 2009.
- [107] RTO (ed.); “**Vortex Breakdown over Slender Delta Wings**”; Final Report TR-AVT-080; NATO Research and Technology Organization, 2009.
- [108] RTO (ed.); “**Assessment of Stability and Control Prediction Methods for NATO Air and Sea Vehicles**”; Final Report TR-AVT-161; NATO Research and Technology Organization, 2012.
- [109] Schlichting, H. and Gersten, K.; “**Grenzschicht-Theorie**”; 10th, rev. Edition; Springer Verlag, ISBN 978-3-540-23004-5, 2006.

References

- [110] Schlichting, H. and Truckenbrodt, E.; **“Aerodynamik des Flugzeuges, Erster Band: Grundlagen aus der Strömungstechnik Aerodynamik des Tragflügels (Teil I)”**; 3rd Edition; Springer Verlag, ISBN 978-3-642-63148-1, 2001.
- [111] Schütte, A., Cummings, R. M., and Loeser, T.; **“An Integrated Computational / Experimental Approach to X-31 Stability & Control Estimation”**; *Aerospace Science and Technology*, Vol. 20, No. 1, 2012, pp. 2–11.
- [112] Schütte, A., Hummel, D., and Hitzel, S. M.; **“Flow Physics Analyses of a Generic Unmanned Combat Aerial Vehicle Configuration”**; *Journal of Aircraft*, Vol. 49, No. 6, 2012, pp. 1638–1651.
- [113] Schütte, A. and Lüdeke, H.; **“Numerical Investigations on the VFE-2 65-Degree Rounded Leading Edge Delta Wing Using the Unstructured DLR TAU-Code”**; *Aerospace Science and Technology*, Vol. 24, No. 1, 2013, pp. 56–65.
- [114] Schütte, A., Einarsson, G., Raichle, A., Schöning, B., and Mönnich, W.; **“Numerical Simulation of Maneuvering Aircraft by Aerodynamic, Flight-Mechanics, and Structural-Mechanics Coupling”**; *Journal of Aircraft*, Vol. 46, No. 1, 2009, pp. 53–64.
- [115] Schütte, A., Boelens, O. J., Oehlke, M., Jirásek, A., and Loeser, T.; **“Prediction of the Flow Around the X-31 Aircraft Using Three Different CFD Methods”**; *Aerospace Science and Technology*, Vol. 20, No. 1, 2012, pp. 21–37.
- [116] Schwamborn, D., Gerhold, T., and Heinrich, R.; **“The DLR TAU-Code: Recent Applications in Research and Industry”**; *4th European Conference on Computational Fluid Dynamics (ECCOMAS CFD 2006)*, Egmond aan Zee, The Netherlands, September 5–8, 2006.
- [117] Seifert, J.; **“SAGITTA - Nationale Forschungskooperation für fortschrittliche UAV-Technologien im Rahmen der Open Innovation Initiative von Cassidian”**; *61st Deutscher Luft- und Raumfahrtkongress, Berlin, Germany, September 10–12, 2012*; No. 1352 in DLRK 2012.
- [118] Smith, A. M. O. and Clutter, D. W.; **“The Smallest Height of Roughness Capable of Affecting Boundary-Layer Transition”**; *Journal of the Aerospace Sciences*, Vol. 26, No. 1, 1959, pp. 229–245.
- [119] Spalart, P. R. and Allmaras, S. R.; **“A One-Equation Turbulence Model for Aerodynamic Flows”**; *30th AIAA Aerospace Sciences Meeting & Exhibit, Reno (NV), United States, January 6–9, 1992*; No. 439 in AIAA 1992.
- [120] Spalart, P. R. and Allmaras, S. R.; **“A One-Equation Turbulence Model for Aerodynamic Flows”**; *La Recherche Aéronautique*, No. 1, 1994, pp. 5–21.
- [121] Stanislas, M., Okamoto, K., Kähler, C. J., and Westerweel, J.; **“Main results of the Second International PIV Challenge”**; *Experiments in Fluids*, Vol. 39, No. 2, 2005, pp. 170–191.

-
- [122] Staudacher, W.; “**Die Beeinflussung von Vorderkantenwirbelsystemen schlanker Tragflügel**”; Dissertation, Universität Stuttgart; 1992.
- [123] Stenfelt, G. and Ringertz, U.; “**Lateral Stability and Control of a Tailless Aircraft Configuration**”; *Journal of Aircraft*, Vol. 46, No. 6, 2009, pp. 2161–2164.
- [124] STO (ed.); “**Reliable Prediction of Separated Flow Onset and Progression for Air and Sea Vehicles**”; Final Report TR-AVT-183; NATO Science and Technology Organization, in press.
- [125] Tani, I.; “**History of Boundary-Layer Theory**”; *Annual Review of Fluid Mechanics*, Vol. 9, No. 1, 1977, pp. 87–111.
- [126] Tani, I., Hama, R., and Mituisi, S.; “**On the Permissible Roughness in the Laminar Boundary Layer**”; Report No. 199; Aeronautical Research Institute Tokyo, 1940.
- [127] Tobak, M. and Peake, D. J.; “**Topology of Three-Dimensional Separated Flows**”; *Annual Review of Fluid Mechanics*, Vol. 14, No. 1, 1982, pp. 61–85.
- [128] Tollmien, W., Schlichting, H., and Görtler, H.; “**Ludwig Prandtl Gesammelte Abhandlungen, Kap.51**”; Springer Verlag, ISBN 978-3-662-11837-5, 1961.
- [129] Tomac, M., Rizzi, A., Nangia, R. K., Mendenhall, M. R., and Perkins Jr., S. C.; “**Engineering Methods Applied to an Unmanned Combat Air Vehicle Configuration**”; *Journal of Aircraft*, Vol. 49, No. 6, 2012, pp. 1610–1618.
- [130] Truckenbrodt, E.; “**Fluidmechanik Band 1: Grundlagen und elementare Strömungsvorgänge dichtebeständiger Fluide**”; 4th, enl. Edition; Springer Verlag, ISBN 978-3-540-79017-4, 2008.
- [131] Truckenbrodt, E.; “**Fluidmechanik Band 2: Elementare Strömungsvorgänge dichte-eränderlicher Fluide sowie Potential- und Grenzschichtströmungen**”; 4th, enl. Edition; Springer Verlag, ISBN 978-3-540-79023-5, 2008.
- [132] Turkel, E.; “**Improving the Accuracy of Central Difference Schemes**”; NASA Contractor Report 181712; National Aeronautics and Space Administration, 1988.
- [133] Vicroy, D. D., Loeser, T. D., and A.Schütte; “**Static and Forced-Oscillation Tests of a Generic Unmanned Combat Air Vehicle**”; *Journal of Aircraft*, Vol. 49, No. 6, 2012, pp. 1558–1583.
- [134] von Doenhoff, A. E. and Horton, E. A.; “**A Low-Speed Experimental Investigation of the Effect of a Sandpaper Type of Roughness on Boundary-Layer Transition**”; NACA Technical Report 1349; National Advisory Committee for Aeronautics, 1958.
- [135] Wagner, S., Bode, A., Satzger, H., and Brehm, M.; “**High Performance Computing in Science and Engineering – Garching/Munich 2014**”; Technical Report; Bayerische Akademie der Wissenschaften, ISBN 978-3-9816675-0-9, 2014.

Appendix A

Experimental Approach

Wind Tunnel Test Facility

Table A.1 and Table A.2 state additional information on the W/T facility A of TUM-AER. On the one hand, the main characteristics in terms of geometric details and performance data are given. On the other hand, corresponding parameters describing the flow quality within the test section are summarized.

Cross-section of the test section	Contraction ratio	Test section length	Maximum power	Maximum velocity
1.8 m x 2.4 m	7:1	4.8 m	420 kW	65 m/s (open) 75 m/s (closed)

Table A.1: Characteristic data of the W/T facility A of TUM-AER.

Turbulence intensity	$Tu_x = Tu_y = Tu_z$	$< 0.4\%$ (open) $< 0.2\%$ (closed)
Angle divergence	$\Delta\alpha = \Delta\beta$	$< 0.2^\circ$
Static pressure deviation	$\Delta p/q_\infty$	$\leq 0.4\%$
Temporal speed non-uniformity at $x = 1.5\text{ m}, r_{ts} \leq 0.8\text{ m}$	$U_\infty \leq 20\text{ m/s} :$ $U_\infty > 20\text{ m/s} :$	$\Delta U_\infty \leq 0.12\text{ m/s}$ $\Delta U_\infty \leq 0.0067 \cdot U_\infty$
Spatial speed non-uniformity at $x = 1.5\text{ m}, r_{ts} \leq 0.8\text{ m}$	$U_\infty \leq 20\text{ m/s} :$ $U_\infty > 20\text{ m/s} :$	$\Delta U_\infty \leq 0.12\text{ m/s}$ $\Delta U_\infty \leq 0.0067 \cdot U_\infty$
Maximum unit Reynolds number	$R_{ts,max}$	$4.9 \cdot 10^6$, per meter

Table A.2: Flow quality of the W/T facility A of TUM-AER.

Appendix B

Analysis of Partly-Developed Leading-Edge Vortices

Applied W/T Corrections

To compare the numerical data of the AVT-183 configuration most efficiently with the experimental results of the semi-span W/T model, Coppin et al. suggested the application of W/T corrections, which consider the lift interference effects between the W/T model and the open-jet boundary [35]. Solid and wake blockage corrections are thought to be comparatively small in this case and are not considered, since the W/T test section is of open-jet type and the W/T model volume is low. The applied W/T corrections overall rely on comprehensive findings that were summarized by Garner et al. in an AGARDograph [45]. The W/T corrections are based on some assumptions, which are briefly summarized:

- The W/T model is mounted on the peniche on the W/T wall. The wall acts as a symmetry plane, see Figure B.1.
- The W/T corrections are calculated for an equivalent W/T tunnel with double the cross-sectional area.
- The W/T corrections are based on boundary correction factors. The upwash is assumed to vary linearly in the free stream direction.
 - δ_0 : Non-dimensional mean value of the W/T tunnel upwash due to lift.
 - δ_1 : Streamwise variation of upwash due to lift.
- The correction factors are accessible from literature [45] and linear theory. They result in $\delta_0 = -0.2$ and $\delta_1 = -0.275$ [35].

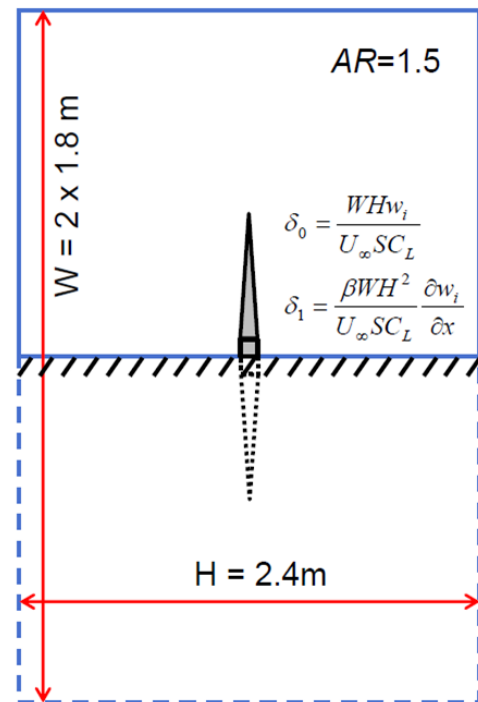


Figure B.1: Sketch of mirrored W/T test section for the applied W/T correction [35].

Analysis of Partly-Developed Leading-Edge Vortices

The W/T corrections are applied to the experimental reference data such that the lift coefficient remains unchanged. In consequence, Equations B.1 to B.3 describe the angle-of-attack correction and the corrections to the drag and pitching-moment coefficient, respectively:

$$\Delta\alpha = \left(\delta_0 + \frac{\bar{c}\delta_1}{2\beta h} \right) \cdot \frac{SC_L}{C} \quad (\text{B.1})$$

$$\Delta C_D = \delta_0 \cdot \frac{SC_L^2}{C} \quad (\text{B.2})$$

$$\Delta C_{my} = \frac{\bar{c}\delta_1}{16\beta h} \cdot \left[\left(\frac{\bar{c}}{\bar{c}} \right)^2 + \frac{1}{3} (\Lambda \cdot \tan \varphi_{50\%})^2 \cdot \left(2 - \frac{\bar{c}}{\bar{c}} \right) \right] \cdot \frac{SC_L}{C} \cdot \frac{\partial C_L}{\partial \alpha} \quad (\text{B.3})$$

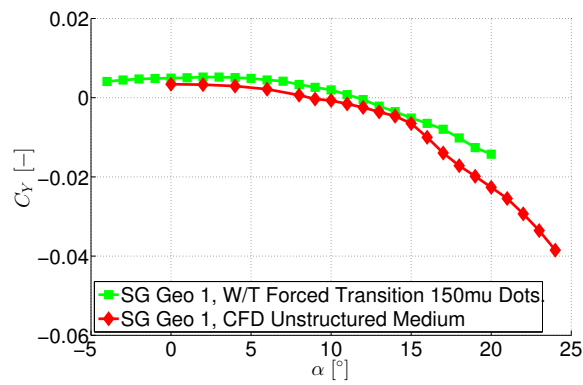
Appendix C

Passive Flow Control by Leading-Edge Contour Modifications

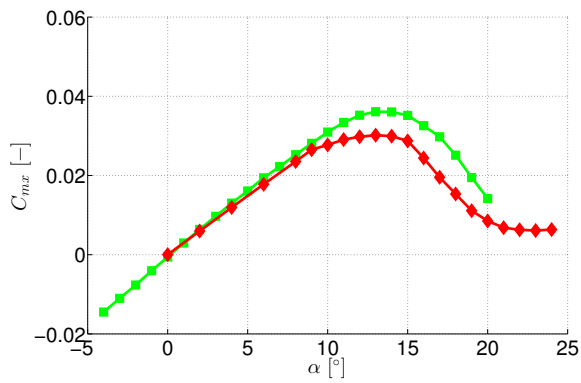
Flow Physics Analysis – Lateral Motion

Additional information on the reference configuration SG Geo 1 is presented. At first, complementary plots with respect to the validation of the numerical method are shown. For the sideslip angle of $\beta = -10^\circ$, Figure C.1 and Figure C.2 depict the aerodynamic coefficients and corresponding surface pressure coefficient distributions in selected chordwise sections. In line with the analysis of Section 6.1.1, both the CFD data and the W/T results are plotted. At low to medium angles of attack, very good correlations are observed. With increasing angle of attack, deviations between the CFD and W/T results become obvious, but the overall trend is matched. The corresponding chordwise pressure coefficient distributions show small differences in the prediction of the IB LE vortex suction peak and the flow separation onset characteristics in the outboard wing section. These observations hold likewise for the sideslip angle of $\beta = 10^\circ$, which in summary leads to small differences in the prediction of the occurring asymmetric flow phenomena between the numerics and the experiments. Finally, this then results in slightly different predictions of the lateral aerodynamic coefficients with increasing angle of attack.

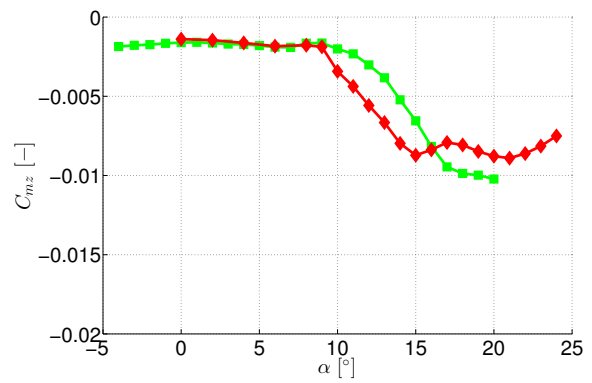
Next, the near-wall flow field characteristics of the lateral motion with a sideslip angle of $\beta = 10^\circ$ are considered, see Figure C.3. The case with $\beta = -10^\circ$ has already been discussed in Section 6.1.2. Compared to the flow physics associated with $\beta = -10^\circ$ and $\beta = 0^\circ$, respectively, no OB or MB LE vortex structures emerge on the right semi-span wing. Instead, the outboard recirculation region of irregular separated flow is even more dominant with increasing angle of attack. Consequently, vortex separation effects are only present due to the inboard sharp leading-edge contour. Overall, the flow field characteristics presented in Figure C.3 at $\beta = 10^\circ$ correspond to those on the left semi-span wing with $\beta = -10^\circ$. In summary, both cases thus define the asymmetric flow phenomena with different flow separation onset and progression characteristics that occur on the reference configuration SG Geo 1 in the lateral motion. These flow phenomena then influence the integral forces and moments in the lateral degrees of freedom as shown in Figure C.1 to Figure C.2.



(a) Side force coefficient.



(b) Rolling-moment coefficient.



(c) Yawing-moment coefficient.

Figure C.1: CFD validation – Lateral aerodynamic coefficients versus angle of attack α at $\beta = -10^\circ$, configuration SG Geo 1.

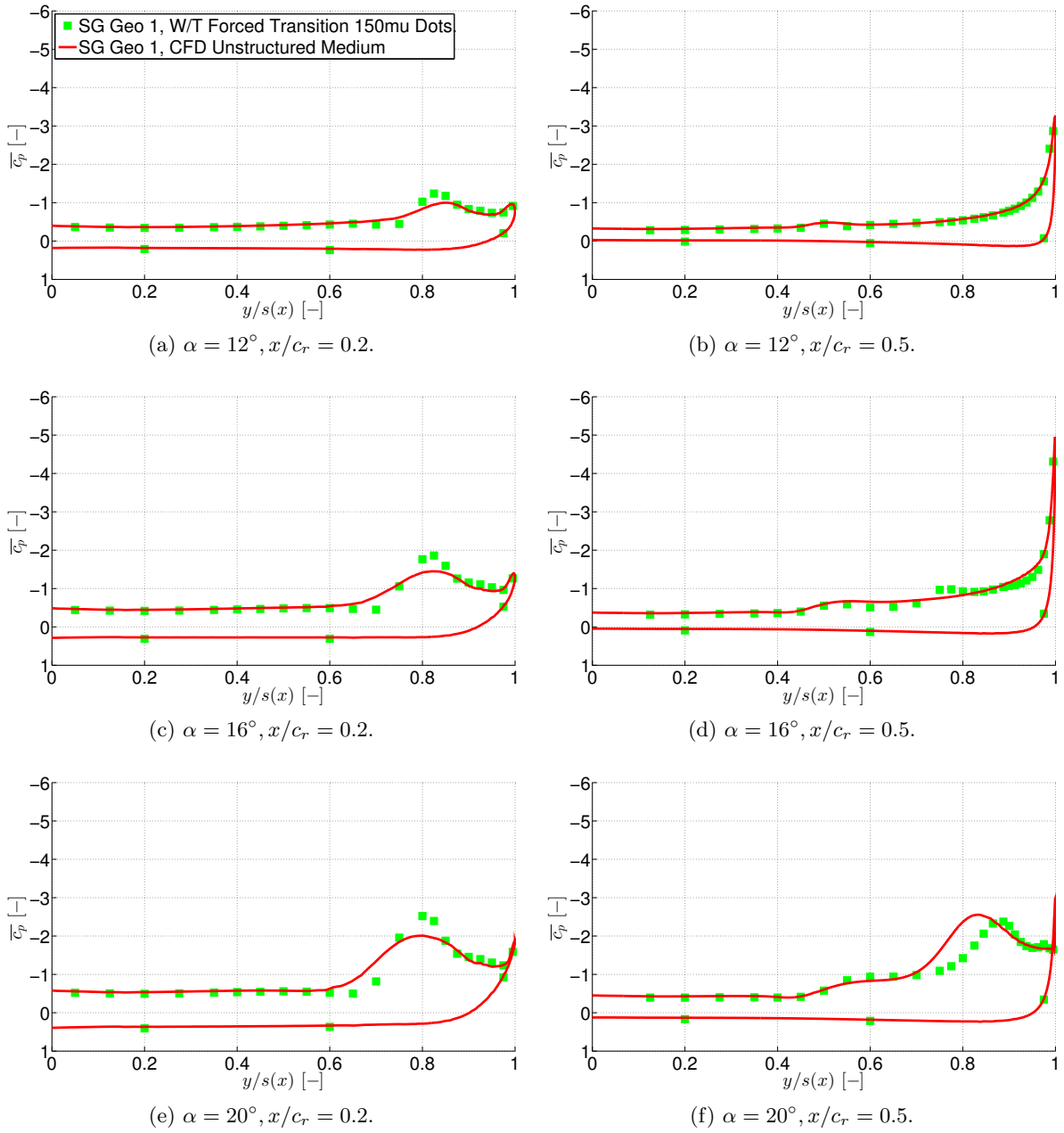


Figure C.2: CFD validation – Surface pressure coefficient \bar{c}_p versus semi-span $y/s(x)$ at $\beta = -10^\circ$, configuration SG Geo 1.

Passive Flow Control by Leading-Edge Contour Modifications

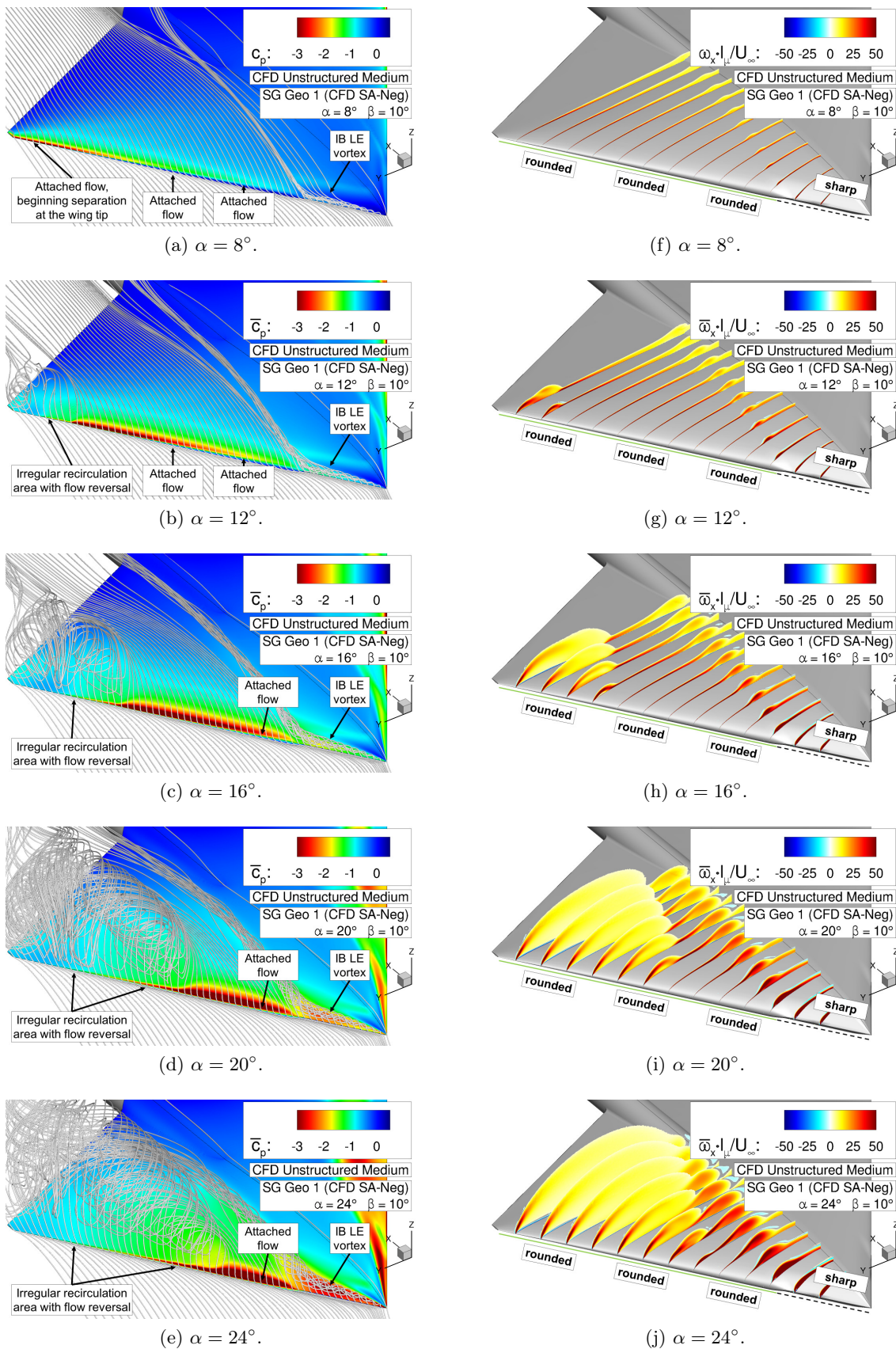


Figure C.3: Flow physics analysis of configuration SG Geo 1 – Surface pressure coefficient \bar{c}_p including streamlines, and axial vorticity contours $\omega_x \cdot l_\mu / U_\infty$ at $\beta = 10^\circ$.